



National Library
of Canada

Bibliothèque nationale
du Canada

Canadian Theses Service Service des thèses canadiennes

Ottawa, Canada
K1A 0N4

NOTICE

The quality of this microform is heavily dependent upon the quality of the original thesis submitted for microfilming. Every effort has been made to ensure the highest quality of reproduction possible.

If pages are missing, contact the university which granted the degree.

Some pages may have indistinct print especially if the original pages were typed with a poor typewriter ribbon or if the university sent us an inferior photocopy.

Reproduction in full or in part of this microform is governed by the Canadian Copyright Act, R.S.C. 1970, c. C-30, and subsequent amendments.

AVIS

La qualité de cette microforme dépend grandement de la qualité de la thèse soumise au microfilmage. Nous avons tout fait pour assurer une qualité supérieure de reproduction.

S'il manque des pages, veuillez communiquer avec l'université qui a conféré le grade.

La qualité d'impression de certaines pages peut laisser à désirer, surtout si les pages originales ont été dactylographiées à l'aide d'un ruban usé ou si l'université nous a fait parvenir une photocopie de qualité inférieure.

La reproduction, même partielle, de cette microforme est soumise à la Loi canadienne sur le droit d'auteur, SRC 1970, c. C-30, et ses amendements subséquents.

UNIVERSITY OF ALBERTA

**INELASTIC TRANSVERSE SHEAR CAPACITY OF LARGE
FABRICATED STEEL TUBES**

BY

KHALED HELMY OBAIA



A THESIS
SUBMITTED TO THE FACULTY OF GRADUATE STUDIES AND RESEARCH
IN PARTIAL FULFILLMENT OF THE REQUIREMENTS FOR THE DEGREE
OF

DOCTOR OF PHILOSOPHY

IN

CIVIL ENGINEERING

EDMONTON, ALBERTA
SPRING 1991



National Library
of Canada

Bibliothèque nationale
du Canada

Canadian Theses Service Service des thèses canadiennes

Ottawa, Canada
K1A 0N4

The author has granted an irrevocable non-exclusive licence allowing the National Library of Canada to reproduce, loan, distribute or sell copies of his/her thesis by any means and in any form or format, making this thesis available to interested persons.

The author retains ownership of the copyright in his/her thesis. Neither the thesis nor substantial extracts from it may be printed or otherwise reproduced without his/her permission.

L'auteur a accordé une licence irrévocable et non exclusive permettant à la Bibliothèque nationale du Canada de reproduire, prêter, distribuer ou vendre des copies de sa thèse de quelque manière et sous quelque forme que ce soit pour mettre des exemplaires de cette thèse à la disposition des personnes intéressées.

L'auteur conserve la propriété du droit d'auteur qui protège sa thèse. Ni la thèse ni des extraits substantiels de celle-ci ne doivent être imprimés ou autrement reproduits sans son autorisation.

ISBN 0-315-66755-9

UNIVERSITY OF ALBERTA

RELEASE FORM

Name of Author: **Khaled Helmy El-Bahi Obaia**

Title of Thesis: **Inelastic Transverse Shear Capacity of
Large Fabricated Steel Tubes**

Degree Granted: **Doctor of Philosophy in Civil Engineering**

Year Granted: **1991**

Permission is hereby granted to the University of Alberta Library to reproduce single copies of this thesis and to lend or sell such copies for private scholarly or scientific research purposes only.

The author reserves other publication rights, and neither the thesis nor extensive extracts from it may be printed or otherwise reproduced without the author's written permission.




Khaled H. E. Obaia
Civil Eng. Dept.
U of A, Edm., AB
T6G 2G7

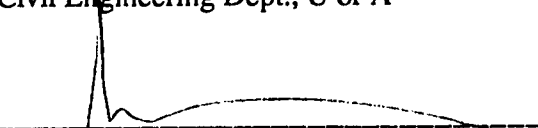
Date: April 3, 1991

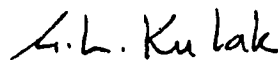
UNIVERSITY OF ALBERTA


FACULTY OF GRADUATE STUDIES AND RESEARCH


The undersigned certify that they have read, and recommend to the Faculty of Graduate Studies and Research for Acceptance, a thesis entitled "Inelastic Transverse Shear Capacity of Large Fabricated Steel Tubes" submitted by Khaled Helmy El-Bahi Obaia in partial fulfillment of the requirements for the degree of doctor of philosophy in Civil Engineering.

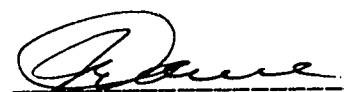

Prof. A. E. Peterson (Chairman)
Civil Engineering Dept., U of A


Prof. A. E. Elwi (Supervisor)
Civil Engineering Dept., U of A


Prof. G. L. Kulak (Co-Supervisor)
Civil Engineering Dept., U of A


Prof. T. M. Hruday
Civil Engineering Dept., U of A


Prof. J. S. Kennedy
Mechanical Engineering Dept., U of A


Prof. J. L. Dawe
Civil Engineering Dept., UNB

Date Jan. 18, 1991

to my father, Helmy

Abstract

Thin-walled cylinders are often used in civil engineering structures. Offshore platforms, storage tanks, nuclear reactor vessels, transmission towers, and material-handling plants are examples of structures incorporating these tubular members. In cases where tubes are subjected to transverse loading, failure may occur in a shear mode due to local buckling. The present study focuses on the inelastic shear buckling capacity of thin-walled fabricated steel tubes.

The problem was investigated in two phases, experimental and numerical. The experimental phase involved testing two specimens of 1270 mm diameter under different boundary conditions. The tests were preceded by finite element simulation in order that possible problems could be identified. Measurement of the geometric imperfections was made prior to testing and the testing itself was carried out in both the pre-buckling and the post-buckling ranges. During the testing the strains and displacements of the specimens and the supports were carefully monitored. The finite element predictions and predictions made using other design equations compared favorably with the test results.

A parametric study was then carried out to examine the effect of several factors on the cylinder behavior. The numerical model used in this analysis consisted of bi-cubic degenerated plate-shell elements and included the geometric imperfections and the initial stresses due to forming that are inherent in large-diameter cylinders.

The results of the analysis were compared with test results when possible.

The numerical phase was followed by two attempts to introduce design methods for determining the inelastic shear capacity of transversely loaded cylinders. A regression model was developed to predict the ultimate shear strength of the available test results with accuracy better than the current design equations. For the prediction of the shear capacity beyond the limit point, a truss model was proposed. The truss model was based on the post-buckling load-carrying mechanism observed in the tests and confirmed by the numerical simulation. The proposed model describes the shear behavior of thin-walled cylinders better than other post-buckling models. The capacity predicted by the proposed model can be used as a conservative predictor of the ultimate shear capacity.

Acknowledgements

This study has been an exceptional learning experience for me, and there are many people to whom I owe special notes of gratitude. First of all, I am deeply indebted to my supervisors, Professor Alaa E. Elwi and Professor Geoffrey L. Kulak, for their immeasurable guidance throughout both the research and the writing stages, for their support in the dark corners often encountered, and above all for their irreplaceable friendship.

I also wish to thank my examiners, Professor Terry M. Hruday and Professor John L. Dawe for their valuable suggestions and comments. I am specially grateful to my colleagues, Gilbert Grondin and Vasile Roman for their timely help and stimulating discussions.

The experimental phase of this study was carried out at the I. F. Morrison Structural Laboratory. The assistance of the lab. technicians Richard Helfrich and Larry Burden is greatly appreciated.

I would like to acknowledge the financial support provided by the Department of Civil Engineering at the University of Alberta, and by grants from the National Science and Engineering Research Council of Canada through Dr. Elwi and Dr. Kulak.

Finally, I would like to express my undying gratitude to my families, the one I always had in Egypt and the one I have discovered in Canada. To Helmy, Fatma, Amr, Hossam, and Salwa, thank you for your endless support, patience, and love.

Table of Contents

1. Introduction	1
1.1 Background	1
1.2 Statement of the Problem	3
1.3 Objectives	3
1.4 Layout of the Thesis	4
2. Literature Review.....	8
2.1 Introduction	8
2.1.1 Historical Review	8
2.1.2 Overview	9
2.2 Buckling of Unstiffened Cylinders	11
2.2.1 Effect of Imperfections and Residual Stresses...	11
2.2.2 Cylinders Subjected to Axial Compression	14
2.2.3 Cylinders Subjected to Pure Bending	19
2.2.4 Cylinders Subjected to Torsion	24
2.2.5 Cylinders Subjected to Transverse Loading	28
2.3 Summary	39
3. Testing of Fabricated Cylinders Subjected to Transverse Loading	46
3.1 Introduction	46
3.2 Test Design	47
3.2.1 Design Equations	47
3.2.2 Finite Element Analysis	50
3.3 Shear Specimen S1	51
3.3.1 Specimen Description	51
3.3.2 Test Frame	54
3.3.3 Instrumentation	55
3.3.4 Spacers	58
3.3.5 Welding	58
3.3.6 Testing Procedure	59
3.3.7 Test Results	60
3.3.8 Discussion	62

3.4 Shear Specimen S2	65
3.4.1 Specimen Description	65
3.4.2 Test Frame	65
3.4.3 Instrumentation	67
3.4.4 Estimated Failure Load	68
3.4.5 Testing Procedure	68
3.4.6 Test Results	70
3.4.7 Discussion	71
3.5 Summary	72
4. Numerical Analysis	98
4.1 Introduction	98
4.2 NISA Code	99
4.3 Preliminary Analysis	103
4.4 Models of Tested Cylinders	105
4.4.1 Specimen S1	106
4.4.2 Specimen S2	111
4.4.3 Other Tests	113
4.5 Parametric Analysis	114
4.5.1 Model Descriptions	114
4.5.2 Ultimate Shear Capacity	116
4.5.3 Post-Buckling Behavior	117
4.6 Summary	120
5. Regression Analysis	149
5.1 Introduction	149
5.2 Regression Variables and Data Set	149
5.3 Regression Analysis of the Data Set	154
5.3.1 Linear Models	154
5.3.2 Nonlinear Models	157
5.3.2.1 Regression Subroutine	157
5.3.2.2 Model Groups	158
5.4 Regression Analysis of the Experimental Data	164
5.5 Shear Capacity Equation	171
6. A Truss Model for the Post-Buckling Shear Capacity	185

6.1 Introduction	185
6.2 Tension Field Models for Thin-Walled Cylinders	186
6.3 Proposed Truss Model	192
6.3.1 Assumptions	192
6.3.2 Derivation of Shear Capacity	196
6.3.3 Model Mechanism	204
6.3.4 Design Charts	205
6.4 Assessment of the Proposed Model	207
6.4.1 Comparison with Tests	207
6.4.2 Comparison with Buckling Equation	210
6.4.3 Comparison with Other Post-Buckling Models...	212
7. Summary and conclusions	231
7.1 Summary and conclusions	231
7.2 Recommendations for future research	234
References	235
Appendix A: Regression Analysis Program	246
Appendix B: Taylor's expansion of Eq. 5.23.....	248
Appendix C: Truss Model Subroutine.....	249

List of Tables

Table		Page
2.1	Test results of steel cylinders under transverse edge shear (Galletly and Blachut, 1985)	42
4.1	Boundary conditions for fixed-ends cylinder model	122
4.2	Boundary conditions for cantilever cylinder models (CNT series)	123
4.3	Slope of the tension field bands (in degrees) at and beyond the ultimate load	124
5.1	Variables of the regression data set	173
5.2	Regression constants of the linear models based on all data records	174
5.3	Regression constants of the nonlinear models based on all data records	174
5.4	Regression constants of the linear models based on experimental data	175
5.5	Regression constants of the nonlinear models based on experimental data	175
5.6	The error measurements of Eqs. 5.38 to 5.42 and of Galletly's equation 5.22	176
6.1	Comparison between measured and predicted buckle slopes	213

List of Figures

Figure		Page
1.1	Lay-out and typical cross section in conveyor gallery....	7
2.1	Residual stress distributions in tubular members	43
2.2	Post-buckling characteristics of different structural members.....	43
2.3	Comparison between theory and tests for cylinders under torsion (after Yamaki 1984).....	44
2.4	Yamaki's elastic buckling shear constant.....	44
2.5	Shear stress factor, $\bar{N}_{x\phi}$, for cylinders under transverse loading	45
2.6	Comparison between torsional and transverse buckling shear stresses	45
3.1	Possible configurations for cylinders with M/VR ratio equal to 1	74
3.2	Specimen S1 configuration.....	75
3.3	Imperfection measurement device.....	75
3.4(a)	The measured imperfection on the north-east quarter of the cylinder (magnified 20 times).....	76
3.4(b)	The measured imperfection on the south-east quarter of the cylinder (magnified 20 times).....	76
3.4(c)	The measured imperfection on the north-west quarter of the cylinder (magnified 20 times).....	77
3.4(d)	The measured imperfection on the south-east quarter of the cylinder (magnified 20 times)	77
3.5	Test set-up for specimen S1	78
3.6	Strain gage locations for specimen S1	79
3.7	Instrumentation for specimen S1	79
3.8	Welding details of the diaphragms of specimen S1	80
3.9(a)	Distribution of longitudinal stresses generated by welding and test set-up	81
3.9(b)	Distribution of longitudinal stresses generated by welding and test set-up	81

3.9(c)	Distribution of circumferential stresses generated by welding and test set-up	8 2
3.9(d)	Distribution of circumferential stresses generated by welding and test set-up	8 2
3.10	Buckled shape of specimen S1	8 3
3.11	Buckled shape of the finite element model (displacements magnified 10 times)	8 3
3.12(a)	Buckled shape of the north-west side of Specimen S1...	8 4
3.12(b)	Buckled shape of the south side of Specimen S1	8 4
3.13	Load-displacement curves for specimen S1	8 5
3.14	Shear stress from the end rosettes	8 6
3.15	Shear stress from the midspan rosettes	8 6
3.16(a)	Strain distribution at the end diaphragm	8 7
3.16(b)	Strain distribution at the middle diaphragm	8 7
3.17(a)	Longitudinal strain distribution along the top generator	8 8
3.17(b)	Longitudinal strain distribution along the bottom generator	8 8
3.18	Stress resultant diagrams for S1 including support movements	8 9
3.19	Numerical analysis of the effects of relaxed boundary conditions	9 0
3.20	Test set-up for specimen S2	9 1
3.21	Strain gage locations for specimen S2	9 2
3.22	Instrumentation for specimen S2	9 2
3.23	Buckled shape of specimen S2	9 3
3.24	Buckled shape of the finite element model (displacements magnified 10 times)	9 3
3.25(a)	Outside view of the buckled shape of specimen S2	9 4
3.25(b)	Inside view of the buckled shape of specimen S2	9 4
3.26	Load-displacement curves for specimen S2	9 5
3.27	Shear at end and middle rosettes	9 6
3.28	Ovalling of the cross section at mid span	9 6
3.29	Longitudinal strain distribution at the end diaphragm..	9 7
4.1(a)	Configuration of the isoparametric degenerated bi-cubic shell element	1 2 5

4.1(b)	Nodal degrees of freedom of the plate shell element in NISA80	125
4.2	Mesh arrangement of CNT models	126
4.3	Load-displacement curves for CNT series	127
4.4	Mesh arrangement of models M1-S1 and M2-S1	127
4.5(a)	Mesh deformation for mode M1-S1 at vertical displacement=1.89 mm (magnified 30 times)	128
4.5(b)	Mesh deformation for mode M1-S1 at vertical displacement=2.38 mm (magnified 20 times)	128
4.6	Load-displacement curves for models of specimen S1....	129
4.7(a)	Average shear distribution for M2-S1 at load equal to 1671 kN	130
4.7(b)	Average shear distribution for M1-S1 at load equal to 1671 kN	130
4.8	Shear distribution across the thickness at load equal to 1671 kN	131
4.9	Average longitudinal stress distribution at load equal to 1671 kN	131
4.10	Principal forces on the developed surface of model M1-S1 at vertical displacement=3.18 mm	132
4.11	Principal forces on the developed surface of model M1-S1 at vertical displacement=6.42 mm	133
4.12	Mesh arrangement of model M1-S2	134
4.13	Average shear distribution for M1-S2 at displacement equal to 0.99 mm	135
4.14	Average shear distribution for M1-S2 at displacement equal to 2.22 mm	135
4.15	Average shear distribution for M1-S2 at displacement equal to 3.41 mm	136
4.16	Average longitudinal stress distribution at displacement equal to 0.99 mm	136
4.17	Average longitudinal stress distribution at displacement equal to 2.22 mm	137
4.18	Average longitudinal stress distribution at displacement equal to 3.41 mm	137

4.19	Principal forces on the developed surface of model M1-S2 at vertical displacement=2.44 mm	138
4.20	Principal forces on the developed surface of model M1-S2 at vertical displacement=4.63 mm	139
4.21	Mesh arrangement of MF series	140
4.22	Load-displacement curves for models with R/t ratio equal to 150	141
4.23	Load-displacement curves for models with R/t ratio equal to 188	141
4.24	Load-displacement curves for models with R/t ratio equal to 250	142
4.25	Load-displacement curves for models with R/L ratio equal to 0.5	142
4.26	Load-displacement curves for models with R/L ratio equal to 0.75	143
4.27	Load-displacement curves for models with R/L ratio equal to 1.0	143
4.28	Principal forces on the developed surface of model MF1 at vertical displacement=0.93 mm	144
4.29	Principal forces on the developed surface of model MF2 at vertical displacement=0.88 mm	144
4.30	Principal forces on the developed surface of model MF3 at vertical displacement=1.30 mm	145
4.31	Principal forces on the developed surface of model MF4 at vertical displacement=0.65 mm	145
4.32	Principal forces on the developed surface of model MF5 at vertical displacement=0.81 mm	146
4.33	Principal forces on the developed surface of model MF6 at vertical displacement=1.10 mm	146
4.34	Principal forces on the developed surface of model MF7 at vertical displacement=0.61 mm	147
4.35	Principal forces on the developed surface of model MF8 at vertical displacement=0.69 mm	147
4.36	Principal forces on the developed surface of model MF9 at vertical displacement=1.01 mm	148

4.37	Deformations of cross section, S-S, in model MF9 (magnified 75 times)	148
5.1	The general shape of the shear capacity vs R/t	177
5.2	The general shape of the shear capacity vs R/L	177
5.3	Predictions of the regression models for different R/t ...	178
5.4	Predictions of the regression models for different R/L ..	179
5.5	Predictions of the regression models for different E/σ_y	180
5.6	Scatter of the test data about the regression Eq. 5.38	181
5.7	Scatter of the test data about the regression Eq. 5.39	181
5.8	Scatter of the test data about the regression Eq. 5.40	182
5.9	Scatter of the test data about the regression Eq. 5.41	182
5.10	Scatter of the test data about the regression Eq. 5.42	183
5.11	Scatter of the test data about Galletly's equation	183
5.12	Scatter of the finite element data about the regression Eq. 5.48	184
6.1	Behavior of large diameter tubes in the post-buckling range (typical)	213
6.2(a)	Tension field action in plate girders	214
6.2(b)	Tension field action in thin-walled cylinders	214
6.3	Tension field action in the Bailey-Kulak model (after Bailey and Kulak, 1984)	215
6.4	Tension field action in the Roman-Elwi model (after Roman and Elwi, 1987)	215
6.5	Proposed truss model	216
6.6	The truss model on the developed surface of the cylinder	217
6.7	Post-buckling principal forces on the developed surface of specimen S2	218
6.8	Effect of biaxial stress state at the crest of a buckle	219
6.9	Distributions of M_c , σ_t , and μ for half buckle wave in the tension field	219
6.10	Effect of thickness ratio on post-buckling shear stress (R/L=1.0, $E/\sigma_y=600$)	220
6.11	Effect of material ratio on post-buckling shear stress (R/L=1.0, R/t=200)	220
6.12	Effect of aspect ratio on post-buckling shear stress	

	(R/t=200, E/σ _y =600)	221
6.13	The truss elements on the developed surface for different R/L ratios (R/t=200, E/σ _y =600)	222
6.14	The truss elements on the developed surface for different R/L ratios (R/L=1.0, E/σ _y =600)	222
6.15	Shear capacity of the truss model	223
6.16	Tension field slope of the truss model	223
6.17	Compression strut slope of the truss model	224
6.18(a)	Post-buckling shear capacity for thin-walled cylinders (E/σ _y =400)	225
6.18(b)	Post-buckling shear capacity for thin-walled cylinders (E/σ _y =600)	226
6.18(c)	Post-buckling shear capacity for thin-walled cylinders (E/σ _y =800)	227
6.19	Comparison between the truss model and full-scale tests	228
6.20	Comparison between the truss model and Galletly's tests	228
6.21	Comparison between the truss model and finite element results	229
6.22	Comparison between buckling and post-buckling strength for different aspect ratios (R/t=200, E/σ _y =600)	229
6.23	Comparison between buckling and post-buckling strength for different thickness ratios (R/L=1.0, E/σ _y =600)	230
6.24	Comparison between buckling and post-buckling strength for different material ratios (R/t=200, R/L=1.0)	230

List of Symbols

<i>a, b, c, d, e</i>	: regression constants
A	: cross sectional area
B	: width of compression field
C	: compression force in truss model
C_v	: vertical shear component of the compression strut
C_x	: horizontal component of compression field
d	: distance between strain gage and weld
D_{avg}	: average diameter in imperfect cylinder
D_{max}, D_{min}	: maximum and minimum diameter in imperfect cylinder
e	: cylinder out-of-roundness, $e = D_{max} - D_{min}$
E	: elastic modulus
E/σ_y	: material ratio.
E_{avg}	: average of the absolute value of E_r -values,
	$E_{avg} = \frac{1}{m} \sum_{i=1}^m E_{r_i} $
E_{max}	: maximum value of E_r -values, $E_{max} = \text{maximum } \{E_r\}$
E_{min}	: minimum value of E_r -values, $E_{min} = \text{minimum } \{E_r\}$
E_r	: residual error as a percentage of the cylinder shear yield capacity, $E_{r_i} = 100 \left(\frac{\hat{Y}_i - Y_i}{Y_{yield}} \right)$
G	: welding voltage
h	: thermal diffusivity
I	: moment of inertia
I_w	: welding current intensity
k_{t1}, k_{t2}	: shear parameters in the Bailey-Kulak model
k_{y1}, k_{y2}	: shear parameters in the Bailey-Kulak model
K	: thermal conductivity
K_f, K_t	: shear buckling parameters
K_s	: Yamaki's shear parameter

L	: shear span length
L/r	: slenderness ratio
m	: number of data records in a regression model
M	: bending moment
M_{cr}	: critical bending moment for compression buckling mode
$\bar{N}_{x\phi}$: Schröder's shear parameter
P_e	: welding efficiency
r	: radius of gyration, $r = \sqrt{I/A}$
r^2	: coefficient of determination, $r^2 = 1 - \frac{SSE}{SST}$
R	: cylinder radius
R/L	: aspect ratio
R/t	: thickness ratio
S^2	: variance of regression errors, $S^2 = \frac{1}{1-m} \sum_{i=1}^m (\epsilon_i - \bar{\epsilon})^2$
SSE	: sum of the squares of the error in a regression model, $SSE = \sum_{i=1}^m (Y_i - \hat{Y}_i)^2$
SST	: sum of the squares of the total error in a regression model, $SST = \sum_{i=1}^m (Y_i - \bar{Y})^2$
S_w	: welding speed
$S_{y/x}$: standard error of estimate of the regression equation \hat{Y} , $S_{y/x} = \sqrt{\frac{\sum_{i=1}^m (\hat{Y}_i - Y_i)^2}{m-2}}$
t	: thickness of cylinder wall
T	: peak temperature for strain gage
T_v	: vertical shear component of the tension field
T_x	: horizontal component of the tension field
u	: translation degree of freedom in direction of X axis
v	: translation degree of freedom in direction of Y axis

V	: shear force
V_{cr}	: critical shear force for the shear buckling mode
V_{max}	: maximum resisted shear force
V_p	: post-buckling shear capacity
V_{tm}	: total shear capacity of truss model
V_u	: ultimate shear strength of cylinder
V_y	: yield shear strength of the cylinder
w	: translation in direction of Z axis
w_i	: deviation amplitude for imperfect cylinder, $w_i = D_i - D_{avg}$
X1, X2, X3	: independent variables in regression model
\hat{Y}	: predicted value of the shear ratio Y
Y	: shear capacity ratio, $Y = V_{max}/V_y$
Z	: curvature parameter, $Z = \sqrt{(1-\nu^2)} (R/t) (L/R)^2$
α, μ	: reduction factors for cross-bending moment
α_m	: imperfection reduction factor for plastic buckling under axial compression
δ	: reduction factor for the effect of the initial imperfections
ϵ_i	: error between observed and predicted variables
Φ	: Yamaki's parameter, $\Phi = (R/L)^{-1.25} (R/L)^{0.5} (E/\sigma_y)$
ϕ	: angle between the projection of the normal to the shell surface on ZY plane and the Y axis
Γ	: empirical reduction factor for plastic buckling under axial compression
γ_s	: Stephens's parameter reflecting material and geometric properties, $\gamma_s = \sqrt{(E/\sigma_y) (t/R)^3}$
η	: slope of compression strut
Λ	: elastic buckling stress for imperfect cylinders
$\theta, d\theta$: angle and elementary angle corresponding to elementary width of the tension field
θ_s	: change in the angle ψ
θ_x	: change in the angle ϕ
ρ	: empirical parameter for buckling stress, $\rho = (E/\sigma_y) (R/t)$

σ_{cm}	: maximum stress associated with cross-bending moment
$\sigma_{cr}, \sigma_{cr1}, \sigma_{cr2}$: critical compressive stress for cylinder subjected to axial compression load
σ_{cre}	: classical elastic buckling stress for cylinder subjected to axial compression load
σ_t	: tension field stress
σ_{ta}	: allowable tensile stress in tension field
σ_{te}	: equivalent uniform tensile stress
σ_y	: static yield stress
τ_{cr}	: critical inelastic shear stress
τ_{cre}	: critical elastic shear stress
τ_e	: elastic buckling shear stress
τ_p	: critical plastic shear stress
τ_{tm}	: maximum shear stress of truss model
ν	: Poisson's ratio
Ψ	: angle between the surface normal and the X axis
ψ	: arc width of tension field
ζ	: slope of tension field

1. Introduction

1.1 Background

Large-diameter thin-walled tubular members are used frequently in civil engineering structures. Because of their efficient shape, tubular sections have higher torsional rigidity and better resistance to wind and pressure loads than conventional sections. Therefore, many structures incorporate these tubular members in applications such as pipelines, liquid storage tanks, grain storage bins, nuclear reactor vessels, offshore platforms, transmission towers, and conveyor galleries.

The cylindrical elements in these structures are subjected to different types of loads, including longitudinal axial compressive loads, bending moments, transverse shear, and internal and external pressure. The investigation reported herein deals with tubes subjected to transverse loads and which have a radius to thickness ratio in the range of 100 to 300. Conveyors that handle bulk material in industrial plants are often housed and supported by large-diameter fabricated steel cylinders that fall within these parameters. In this case the cylinder acts as a simple or continuous beam of spans that may reach 50 m, as shown in Fig. 1.1. The transverse load acting on this cylinder produces a shear force and bending moment of considerable magnitude on the cross-section. Due to the slenderness of the cylinder wall, these forces can cause local buckling at critically stressed parts of the cylinder.

The strength of thin-walled tubes is, therefore, usually governed by local buckling strength. Stiffeners around the cross-section (rings) and along the axis (stringers) can be used to prevent premature buckling of the cylinder. Depending on the shell radius to thickness ratio, the radius to unstiffened length ratio, and the stiffener arrangements, buckling of cylinders under transverse load can be the result of compressive stresses (flexural buckling) or shear stresses (shear buckling). This study deals with the local shear buckling of thin-walled longitudinally unstiffened cylinders subjected to transverse loads.

The shear buckling capacity of thin-walled cylinders is influenced by several parameters. In addition to the geometry, material properties, and boundary conditions of the cylinder, the level of initial imperfections and residual stresses introduced during the production process potentially play a role and should be considered in determining the capacity. However, little research has been carried out to explore the effect of these parameters.

Currently, North American practice is to use a reduced version of the elastic buckling stress of cylinders under torsion as the design basis for cylinders under transverse loads. European specifications (European Convention for Constructional Steelwork, 1988) use an interaction equation for the inelastic shear buckling stress. This equation is also a function of the elastic torsional shear buckling stress. Another empirical formula is the quadratic interaction equation proposed by Galletly and Blachut (1985). This equation is based on the results of a single group of small-scale physical tests.

The tests consisted of specimens fabricated from gradual-yielding steel sheets. In practical structures, tubes are usually fabricated from hot-rolled steel plates (sharp-yielding) and have much larger diameters than those used in the scaled specimens.

Clearly, there are insufficient theoretical and experimental studies which address the problem of the shear capacity of large-diameter thin-walled tubes. Thus, more tests of full-scale cylinders are essential to establish a satisfactory level of confidence in design techniques. Also, empirical design formulas and alternate analytical methods for design are highly desirable.

1.2 Statement of the Problem

The present study investigates the inelastic shear buckling behavior of large-diameter thin-walled fabricated steel cylinders subjected to transverse loads. The cylinders under consideration are longitudinally unstiffened, fabricated from hot-rolled steel plates, and have a radius to thickness ratio in the range of 100 to 300.

In this report, the characteristics of inelastic shear buckling are explored both experimentally and numerically. Two models, a regression model and a truss model, are proposed for the prediction of the cylinder shear capacity at and beyond the limit point.

1.3 Objectives

This study is a continuation of an investigation of the shear capacity of large diameter fabricated steel tubes that has been underway at the University of Alberta since 1984. Preliminary tests

have been performed by Bailey and Kulak (1984) and numerical investigations have been carried out by Mok and Elwi (1986) and Roman and Elwi (1987).

The present research has the following objectives:

1. To test thin-walled cylinders under transverse shear. The test specimens should represent material properties and fabrication procedures that are typical of practical structures.
2. To use a numerical analysis technique that can simulate the response of the tested specimens and to extend this analysis to the prediction of the behavior of any cylinder under the same general conditions but whose particular parameters are outside of the scope of the physical tests.
3. To develop an efficient ultimate shear capacity formula based on a statistical analysis of all the available data and compare it with the current design approaches.
4. To develop an alternate mechanistic method of design that depends on the post-buckling strength rather than on the ultimate strength.

1.4 Layout of the Thesis

Chapter 2 contains a review of the research work done by others on the buckling of thin-walled tubes, with a clear emphasis on

cylinders subjected to transverse loads. The chapters following introduce theoretical and experimental investigations of the problem.

The experimental phase of the present study is described in Chapter 3. Testing of two large-diameter fabricated steel cylinders is reported in detail and the results of these tests are compared with other theoretical predictions.

In Chapter 4, a nonlinear finite element analysis of both the tested specimens and the results of work by others is introduced. The ability of the numerical model to simulate the actual behavior of thin-walled fabricated steel tubes is demonstrated and discussed. A parametric analysis of nine cantilever models is reported.

Sophisticated numerical analyses are generally not convenient for design purposes, hence attention is also given to empirical equations. Chapter 5 describes a nonlinear regression analysis of the experimental and numerical results. From this analysis, an ultimate shear strength equation is recommended for design. The predictions of the equation are compared with test results and with other empirical equations.

Post-buckling behavior is investigated in Chapter 6. A truss model, which is based on observations from the experimental and numerical results, is developed to estimate the stable post-buckling shear capacity of thin-walled cylinders. Predictions made using this model are presented in the form of curves suitable for design purposes.

Chapter 7 summarizes the results of the experimental and numerical analyses. Two different methods are recommended for the design of thin-walled fabricated steel cylinders subjected to transverse loading; an ultimate inelastic shear formula for the buckling capacity and a truss model for the post-buckling capacity.

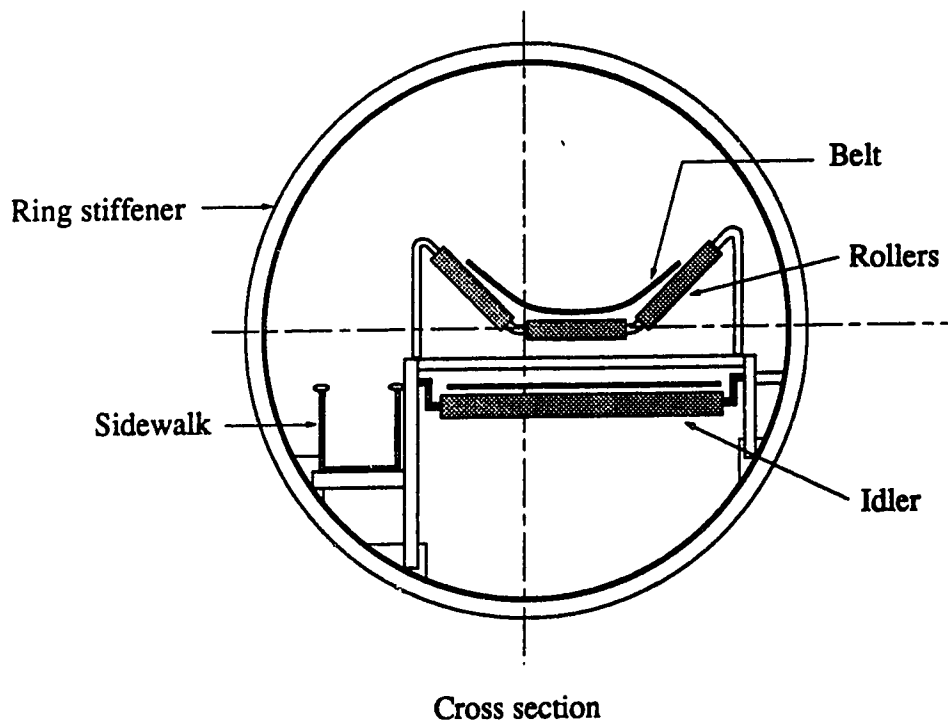
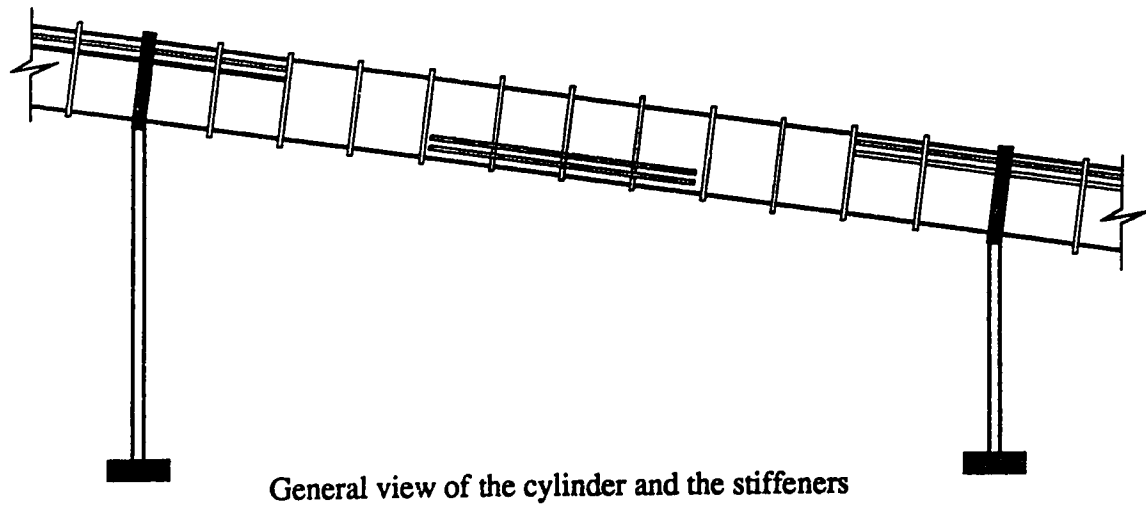


Fig. 1.1 Layout and typical cross section in conveyor gallery

2. Literature Review

2.1 Introduction

2.1.1 Historical Review

In the early decades of this century, mechanical engineering and aerospace applications provided the need for extensive research investigation of cylindrical shells. In the 1930's, the National Advisory Committee for Aeronautics (NACA) sponsored several studies to investigate the behavior of very thin cylinders under different loading conditions. In recent years, the extensive use of offshore platforms has led to research into the behavior of the cylindrical tube when used as a structural member.

One of the earliest studies on buckling strength of structural tubes is that by Wilson and Newmark (1933), in which axially compressed cylinders were tested. In the mid-sixties, a landmark paper on the strength of structural tubes was presented by Schilling (1965). In this paper, he summarized much of the preceding work and presented strength criteria for the design of structural tubes.

After about 1975, the research effort on structural tubes has been greatly expanded. Most activities have been directed toward offshore structures, although some have been directed toward the use of tubes in land-based construction. A comprehensive survey report on the buckling of both unstiffened and stiffened cylinders used in offshore structures was sponsored by the Department of Energy in Britain (Ellinas, 1984.) Another thorough theoretical and

experimental treatise of the elastic buckling of thin-walled cylindrical shells was performed at Tohoku University (Yamaki, 1984.)

At the present time, fabricated cylinders are the subject of research in locations such as England, Australia, Norway, Japan, and North America. For example, investigation of the interaction between axial load and external pressure in cylindrical shells is continuing at University of Liverpool (Galletly et al., 1987), studies on buckling behavior of tanks are proceeding at the University of Sydney (Rotter, 1986), and tests of tubes under combined bending and external pressure are being conducted at the University of Texas, Austin (Corona and Kyriakides, 1988). An ongoing research at the University of Alberta includes an examination of the strength and stability of large diameter fabricated steel cylinders under axial compression, bending, and transverse shear (Stephens et al., 1982, Bailey and Kulak, 1984, Roman and Elwi, 1987). At the University of Wisconsin Sherman is reviewing the design rules for pipes in flexure (Sherman, 1989) and a study on the local stability of beam and beam-column cylinders is underway at Purdue University (Chen et al., 1989). The behavior of pipelines and tanks under seismic loading is being investigated at the University of California, Berkeley (Chalhoub and Kelly, 1988).

2.1.2 Overview

Thin-walled cylindrical shells have been extensively used in many branches of engineering. In particular, tubular members

fabricated from steel plates are becoming common in civil engineering structures. Some examples of structures incorporating these tubular members are pipelines, liquid storage tanks, grain storage bins, nuclear reactor vessels, components of offshore platforms, transmission towers, and conveyor galleries.

Because of their round cross-section, tubular members are ideal for air tightness, wind resistance, and three-dimensional loading. The circular cross-section has a superior wind shape factor as compared to that of a conventional rectangular section. The round cylinder also provides the most efficient shape available for centrally loaded columns with no intermediate lateral support.

Cylindrical shells that have a small radius (R) relative to the wall thickness (t) or length (L) are usually unstiffened. If the thickness ratio, R/t , or the aspect ratio, R/L , is large enough, longitudinal and/or ring stiffeners are often used to provide additional strength. The study reported herein is concerned only with longitudinally unstiffened cylinders.

In the design of cylindrical shells, as in all types of lightweight structures, the determination of the buckling load is required. The shell buckling problem is complex, and in addition, the influence of initial imperfections, residual stresses, and material properties must be considered.

Tubes may be subjected to axial compression, bending, torsion, transverse loading, internal or external pressure, or to any combination of these loads. The literature review in this chapter is

directed mainly toward cylinders subjected to transverse loading. However, a short commentary on cylinders subjected to axial compression, bending, and torsion is also presented because of the relationship between these loading types and transverse loading.

2.2 Buckling of Unstiffened Cylinders

2.2.1 Effect of Imperfections and Residual Stresses

The behavior of tubular members is influenced by the level of geometric imperfections and residual stresses introduced in them during the production process. Tubular members are either manufactured or fabricated. A manufactured tube is any tube produced by piercing, forming and welding, cupping, extruding, or other related methods in a plant dedicated specifically to the production of tubes. Fabricated tubes are constructed by cold-rolling a flat plate into a cylindrical form and then welding the longitudinal seam.

In general, fabricated cylinders do not receive a finishing treatment and it is generally expected that they will have larger magnitudes of imperfections than do manufactured cylinders. For axially compressed cylinders, where local buckling is strongly influenced by the level of imperfection, the strength of a fabricated tube is normally below that of a comparable manufactured tube.

Long large-diameter tubes are usually constructed by joining several short "cans" with circumferential welds. Such circumferential joints are particularly susceptible to local buckling unless carefully

made, because they often produce a discontinuity in the form of a slight depression in the tube. Longitudinal joints may also cause discontinuity, especially if made by riveting or bolting, but not to the same extent as the circumferential joints.

The unfavorable effect of the geometric imperfections on the buckling strength changes considerably according to the type of loading, the shape and level of imperfections, and the dimensions of the tube. This effect can be estimated by either complicated analytical methods or empirical formulas. Due to the random nature of the geometric imperfections, empirical formulas are more practical for design purposes.

Residual stresses in tubes usually arise from the forming and welding operations that are part of the production process. High levels of circumferential residual stress are created in a tube if it is cold-formed and welded longitudinally in a continuous operation without allowing any springback. If springback is allowed before welding, the residual stresses will be considerably smaller. It has been shown (Pascoe, 1971 and Roman and Elwi, 1987) that these stresses can be predicted with a reasonable degree of accuracy by simple plastic theory. An example of the residual stress distribution across the cylinder thickness due to cold-rolling is shown in Fig. 2.1(a). It can be seen that allowing for springback reduces the surface stresses considerably.

Longitudinal residual stresses that arise from the shrinkage of a longitudinal weld in cylinders of the type used in offshore

structures were investigated by Ross and Chen (1976). A typical distribution of these stresses around the cylinder perimeter is shown in Fig. 2.1(b). The distribution has a region of yield tension at the welds balanced by compression stress adjacent to it.

It can be expected that residual stresses will have a significant effect on the inelastic buckling strength of tubular members. The stress-strain curve of a tubular cross-section may change from a sharp yielding type to a gradual yielding type due to the existence of residual stresses. For tubes that have a known gradual yielding stress-strain curve, the inelastic buckling stress can be determined by using an effective modulus of elasticity, as proposed by Gerard (1956). However, if the stress-strain curve of the cross-section is unknown, which is usually the case, then the inelastic effect can be predicted for specific production techniques by means of empirical equations.

The material properties (the elastic modulus, E , and the yield stress, σ_y) are usually determined from coupon tension tests. When used in buckling equations, these values have to be representative of the behavior of compressed members. The difference between the material properties measured from coupon test and the actual properties of the tubular cross-section was investigated by Ross and Chen (1976). They tested both full-size fabricated welded cylinders in compression (stub-column test) as well as tension coupons from the same steel plate. The tensile coupons exhibited sharp yielding behavior whereas the compression stub column tests exhibited gradual yielding behavior because they included the influence of the

residual stress. The compressive yield stresses were slightly lower than the corresponding static tensile yield stresses. Ross and Chen reported that the difference is dependent on the method of production and the size of the tube. After comparing several test results, Ellinas (1984) suggested that the tensile value is a good representation of the yield stress for the solution of buckling problems in offshore-type cylinders.

2.2.2 Cylinders Subjected to Axial Compression

For convenience, axially compressed cylinders may be classified into three groups according to their buckling behavior: short, moderate, and long. Buckling of short cylinders is dependent on both the thickness ratio (R/t) and the aspect ratio (R/L), in a manner similar to the buckling behavior of flat plates, whereas buckling of moderate cylinders is dependent only on the (R/t) ratio. Buckling of long cylinders is dependent on the slenderness ratio, (L/r), in a manner similar to the behavior of columns.

The geometries which describe the limits of each group have been identified by Gerard (1962) as a function of a curvature parameter, Z , that involves the dimensions of the cylinder and Poisson's ratio, ν . The limits are given by:

$$Z \leq 2.85 \quad \text{for short cylinders} \quad (2.1)$$

$$2.85 < Z < 6(1-\nu^2) \left(\frac{R}{t}\right)^2 \quad \text{for moderate cylinders} \quad (2.2)$$

$$Z \geq 6(1-\nu^2) \left(\frac{R}{t}\right)^2 \quad \text{for long cylinders} \quad (2.3)$$

where $Z = \sqrt{(1-\nu^2)} (R/t) (L/R)^2$ is the curvature parameter.

According to these limits, the moderate length region has aspect ratios (R/L) between $0.418 \sqrt{t/R}$ and $0.578 \sqrt{R/t}$. This is believed to cover most of the common geometries used in civil engineering applications, and it is this region that is emphasized in the following.

The theoretical solution for buckling of axially compressed cylindrical shells was obtained as early as 1910. The solution was based on the small displacement theory, also called linear theory, which requires that the analyzed member be perfectly elastic and that there be a linear relationship between strains and displacement derivatives. The small displacement theory can only determine the buckling load at bifurcation, i.e. it cannot determine the equilibrium path in the post-buckling region. The elastic buckling stress for geometrically perfect cylinders according to this classical theory is given as (Timoshenko and Gere, 1961):

$$\sigma_{cre} = \frac{1}{\sqrt{3(1-\nu^2)}} E \frac{t}{R} \quad (2.4)$$

where σ_{cre} is the elastic buckling stress.

The results of the numerous experiments made to verify the theoretical solution showed a large degree of scatter and buckling loads generally much less than those predicted by Eq. 2.4. Some test cylinders buckled at stresses as low as 20% of the critical stress given by Eq. 2.4 (Ellinas, 1984.)

In 1934, Donnell realized that the classical theory is inadequate for analyzing axially compressed cylinders because, unlike columns and plates, the post-buckling behavior of cylinders is unstable. In other words, Donnell realized that it was not sufficient to determine the load at bifurcation, but that an investigation of the post-buckling behavior was required as well. A schematic presentation of the post-buckling behavior of three different structural members- plates, columns, and cylinders, is shown in Fig. 2.2. The behavior of a corresponding imperfect member in each case is also shown in Fig. 2.2. Because the post-buckling stress of a perfect cylinder drops sharply from the bifurcation buckling stress, the maximum stress of cylinders with small imperfections is well below the classical buckling stress.

Donnell and Wan (1950) developed a large displacement theory that introduces the effect of initial imperfections into the stability analysis. Their solution showed that the reduction in the buckling stress depends on the imperfection magnitude and the value of the R/t ratio. They concluded that the initial imperfections are responsible for the discrepancy between the classical theory and experiments. To confirm this conclusion, Tennyson (1964) manufactured four near-perfect shell specimens and found that the observed buckling loads were very close to the classical theoretical buckling load.

Arbocz and Babcock (1974, 1976, and 1980) applied more accurate numerical techniques to simulate statistically random imperfection amplitudes in the analysis as a double Fourier series.

They reached a point where the buckling load can be predicted with considerable accuracy, provided that the actual imperfection profiles are mapped and used in the calculations.

Pinkney et al. (1983), using finite element analysis, were able to predict the buckling load of two axially loaded fabricated steel cylindrical shells with excellent agreement with the experimental results obtained by Stephens et al. (1982). In their analysis, the initial imperfections measured in the actual tests were modeled by the first buckling mode shape and incorporated into the finite element model.

Sophisticated analytical or numerical techniques similar to those mentioned above are generally not suitable for design purposes, however. As an alternative, empirical and semi-empirical formulas based on many test results have been developed for the design of imperfect shells.

The dependency of the buckling strength on the degree and shape of the imperfections led the writers of design specifications to classify steel tubes into groups with similar imperfection levels. In fact, design codes require that their equations be applied with certain conditions depending on the type of tests used in developing the equations. For manufactured tubes with sharp yielding materials, one of the early equations for ultimate strength was that proposed by Plantema (1946). A conservative modification of Plantema's formula was also adopted for fabricated cylinders.

Several formulas were developed for specific classes of materials and cylinder thickness. A comparative study of design formulas recommended by the American Iron and Steel Institute (AISI), American Water Works Association (AWWA), American Society of Mechanical Engineers (ASME), and European Convention for Constructional Steelwork (ECCS) codes is reported by Stephens et al. (1982), who have themselves proposed an equation for fabricated cylinders of geometries and material properties of the type used in conveyor galleries. Another excellent compilation of test data and design equations recommended by the American Institute of Steel Construction (AISC), Det Norske Veritas (DnV), and British Standards Institution (BSI) codes is reported by Ellinas et al. (1984).

Stephens et al. (1982) concluded that the ultimate capacity of fabricated cylinders under axial compression is best approximated by the AWWA formula if the cylinder wall thickness is less than 6.35 mm (1/4 in) and by the ASME formula if the cylinder wall thickness is greater than 6.35 mm. The two formulas are shown below.

The ASME formula for cylinders with wall thicknesses not less than 6.35 mm is given by:

$$\sigma_{\alpha} = \Gamma \Lambda \quad (2.5)$$

where $\Lambda = \alpha_m \frac{1}{\sqrt{3(1-\nu^2)}} E \frac{t}{R}$

$$\Gamma = 1.0 \quad \text{for } \Lambda \leq 0.55$$

$$\Gamma = 0.18 + \frac{0.45}{\Lambda} \quad \text{for } 0.55 < \Lambda < 1.6$$

$$\Gamma = \frac{1.31}{1 + 1.15 \Lambda} < \frac{1}{\Lambda} \quad \text{for } \Lambda \geq 1.6$$

$$\alpha_m = 0.207 \quad \text{for } 600 \leq R/t \leq 1000$$

$$\alpha_m = \text{smaller of } (\alpha_{m1} \text{ and } \alpha_{m2}) \quad \text{for } R/t < 600$$

$$\alpha_{m1} = 1.52 - 0.473 \log (R/t)$$

$$\alpha_{m2} = 300 (\sigma_y / E) - 0.033$$

In these equations, σ_{cr} is the critical compressive stress, α_m is an imperfection parameter based on Donnell's theory and Γ is an empirical reduction factor for plastic buckling. It is obvious that the ASME formula can be tedious for design purposes. On the other hand, the easy-to-use AWWA formula for cylinders fabricated from mild steel with yield stress not less than 200 MPa is given by:

$$\sigma_{cr} = \sigma_y \left(0.138 \rho - 0.00475 \rho^2 \right) \quad \text{for } \rho < 14.5 \quad (2.6a)$$

$$\sigma_{cr} = \sigma_y \quad \text{for } \rho > 14.5 \quad (2.6b)$$

where $\rho = (E/\sigma_y) (R/t)$. It is to be noted that the AWWA code recommended this formula for a different thickness range than the one suggested by Stephens et al.

2.2.3 Cylinders Subjected to Pure Bending

The buckling of cylinders as a result of flexure has not been explored as fully as has the buckling of cylinders under axial

compression. However, the local buckling behavior of the compressed part of a cylindrical tube in bending is similar to that of a tube under axial compression, and is usually linked to it.

Early tests of tubes in flexure were performed by Lundquist (1933), who tested 58 thin-walled Duralumin cylinders in pure bending. The test specimens had wall thicknesses that ranged from 0.28 to 0.56 mm, radii from 190 to 380 mm, and lengths from 50 to 940 mm. This range of the thickness ratio (R/t between 339 and 1357) is characteristic of aerospace applications.

It was observed that the shape and size of the buckles in the failed cylinders were approximately the same as those obtained in axial compression tests of the same R/t ratio. Lundquist reported that the buckling stresses did not appear to be a function of the R/L ratio, but were dependent on the R/t ratio and the initial imperfections. The maximum compressive flexural stresses at failure were about 30% to 80% more than the compressive stresses of the axially loaded cylinders having the same R/t ratio.

Donnell (1934) tested about one hundred steel and brass cylinders. The tests were run on matched cylinders, some of which were tested in axial compression and some in pure bending. The test specimens had R/t ratios in the same range as Lundquist's tests but the cylinders themselves were much smaller. The radius of the test cylinders ranged from 24 to 72 mm and the thickness from 0.05 to 0.07 mm. The length to radius ratio varied from 1 to 15.

The test results showed that the ratio of the critical stress in bending to the critical stress in axial compression ranged from 0.86 to 1.69 for the steel cylinders and from 0.80 to 2.62 for the brass cylinders. Donnell suggested that the critical stress in bending can be taken as 1.4 times the critical stress in axial compression, which is the average value of the above ratios.

It should be noted that there is considerable scatter in the test data reported by Donnell and Lundquist. The scatter was largest for the brass cylinders and least for the Duralumin cylinders. The average 40% increase in the bending critical stress suggested by Donnell and Lundquist should be viewed in the context of the material and the size of specimens used in the tests. The level of imperfections and residual stresses in the small specimens may be significantly different from that in actual large diameter tubes.

Other investigators (Gerard and Becker, 1957) have suggested that the elastic local buckling stress for bending can be taken conservatively as 1.3 times the local buckling stress for axial compression. This was based on test results and some theoretical considerations. This higher elastic buckling stress for bending results from the beneficial effect of the stress gradient that exists in bending.

Seide and Weingarten (1961) also investigated the stability of circular cylindrical shells under pure bending. Using the small displacement theory, they proved that the critical compressive stress

in bending is equal to the critical compressive stress for the axial load case.

Seide and Weingarten admitted that, without a large displacement solution for cylinders in bending, no argument about the flexural buckling stress can be complete. However, they suggested that the similarity in the experimental buckle deformations for bending and compression would appear to indicate similar theoretical post-buckling behavior and similar strength.

This argument can be twisted in favour of the proposed increased strength for the bending case because the sensitivity of the compressive stresses to initial imperfections would decrease with the inherent stress gradient in bending. Consequently, the role of initial imperfections in reducing the buckling strength would be smaller in cylinders under pure bending than it would be in cylinders under uniform compression.

There have been very few tests on large diameter fabricated steel cylinders under bending. Two of these were carried out by Stephens et al. (1982). They tested full-scale fabricated cylinders with dimensions that resemble the tubular members used in the materials-handling operations of industrial plants. The two test specimens were fabricated from 3.5 and 5 mm thick steel plates, respectively. Both had a diameter of 1525 mm and a central length of 1830 mm. Both cylinders failed at the extreme compressed fiber near the circumferential weld which was a major source of geometric imperfection and residual stress.

Stephens et al. proposed a local buckling ultimate strength formula for such cylinders under either compression or bending. Using the limited test data in bending, it was shown that the proposed equation was as accurate as the equations recommended by the ASME and the ECCS codes. Stephens' equation is particularly suited for design and is given by:

$$\sigma_{cr} = \sigma_y (119.3 \gamma_s) \quad \text{for } \gamma_s \leq 0.0036 \quad (2.7a)$$

$$\sigma_{cr} = \sigma_y (1.625 + 0.489 \log \gamma_s) \quad \text{for } 0.0036 < \gamma_s < 0.0527 \quad (2.7b)$$

$$\sigma_{cr} = \sigma_y \quad \text{for } \gamma_s \geq 0.0527 \quad (2.7c)$$

where σ_{cr} is the critical compression stress and $\gamma_s = (E/\sigma_y)^{0.5} (t/R)^{1.5}$ is a non-dimensional factor reflecting material and geometric properties.

Unlike the ECCS code, which increases the critical compressive stress for tubes subjected to bending above that for tubes in axial compression, Stephens et al. suggested that the same critical compressive stress be used for large diameter fabricated steel cylinders in bending and axial compression. Stephens' recommendation was based on the results of the full-scale tests.

Another large size welded fabricated cylinder was tested in bending by Bailey and Kulak (1984). The test specimen was fabricated from a 5 mm thick steel plate and had a diameter of 1753 mm and central length of 1219 mm. The cylinder failed with the typical diamond shaped buckles formed adjacent to the circumferential weld, similar to the two cylinders tested by Stephens

et al. The maximum compressive stress calculated from the measured strains was 99% of that predicted by the Stephens et al. formula. Bailey and Kulak supported the use of this equation for fabricated steel tubes with values of γ_s in the range of 0.005 to 0.02.

2.2.4 Cylinders Subjected to Torsion

Buckling of thin-walled cylinders loaded in torsion is not accompanied by immediate collapse, as is the case with axially compressed cylinders. It was observed (Lundquist, 1932 and Donnell, 1933) that small initial imperfections on the surface of the test cylinders did not seem to affect the buckle formation or the buckling strength. Nevertheless, the strengths of tubes tested in torsion tend to be roughly 15% below the theoretical predictions, apparently as a result of initial imperfections.

Lundquist (1932) tested 180 Duralumin cylinders in torsion. The cylinders had R/t ratios that ranged from 323 to 1455 and R/L ratios that ranged from 0.5 to 2.0. The test specimens were fabricated by wrapping the Duralumin sheet about two end bulkheads. A butt strap was fitted and bolted in place to close the seam and steel bands were used to clamp the Duralumin sheets to the bulkheads. It was observed that short cylinders showed a more stable failure pattern than the long cylinders.

Lundquist reported that both the nominal shearing stress at failure and the slope of the buckles decrease as the value of the R/L ratio decreases for a constant cylinder thickness or as the value of

the R/t ratio increases for a constant cylinder length. Based on the test data, the following empirical equation was proposed:

$$\tau_e = K_t E \left(\frac{t}{R} \right)^{1.37} \quad (2.8)$$

where τ_e is the elastic buckling shear stress and K_t is a function of the ratio R/L . Regarding the sensitivity to initial imperfection, Lundquist commented that the presence of slight imperfections in the cylinder may cause the buckles to initiate at a smaller load but does not reduce the strength at failure. It is to be noted that in the absence of a theoretical solution, Lundquist's comment on the effect of the initial imperfections can only be approximate.

Batdorf et al. (June, 1947) determined a solution for thin-walled cylinders loaded in torsion based on Donnell's linear assumptions. The elastic buckling stress was introduced by:

$$\tau_e = K_f E \frac{\pi^2 t^2}{12(1-\nu) L^2} \quad (2.9)$$

where K_f is a parameter given in the form of logarithmic plots for cylinders with either simply supported or clamped edges. For intermediate values of the curvature parameter Z , which corresponds to $50 < Z < 10(R/t)^2$ or $0.309\sqrt{t/R} < R/L < 0.138\sqrt{R/t}$, the curves which define K_f are straight lines. In this case, Eq. 2.9 becomes:

$$\tau_{cre} = K_s E \left(\frac{t}{R} \right)^{\frac{5}{4}} \left(\frac{R}{L} \right)^{\frac{1}{2}} \quad (2.10)$$

where K_s is a constant equal to 0.74 for simply supported cylinders and 0.81 for clamped end cylinders. Batdorf's solution was compared with previous theoretical solutions and proved to be in somewhat better agreement with experimental results reported by other investigators (Lundquist, 1932 and Bridget et. al., 1934). However, it should be noted that, in this comparison, only a few test specimens were made of steel. Also, the comparison plot reported by Batdorf was somewhat optimistic. The difference between the theory and the data appears to yield reasonable agreement in the logarithmic plot, but if plotted linearly the difference can reach 40% (Gerard, 1962.)

It was suggested by Gerard (1962) and Schilling (1965) that a reduction of 15% be applied to Eq. 2.10 to account for the difference between theory and test. The percentage selected is an average value taken from the test results.

Yamaki (1984) presented a more complete picture of the pre-buckling and post-buckling behavior of cylinders subjected to torsion in the elastic range. In addition to presenting better values for the constant K_s in Eq. 2.10, a reasonably accurate prediction of the post-buckling equilibrium path and the buckle formation of earlier experiments was achieved.

The experiments (Yamaki, 1976) were conducted using six polyester test cylinders with a radius equal to 100 mm, a thickness equal to 0.25 mm, and lengths ranging from 23 to 161 mm. The corresponding curvature parameter, Z , for these specimens was 20, 50, 100, 200, 500, and 1000. The critical load measured in the tests

was between 87% and 94% of the theoretical value, and the number of buckles was also close or equal to that predicted by the theory. The post-buckling characteristics of these tests are plotted together with the theory in Fig. 2.3.

As shown in Fig. 2.3, the equilibrium torque of the tested cylinders decreases after buckling. For short cylinders ($Z < 200$), the equilibrium torque increases after reaching a minimum post-buckling value. The cylinder with $Z=20$ did not exhibit any reduction after buckling. For long cylinders ($Z > 200$), the equilibrium torque decreases for a large angle of twist before it begins to increase again. When Z reached 1000, the reduction was almost 60% of the buckling torque. It is also noted that the theoretical curves are fairly close to the test curves, both before and after buckling.

Yamaki showed that the shear constant K_s in Eq. 2.10 is dependent on the value of Z as well as on the restrained deformation and forces at the boundaries. However, his tables showed that the value of K_s may be approximately taken as 0.80 for cylinders with Z values that range from 200 to 1000. The shear constant K_s , reproduced from the work tables of Yamaki (1984), is plotted in Fig. 2.4 for different cylinder geometries. It can be seen from Fig. 2.4 that cylinders with relatively thin walls ($R/t > 200$) and long shear spans ($R/L < 1.0$) have a value of K_s of about 0.80, while cylinders with relatively thick walls ($R/t < 200$) and short shear spans ($R/L > 1.0$) have considerably higher values of K_s , which may reach a value of 1.50.

To clarify the effect of imperfections on the critical load, Yamaki introduced an imperfection amplitude into the stability analysis. The analysis confirmed the dependency of the imperfection sensitivity on the value of Z and the imperfection amplitude.

Equations 2.8 through 2.10 predict the buckling stress in the elastic range. In the inelastic range, the buckling strength may be reduced due to the presence of residual stress. In this case, reduction factors are needed to account for the plasticity effect.

2.2.5 Cylinders Subjected to Transverse Loading

Failure under transverse shear can result from either local buckling or yielding of the material or as a combination of both. Local buckling may occur in a flexural mode or in a shear mode. Extensive yield may take place close to the neutral axis in zones of low bending moment and high shear forces, or it may take place in tensile zones under flexure of longitudinally stiffened tubes. In the following, the discussion is limited to thin-walled unstiffened tubes. Thus, material failure as a separate phenomenon is not of interest.

Using simple flexural beam theory, the pre-buckling membrane stresses in a cylinder are related to the bending moment and shearing forces as follows:

$$M = \sigma \pi t R^2 \quad (2.11)$$

$$V = \tau \pi t R \quad (2.12)$$

where σ is the maximum longitudinal stress due to bending, τ is the maximum shear stress, and where the moment of inertia for a thin-walled tube is taken as $\pi t R^3$. It can be seen from Eqs. 2.11 and 2.12 that the ratio of σ/τ in the pre-buckling range is the same as the ratio of M/RV .

The earliest test data in the elastic buckling of transversely loaded cylinders is reported by Lundquist (1935). The test cylinders had R/t ratios that ranged from 323 to 1455 and R/L ratios that ranged from 0.5 to 2.0. The specimens were fabricated in the same way as those described in Section 2.2.4 (Lundquist, 1935).

Lundquist showed that the value of the ratio M/RV is descriptive of the buckling mode of cylinders under combined shear and moment. For small values of M/RV (less than 2), failure occurred in shear by the formation of diagonal buckles on the side of the cylinder. The size and form of the buckles at failure were similar to those which were observed for the corresponding cylinders that had been loaded in torsion. As M/RV approaches zero, the maximum shearing stress was between 1.20 and 1.38 times the critical shearing stress in torsion.

For large values of M/RV (more than 3), failure occurred in bending by a sudden collapse of the region that was in maximum compression. The buckle size and the maximum longitudinal stress were similar to the comparable cylinders that had been loaded in pure bending. At intermediate values of M/RV (between 2 and 3),

there was a transition from shear to bending mode accompanied by a reduction in strength.

Based on Lundquist's test results, Schilling (1965) suggested that the elastic buckling shear stress in transverse shear could be taken as 1.25 times the critical elastic shear stress in torsion. However, for the inelastic range, Schilling proposed that no increase in the shear stress be permitted so as to account for the corresponding reduction in the buckling strength.

Lu (1965) derived two theoretical bounds for the bending buckling load of a cantilever cylinder subjected to a concentrated load at the end. The upper bound (σ_{cr1}) was obtained from linear elastic theory, while the lower bound (σ_{cr2}) was obtained from finite displacement theory. The two bounds are:

$$\sigma_{cr1} = \frac{2.536}{\sqrt{3(1-\nu^2)}} E \frac{t}{R} \quad (2.13)$$

$$\sigma_{cr2} = \frac{0.6594}{\sqrt{3(1-\nu^2)}} E \frac{t}{R} \quad (2.14)$$

Lu did not provide any solution for the critical shear stress, nor did he elaborate on which of the two critical compressive stresses is more likely to occur.

Schröder (1972) solved the theoretical buckling problem of perfect cylindrical shells under transverse loads. Starting with Donnell's linear assumptions, Schröder derived the governing differential equations for a perfect cylinder supported at one end

and loaded at the free end by edge force. The equations were then solved using the Galerkin integration method.

Schröder showed that perfect cantilever cylinders subjected to transverse loading may buckle in a shear mode or in a bending mode depending on the R/L and R/t ratios. For high values of the R/L ratio (about 0.35 or more), the buckling stress for shear buckling is considerably smaller than that for bending buckling. By examining the solution, Schröder concluded that coupling between the two modes is unlikely to occur. The critical shear stress, expressed in terms of the geometry and material properties of the cylinder, is given by:

$$\tau_e = \bar{N}_{x\phi} E \left(\frac{t}{R} \right) \left(\frac{R}{L} \right) \frac{1}{\sqrt{3(1-\nu^2)}} \quad (2.15)$$

in which $\bar{N}_{x\phi}$ is a dimensionless parameter which depends on the values of the ratios R/t and R/L. In the original work by Schröder, two sets of curves were presented. Each set defines the values of $\bar{N}_{x\phi}$ for one of the two buckling modes. The curves that correspond to the bending mode must be considered not realistic because the profound effect of the initial imperfections on the critical bending stress was not included in the analysis. On the other hand, the curves that correspond to the shear buckling mode can be assumed to be reasonably accurate because shear buckling appears to be relatively insensitive to the presence of initial imperfections. Those curves are plotted in Fig. 2.5.

Yamaki et al. (1979) carried out an experimental study on the buckling of clamped cylindrical shells under combined action of transverse load and internal hydrostatic pressure. The test cylinders were made of a 0.247 mm thick polyester film rolled on a 100 mm diameter mandrel and lap-jointed along the longitudinal seam. The cylinder lengths varied from 22.8 to 228 mm. In order to distribute the end load, an 18 mm thick Duralumin end plate was attached to each end of the cylinder

Yamaki et al. found that the critical transverse loads obtained under a condition of zero hydrostatic pressure were between 99% and 106% of those theoretically predicted by Schröder (Eq. 2.15.) The theoretical critical stress of fixed cylinders under torsion (Eq. 2.10 with Yamaki's definition of K_s) was also compared to the test results and found to be in slightly less satisfactory agreement. Yamaki et al. concluded from the closeness of the two solutions that the elastic critical shear stress of cylinders under transverse load is nearly equal to that of cylinders under torsion.

To examine the accuracy of Yamaki's conclusion in the range of dimensions that are important in this study, Schröder's solution and Yamaki's solution for the clamped edge condition are plotted together in Fig. 2.6. The ratio of the critical shear stress to the elastic modulus is shown for a selected range of R/L and R/t ratio. It can be seen from Fig. 2.6 that the critical torsional shear stress is a fairly good estimate of the transverse shear stress except in the case of short stocky cylinders, where the difference is apparent. It should also be noted that the ratio of the yield shear stress to the elastic modulus

for steel with a tensile yield strength of 450 MPa is approximately 0.0013. The difference between the two solutions is most important only below this limit.

Yamaki et al. also compared the results of Lundquist's tests (1935) to the two theoretical solutions, Eqs. 2.10 and 2.15. Lundquist reported the load at which wrinkling appeared as well as the failure load. Yamaki et al. found that the "failure" loads were higher than the theoretical predictions while the "first wrinkle" loads were lower. Yamaki et al. questioned the accuracy of Lundquist's data and criticized the fabrication procedure used in the tests.

Baker and Bennett (1984) investigated the buckling interaction curves for both unstiffened and ring-stiffened cylinders. They designed an apparatus that can apply different ratios of axial compression and shear loads on test specimens. The cylinders, which were made of 0.38 mm thick Lexan plate and were used repeatedly, had geometries that are characteristic of nuclear steel containment vessels. They had a value of R/t equal to 460 and a value of R/L equal to 0.57.

Baker and Bennett reported that the unstiffened cylinders demonstrated a smooth transition from the classical diamond-shaped buckling mode when loaded in axial compression into the diagonal wave buckling mode when loaded in transverse shear. The study also showed that the effect of using closely spaced ring stiffeners on the shear buckling load is very favorable (more than three times the

capacity obtained in the unstiffened test for the particular spacing and stiffness of the ring stiffeners used in the stiffened test).

The first study of the shear capacity of fabricated steel cylinders in the plastic range was done by Bailey and Kulak (1984.) They tested two steel cylinders (referred to as B1 and B2) loaded in transverse shear. In each case, the cylinder was fixed at both ends and loaded in the middle by a central load. The first specimen, B1, was fabricated from 0.76 mm thick steel sheet. It had an R/t value equal to 251 and an R/L value equal to 0.50. Large deformation was induced during the welding process in one of the two shearing spans, but no significant differences in the behavior between the two spans was observed during the test. Cylinder B1 failed as a consequence of a series of successive inclined buckles (at 22.5, 26.0, and 29.4 kN, consecutively) followed by compression buckles at the extreme fiber. The successive buckling observed in the B1 test is not a typical behavior for shear tests. The load is expected to drop after the first buckle.

The second specimen, B2, was fabricated from 5 mm thick steel plates. For this specimen, R/t was 75 and R/L was 0.50. Buckling occurred at 967 kN on one side of a shear span, after which the load dropped. Soon after, another buckle formed at 890 kN on the other side of the same shear span. The load then dropped to 660 kN where it stabilized. Both tests showed clearly a stable post-buckling equilibrium path.

Bailey and Kulak hypothesized a similarity between the post-buckling behavior of plate girders and that of thin-walled cylinders under transverse load. They investigated the possibility of adapting Basler's tension field theory for plate girders (Basler, 1961) to fit thin-walled cylinders. Bailey and Kulak suggested a possible form of the ultimate shear strength equation based on the experimental observations. This form is expressed as follows:

$$V_u = k_{t1} T_v \quad (\text{high } R/t \text{ ratio}) \quad (2.16a)$$

$$V_u = k_{t2} T_v + k_{y1} T_y \quad (\text{intermediate } R/t \text{ ratio}) \quad (2.16b)$$

$$V_u = k_{y2} T_y \quad (\text{low } R/t \text{ ratio}) \quad (2.16c)$$

where V_u is the ultimate shear strength of the cylinder, T_v the tension field shear strength, T_y the yield strength of the cylinder and k_{t1} , k_{t2} , k_{y1} , and k_{y2} are functions of R/t ratio and the material properties. Bailey and Kulak noted that the ratio R/t is an important factor in determining the failure mode. Cylinders with low values of the R/t ratio are expected to fail primarily due to yielding, while cylinders with high values of the R/t ratio may buckle long before yielding occurs.

Another shear study in the inelastic range was reported by Galletly and Blachut, (1985) who tested fourteen short cantilever cylinders under end loads. The cylinders were made by wrapping steel sheets around a 150 mm radius mandrel and then welding the longitudinal seam. Heavy flanges were welded onto the cylinder ends

where the end load was applied. The dimensions, material properties, and the buckling shear stress of the cylinders are listed in Table 2.1.

As Table 2.1 shows, duplicates were made of the first five models; G1, G3, G5, G7, and G9. (The duplicates are G2, G4, G6, G8, and G10, respectively). The largest variation in buckling stresses between any duplicate pair was 10% (G9 and G10). In addition to these results, each cylinder was tested twice: after a given cylinder was buckled the first time, the load was reapplied in the opposite direction and increased until buckling occurred a second time. By this repetitive testing in opposite directions, the effect of relatively large imperfections (the buckles that remained from the first test) could be examined. For all but one of the cylinders, the second buckling load was at least 90% of the first one. (These results are not shown in Table 2.1). Galletly and Blachut therefore concluded that shear buckling is not very sensitive to the level of initial imperfections in the tube. Although this conclusion seems reasonable, it must be noted that formation of permanent buckles in the first test could have a stiffening effect against buckling when the direction of loading is reversed.

Galletly and Blachut found that for their tests, the maximum shear stress can be accurately predicted by a quadratic interaction equation in the following form:

$$\frac{1}{\tau_p} = \frac{1}{\tau_e} + \frac{1}{\tau_y} \quad (2.17)$$

where τ_y is the yield shear stress, τ_e is the elastic critical shearing stress of a perfect cylinder in torsion (Eq. 2.10), and τ_p is the plastic critical shear stress of the cylinder due to transverse shear loads. The ratio between the critical shear stress measured in the test and that predicted by Eq. 2.17 is also given in Table 2.1. In most cases, this ratio is greater than 1.0, i.e., the predicted value is on the safe side. The only two tests where the ratio was less than 1.0 (G7 and G9) had reported higher initial imperfection than the rest of the tests. It should be noted that Galletly and Blachut used the value 0.74 for the shear constant in Eq. 2.10. This is conservative for the fixed boundary condition and the geometries of the tested cylinders ($125 < R/t < 188$, and $0.83 < R/L < 1.37$). A more accurate value of the shear constant, K_s , would be 0.825 (see Fig. 2.4.)

The European specifications (European Convention for Constructional Steelwork, 1988) use an interaction equation similar to Eq. 2.17 to calculate the inelastic shear buckling stress. This equation is also a function of the elastic torsional shear buckling stress, as shown following:

$$\frac{\tau_p}{\tau_y} + 0.25 \frac{\tau_y}{0.65 \tau_e} = 1.00 \quad (2.18)$$

where the factor before the elastic shear stress (0.65) reflects what the ECCS suggests as the effect of the geometric imperfections on the elastic buckling stress. The predictions of the ECCS equation are generally close to those of Eq. 2.17, but are less conservative for moderate values of R/t ratio (200 to 300).

Mok and Elwi (1986) carried out a numerical investigation of the shear behavior of large diameter cylinders using a nonlinear finite element analysis program. They examined the effect of loading conditions and boundary conditions on the buckling mode. Mok and Elwi used the first buckling mode shape to incorporate initial imperfections in the numerical analysis. However, they did not recommend this procedure for further investigations because of the difficulty of determining the correct scaling factor. The analysis which employed small size of imperfections agreed well with the theoretical results by Batdorf et al. (May, 1947) but did not agree well with the experimental results of Bailey and Kulak (1984).

In addition to the numerical study, Mok and Elwi continued the work by Bailey and Kulak on the development of a tension-field-based ultimate shear equation. They derived an ultimate shear equation that consisted of two components, a beam component and a tension field component. However, the critical shear stress which forms an integral part of the beam component was not completely defined.

Further numerical investigation was carried out by Roman and Elwi (1987). They traced the equilibrium path in the pre-buckling as well as the post-buckling range. The initial imperfections were incorporated naturally in the numerical model with the help of a three dimensional degenerated shell element. The analysis also accounted for the initial residual stresses inherent in thin-walled cylinders due to cold forming and welding.

Roman and Elwi confirmed the experimental observations of Galletly and Blachut that the shear capacity is not very sensitive to initial imperfections, especially flute-type imperfections. The analysis also suggested that the residual stresses inherent in some fabrication techniques may have a significant effect on the ultimate shear capacity.

Based on the results of their numerical study, Roman and Elwi proposed an analytical theory for the tension field contribution to the shear capacity of large diameter cylinders. They developed a truss model which simulates the load carrying mechanism of the cylinders in the post-buckling range. In spite of the good agreement between the model and the numerical analysis, the model did not include some of the parameters that govern the behavior of transversely loaded cylinders and, therefore, did not agree satisfactorily with some of the experimental results.

2.3 Summary

The buckling load of cylindrical shells has been a crucial problem in the design of these members because of the several factors that influence the shell capacity. In the elastic range, random geometric imperfections introduced during the production process play an important role in developing the critical load. In the inelastic range, residual stresses developed by forming and welding techniques can have a detrimental effect on the buckling strength.

Cylinders subjected to axial compression or torsion have been extensively investigated, both experimentally and analytically.

Solutions based on large displacement theory are available for each case. Such solutions assist in determining the role of initial imperfections on the critical load.

For axially compressed cylinders, empirical formulas based on numerous test results (Eqs. 2.5 and 2.6) are available for design purposes. As is the case for cylinders subjected to torsion, the elastic buckling shear stress is accurately predicted by the theoretical solution, Eq. 2.10.

Cylinders subjected to pure bending or to transverse shear have not been examined as thoroughly as have the other loading cases, perhaps due to their limited applications in offshore structures. No solution based on the large displacement theory is available for these loading cases and very few experiments are reported in these areas.

In the elastic range, theoretical solutions based on small displacement theory do exist for cylinders subjected to pure bending or transverse shear. For perfect elastic tubes under transverse shear, Schröder's solution (Eq. 2.15) seems to yield fairly accurate predictions of the buckling load. The sensitivity of the buckling load to geometric imperfections can only be estimated from test results and numerical analyses.

The inelastic buckling of cylinders subjected to transverse shear was experimentally investigated by Galletly and Blachut who tested small cantilever models and proposed an interaction equation for the maximum plastic shear stress, Eq. 2.17. However, this

equation, which has a rational basis, does not produce the best fit of the test data, i.e. the error of estimating the shear capacity based on the test results was not minimized. The predictions of this empirical equation were, of course, compared only to the results of the small cantilever tests: full-scale test results should also be used.

The only tests of large diameter fabricated steel tubes under bending or transverse shear were carried out at the University of Alberta (Stephens et al. and Bailey and Kulak). The actual effect of the initial imperfections and residual stresses is correctly represented in the results of these tests. Initial numerical analyses of one bending specimen and one shear specimen did not agree satisfactorily with the test results.

The post-buckling behavior of Bailey's test initiated the search for a physical model that can predict the post-buckling capacity of transversely loaded cylindrical shells. The attempts made so far do not compare well with the few available tests.

Model No.	Material	t (mm)	R/t	R/L	E (1000 MPa)	τ_y (MPa)	τ_{exp} (MPa)	$\frac{\tau_{exp}}{\tau_y}$ (MPa)
G1	Mild steel	0.8	188	1.00	200	172	149	1.11
G2	Mild steel	0.8	188	1.00	200	172	142	1.06
G3	Mild steel	1.0	150	1.00	195	134	134	1.12
G4	Mild steel	1.0	150	1.00	195	134	132	1.10
G5	Mild steel	1.2	125	1.00	200	164	168	1.13
G6	Mild steel	1.2	125	1.00	200	164	161	1.08
G7	Structural steel	1.0	150	1.00	190	240	170	0.95
G8	Structural steel	1.0	150	1.00	190	240	182	1.02
G9	Structural steel	1.2	125	1.00	195	206	163	0.92
G10	Structural steel	1.2	125	1.00	195	206	179	1.01
G11	Structural steel	1.2	126	1.37	195	206	194	1.06
G12	Structural steel	1.0	151	1.37	190	240	192	1.06
G13	Structural steel	1.2	129	0.83	195	206	171	1.01
G14	Structural steel	1.0	155	0.83	190	240	172	1.02

**Table 2.1 Test results of steel cylinders under transverse edge shear
(after Galletly and Blachut, 1985)**

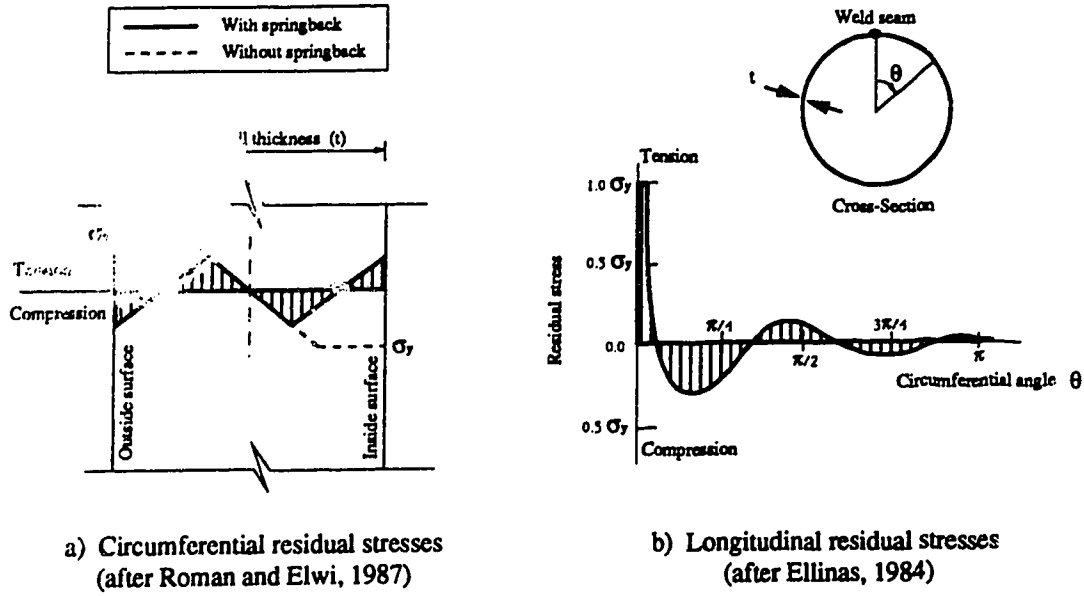


Fig. 2.1 Residual stress distributions in tubular members

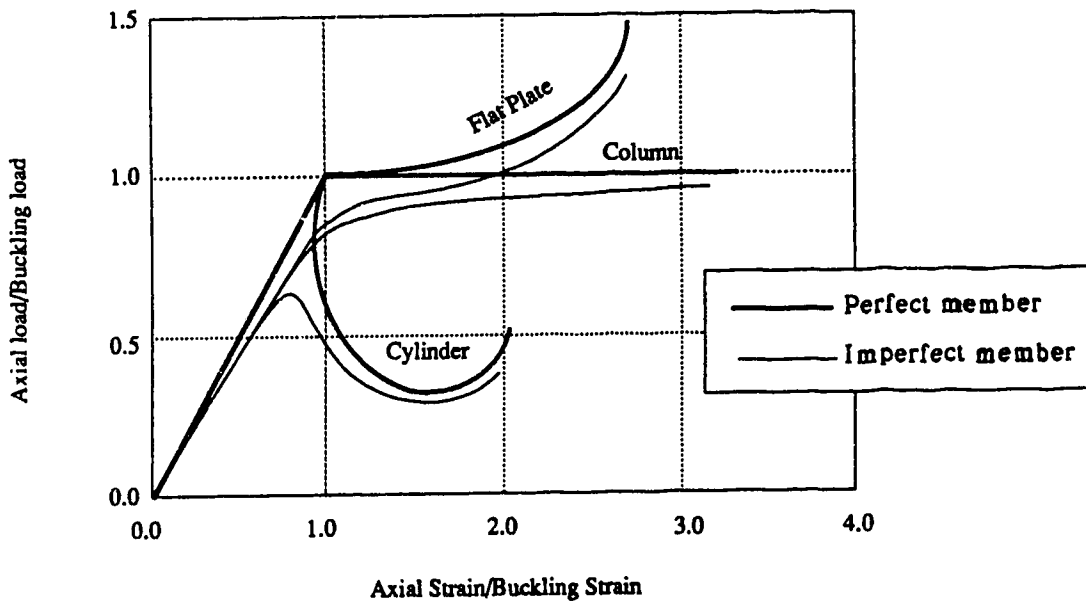


Fig. 2.2 Post-buckling characteristics of different structural members

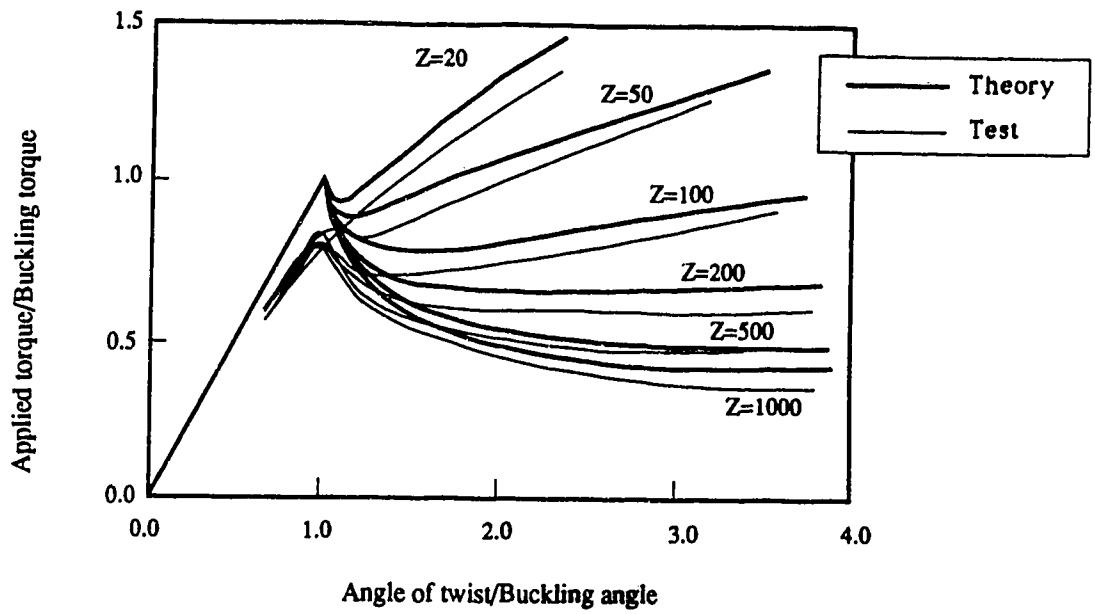


Fig. 2.3 Comparison between theory and tests for cylinders under torsion (after Yamaki, 1984)

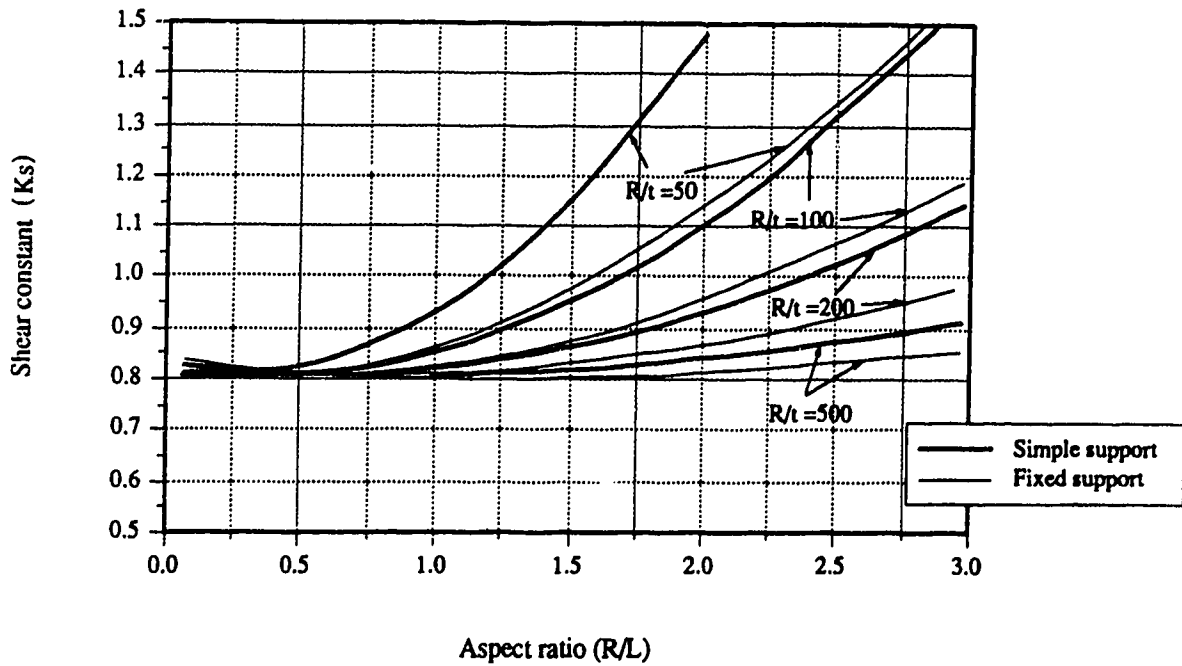


Fig. 2.4 Yamaki's elastic buckling shear constant

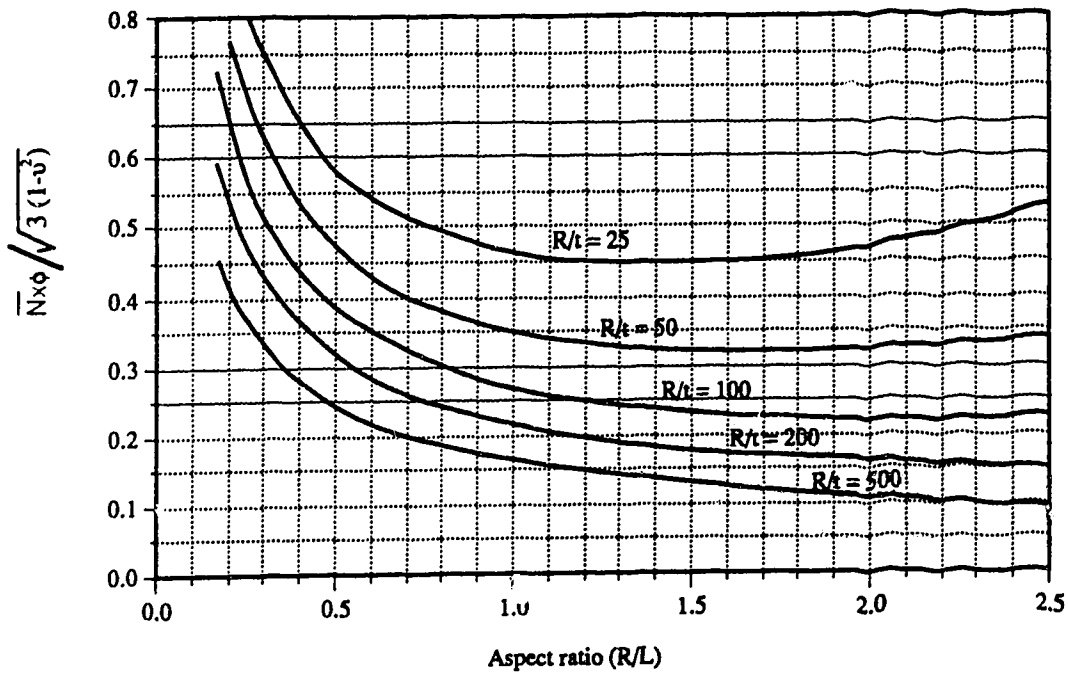


Fig. 2.5 Shear stress factor, $\bar{N}_{x\phi}$, for cylinders under transverse loading

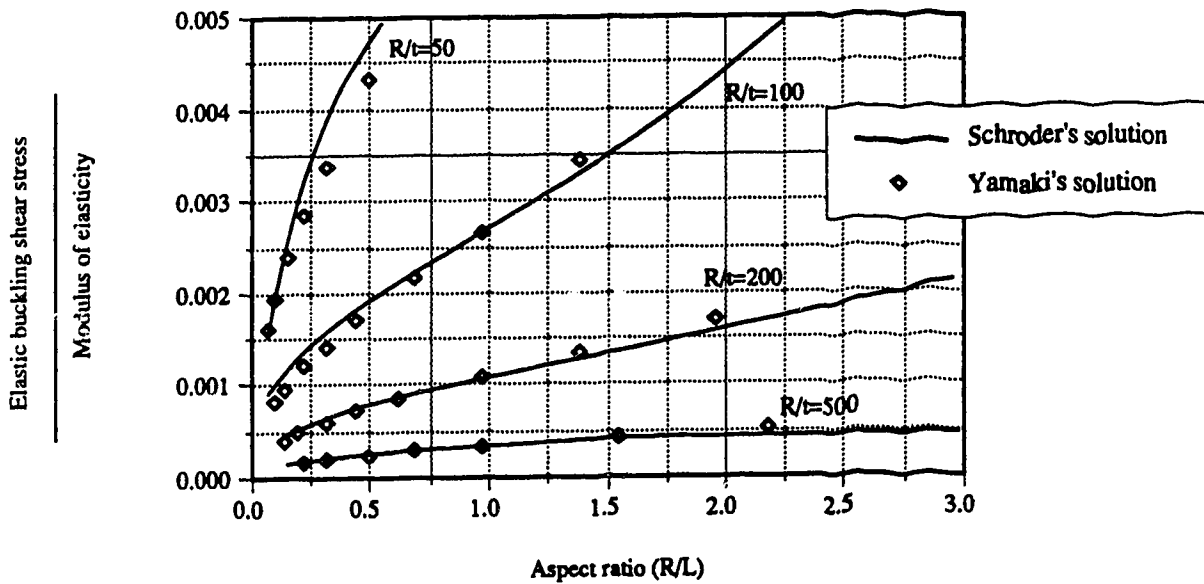


Fig. 2.6 Comparison between torsional and transverse buckling shear stresses

3. Testing of Fabricated Cylinders Subjected to Transverse Loading

3.1 Introduction

The purpose of the experimental program described herein was to investigate the shear buckling behavior of large diameter thin-walled fabricated steel cylinders under transverse loading. Cylinders of the geometry investigated have a number of civil engineering applications, for example, as tubular conveyor galleries. Typically, these members range from about 2500 mm to 4000 mm in diameter and are fabricated from hot-rolled steel plates of about 5 mm to 8 mm in thickness. This gives a radius to thickness ratio (R/t) in the range of 150 to 400. Practically all tubes of the proportions described have ring stiffeners, but longitudinal stiffeners may or may not be present. This study considers only longitudinally unstiffened members.

Very few tests have been conducted on members of this description. One group of tests was carried out by Bailey and Kulak (1984). Two specimens, one fabricated from hot-rolled steel plates and the other fabricated from cold-rolled steel plates, were tested as a beam with fixed end support. These specimens had R/t ratios of 75 and 250, respectively, and a radius to shear span ratio (R/L) of 0.5. Another group of cylinders was tested by Galletly and Blachut (1985). Fourteen specimens fabricated from cold-rolled steel sheets were tested as cantilevers. The specimens had R/t ratios ranging

from 125 to 188 and R/L ratios ranging from 0.83 to 1.37. The radius of these specimens was held constant at 150 mm.

The tests reported herein were on cylinders fabricated from hot-rolled steel plates. They had an R/t ratio of 185. One specimen, S1, was tested as a beam with fixed end supports and had an R/L ratio of 0.53, while the second specimen, S2, was tested as a cantilever and had an R/L ratio equal to 0.76. The nominal diameter of each of these specimens was 1270 mm. These tests, and one of the Bailey and Kulak test pieces (R/t=75), are considered to be the only available test results that reflect the material, proportions, and fabrication practice that are representative of full-size tubes. (The Bailey and Kulak specimen is somewhat stockier than usually encountered in practice, however).

3.2 Test Design

3.2.1 Design Equations

Since cylinders under transverse loads may buckle either due to shear or due to bending, estimates of the critical shear stress (for shear buckling) and the critical compressive stress (for bending buckling) are required in order that design of the test specimen can be carried out in such a way that failure by shear buckling can be expected.

When the elastic buckling shear stress approaches the yield shear stress, the cylinder buckles in an elastic-plastic mode at loads smaller than those predicted by the elastic equation. An estimate of

the inelastic critical shear stress for cylinders under transverse shear has been proposed by Galletly and Blachut (1985). This estimate, which is based on experimental test results, is calculated as follows:

$$\tau_p = \frac{\tau_y}{\sqrt{1 + \left(\frac{\tau_y}{\tau_e}\right)^2}} \quad (3.1)$$

where τ_p is the inelastic critical shear stress, τ_y is the shear yield stress, and τ_e is a conservative estimate of the elastic buckling shear stress of cylinders under torsion and is given by:

$$\tau_e = 0.74 E \left(\frac{t}{R}\right)^{1.25} \left(\frac{R}{L}\right)^{0.5} \quad (3.2)$$

in which τ_e is the elastic buckling shear stress, E is the elastic modulus, R is the cylinder radius, L is the length of the shear span, and t is the cylinder wall thickness. This is the Batdorf et al. (1947) solution given by Eq. 2.10 with K_s as 0.74.

The best estimate for the critical compressive stress for a cylinder under transverse shear is probably that proposed by Stephens et al. (1982) which has been discussed thoroughly in Section 2.2.3 and represented by Eqs. 2.7(a), 2.7(b), and 2.7(c). However, these researchers also suggested that for cylinders with wall thickness less than 6 mm, a more conservative estimate of the critical stress is the AWWA (1979) formula represented by Eqs. 2.6(a) and 2.6(b). Since this estimate is conservative, it can be interpreted as a lower bound for bending failure and therefore its use helps in designing the shear failure tests.

Using beam theory, these critical stresses can be translated to critical forces as follows :

$$M_{cr} = \sigma_{cr} \pi R^2 t \quad (3.3)$$

$$V_{cr} = \tau_{cr} \pi R t \quad (3.4)$$

in which M_{cr} is the critical bending moment for the compression buckling mode case and V_{cr} is the critical shear force for the shear buckling mode case. As explained in Section 2.2.5, the value of the σ_{cr}/τ_{cr} ratio, or the M/VR ratio, identifies the buckling mode. This ratio can be calculated for specific material and geometrical properties using Eqs. 3.1, 3.2, 2.6 and 2.7.

An R/L ratio around 0.5 is considered to represent practical cases. The values of the elastic modulus and the yield stress are assumed to be 200×10^3 MPa and 300 MPa, respectively. In order to be able to use hot-rolled steel plates, as would be employed in practice for large diameter fabricated steel tubes, the cylinder wall thickness had to be larger than 3.2 mm (1/8 in.). For the commonly used range of R/t values, a value around 200 was considered appropriate for the selected wall thickness and the capacity of the testing equipment available. The selected ratio implies that the cylinder will buckle in shear in an inelastic mode. The diameter of the test specimen that results from this R/t ratio is about 1280 mm.

Calculating τ_{cr} and σ_{cr} from Eqs. 3.1, 3.2, and 2.6, the maximum M/VR ratio in a span has to be less than 1.13 to allow for buckling in a shear mode before buckling in a bending mode. By choosing a

conservative value of the M/VR ratio (1.0), the cylinder had to be tested either as the fixed-ended beam shown in Fig. 3.1(a) or as the cantilever beam shown in Fig. 3.1(b). The fixed-ended beam solution, which has a constant shear, was chosen for its simplicity and convenience. The specimen tested in that configuration, which also used constant thickness, was called S1.

When S1 was tested, only one of the two shear spans showed signs of failure or yielding in shear or bending; the other span recovered completely upon removal of the load. It was decided, therefore, to modify the specimen by cutting away the damaged span and testing the remaining intact shear span. This was designated as specimen S2. It was tested as a cantilever beam with an R/L ratio of 0.76. This is the longest shear span that allows a shear buckling mode to occur according to the predictor equations.

3.2.2 Finite Element Analysis

In addition to the design equations mentioned above, numerical analysis was also used to predict the failure load and the failure mode of specimens S1 and S2. Roman and Elwi (1987) utilized the finite element method to analyze the problem in hand with a reasonable degree of confidence. Prior to testing the specimen, a finite element analysis was carried out to predict the behavior and capacity of the specimens. The analysis predicted that both specimens could be expected to fail due to shear buckling.

For Specimen S1, the finite element mesh used was a 6×6 mesh of three dimensional degenerated bi-cubic Lagrangian thin shell

elements which modeled one quarter of the cylinder. The load-displacement curve and the shape of the deformed mesh were obtained in the pre-buckling and post-buckling range. The results are presented in Section 3.3.4. For Specimen S2, a 4x4 mesh which modeled one half of the cylinder was adopted in a similar manner for the analysis of S1. The analytical results are compared with the test values in Section 3.4.4. A detailed description of the numerical analysis of S1 and S2 is reported in Chapter 4.

3.3 Shear Specimen S1

3.3.1 Specimen Description

Geometry and Fabrication

It is possible that the buckling behavior of a fabricated tube is affected by the method of construction. Therefore, the fabrication techniques employed were carefully observed. The specimens were fabricated by a local steel fabricator using their standard procedure. Two 3.44 mm thick grade 300W hot-rolled plates (P1 and P2) meeting CSA Standard G40.21 (specified minimum yield and ultimate strength of 300 MPa and 450 MPa, respectively) were cold-formed in rollers to the desired curvature and then joined longitudinally with full-penetration groove welds to form two cans. The two cans were then welded together to form the specimen S1, as shown in Fig. 3.2. In one method of fabrication, flat plates are rolled to a radius smaller than the final radius and released to spring back to the desired radius, thereby releasing some of the residual stresses created by rolling. However, in this case the plates were rolled to the desired

curvature, clamped, and then welded without allowing any spring-back.

Material Properties

Coupons were cut from the base material prior to rolling in order to determine the elastic modulus and the yield strength of the material. The 50 mm gage length coupons were prepared in accordance with the ASTM Standard (1989), and were oriented so that material properties would be measured parallel to what would be the longitudinal axis of the specimen. Three coupons taken from plate P1 (see Fig. 3.2) were tested. They had an average static yield stress of 337 MPa and an average elastic modulus of 218×10^3 MPa. The coefficients of variation for these average values were 3.7% and 2.5%, respectively. Three coupons taken from plate P2 had an average static yield stress of 335 MPa and an average elastic modulus of 215×10^3 MPa. The coefficients of variation for these average values were 4.2%, and 0.8%, respectively. All coupons demonstrated the sharp yielding plateau characteristic of hot-rolled steel and had a ductility of approximately 30%.

Initial Imperfection Measurements

The initial geometric imperfections resulting from fabrication, welding, and preparation of the specimen for testing were carefully measured in order to determine the imperfection level and the shape of the fabricated cylinder.

The overall shape deviation of the cross-section was established by measuring the cylinder out-of-roundness, e , which is defined as the difference between the maximum diameter, D_{\max} , and the minimum diameter, D_{\min} :

$$e = D_{\max} - D_{\min} \quad (3.5)$$

In addition, local bulges and depressions in the cylinder wall were measured along both longitudinal generators and the circumference. The surface imperfection was characterized by the deviation amplitude, w_i , defined as the offset between points on the wall surface and the corresponding points on a perfect cylinder with average diameter. Thus:

$$w_i = D_i - D_{\text{avg}} \quad (3.6)$$

The apparatus used to measure the imperfections, shown in Fig. 3.3, permitted the measurement of the specimen radii at discrete points on the inside surface of the cylinder with respect to an assumed longitudinal axis. It consisted of an aluminum tube 56 mm in diameter and 2650 mm long placed between the centers of the two end fixtures so that it would coincide with the longitudinal axis of the cylinder and could rotate about it. A linear variable differential transformer LVDT was mounted at the top of a steel bar so that total length of the bar and the LVDT probe is as same as the mean radius of the cylinder (635 mm). This bar was welded normal to a car which can move on a track along the aluminum tube. The voltage changes from the LVDT were converted to changes in the cylinder radius. By pushing the car, the LVDT was able to reach any

point on the inside surface along a line parallel to the longitudinal axis of the cylinder. By rotating the aluminum tube, the LVDT was able to reach any point along the inside circumference of the cylinder.

The first set of measurements consisted of 540 readings. The radius was measured at 15 stations along the longitudinal axis. At each station the radius was measured at 36 points equally spaced about the circumference. The second set of measurements consisted of 70 readings. These were taken along the longitudinal weld and the transverse weld seams. The imperfections, measured just before testing, on each quarter of the cylinder are magnified 20 times and shown in Fig. 3.4. The four quarters of the cylinder will be named according to their orientations, e.g. the southwest side of the cylinder is the quarter which lies between the west set of columns and the midspan and faces south. For the imperfection measurements taken, the average radius was 637 mm, the cylinder out-of-roundness (e) was 14 mm and the average deviation amplitude (w_i) was 2.54 mm.

3.3.2 Test Frame

The test set-up used for specimen S1 is illustrated in Fig. 3.5. It is simply a 2650 mm long cylinder placed horizontally between two sets of supporting columns, one set at the east and the other at the west, and loaded at the midspan.

The load was transferred to the cylinder through two 19 mm thick diaphragms, which were designed to carry 2000 kN vertical concentrated force from the testing machine and transfer it through

the weld by means of shear flow into the thin wall of the cylinder. At each end, the cylinder was welded to a 19 mm thick diaphragm. These end diaphragms were bolted to the supporting columns with 40 ASTM A325 bolts of 25 mm diameter. Each set of supporting columns consisted of five individual columns. Three of these, W310X118 sections, were tied to the floor. It was not possible to bolt the others (W310X79 sections) to the floor, and they were hung from the diaphragm. The five columns were connected together by two horizontal beams (W200X36) bolted to each one of them. To minimize column rotations, two channels (C250X23) were inserted longitudinally between the two ends.

3.3.3 Instrumentation

Strain gages

Shear buckling of thin-walled tubes can be significantly influenced by the residual stresses induced in the cylinder due to fabrication and installation processes (Roman and Elwi, 1987). Therefore, an attempt was made to measure the stresses induced by forcing the specimen into a circular shape, by welding, and by the test set-up itself. This was done by installing strain gages on the tube wall prior to attaching the cylinder to the test frame and prior to welding the diaphragm plates. Moreover, the gages had to be placed far enough from the weld locations so as not to be damaged by the welding process. This distance is governed by the maximum temperature that the strain gage can withstand and the heat input

from welding, and it can be calculated from a standard heat transfer equation, (Adams, 1958):

$$d = \frac{4 h}{S_w} \left(\left(\frac{P_e G I_w}{8 t K T} \right) - \frac{1}{5} \right) \quad (3.7)$$

in which d is the distance between strain gage and weld, S_w is the welding speed (10 mm/sec), P_e is the welding efficiency (95%), G is the welding voltage (21 volt), I_w is the welding current intensity (140 amp), K is the thermal conductivity (0.052 Cal./mm.sec. $^{\circ}$ C), h is the thermal diffusivity (13.54 mm 2 /sec), and T is the peak temperature for the strain gages (100 $^{\circ}$ C). Substitution of these values in the above equation gives d equal to 113 mm.

The tube was first placed vertically so that the cross-section would take its free shape. Using a level and a plumb-bob, twelve longitudinal generators 30 degrees apart were drawn on the outside tube surface. Electrical resistance strain gages (N11-FA-5-120-11) were then mounted on the outside surface of the cylinder.

The strain gages were grouped in four groups or "rings". Two rings were placed near the ends and two near the middle. Each ring consisted of one pair of strain gages at each of the twelve generators and each pair was oriented in the longitudinal and circumferential directions except at the neutral axis where rosettes were used instead. An additional eight rosettes were mounted at the middle of the shear spans, where zero bending moment was expected, on both the inner and the outer surfaces of the specimen. A total of 120 strain gages were applied. Their locations are illustrated in Fig. 3.6.

All data from the strain gages and LVDT's were recorded using a Fluke 2400 data acquisition system through which the signals were conditioned, converted from analog to digital form, and stored on disk. With this recording equipment, a large number of virtually simultaneous readings were taken.

The strain gages were connected to the Fluke and initial readings as well as measurements of the diameter were taken. The initial cross section had an ellipse-like shape with a difference between the maximum and the minimum diameter equal to 55 mm.

Displacement measurement devices

The bending moment distribution and the midspan deflection of the fixed end cylinder are sensitive to the support movements. Although the end fixtures were intended to model fixed end conditions, small rotations were inevitable. Therefore, eight LVDT's (L1 through L8), as shown in Fig. 3.7, were mounted normal to the corners of the end diaphragms to measure their rotations. Six dial gages (D1 through D6) were also mounted in the plane of the end diaphragms to measure the vertical and horizontal displacements. Four dial gages (D7 through D10) were mounted normal to the columns to measure their rotation in case the bolts holding the columns to the diaphragms stretched under loading.

The vertical displacement at the midspan is considered the most important measurement; therefore, four vertical LVDT's (L9 through L12) were mounted at the centerline and the bottom of the middle diaphragms. Although care was taken to center the specimen

under the loading head and between the end supports, two LVDT's (L13 and L14) were mounted on the middle diaphragm to detect any sway movement from the cylinder, and two (L15 and L16) were mounted normal to the middle diaphragms to measure their rotations. All the LVDT's and the dial gages are shown in Fig. 3.7.

3.3.4 Spacers

In order to make the cylinder cross section as close as possible to a circular shape, 50x100 mm wood posts with the same length as the inside diameter of the tube were inserted at the ends and the middle of the tube. The tube was then turned over on its side and the posts were adjusted until the difference between the maximum and minimum diameters was reduced to 14 mm.

3.3.5 Welding

The loads and reactions were transferred to the cylinder through four plates or diaphragms. The middle diaphragms were aligned, centered, and welded to the cylinder using the shielded metal-arc welding process. The end diaphragms were first bolted to the supporting columns, then welded to the cylinder using the shielded arc welding process. The welding details are shown in Fig. 3.8.

A set of strain readings was taken after the welding of the tube to the diaphragms had been completed. The longitudinal and circumferential stresses induced due to insertion of the spacers and to the welding process are shown in Fig. 3.9. The weld was left to cool

to room temperature before the supporting columns were tied to the floor.

3.3.6 Testing Procedure

After initial imperfections were measured and the specimen was installed in the test frame, a set of strain gage readings was taken to evaluate all the stresses induced in the specimen before testing. These stresses were not significantly different from those shown in Fig. 3.9, which were measured before the specimen was installed. The load was applied using an MTS 6000 universal testing machine. A trial load of 400 kN (25% of the expected maximum load) was applied and released several times to check the instrumentation and the support behavior.

The cylinder was loaded gradually in 100 kN increments. At every load step, dial gage and LVDT readings were recorded. The testing machine was on displacement control mode in order to be able to trace the behavior in the post-buckling stage. The load vs. central displacement curve was plotted using the instrumentation of the MTS machine and separately traced using LVDT L12. When the load reached 1300 kN, the cylinder started to show nonlinear displacement. The loading interval was then decreased to 50 kN. At a load level of 1700 kN, the cylinder buckled at the northwest side with a loud detonation. The whitewash which had been applied to the specimen before testing did not flake anywhere prior to this. The buckle consisted of two diagonal waves (locations 1 and 2 in Fig. 3.10) inclined at about 23 and 25 degrees to the longitudinal axis

of the cylinder. Upon buckling, the load dropped to 1490 kN, then started to increase again at about the previous rate until it reached 1563 kN when a second buckle occurred at the southwest side of the specimen. It also consisted of two diagonal waves, inclined at about 24 and 27 degrees. The load dropped to 1290 kN, recovered to 1380 kN, and then stayed nearly constant. When the vertical displacement at midspan approached 5.0 mm, a single depression buckle occurred at 115 mm from the west middle diaphragm (location 3 in Fig. 3.10) together with three small buckles at the extreme compression fiber of the central test section between the two middle diaphragms (location 4 in Fig. 3.10). However, the load remained constant with continuing deformation. The test was terminated when the central vertical displacement had reached slightly over twice its magnitude at the time of buckling. The central displacement had almost the same value before buckling for the four different LVDT's (L9, L10, L11 and L12). Fig. 3.10 shows a schematic of both the shear buckles and the subsequent compression buckles, while the deformed shape of one half of the cylinder as plotted from the finite element analysis is shown in Fig. 3.11. Photos of the buckled shape of specimen S1 from both the north side and the south side are shown in Figs. 3.12(a) and 3.12(b).

3.3.7 Test Results

The load applied from the MTS machine was plotted against the vertical displacement of the cylinder neutral axis at the location of the loading diaphragm. The displacement was taken as the average of LVDT's L9 and L10, then corrected for the support deformation.

The first correction was made to adjust for the end support rotation which was measured by LVDT's L1 through L8. A second correction was made to adjust for the vertical settlement of the supporting columns, as measured by the dial gages D1 and D2. Modeling the specimen as a beam with fixed ends, the measured support deformations were used to calculate the change in the displacement at the LVDT locations. The correction resulted in a decrease in the measured central deflection by 0.000436 mm/kN up to the ultimate load, at which time the reduction was 20% of the measured value. The corrected load vs. displacement curve as measured in the test and the calculated displacement from the finite element analysis are both shown in Fig. 3.13. The load vs displacement curve of the test is linear before reaching about 800 kN, following which the slope gradually flattens. The slope of the load vs. displacement curve predicted by finite element analysis is slightly larger than the actual slope. The ultimate load measured in the test is 1700 kN. The ultimate load predicted by the finite element analysis is 1716 kN.

Shear stresses measured prior to buckling from the rosettes located close to the supports and at the theoretical zero-moment locations are plotted in Fig. 3.14 (end rosettes) and Fig. 3.15 (mid-span rosettes). The stresses were calculated from the measured strain assuming plane stress relationships. Figure 3.14 shows that the west span had slightly higher values of shear stresses than the east span (a difference of about 8% at the ultimate load). Similar observations can be seen in Fig. 3.15 for the mid-span rosettes located at the south side of the specimen. One exception to this

criterion is the rosettes located at the north side of the specimen, where the readings indicates that the stresses in the unbuckled side (the north-east side) were about 10% larger than those measured in the buckled side (the north-west side) at the time of buckling. The only explanation that can be offered in this case is that these two rosettes were not accurate. Figure 3.15 also shows that the shear stresses at the inner surface of the northeast and southwest quarters of the specimen are smaller than those at the outer surface.

The longitudinal strain distributions around the cross-section near the fixed ends and the middle diaphragms are shown in Figs. 3.16(a) and 3.16(b), respectively. It is noticed that the second pair of strain gages from top and bottom gave readings which were particularly smaller than the theoretical predictions based on the beam theory. An attempt to explain this difference is described below (Section 3.3.8).

The longitudinal strain distribution along the top and bottom generators of the cylinder is shown in Figs. 3.17(a) and 3.17(b), respectively. It is clear that the strain readings at the middle gages are larger than those of the end gages: this is a direct effect of the end fixture rotation.

3.3.8 Discussion

Test specimen S1 had an elastic linear response under transverse loads up to a proportional load limit, after which the slope of the load vs. displacement curve was slightly smaller than the slope before the proportional load. The ultimate load was reached when

buckling occurred. Beyond the ultimate load, the carrying capacity dropped and stayed stable at a lower load level (about 82% of the ultimate load). The stability of the carrying capacity was accompanied by the development of a tension field in the direction of the buckles between the middle diaphragm and the supporting diaphragm. This post-buckling capacity was maintained until the compression buckles occurred near the middle diaphragm.

The best prediction of the ultimate load was achieved by the finite element model, which estimated the failure load to within 1% of the actual load. The buckling mode predicted by the numerical analysis was a shear mode similar to the observed mode in the test. However, the number of buckles appeared in the deformed finite element mesh (three buckles) did not agree with the number of buckles which actually occurred in the test (two buckles).

The relative movement between the east and the west supports may have caused the shear force to differ from one span to the other. Figure 3.18 shows the shear force diagram that corresponds to the measured settlement and rotations at the supports. The shear force that existed on the west span according to this figure is 966 kN. The maximum shear force predicted by Eqs. 3.1 and 3.4 is 772 kN which is 20% smaller than the west span shear force. A better agreement is obtained from the numerical model where the predicted shear force is 858 kN or 11% smaller than the west span shear force.

The shear stress in the west shear span was larger than the shear stress in the east span, probably because of some eccentricity in the applied load or because the deformations at the east support were larger than those at the west support. These factors added more shear to the west span of the specimen and presumably triggered buckling in it. The difference between the shear stress measured at the inside and the outside surface of the specimen can be attributed to the presence of a cross bending moment associated with the initiation of the buckles.

Both the finite element analysis and the previous tests (Stephens et al., 1982, and Bailey and Kulak, 1984) showed linear strain distribution through the cross section before buckling. However, in this test, some strain gages seemed to give unreasonable readings (Fig. 3.16). It was noted in Section 3.3.3 that the amount of heat transmitted to the strain gages is dependent on the welding speed which was controlled manually and might not have been constant at all times. A speed higher than 10 mm/sec may overheat some of the strain gages and affect their performance.

In addition to the overheating effect, the longitudinal strains at the end diaphragm were sensitive to the support deformations. This could have resulted from the fact that the supporting columns attached near these strain gages were less stiff than the supporting columns near the other gages. A numerical analysis of an elastic cylinder with boundary conditions reflecting relaxed end fixture deformation was carried out (see Fig. 3.19). In this analysis, the deformations of the locations attached to the less stiff columns were

allowed. The results of the analysis in the region close to the end diaphragm showed that a very small displacement in the longitudinal direction was enough to significantly reduce the longitudinal strain at this location. The longitudinal stress distribution near the support and the corresponding longitudinal displacement distribution are shown in Fig. 3.19.

Thus, despite the fact that the gages placed close to the end diaphragms were useful in measuring the stresses generated by welding and test set-up, their usefulness in measuring the end stresses was diminished in the light of the boundary condition changes shown in Fig. 3.18. Their usefulness was further reduced according to the above analysis.

3.4 Shear Specimen S2

3.4.1 Specimen Description

Specimen S2 was prepared by cutting the undamaged span of S1 about 1400 mm from the east support. This part did not show any signs of failure or yielding during the first test and recovered completely upon removal of the load. The east end fixture was left attached to the specimen to be used as a part of the set-up for S2. The material properties of S2 correspond to P1 coupons. The initial imperfection and overall geometry are, of course, the same as for the east span of S1.

3.4.2 Test Frame

Specimen S2 was tested as a cantilever beam, as shown in Fig. 3.20. The overturning moment of the cantilever was supported by a triangular frame composed of the end fixture, bracing members, and reaction columns. The moment was transferred from the end fixture to the bracing members and hence to the reaction frame. The end fixture was the east end fixture of specimen S1, which consisted of three long columns resting on the floor and two short columns hung between them. The five columns were bolted to the end diaphragm from one side and to two horizontal beams from the other side. The bracing members consisted of three inclined channels (C250X23) and three horizontal beams (W200X31). These six members were bolted at one end to the three long columns and at the other end to the reaction columns. The three reaction columns (W310X118) were connected together and prestressed to the floor to support the horizontal movement of the test frame.

A universal testing machine was used to apply load to the cylinder through a 19 mm thick diaphragm. The loading diaphragm was welded to the cylinder at a distance 825 mm from the end plates using the gas-shielded arc welding process. In order to increase its stability, the loading diaphragm was connected to a dummy diaphragm which remained from the first test set-up. Two rollers 300 mm wide were placed above the loading diaphragm to allow for the horizontal component of the edge rotation. A 37 mm thick

horizontal plate and eight 25 mm thick stiffeners were used to seat and center the rollers above the diaphragm.

3.4.3 Instrumentation

Strain gages

A ring of twelve rosettes 30 degrees apart around the circumference was mounted at a distance 65 mm from the end diaphragm. Another ring of four rosettes was mounted at the middle of the shear span. The strain gage locations are shown in Fig. 3.21.

Displacement measurement devices

The rotation of the end support was measured by two LVDT's (L1 and L2) and a dial gage (D1) at the top, bottom, and middle, respectively, of the end diaphragm. The vertical settlement of the columns was measured by one LVDT (L3) attached to the bottom of the end diaphragm.

The vertical displacement of the cylinder at the loading diaphragm was measured by two LVDT's (L4 and L5) at the neutral axis of the cross section and one LVDT (L6) at the bottom of the loading diaphragm.

Ovalling of the cylinder was measured at the middle of the shear span by two LVDT's (L7 and L8) in the horizontal direction and another two (L9 and L10) in the vertical direction.

The rotation of the loading diaphragm at the neutral axis was measured by a rotational gage (R1) and the change in the diaphragm

width was measured by two LVDT's (L11 and L12). The LVDT locations are shown in Fig. 3.22.

3.4.4 Estimated Failure Load

Unlike the situation for Specimen S1, the bending moment and shear force diagrams in S2 are easily calculated because the system is statically determinate. The expected failure load in a shear buckling mode for Specimen S2 is 968 kN according to Eq. 3.1 and the expected failure load in a bending buckling mode is 745 kN or 1142 kN according to Eq. 2.6 or Eq. 2.7. Also, the finite element analysis predicted failure due to shear buckling at an ultimate load of 1054 kN. Although Eq. 2.6 (the AWWA formula) anticipates failure in a bending mode rather than a shear mode, its conservative nature together with the predictions of Eq. 2.7, Eq. 3.1, and the finite element analysis minimizes this possibility. The conservative nature of the AWWA formula can be easily seen from the results of specimen S1. The maximum load resulting in bending failure of specimen S1, as predicted by this equation under the conditions shown in Fig. 3.18, is 1435 kN, which is smaller than the actual failure load measured in the test (1700 kN) and which occurred in a shear mode.

3.4.5 Testing procedure

The inside and outside surfaces of the specimen were painted with whitewash. The strain gages and the LVDT's were connected to the data acquisition system. The load was applied up to 400 kN and

removed several times to check the instrumentation and the support behavior.

The loading started in increments of 50 kN. After each load step, a set of readings was taken from all the instrumentation. When the load reached 500 kN, the increment was decreased to 30 kN. At a load level of about 700 kN the slope of the load vs vertical displacement curve, plotted simultaneously by the MTS machine, started to show nonlinear behavior. The loading increment was decreased to 20 kN. At a load level of about 830 kN the nonlinearity increased and the increment was decreased to 15 kN until the ultimate load was reached.

At a load of 940 kN the cylinder buckled at the north side and the whitewash flaked along two diagonal lines (shown in Fig. 3.23 as 1 and 2) that were inclined at 21 and 27 degrees from the horizontal. The load dropped to 790 kN, then started to increase at a rate much smaller than that which was predicted before the first buckle. When it reached 920 kN, the cylinder buckled again at the same side, but at a location below the first two buckles (shown as 3), and the load dropped to 720 kN. The load was removed and the displacement which had occurred prior to the first buckling was recovered. Fig. 3.23 shows a schematic of the shear buckles while the deformed shape of one half of the cylinder as plotted from the finite element analysis is shown in Figs. 3.24. Photos of the buckled shape of specimen S2 from both the outside and the inside surface are shown in Figs. 3.25(a) and 3.25(b).

3.4.6 Test Results

The load applied from the MTS machine is plotted in Fig. 3.26 against the vertical displacement of the cylinder neutral axis at the loading diaphragm. The displacement was taken as the average of LVDT's L4 and L5 and corrected for boundary conditions. The first correction was made to adjust for the end support rotation as measured by LVDT's L1 and L2 and the dial gage D1. The rotation was linear with the load and resulted in 2.15 mm vertical displacement at ultimate load at the loading diaphragm. The second correction was made to adjust for the vertical settlement of the supporting columns as measured by LVDT L3 and resulted in 0.84 mm vertical displacement at ultimate load at the middle diaphragm. The total correction resulted in a decrease of the measured central deflection by 0.0032 mm/kN up to the ultimate load, at which time the reduction was 65% of the measured value. The corrected load vs. displacement curve from the test is compared to the response predicted by the finite element analysis in Fig. 3.26.

The shear stresses measured from the four rosettes at the neutral axis are plotted in Fig. 3.27. The buckled side of the specimen (the north side) appears to have slightly larger shear stresses than the other side. The difference was significant only just before reaching the buckling load, however.

Ovalling of the cross section is depicted in Fig. 3.28. The increase in the horizontal diameter and the decrease in the vertical diameter are plotted against the load. At the ultimate load level, the

vertical diameter decreased by 0.10% and the horizontal diameter increased by 0.25%. These small values of diameter change support the application of the beam theory in the case of S2 before buckling.

The longitudinal strains measured from the strain gages around the cross section are plotted in Fig. 3.29. The strain distribution before buckling is almost linear except for the second reading from the top and bottom. These correspond to the strain gages at 30, 150, 210 and 330 degrees. As already described for Specimen S1, the end diaphragm at these locations was attached to two short W310X79 columns which were supported by the more rigid columns that were seated on the floor. Although the short columns were rigidly connected to the long ones through two horizontal W200X36 beams, this connection inevitably allowed for a small movement. This movement was enough to reduce the measured strain according to the numerical analysis shown in Fig. 3.19.

3.4.7 Discussion

Specimen S2 demonstrated a linear response under transverse loading up to a load level of 800 kN. The carrying capacity dropped after it reached an ultimate load of 940 kN. The tension field, which appeared after buckling, had the same direction as the buckles. The post-buckling load of S2 was about 80% of the ultimate load.

The best prediction of the ultimate load was achieved by Eq. 3.1 which estimated the failure load within 3%. The behavior of specimen S2 can be traced by the finite element analysis. Although the numerical model predicted the slope of the load-displacement

curve and the deformed shape of the buckles specimen fairly closely, the ultimate load predicted by the finite element model was 12% larger than the ultimate load attained in the test.

The shear stress measured at different locations of the specimen confirms the presence of a constant shear stress on both halves of the circular cross-section. However, the shear stresses in the buckled half of the specimen increased rapidly just before buckling. This increase can only be related to the initiation of the buckles.

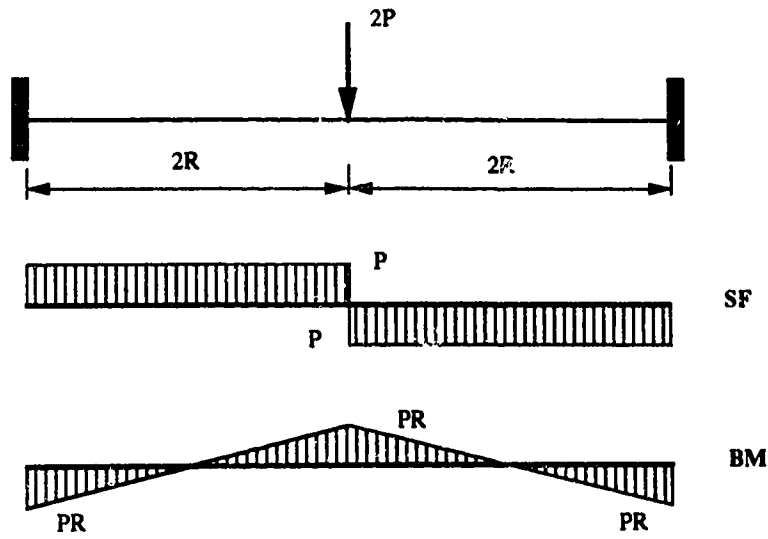
The linearity of the longitudinal strain around the cross-section can be observed in Fig. 3.29. The odd readings of the second pair of strain gages from top and bottom are explained by the change in the boundary conditions as discussed in Section 3.3.8.

3.5 Summary

Two large-diameter fabricated steel cylinders were tested under transverse shear. Both specimens failed in an inelastic shear buckling mode. Before buckling, the behavior of the specimens was linearly elastic up to a proportional load level. Following this, the response became gradually non-linear until inelastic buckling occurred.

The ultimate load for both specimens is reasonably estimated by the interaction equation proposed by Galletly and Blachut, Eq. 3.1. The finite element method can also be used to provide a good estimate of the failure load and to simulate the deformed shape.

After buckling, the carrying capacity of each specimen dropped by approximately 20%, after which it remained stable. This suggests a significant secondary post-buckling capacity. This post-buckling behavior, which has also been observed by other investigators (Bailey and Kulak, 1984), is used to develop a post-buckling shear capacity formula for thin-walled cylinders under transverse shear as described in Chapter 6.



1.0

Fig. 3.1(a) The fixed-ended beam solution

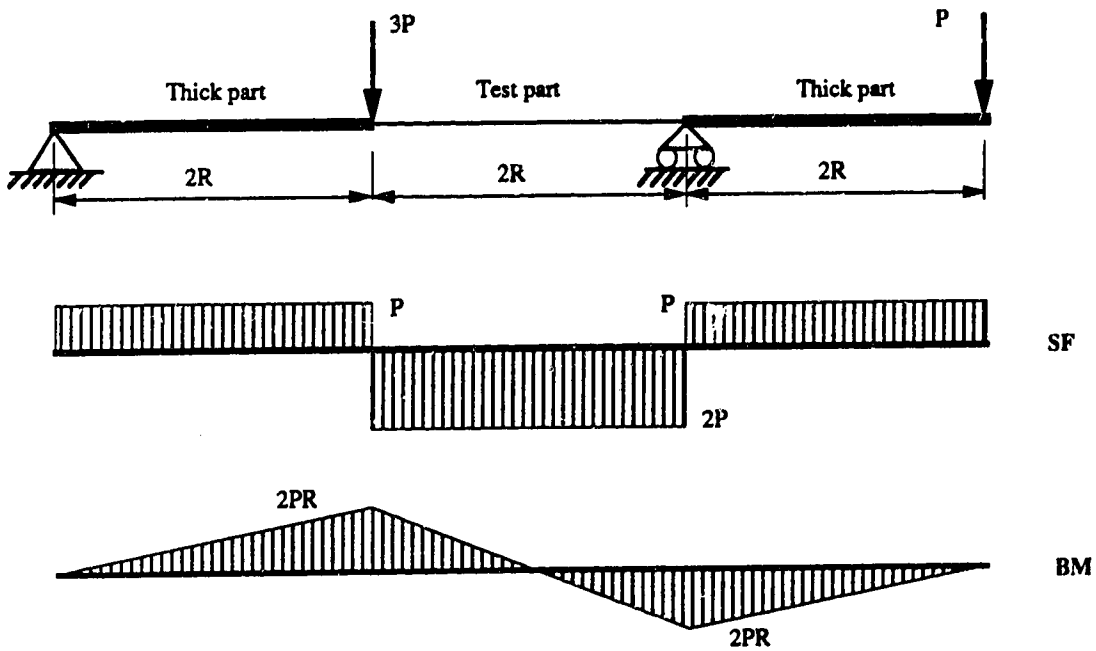


Fig. 3.1(b) The cantilever beam solution

Fig. 3.1 Possible configurations for cylinders with M/VR ratio equal to 1

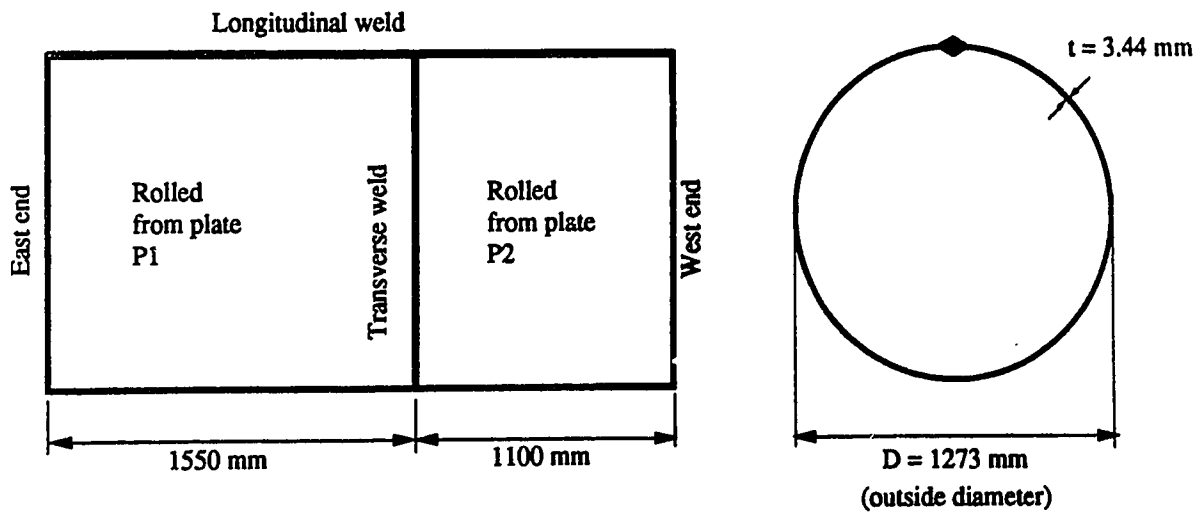


Fig. 3.2 Specimen S1 Configuration

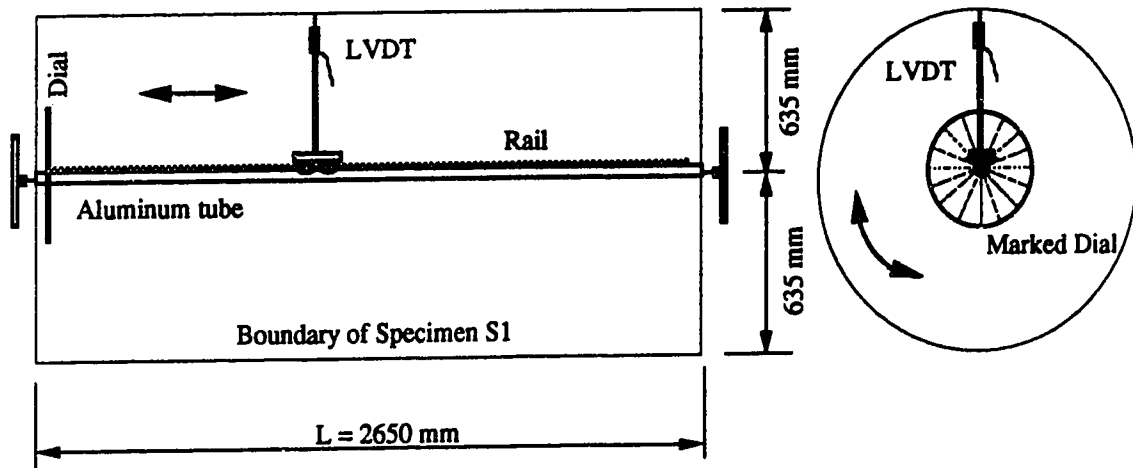


Fig. 3.3 Imperfection measurement device

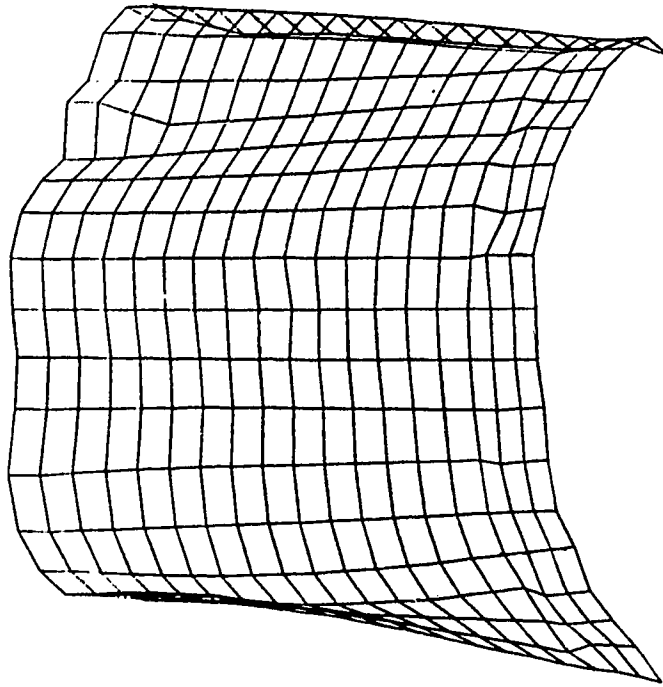


Fig. 3.4(a) The measured imperfection on the north-east quarter of the cylinder (magnified 20 times)

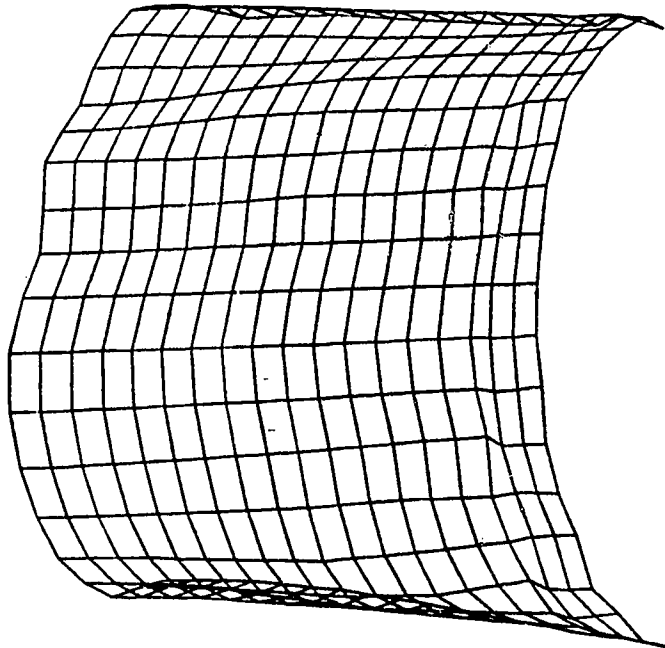


Fig. 3.4(b) The measured imperfection on the south-east quarter of the cylinder (magnified 20 times)

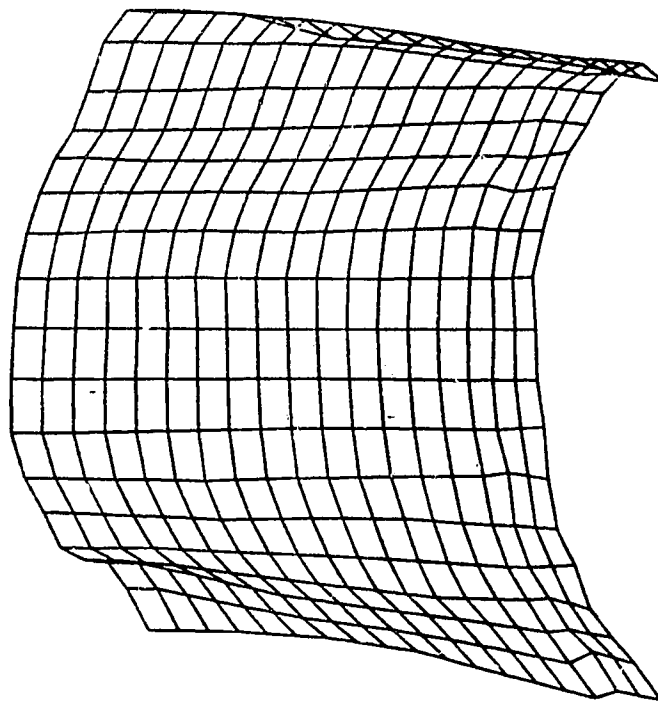


Fig. 3.4(c) The measured imperfection on the north-west quarter of the cylinder (magnified 20 times)

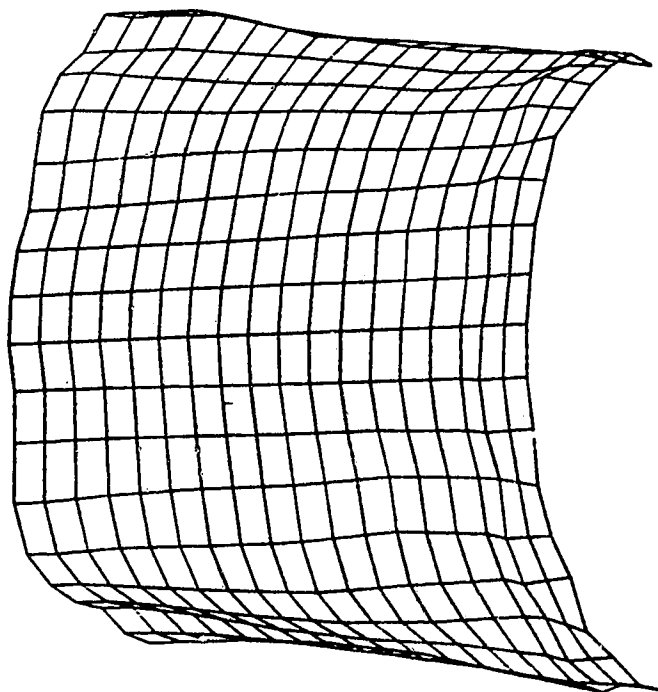


Fig. 3.4(d) The measured imperfection on the south-west quarter of the cylinder (magnified 20 times)

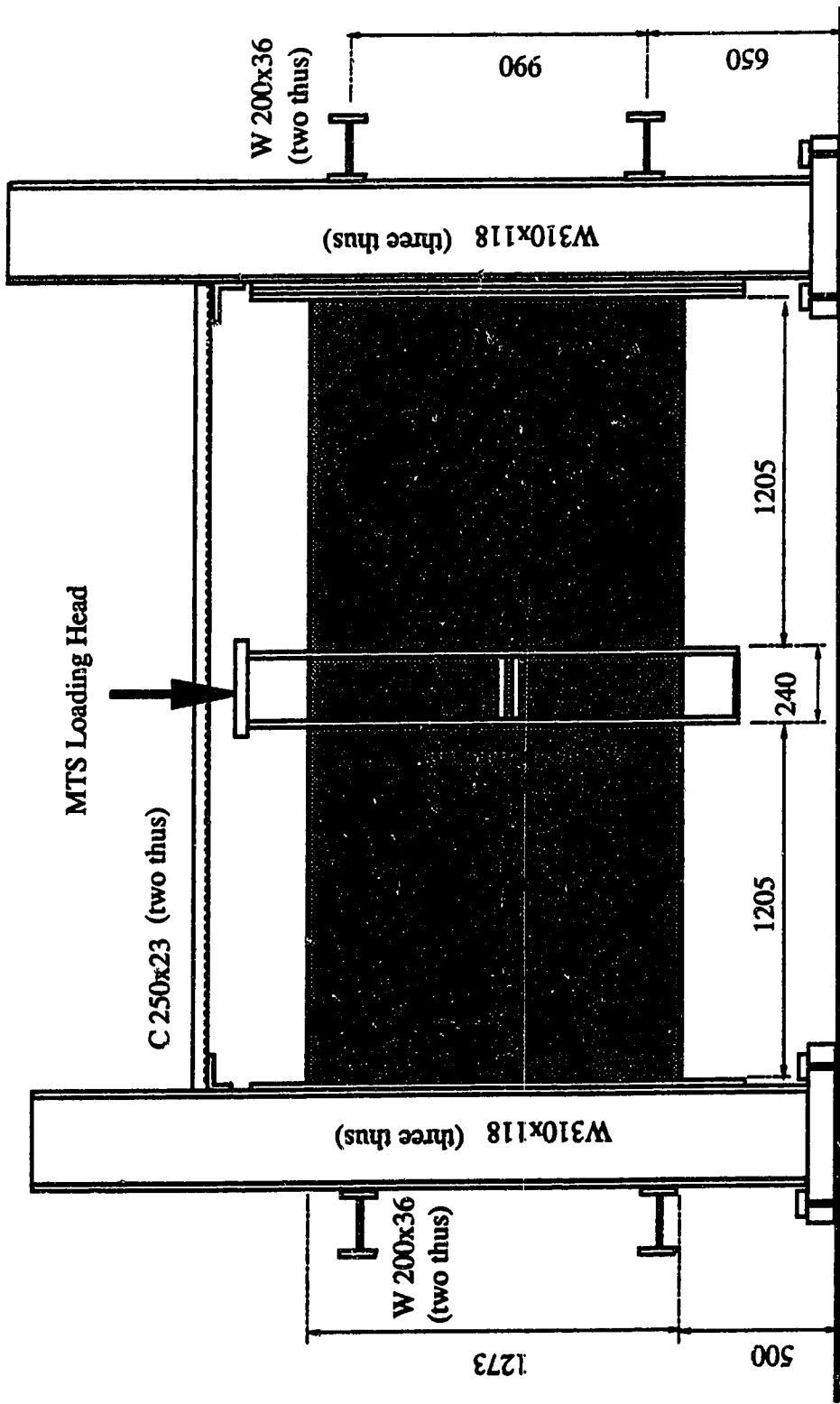


Fig. 3.5 Test set-up for specimen S1

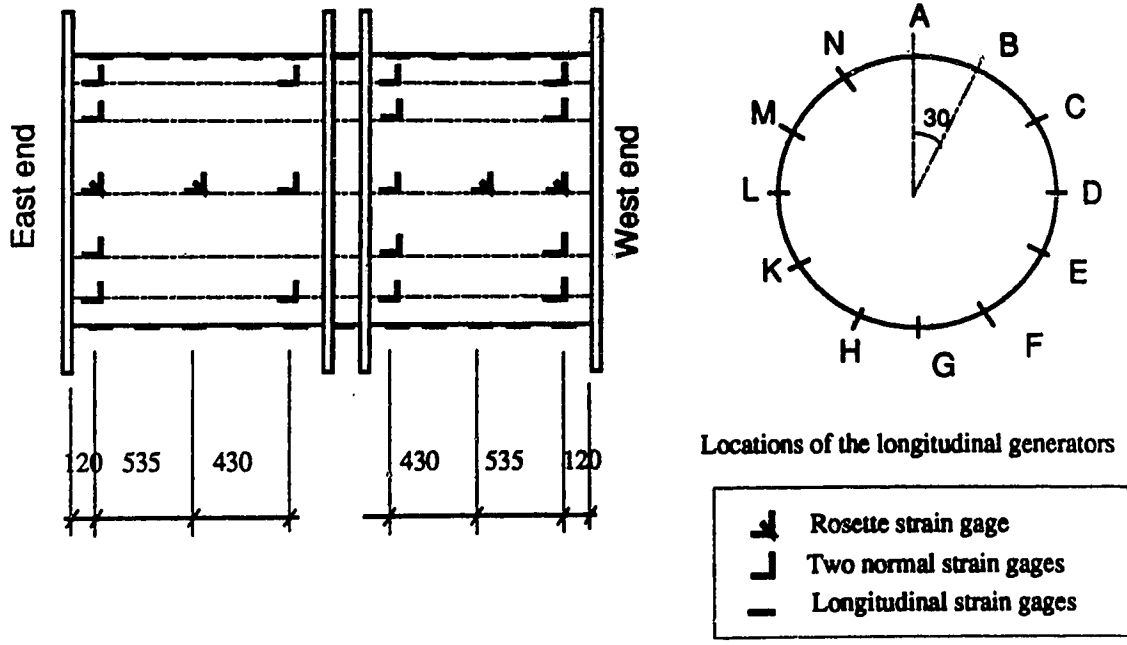


Fig. 3.6 Strain gage locations for specimen S1

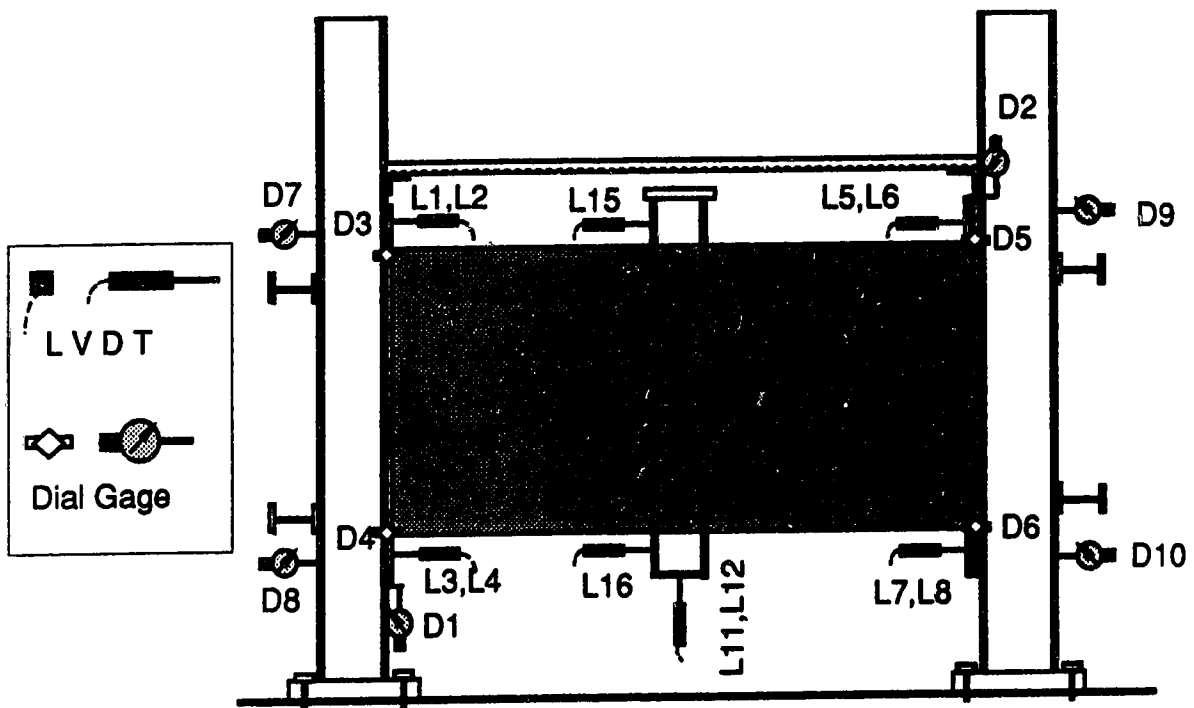


Fig. 3.7 Instrumentation for specimen S1

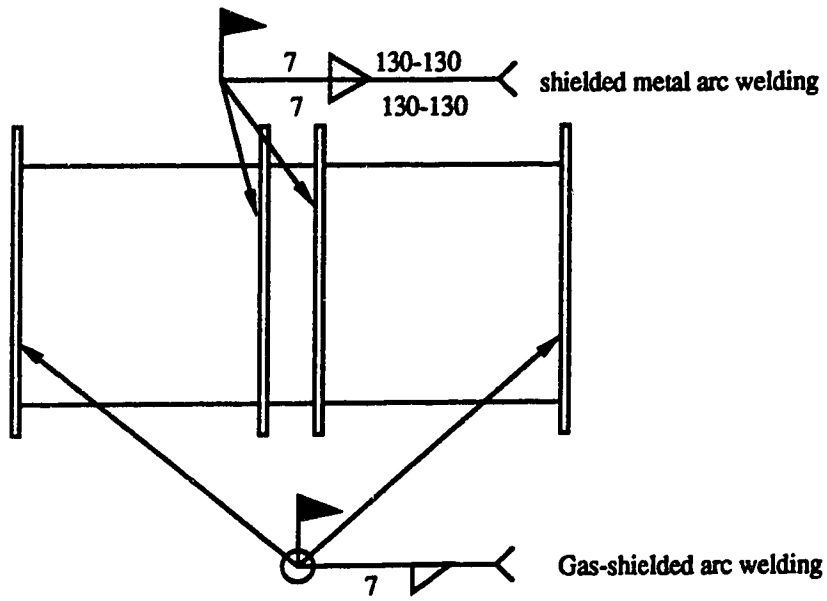


Fig. 3.8 Welding Details at the diaphragms of specimen S1

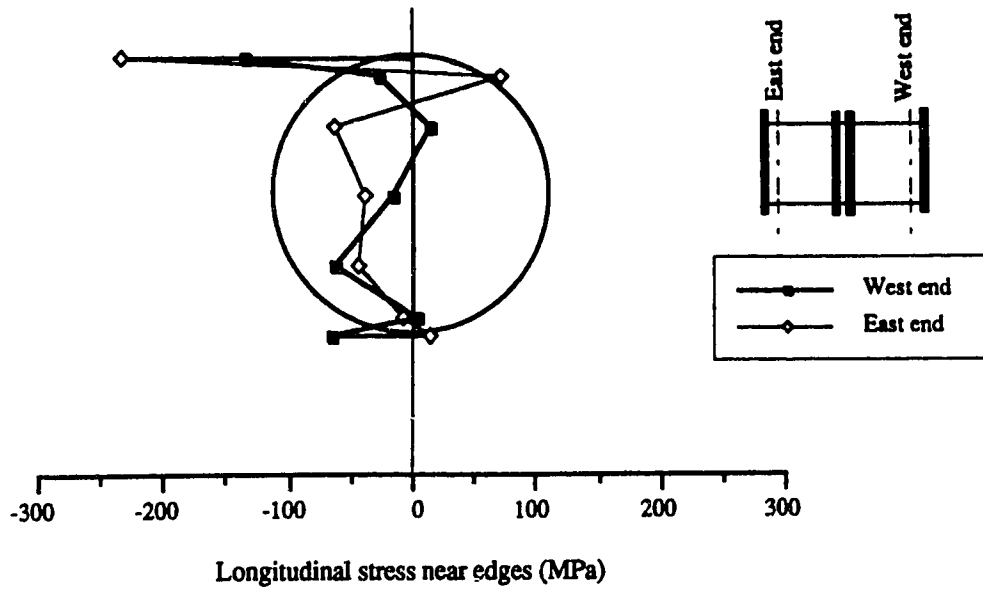


Fig. 3.9(a) Distribution of longitudinal stresses generated by welding and test set-up

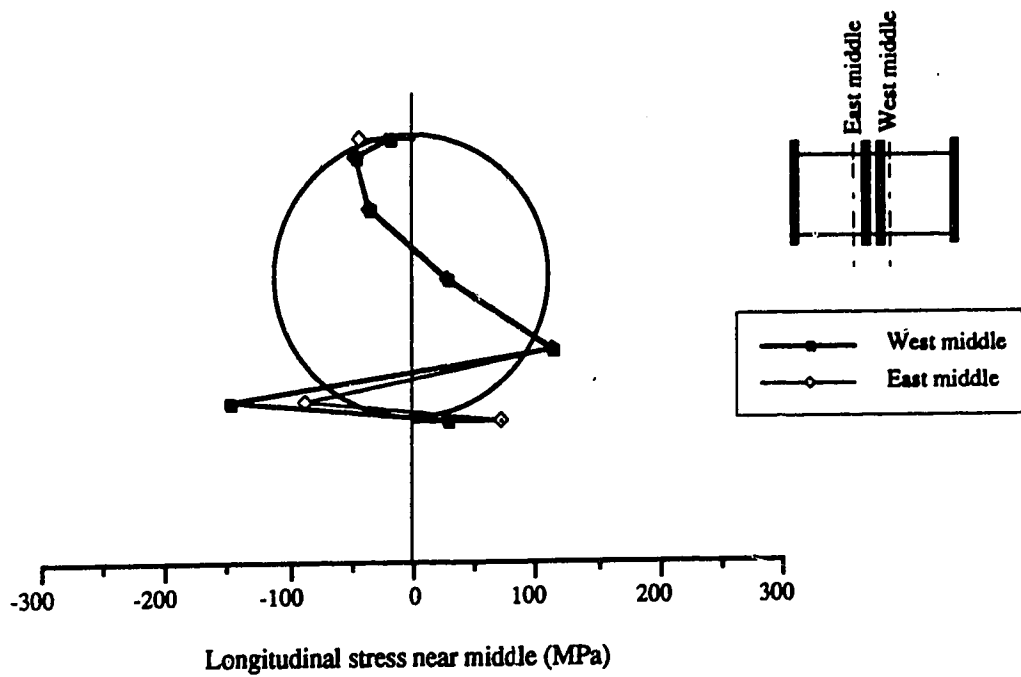


Fig. 3.9(b) Distribution of longitudinal stresses generated by welding and test set-up

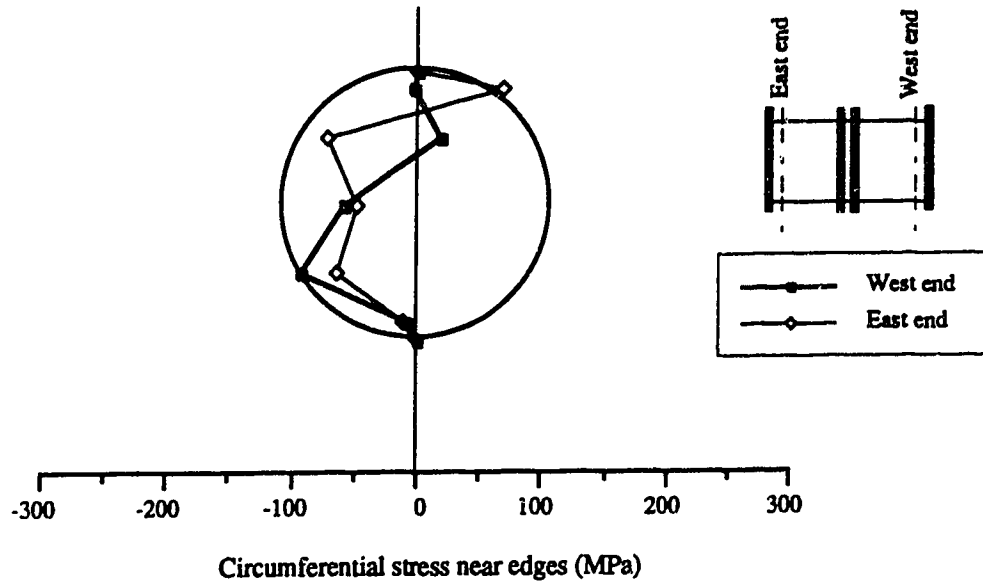


Fig. 3.9(c) Distribution of circumferential stresses generated by welding and test set-up

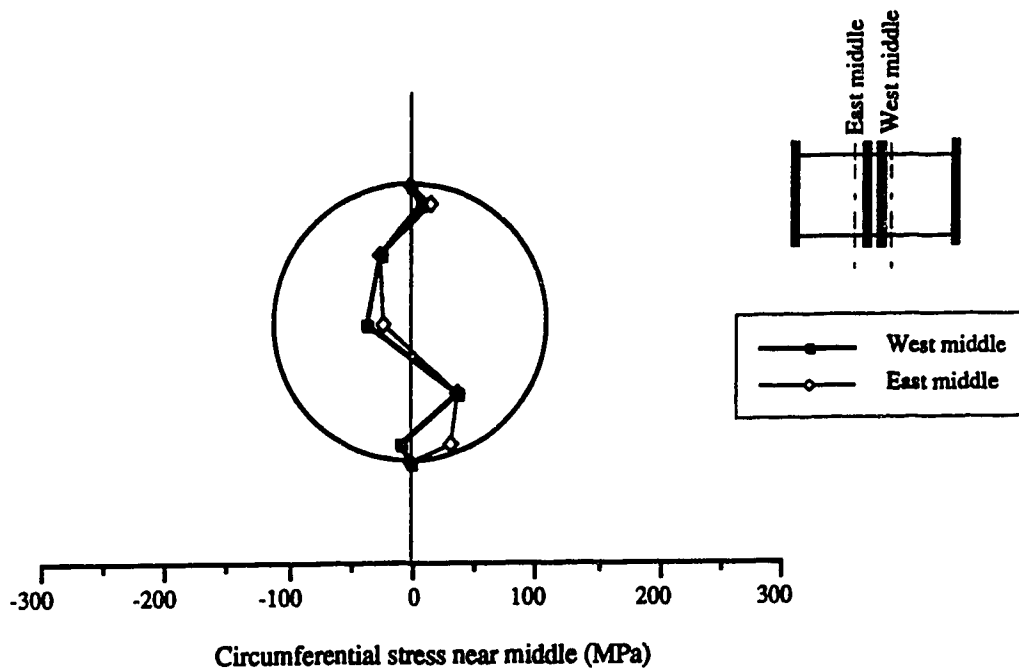


Fig. 3.9(d) Distribution of circumferential stresses generated by welding and test set-up

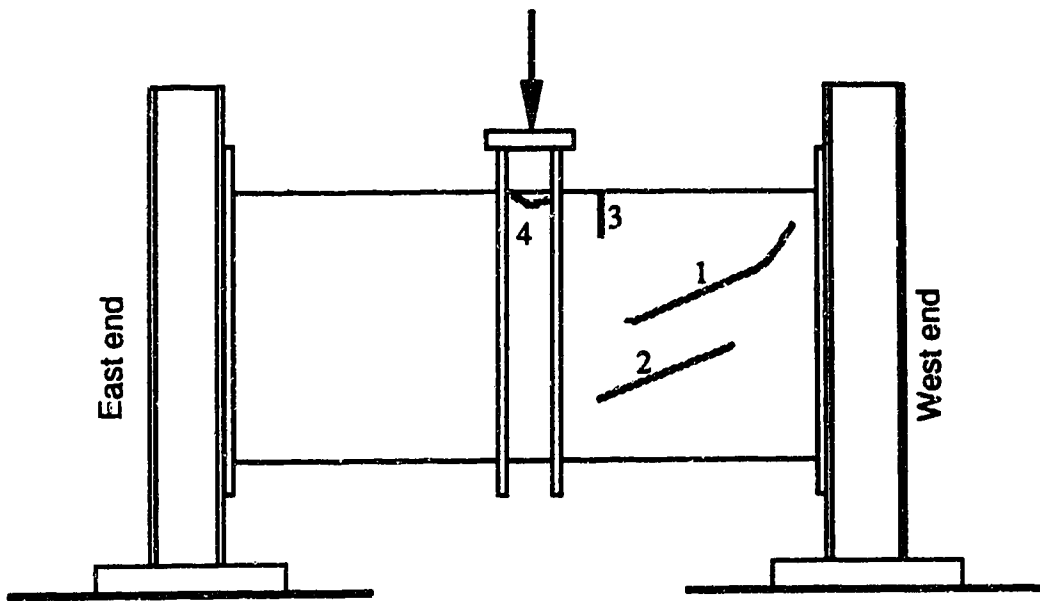
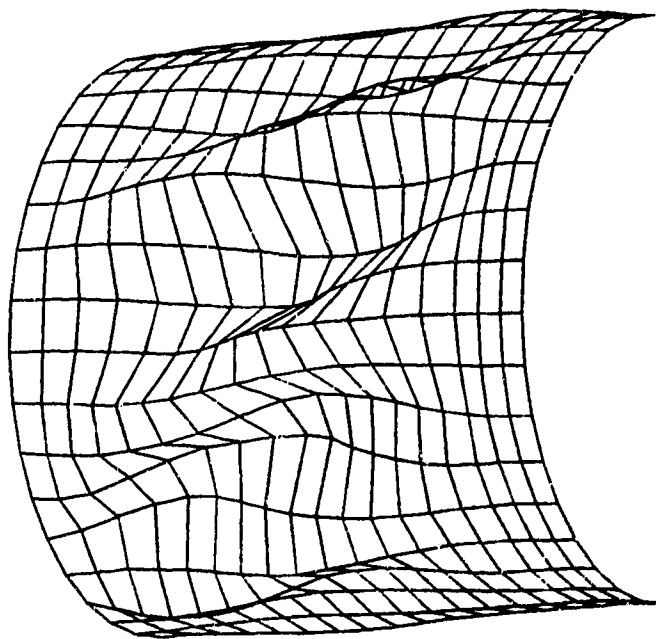


Fig. 3.10 Schematic of the buckles in specimen S1



**Fig. 3.11 Buckled shape of the finite element model
(displacements magnified 10 times)**

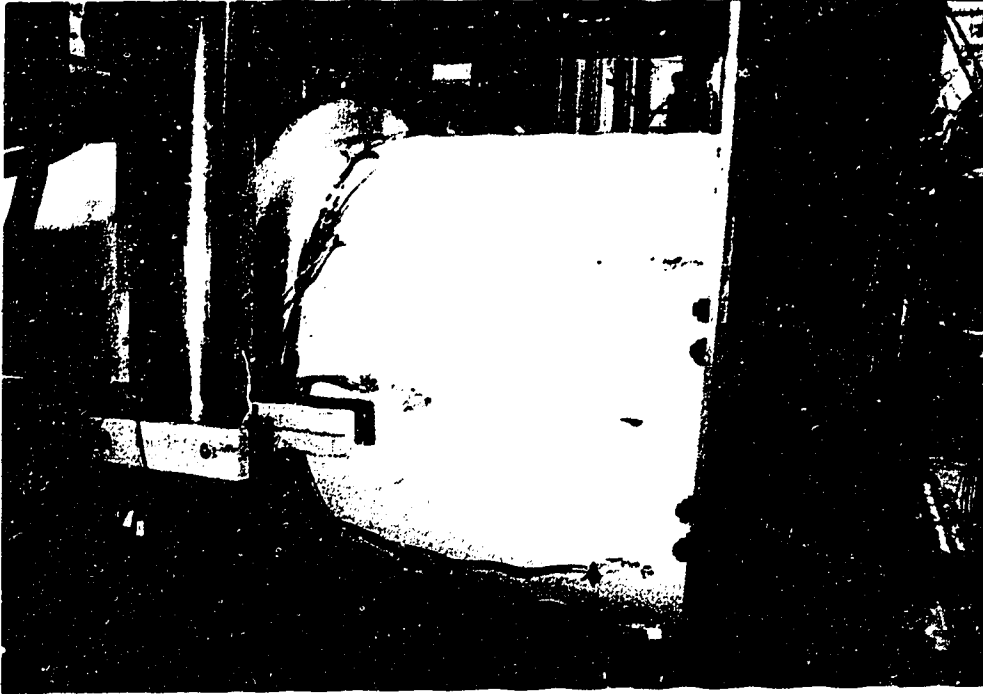


Fig. 3.12(a) Buckled shape of the north-west side of Specimen S1



Fig. 3.12(b) Buckled shape of the south side of Specimen S1

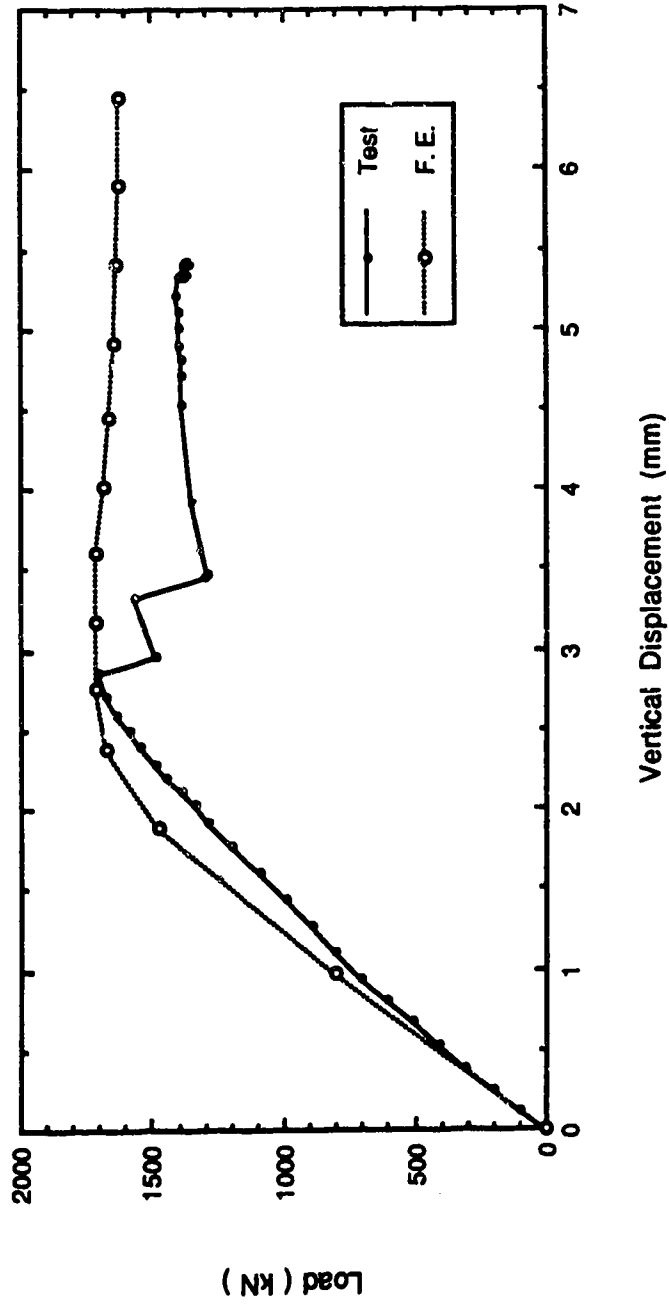


Fig. 3.13 Load-displacement curves for specimen S1

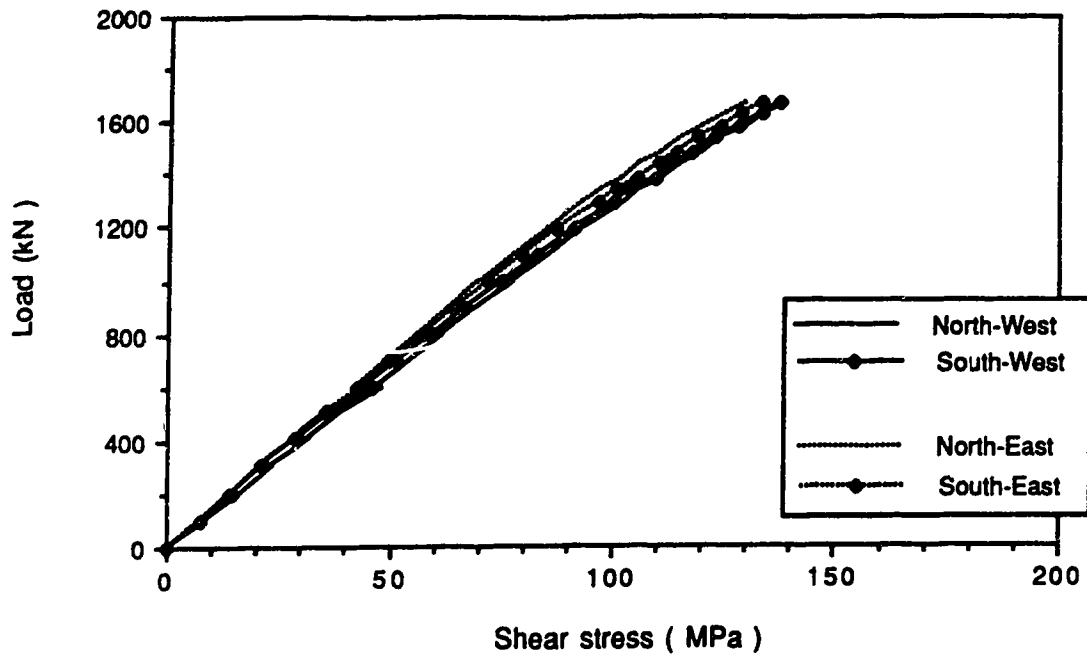


Fig. 3.14 Shear stress from the end rosettes

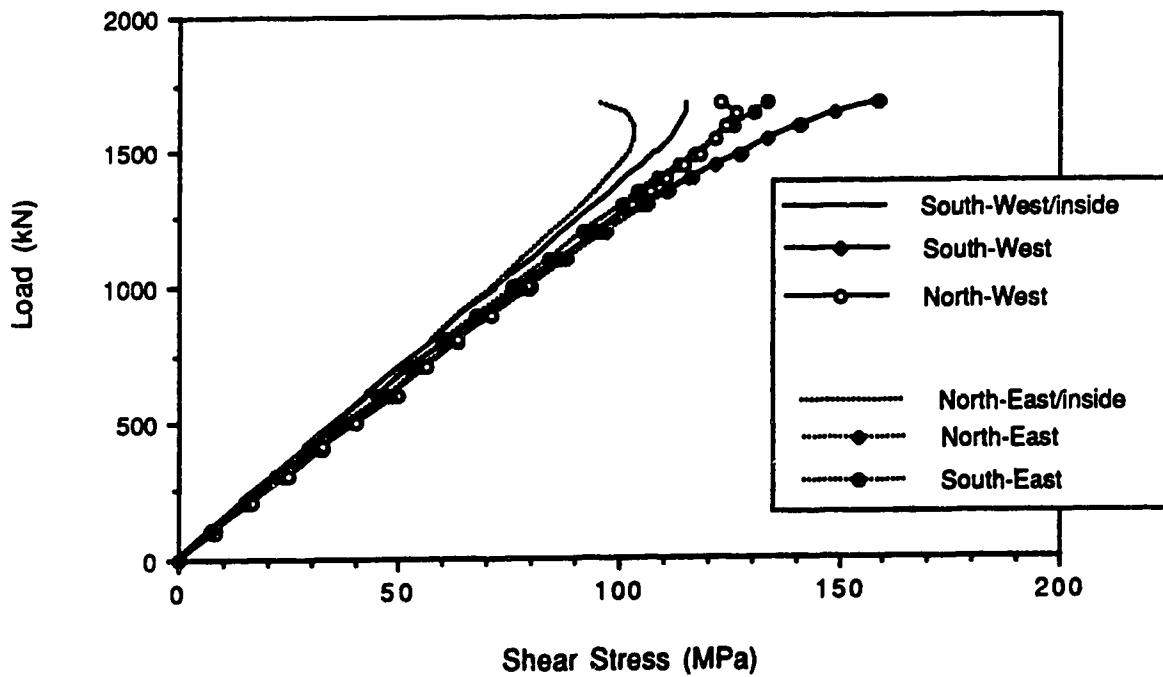


Fig. 3.15 Shear stress from the midspan rosettes

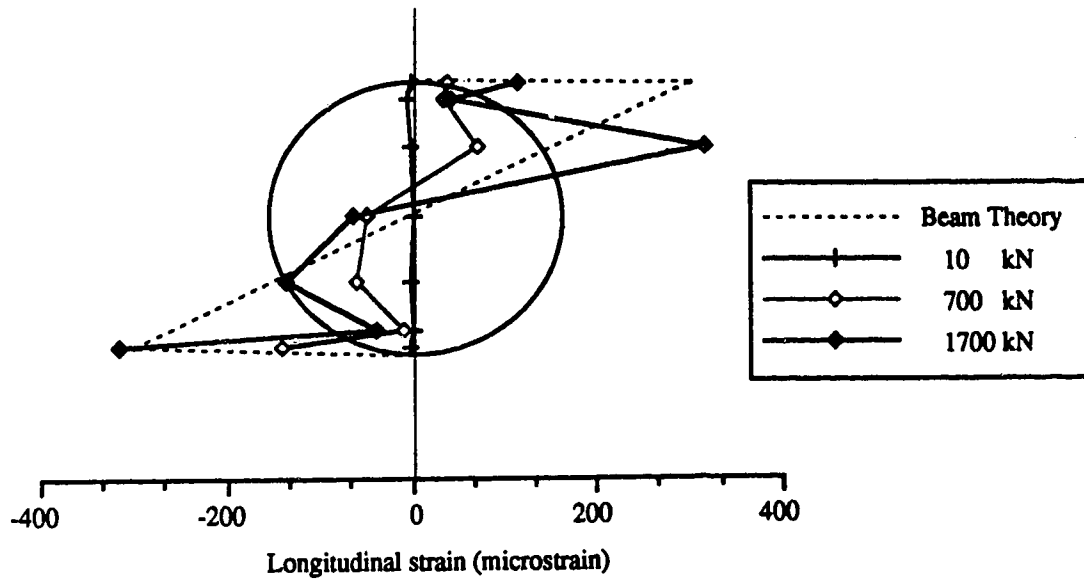


Fig. 3.16(a) Strain distribution at the end diaphragm

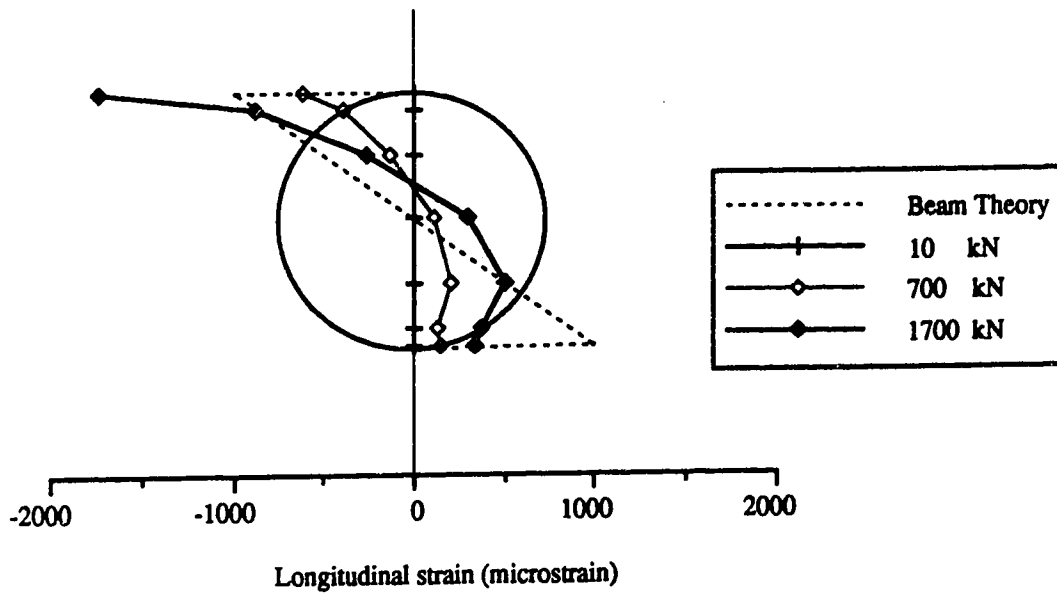


Fig. 3.16(b) Strain distribution at middle diaphragm

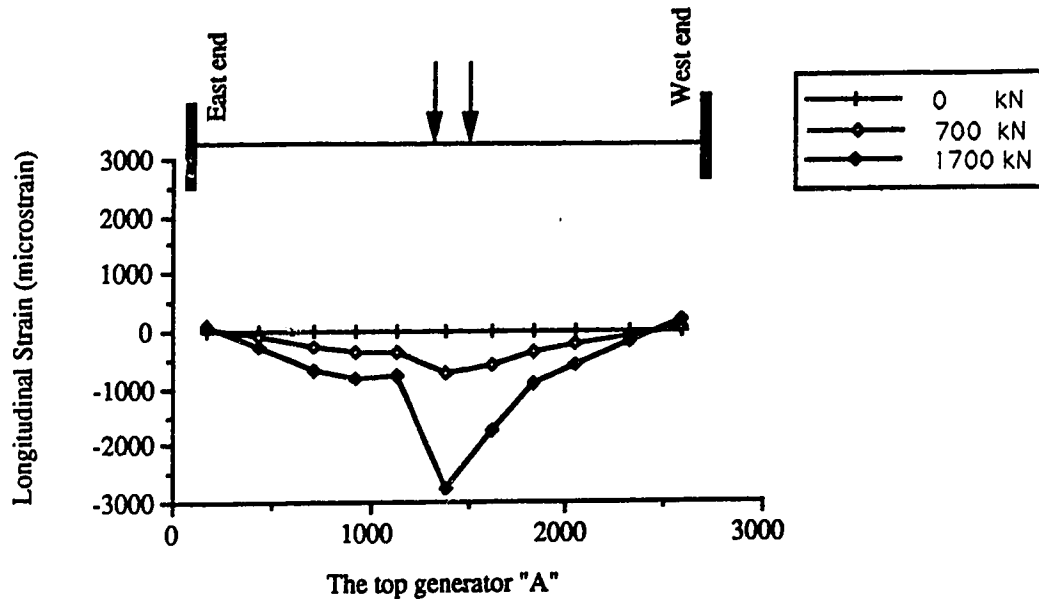


Fig. 3.17(a) Longitudinal strain distribution along the top generator

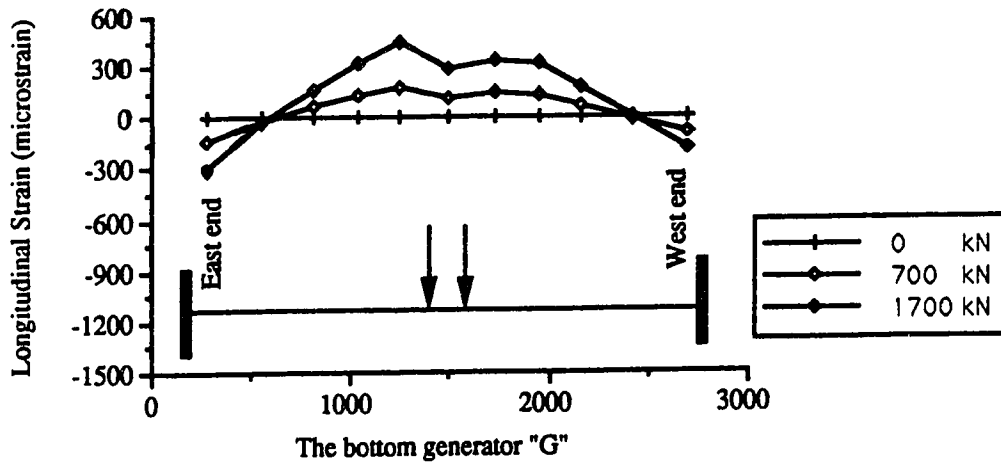


Fig. 3.17(b) Longitudinal strain distribution along the bottom generator

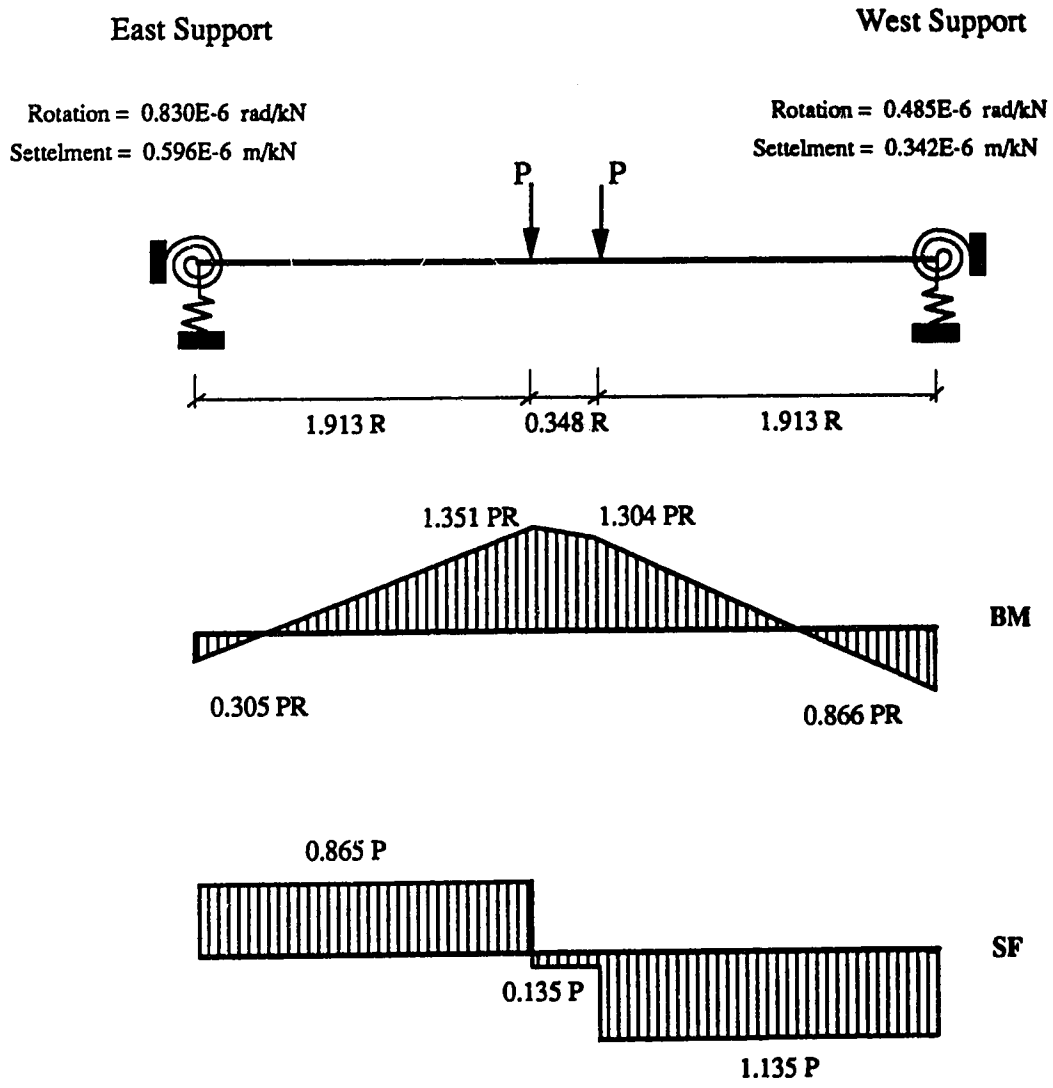
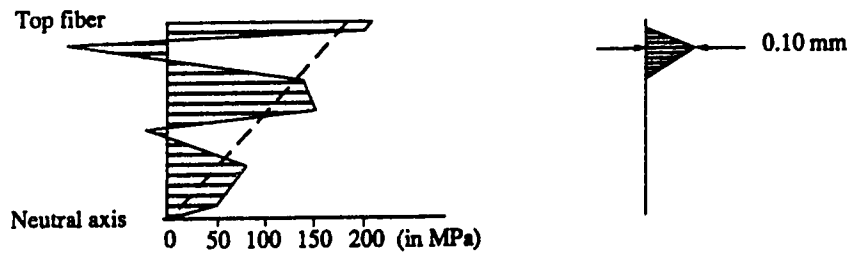
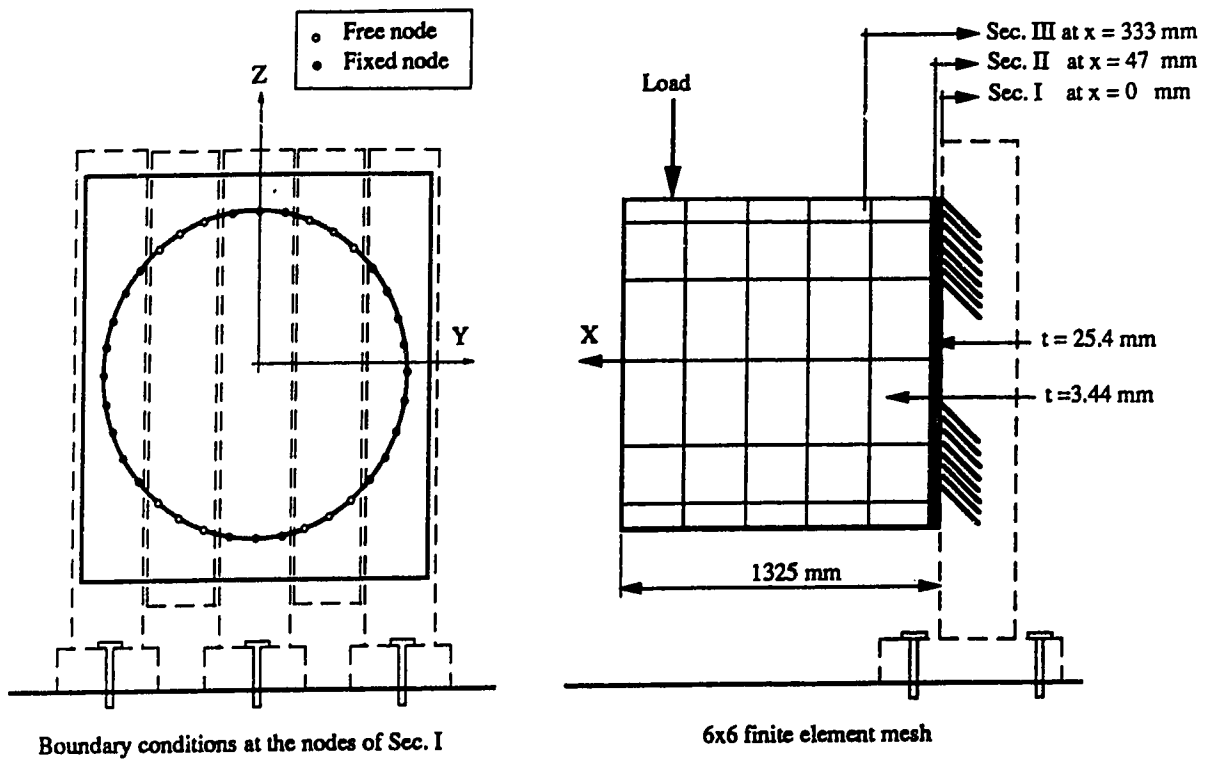
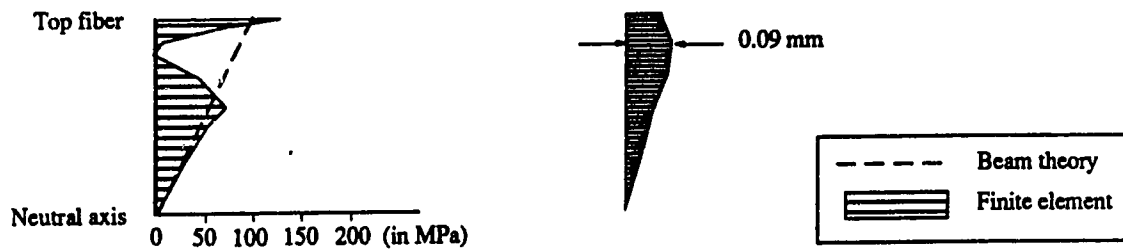


Fig. 3.18 Stress resultant diagrams for S1 including support movements



Longitudinal stress and displacement distributions at Sec. II



Longitudinal stress and displacement distributions at Sec. III

Fig. 3.19 Numerical analysis of the effects of relaxed boundary conditions

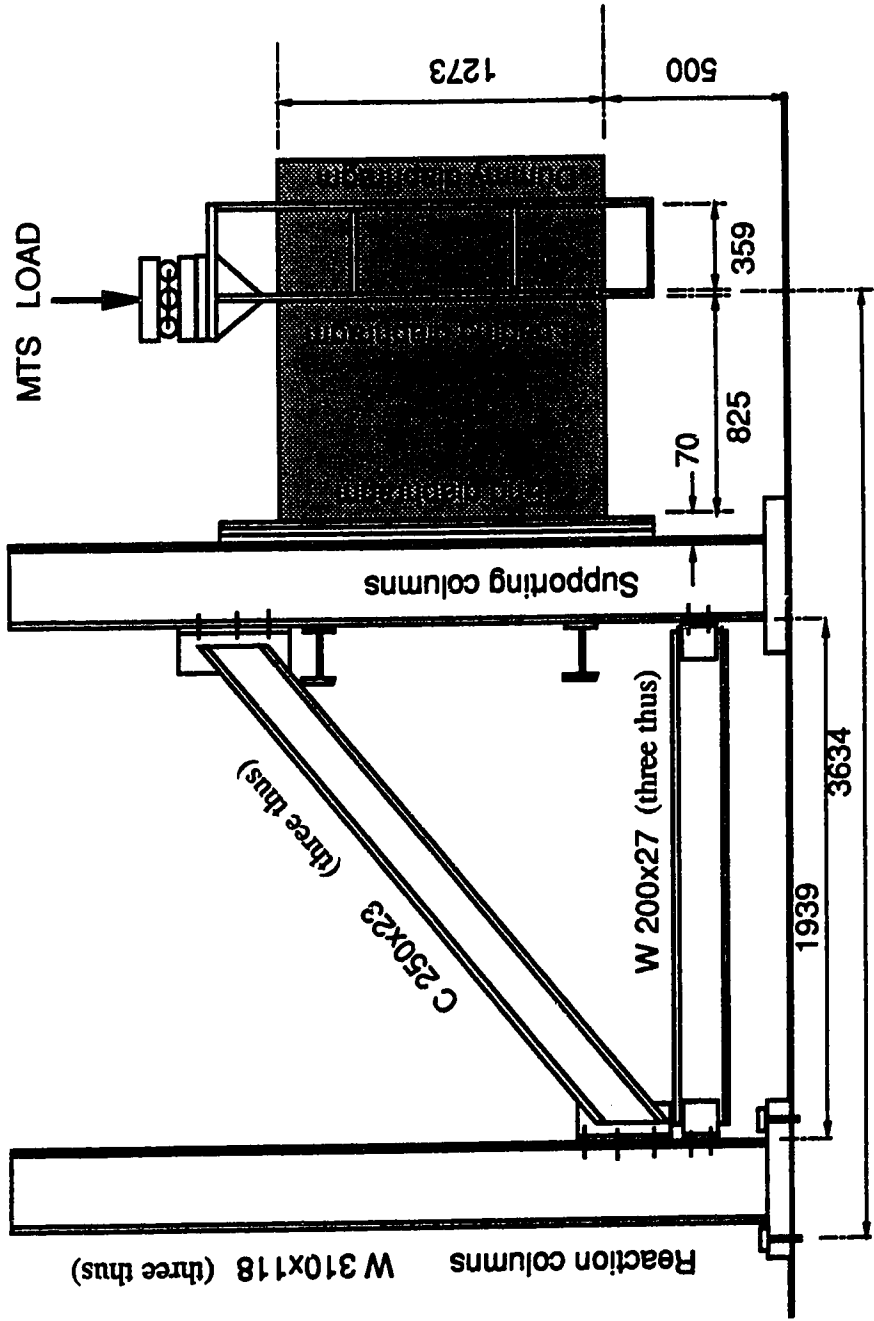


Fig. 3.20 Test set-up for specimen S2

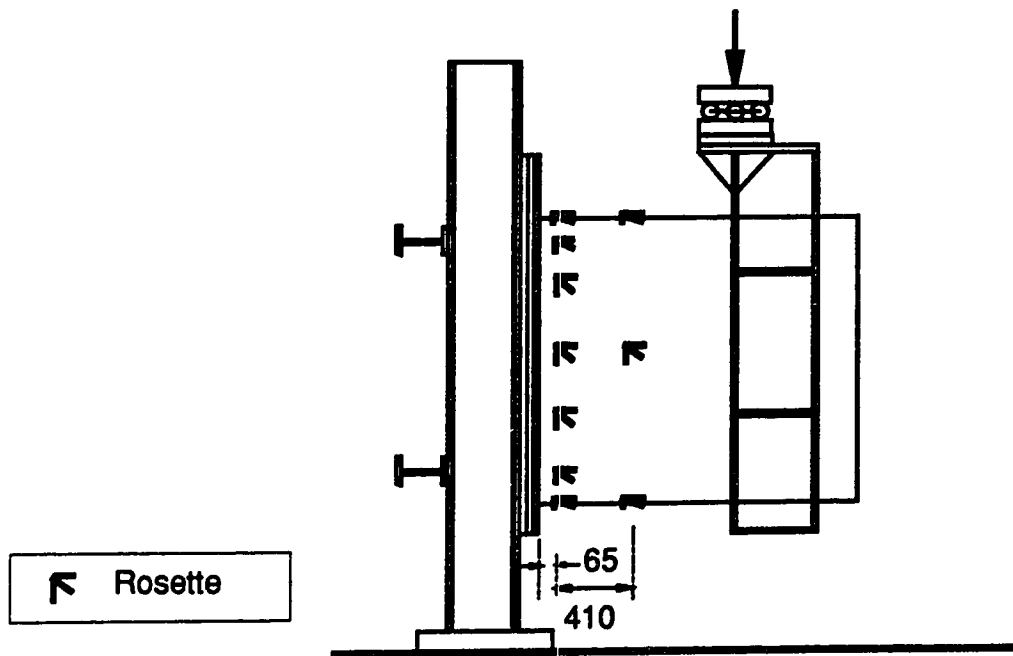


Fig. 3.21 Strain gage locations for specimen S2

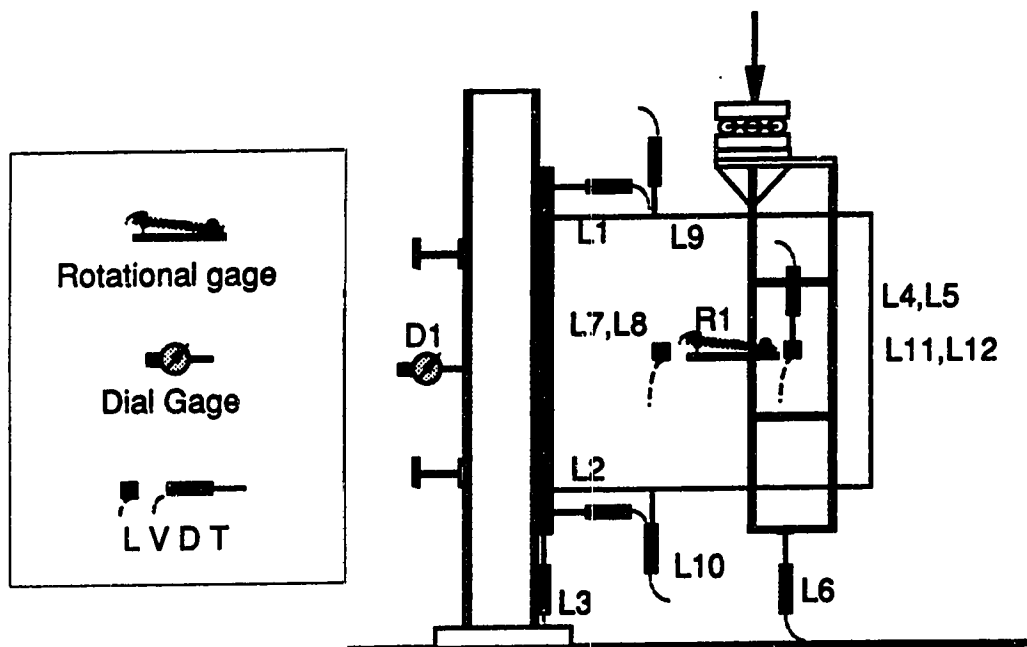


Fig. 3.22 Instrumentation for specimen S2

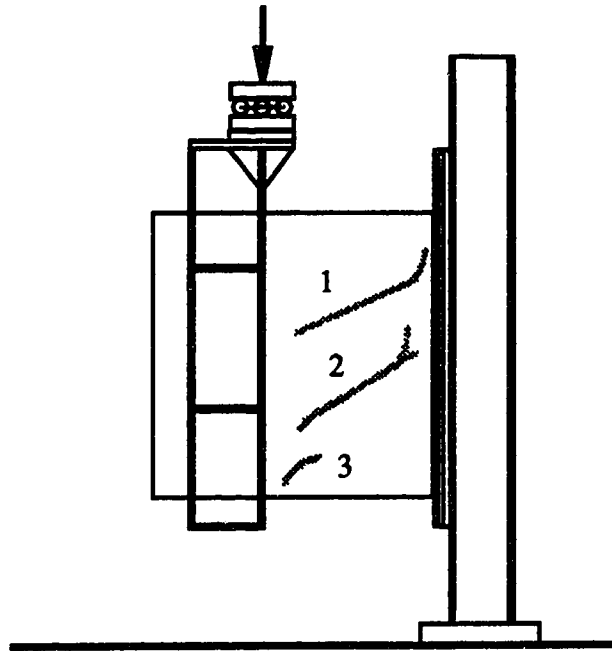
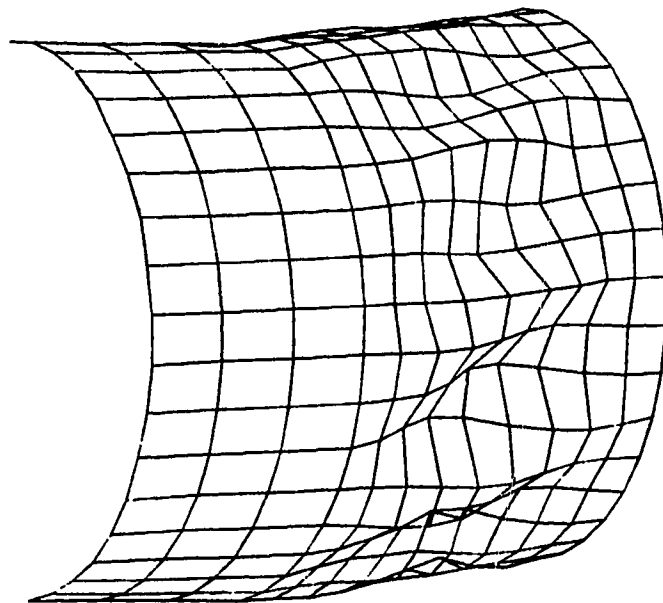


Fig. 3.23 Schematic of the buckles in specimen S2



**Fig. 3.24 Buckled shape of the finite element model
(displacements magnified 10 times)**

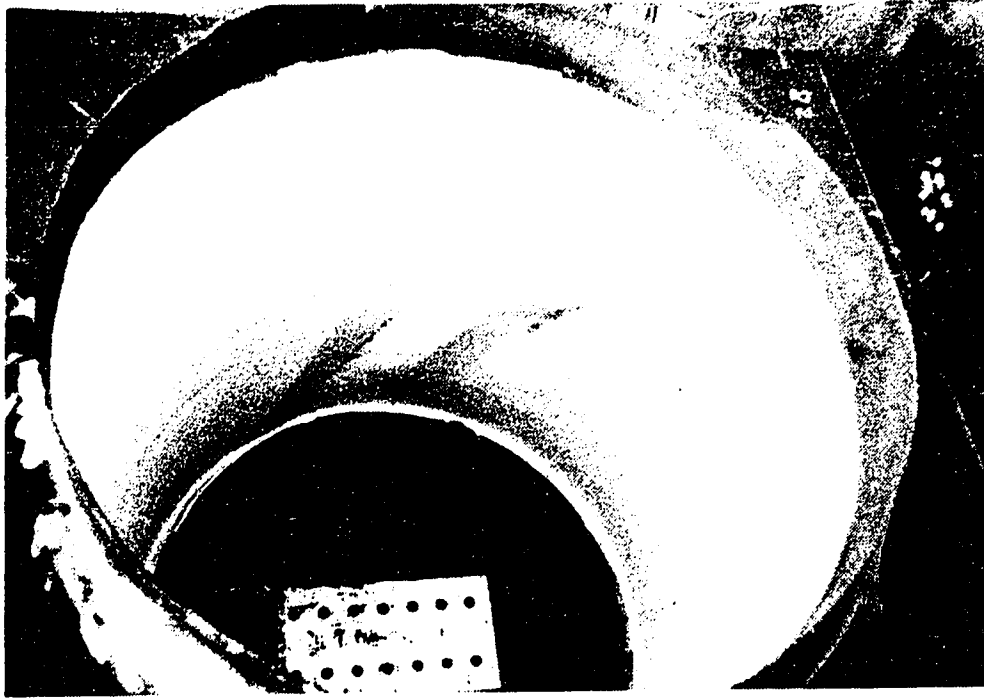


Fig. 3.25(b) Inside view of the buckled shape of Specimen S2

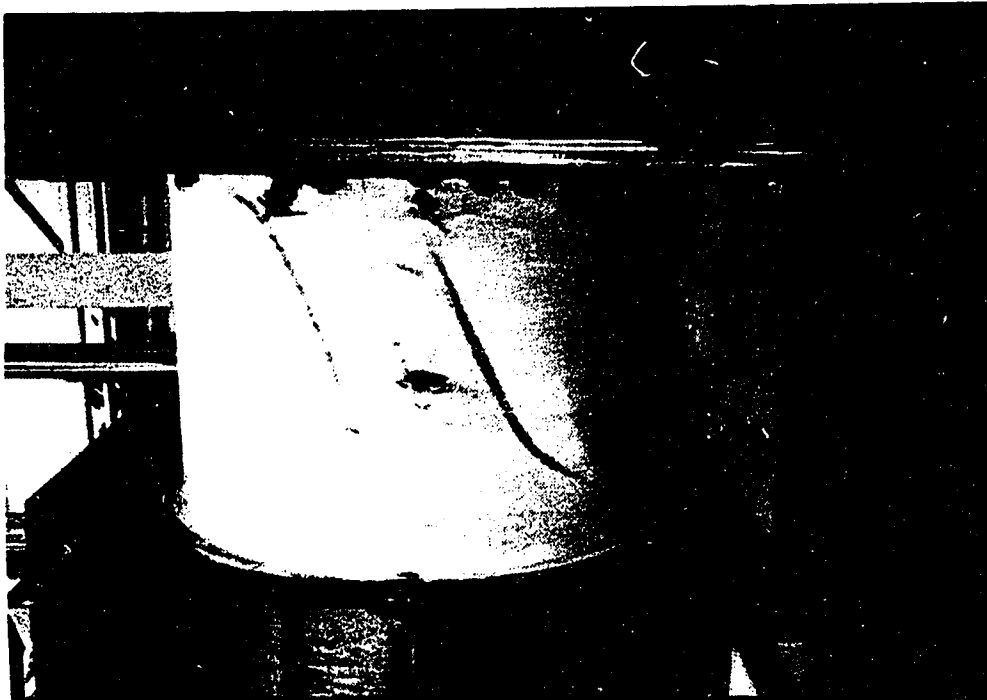


Fig. 3.25(a) Outside view of the buckled shape of Specimen S2

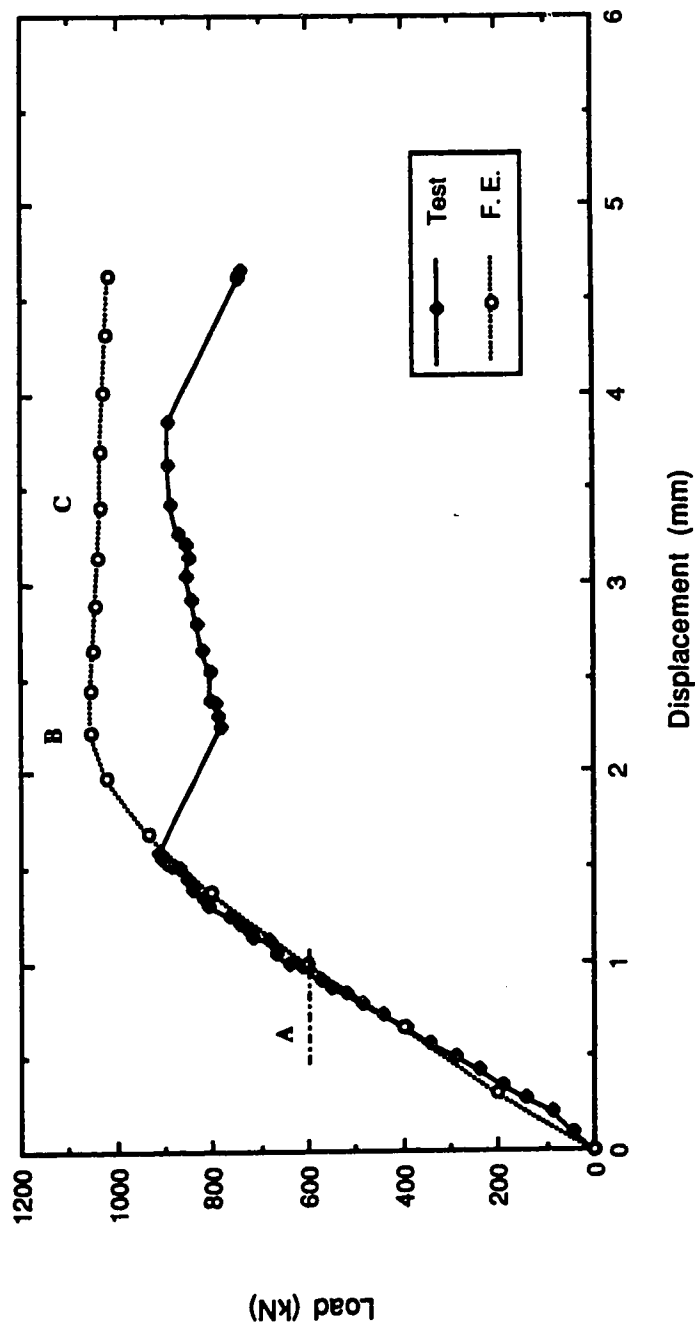


Fig. 3.26 Load-displacement curves for specimen S2

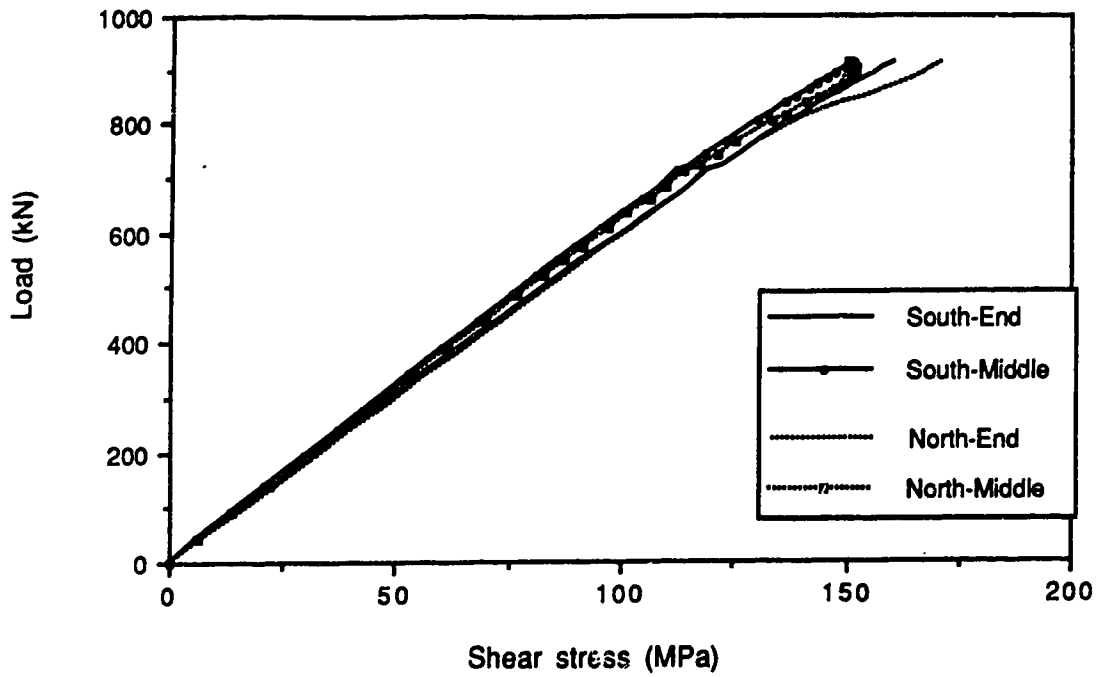


Fig. 3.27 Shear stress at end and middle rosettes

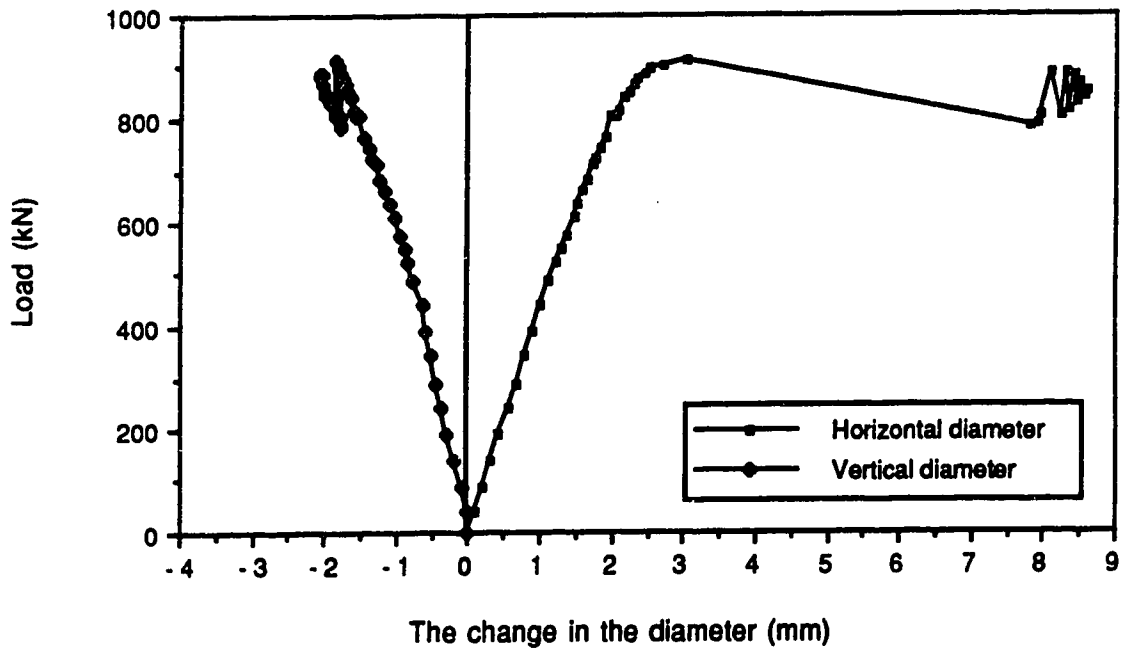


Fig. 3.28 Ovalling of the cross section at midspan

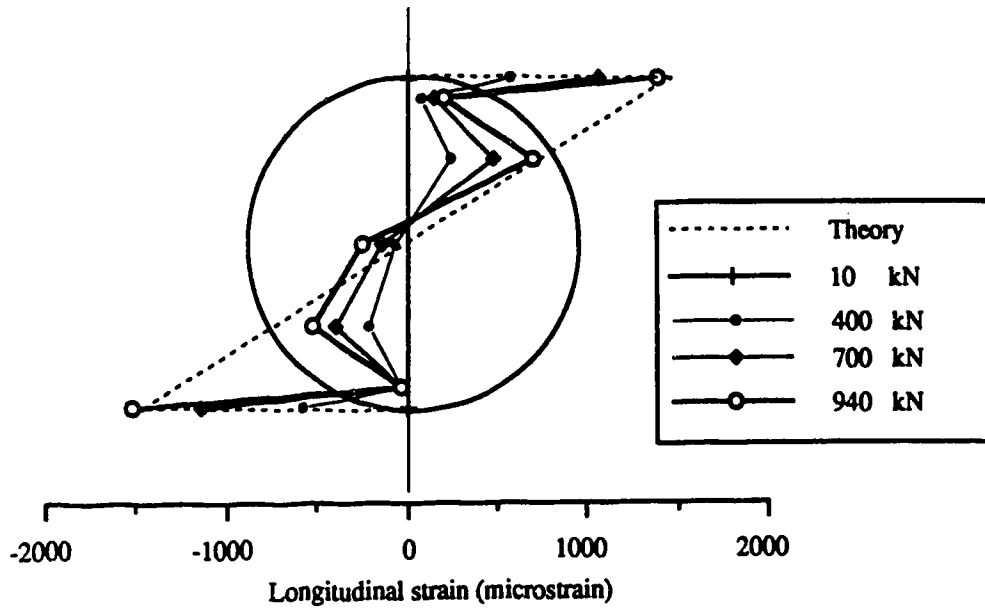


Fig. 3.29 Longitudinal strain distribution at end diaphragm

4. Numerical Analysis

4.1 Introduction

In Chapter 3, the behavior of thin-walled cylinders under transverse load was experimentally investigated for a limited range of cylinder geometries. Alternatively, theoretical approaches are of more general use in studying the same problem. It was shown in Chapter 2 that analytical solutions, based on solving the governing differential equations for shells, are available for the case of ideal cantilever cylinders subjected to transverse shear (Schrüder, 1972). However, the complexity of the shell buckling problem limits such solutions to linear elastic perfect cylinders. Consequently, the solution is restricted because some factors which may affect the behavior and the capacity of cylinders cannot be included. Some of these factors are the initial imperfections inherent in real cylinders, the cold bending stresses introduced in cylinders during fabrication processes, and the effect of different types of boundary conditions. Experimental investigation is possibly the best approach to study these effects. However, this approach is costly. In the course of this work, two full-scale specimens were tested.

An alternative approach is to use numerical analysis, namely the finite element method. This method has been used successfully in modeling different types of structures including thin and thick shells and plates. For example, Roman and Elwi (1987) analyzed thin-walled cylinders under transverse shear using a finite element model. Their study included both the effect of different types of

initial imperfections and the effect of initial stresses that exist in fabricated steel cylinders due to longitudinal seam welding and cold bending. Such factors are difficult to investigate by solution of the differential equations of the shell. The numerical analysis can also help to determine the stress and strain distributions after buckling, which are hard to evaluate experimentally.

The objective of the finite element analysis presented in this chapter is to examine the inelastic buckling behavior of transversely loaded thin-walled cylinders. In the following sections, the effects of boundary conditions, actual measured geometric imperfections, and initial stresses on buckling behavior are discussed, the numerical model is compared with the physical tests, the relationships between the shear capacity and different geometric variables are explored, and the development of tension field mechanism in the post-buckling region is investigated. The finite element program NISA80 (Häfner et al., 1981 and Stegmüller, 1984) has been chosen as the numerical analysis tool for the problem. A description of the program and the options available are briefly presented in the following.

4.2 NISA80 Code

NISA80 (Nonlinear Incremental Structural Analysis) is, as the name implies, a nonlinear finite element program for the analysis of large-displacement large-strain problems. The program can trace the equilibrium path of nonlinear structures from an initial state up to the limit point and beyond it to the post-buckling stage. It can also perform eigenvalue analysis on nonlinear element groups. NISA80

includes a truss element, a two-dimensional degenerated curved beam element, a beam element with thin-walled open cross-section, a two-dimensional plane stress plane strain axisymmetric element, and a family of three dimensional degenerated plate shell elements. Only the degenerated shell elements are of interest here.

The degree of success expected from the finite element analysis in simulating the behavior of real shell structures is dependent on, among other things, the ability of the chosen element to model the curved shape of the shell and its complicated behavior throughout the equilibrium path. Therefore, a brief introduction of the degenerated elements is presented in the following.

In the early 1970's, three-dimensional isoparametric degenerated elements were introduced to model the behavior of general arbitrary shapes of shells and plates (Ahmad et al., 1970). The element avoided the normality (Kirchhoff) conditions by choosing separate interpolation functions for the displacements and the rotations. The degenerated element was derived from a full three-dimensional form, the hexahedral element, by prescribing linear displacement variation across the thickness and suppressing the strain energy due to stresses normal to the shell middle plane. Since the strain normal to the shell surface was assumed to be negligible, the displacements throughout the element were uniquely defined by five degrees of freedom for each node: three displacements and two rotations, as shown in Fig. 4.1(a).

Although degenerated elements have been effectively used in thick shell simulations (Ahmad et al., 1970), they demonstrated an excessive stiffness when used in thin shells, mostly because they were not capable of representing pure bending without shear or membrane effects. Shear or membrane locking is present in most curved elements, but is less pronounced in elements with higher order interpolation polynomials, as for example in the 16-node bi-cubic element. To overcome the locking problem, several schemes have been proposed, for example using elements with shear-strain constraint (Crisfield, 1984 and Huang and Hinton, 1984) or elements that are based on discrete Kirchhoff theory (Kui et al., 1985 and Bathe and Ho, 1981), but the most common method is to use uniform or selective reduced integration (Zienkiewicz et al., 1971 and Pawsey and Clough, 1971). In 1977, Ramm modified and extended the use of quadratic and cubic degenerated elements to arbitrary large rotation problems.

Among the family of degenerated elements available in NISA80, the fully integrated bi-cubic Lagrangian element is recommended by Stegmüller et al. (1984). Ramm (1986) also confirmed that the 16-node element is reliable, but noted that some membrane locking may still be present if full integration is used. Roman and Elwi (1987) have used the bi-cubic element with both 4×4 and 3×3 integration schemes to model transversely loaded cylinders. No shear locking was encountered and the results obtained using full integration (4×4) were the same as those obtained using reduced integration (3×3), except that the former was much more

costly. Based on these experiences, the 16-node bi-cubic Lagrangian degenerated plate shell element with uniform 3x3 reduced integration is used in the present study to model thin-walled cylinders under transverse shear loads. The nodal degrees of freedom of the plate shell element are described in Fig. 4.1(b). The rotations θ_x and θ_s are defined as the change in the angles ϕ and Ψ shown in Fig. 4.1(b). Angle Ψ is measured from the surface normal to the X axis and angle ϕ is measured from the projection of the normal on ZY plane to the Y axis.

The NISA80 code contains different types of incremental displacement formulations. In addition to small displacement formulation, it incorporates a total Lagrangian formulation and an updated Lagrangian formulation. Total Lagrangian is useful in large-displacement small-strain problems, whereas updated Lagrangian is more general in the sense that it can be used for large-displacement large-strain problems. For the magnitude of deformations experienced in testing specimens S1 and S2 (Chapter 3), the total Lagrangian formulation was considered to be sufficient in this case.

The program accommodates elastic and elastic-plastic strain-hardening material models. The resulting nonlinear stress distribution across the thickness is accommodated by using the Simpson integration rule. The number of integration points used in the present study is five points, which is the minimum of the number of points recommended by Stegmüller (five, seven, or nine). Although the material nonlinearity would have been modeled more

accurately using seven, or nine points, the solution time would have increased accordingly.

The NISA80 program employs two main solution strategies: load control and displacement control. Load control is applied through the modified Newton-Raphson or the standard Newton-Raphson iterative strategy, while the displacement control is applied through a modified constant-arc-length iterative strategy (Ramm, 1981). The latter method is especially recommended for tracing nonlinear descending equilibrium paths, which cannot be done using the more common load control methods.

The solution strategy used in this study was varied along the equilibrium path. A modified Newton-Raphson method was found to be suitable before reaching the limit load because the response was almost linear in this range. In the neighborhood of the limit load, the Newton-Raphson iteration diverges. Therefore, the solution strategy was switched to the constant-arc-length method. At the limit load, the initial arc length was reduced in order to achieve convergence in this highly nonlinear part of the equilibrium path. As the cylinder capacity stabilizes in the post-buckling region, convergence could be achieved with a larger arc length.

4.3 Preliminary Analysis

The objective of the preliminary analysis is to search for the most accurate way to model the boundary conditions. Two different cases need to be investigated: one for cylinders with fixed-ends and the other for cantilever cylinders.

The effect of a fixed-end boundary condition, e.g. specimen S1 (Fig. 3.5), on the buckling mode was studied by Mok and Elwi (1986). They found that coupling some nodal degrees of freedom at the loading diaphragm and at the symmetric edge leads to the desired diagonal buckling mode. The suggested representation of the boundary conditions is detailed in Table 4.1. It can be seen that coupling the translational Z displacement at the loaded nodes ensures that the circular shape of the cross section remains undistorted during loading, which is what would be expected if infinitely stiff loading diaphragms were used. Using the above representation of the fixed boundary conditions, the buckling load and mode can be closely predicted.

The boundary conditions at the loading diaphragm for cantilever cylinders, e.g. specimen S2 (Fig. 3.18), cannot be represented by coupling the translational Z displacement due to the rotation of the loading edge. Instead, the loading diaphragm may be represented by relatively thick elements or by fixing the shape of the cross-section at the diaphragm location. Four possible models, (CNT1, CNT2, CNT3, and CNT4) are proposed and shown in Fig. 4.2. The boundary conditions of these models are shown in Table 4.2. All the models have a radius of 635 mm, shear span of 835 mm, and a thickness of 3.44 mm. The material model is assumed elastic perfectly plastic with elastic modulus of 217×10^3 MPa and a yield stress of 337 MPa. The transverse load is applied in the vertical direction at all the nodal points on the loading diaphragm.

The load vs. displacement curves for the four models are shown in Fig. 4.3. During the solution phase, numerical difficulties were observed in models CNT2 and CNT4 and the ultimate load could not be reached. On the other hand, the equilibrium paths of models CNT1 and CNT3 were completely traced. It can be shown that the ultimate load, the stiffness, and the buckling shape of models CNT1 and CNT3 are close to each other. It was decided to adopt the representation of CNT1 for cantilever boundary conditions because the vertical displacement of different locations on the loading diaphragm of specimen S2, which had the same geometric and material properties as the CNT series, was closest to the values obtained using model CNT1.

4.4 Models of Tested Cylinders

Previous studies have used the degenerated bi-cubic element in the context of the NISA80 program to simulate the behavior of thin-walled fabricated steel cylinders under transverse shear or pure bending (Petrick, 1985, Mok and Elwi, 1986, and Roman and Elwi, 1987). When the results of these numerical analyses were compared with results of tests that have the same conditions, the agreement was not satisfactory. One major difference was the apparent stiffness of the finite element model compared to the actual test. This problem was discussed in Chapter 3, where the discrepancy was attributed to the inevitable support rotations during the experiment. To avoid such unknown boundary conditions, the support movements have to be monitored throughout the test and then used to correct the measured specimen displacements.

Another reason for the disagreement between the finite element model and the test is failure to include the geometric imperfections and the initial stresses that exist in the real structure. Petrick (1985) and Mok and Elwi (1986) used an eigenmode scaling technique to incorporate the initial imperfections into the analysis. They extracted a scaling factor from the first buckling mode shape and the measured imperfections in the tests. The scaling factor was then used with the eigenvectors to describe the initial imperfections in the model. This technique resulted in models that gave higher ultimate load and greater stiffness than those measured in the tests. A better and more natural method is to incorporate the initial imperfections actually measured in the specimens into the model geometry (Roman and Elwi, 1987).

In the following sections, the fixed-ends and the cantilever models are used to predict the response of the test specimens S1 and S2 (Chapter 3) and the four other experiments reported by Galletly and Blachut (1985).

4.4.1 Specimen S1

The dimensions and boundary conditions of specimen S1 are shown in Fig. 3.5. Because of symmetry, only one quarter of the specimen needs to be modeled. The model, M1-S1, consists of 36 elements arranged as shown in Fig. 4.4. The boundary conditions used in M1-S1 are described in Table 4.1. The geometric imperfections were measured for each quarter of the test specimen

(see Fig. 3.4) and the one with the largest average imperfections, the south-west quarter, was incorporated into the model M1-S1.

The cold bending stresses inherent in the real structures due to fabrication processes are introduced in the M1-S1 model. Roman and Elwi (1987) used temperature gradient through the shell thickness to produce an initial state of stress. They calculated the temperature gradients needed to produce strains equivalent to bending a flat plate to form a cylindrical shape and introduced these temperatures in the finite element model. Assuming a state of plane strain in the longitudinal direction of the cylinder, the relationships between the stress and strain in both the circumferential and the longitudinal directions can be derived and used to check the results. Following the same procedure, the required temperature gradient for specimen S1 is calculated as -231.5 degrees at the outer surface of the element to +231.5 degrees at the inner surface. The stresses produced in model M1-S1 after the temperature loading were found to match the calculated theoretical stresses.

After introducing the initial stresses, the analysis was continued by adding the transverse loads. The loading steps were chosen at equal intervals of about 20% of the expected limit load. When the model response started to be nonlinear, the solution strategy was switched from modified Newton-Raphson to CALM with an assumed initial arc length. As the displacements increased, the strains increased and the shear stresses reached the yield value at the locations of maximum stresses. At this stage, the deformed shape of the model started to show a form of diagonal buckling at the

elements near the neutral axis. The deformed shape of the model before it reached the ultimate load is shown in Fig. 4.5 for two different displacements. The load levels at which these deformation occurred are 1473 and 1671 kN. It is to be noted that the deformations in Figs. 4.5(a) and 4.5(b) are magnified 30 and 20 times, respectively. It can be seen that the initiation of the diagonal buckles starts before the ultimate load is reached and the buckles then increase as the deformation increases. The relationship between the applied load and the vertical displacement at the location of the loading diaphragm is shown in Fig. 4.6 for the whole loading path. Points C and B in Fig. 4.6 correspond to the stages where the deformed shapes in Fig. 4.5 were observed.

As the model deformed further, the buckles folded more and plastification of the cross section propagated through the thickness. Consequently, the stiffness of the model decreased gradually until it almost diminished. This "gradual yielding" is primarily due to the existence of the initial stresses. In fact, if the initial stresses were eliminated, the response of the model would have been linear up to the limit point. To show the effect of the initial stresses on the model behavior, another model, M2-S1, was analyzed. This model was similar to M1-S1 but without initial stresses. Both models are shown in Fig. 4.6 for comparison. The ultimate load of M2-S1 is much higher than the measured load of the test. After the ultimate load, the capacity drops quickly and then decreases with a smaller rate. The ultimate load reached by model M1-S1 is only 1% different than the ultimate load obtained in the test. However, the model did not show

the sudden drop in the shear load observed in the test after the limit load was reached. The deformed mesh of model M1-S1 in the post-buckling region is shown in Fig. 3.11 (deformations are magnified 10 times).

It is often assumed (Yamaki, 1984, and Galletly and Blachut, 1985) that the shear stress and the longitudinal stress in thin-walled cylinders in the pre-buckling region can be calculated according to the classical beam theory. The average shear stresses along the cross section obtained using models M2-S1 and M1-S1 are plotted in Figs. 4.7(a) and 4.7(b), respectively. The reference load level is 1671 kN (points A and B in Fig. 4.6), and the location of these stresses is at the section of zero moment. Figure 4.7(a) shows that the M2-S1 model shear stresses are close to the predictions obtained using beam theory. In fact, it can be shown that the finite element model predicts stresses very close to beam theory predictions when the model is perfect (no initial imperfections and initial stresses). On the other hand, the deviation of the imperfect model, M1-S1, from the beam theory is clear as shown in Fig. 4.7(b). It is noted that the shear stress at the neutral axis is higher than the beam theory predictions in both cases, M1-S1 and M2-S2. It is therefore reasonable to believe that the initial geometric imperfections trigger the variation in the stresses which are then magnified by the initial stresses. In addition, the distribution of the shear stress across the cylinder thickness, shown in Fig. 4.8, is almost uniform in model M2-S1, which is close to the beam theory predictions. Meanwhile, the imperfect model, M1-S1, has an uneven distribution of shear stress across the

thickness, with maximum value at the middle and minimum values at the surfaces due to the introduced state of initial stresses.

The distribution of the longitudinal stresses along the cylinder cross-section as obtained from models M1-S1 and M2-S1 is shown in Fig. 4.9. The stresses are taken at the nearest Gauss points to the fixed boundaries. As was the case for shear stresses, the longitudinal stresses of the model that did not include initial stresses, M2-S1, corresponded closely to the beam theory while the imperfect model, M1-S1, showed considerable discrepancy from the beam theory results. This discrepancy is also a magnification of the deviations of model M2-S1.

The post-buckling behavior of specimen S1 was described in Chapter 3. It was observed that the load carrying mechanism changed after buckling. As soon as the cylinder buckles, a tension field is formed in the direction of the buckles. The tension field anchors in the stiff boundaries of the shear span. These observations can also be seen in the results of the finite element model. Figures 4.10 and 4.11 show plots of the internal principal forces of model M1-S1. The forces are calculated by integrating the stresses throughout the thickness and are plotted to scale at the Gauss points. The plots show the three-dimensional mesh in a two-dimensional plane by unfolding the circumference of the cylinder. The resulting view is referred to as the developed surface.

Figure 4.10 shows the principal forces on the developed surface when the model reached the ultimate load. It is noticed that the

tensile forces dominate at the locations of the buckles and are in the same direction, while the compressive forces dominate at the top and bottom fibers of the cross section, far away from the buckles. The slope of the tensile forces is constant in the central portion of the developed surface and changes near the boundaries where the forces find anchorage in the diaphragm.

Figure 4.11 shows the principal forces after the buckles have been completely developed. It can be noticed that the tensile forces separate into bands. The direction of the forces becomes more unified and their magnitudes increase to the yielding values. The compressive forces do not seem to separate into bands, but their magnitudes increase with distance from the neutral axis. It is suggested (Roman and Elwi, 1987) that the tensile and compressive forces offer a mechanism to carry the load in the post-buckling range. This argument is discussed in detail in Chapter 6.

4.4.2 Specimen S2

The dimensions and boundary conditions of specimen S2 are shown in Fig. 3.20. Because of symmetry, only one half of the specimen needs to be modeled. The model, M1-S2, consists of 24 elements arranged as shown in Fig. 4.12. The boundary conditions used in model M1-S2 are the same as those used for model CNT1. The geometric imperfections used in M1-S2 are shown in Fig. 3.4(a). The stresses produced in the cylinder due to cold rolling were incorporated in the analysis. The transverse loads were then applied in a similar way to that described for model M1-S1. The relationship

between the applied load and the vertical displacement at the location of the loading diaphragm is shown in Fig. 3.26. The behavior of the model is essentially the same as that for model M1-S1 except for the amount of difference between the model and the test. (The ultimate predicted load of model M1-S2 is 12% higher than that obtained in the test). Again, the model failed to represent the drop in the load after buckling that was observed in the test. However, the deformed mesh of the model, shown in Fig. 3.24, is close to the buckled shape observed in the test. The post-buckling behavior of the finite element model, as shown later in the parametric study, is dependent on the pattern and magnitude of the introduced initial stresses. The observed differences between the models and the tests indicate that the assumed state of initial stresses is not yet complete.

In order to follow the change in the stress distribution as the model deforms, the average shear stress along the cross-section at three consecutive load levels (marked as A, B, and C in Fig. 3.26) is plotted in Figs. 4.13 through 4.15. Similarly, the average longitudinal stress is plotted in Fig. 4.16 through 4.18. The shear stress is taken at the middle of the shear span and the longitudinal stress is taken near the fixed support. It can be noticed that the deviation of the imperfect model from the beam theory increases as the deformations increase. Due to the existence of the initial stresses, some points in the model reach the yield stress before the model can reach the ultimate load. Consequently, a redistribution of the stresses takes place until equilibrium is satisfied. As the buckles form after reaching the ultimate load, further redistribution is needed to

accommodate the local bending moments associated with the buckles. It should be noted that the stress distributions in Fig. 4.13 through Fig. 4.18 represent the average stress across the cylinder thickness.

The principal forces at buckling and in the post-buckling region are plotted in Figs. 4.19 and 4.20, respectively. The tensile forces stretched diagonally between the loading diaphragm and the fixed boundary. It is noticed that the slope of the tensile forces on the developed surface of the cylinder is approximately constant. As the deformations increased, the tension field separated into bands of forces. The compressive forces dominated at the top fibers of the cross section but did not separate into bands.

4.4.3 Other Tests

Other cantilever tests were carried out by Galletly and Blachut (1985). The ultimate load of these tests was reported but the load-displacement curves and the geometric imperfections were not reported. The tests had boundary conditions similar to specimen S2. Therefore, the models that represent them are similar to the M1-S2 model. Two models, M-G12 and M-G34, are proposed to predict the ultimate load of a sample of four tests from Galletly and Blachut tests. Model M-G12 represents the dimensions and material properties of specimens G1 and G2 while model M-G34 represents the dimensions and material properties of specimens G3 and G4 (see Table 2.1). No geometric imperfections are used in these models but the initial stresses are incorporated as before. The ratio of the ultimate load predicted by the first model, M-G12, and the measured

test load is 1.03 for G1 and 1.08 for G2. The ratio of the ultimate load predicted by the second model, M-G34, and the measured test load is 0.94 for G3 and 0.95 for G4. The comparison between the finite element models and the test results shows that the ultimate load can be estimated within a reasonable margin of error.

4.5 Parametric Analysis

The above simulations establish a reasonable level of confidence in the ability of the numerical model to predict results that are in agreement with test results. Reliable full scale test results are still limited, even in view of the tests carried out in this study. In order to extend the data base in terms of failure mechanism, failure loads, stress distributions, etc., one is led to numerical analysis as a viable tool. Hence, a parametric study intended to fill in the gaps in experimental results was carried out. This study is reported in the following.

4.5.1 Model Descriptions

Nine models, MF1 through MF9, are analyzed in this section. The aim is to investigate the relationship between the ultimate shear load and the geometric variables of the cylinder in the inelastic range. The MF series represents a cantilever cylinder and uses boundary conditions similar to model CNT1. A typical mesh of the MF series is shown in Fig. 4.21.

The diameter, thickness, and shear span of each model, shown in Fig. 4.21, are the parametric variables in this analysis. These

variables were chosen so that the cylinders are susceptible to inelastic shear buckling. The chosen aspect ratio, R/L , is between 0.5 and 1.0. Cylinders with R/L ratio outside this range may buckle in a flexural mode (for cylinders with shear span longer than their diameter) or yield due to excessive shear stresses (for cylinders with shear span shorter than their radius). The thickness ratio, R/t , was chosen to be between 150 and 250. Cylinders with R/t ratios higher than 250 may buckle in an elastic mode. Cylinders with R/t ratio lower than 150 were not considered so as to limit the number of models. The lower limit of the R/t ratio selected was thought to be a reasonable minimum value for some practical applications (e.g. conveyor galleries).

The MF models have very small magnitudes of initial imperfections, just enough to trigger the buckle formations. The imperfections were scaled down from the imperfections of the test specimen S2. The models have the same material properties, an elastic modulus of 200×10^3 MPa and a yield stress of 300 MPa, and they include cold bending initial stresses. The analysis of each model is carried out by introducing a temperature gradient through the element thickness and then applying the transverse loading, a procedure similar to the M1-S1 and the M1-S2 models. The solution was terminated when the post-buckling deformations had been completely developed.

4.5.2 Ultimate Shear Capacity

The load resisted by each model is plotted against the vertical displacement of the neutral axis of the cross section in Figs. 4.22, 4.23, and 4.24. To normalize the results, the shear load is replaced by a shear ratio which is the ratio of the shear load to the shear force required to cause yield shear stress at the neutral axis. The load-displacement curves are arranged to show the effect of R/L ratio on the inelastic shear capacity. Figure 4.22 shows the models that have a constant R/t ratio of 150 and different aspect ratios. It is clear from Fig. 4.22 that the shear capacity decreases as the aspect ratio (R/L) decreases. The stiffness of the model also decreases as R/L decreases because it is dependent on the length of the shear span. The same conclusions can be drawn from both Fig. 4.23 (models with R/t=188) and Fig. 4.24 (models with R/t=250).

The effect of the thickness ratio (R/t) can be demonstrated by grouping the models according to R/L ratio, as shown in Figs. 4.25, 4.26, and 4.27. The ultimate shear load of the finite element models decreases slightly as the thickness ratio increases, while the post-buckling load clearly decreases as the R/t ratio increases. However, the main effect of R/t ratio is upon the shape of the load-displacement curve. It can be seen that the stockier models (models with small R/t ratio) experience nonlinear deformations earlier than the thinner models (models with large R/t ratio). After reaching the ultimate load, the stockier models lose their stiffness more gradually than the thinner models. It is possible that this behavior is related to

the initial stresses introduced in the model. As the cylinder radius takes smaller values, more strain is required to form a cylinder by bending a flat plate, which in turn increases the portion of the cylinder thickness that exhibits yielding. As a result, the behavior of the cylinder changes from sharp yielding (e.g. model MF9) to gradual yielding (e.g. model MF3). In fact, the same argument applies for the difference between model M1-S1, which contained initial stresses, and model M2-S1, which did not contain any initial stresses.

By comparing model MF5 with model M1-S2, it is clear that the dimensions of the cylinder do not influence the ultimate shear ratio. The two models have different radius, shear span, and thickness but they have similar R/t ratios, 185 and 188, similar R/L ratios, 0.76 and 0.75, and similar E/σ_y ratios, 643 and 667. The resulting ultimate shear ratios are 0.79 for M1-S2 and 0.81 for MF5, which is also close. The cylinder dimensions, however, affect the ultimate load resisted by the cylinder.

4.5.3 Post-Buckling Behavior

The first attempt at analysis using MF models employed a mesh of 18 elements with the transverse load applied at the edge. The model stiffness in this analysis started to rise instead of decline and the solution diverged shortly after, even though a very small arc length was used in the context of CALM solution strategy. It was then realized that applying the load at the edge is responsible for the stiffening behavior and that the presence of an additional part of the cylinder under the loading edge is necessary. This end part, which

has a length of 75 mm in the typical model shown in Fig. 4.21, may be useless in the early stages of applying the transverse load but as soon as the carrying mechanism starts to change from "beam" type to "tension field" type, the end part provides the needed support to anchor the inclined force fields.

The load carrying mechanism of thin-walled cylinders after buckling can be studied by examining the force fields in the models. The plots of the principal forces at the maximum displacement of each of the nine models are shown in Figs. 4.28 through 4.36. The models in MF series demonstrate the same basic post-buckling characteristics as did models M1-S1 and M1-S2. The observations that follow are obtained by inspection of Figs. 4.28 through 4.36.

After the cylinder reaches the ultimate load, two main force fields start to develop in the cylinder; a tension field that takes the general direction of the diagonal buckles and a compression field that takes a crossing direction. The inclined field forces anchor in the stiff vertical boundaries (diaphragms or fixed ends).

As the deformations grow, the shape of these fields crystallizes. The tension field separates into bands of intense forces at the center of the bands and little or no forces in between the bands. The number of bands in the tension field varies from two to four. On the other hand, the compression field does not separate into bands, but the forces in the field tend to intensify near the top corner of the cross-section and diminish towards the neutral axis.

The unloaded parts of the tension field seem to match the valleys of the buckles, while the loaded parts match the crests of the buckles. To demonstrate this, the deformed shape of a cross-section in model MF9 is shown in Fig. 4.37. By comparing the node locations in Fig. 4.37 and Fig. 4.36, it can be seen that nodes 141 and 145, for example, lie between the tension bands and therefore are deflected toward the center of the cross section, while nodes 139, 143, and 147, which lie in the tension bands, are deflected outward from the center. The same observation was reported by Roman and Elwi (1987).

The slope of the tension field changes as the deformations increase after reaching the ultimate load, but it becomes approximately constant as the equilibrium path flattens. It is to be noted, however, that the tensile forces tend to tilt at the proximity of the boundaries where they anchor in the stiff vertical edges. This tilting is considered to be an inevitable local effect of the boundary conditions. The slope of the tension bands referred to here is, therefore, measured some distance away from the boundaries. The slope of the tension bands for MF series and the two models M1-S1 and M1-S2 are shown in Table 4.3. The slope is measured on the developed surface of the cylinders and it is reported at the ultimate load and at the maximum displacement obtained in each model. The slopes range from 32 to 48 degrees. They are generally higher at the ultimate load than at the maximum displacement and are also higher for the top band than for the bottom band. No relationship between the slope of the tension bands and the R/t ratio is observed.

However, it is clear that the slope lessens as the aspect ratio, R/L , decreases.

Using the scales shown in Figs. 4.28 to 4.36, the forces in the tension field could be measured. It can be shown that some of these forces reach maximum value (which corresponds to average yield stress across the thickness). The forces in the compression field also increase, especially near the top. Figures 4.28 to 4.36 also show that the slopes of the compression forces do not show any parallel pattern.

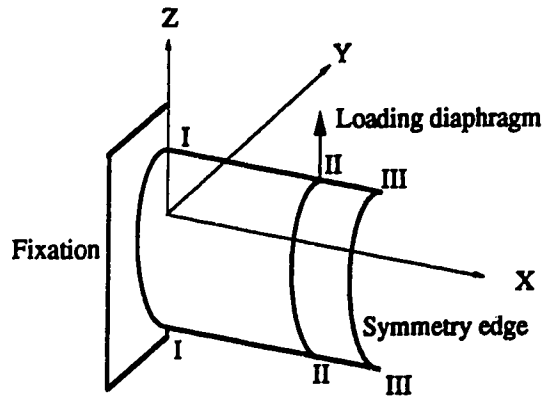
The above observations show clearly that there is a common pattern in which thin-walled cylinders carry the transverse load in the post-buckling region. This behavior can be modeled so that the shear capacity of the cylinder may be estimated. The attempt to do so is described in Chapter 6.

4.6 Summary

The 16 node degenerated plate shell element can be used successfully to model the shear behavior of transversely loaded thin-walled steel tubes, provided that certain aspects are treated properly. The correct representation of the test boundary conditions is crucial to the stiffness of the finite element model. As discussed in Section 4.4, this factor is considered to be the reason for the discrepancy between the finite element model and previous tests. In this Chapter, it has been shown that good agreement exists between the results of two full scale tests and the predictions of the numerical model.

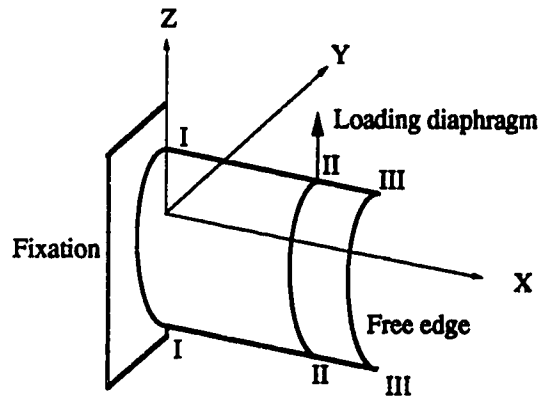
A parametric study of nine models was carried out in order to extend the information available about the ultimate shear capacity of thin-walled cylinders and their failure mechanism. The study investigated the effect of the thickness ratio (R/t) and the aspect ratio (R/L) on the ultimate shear capacity of the cylinders. The numerical analysis was most useful in examining the post-buckling behavior. The analysis provided a clear picture of the force fields responsible for carrying the shear load in the post-buckling region. All models demonstrated a common load-carrying pattern that can be used to determine the post-buckling capacity.

The study showed that the magnitude and distribution of the initial stresses introduced in the finite element model to account for the cold bending inherent in fabricated steel tubes are critical in determining the ultimate capacity of the numerical model as well as its post-buckling capacity. Further refinement of the initial stress is needed to include both the longitudinal and circumferential welding stresses.



Section	Fixed DOF	Free DOF	Coupled DOF
I-I	$u, v, w, \theta_x, \theta_s$	----	----
II-II	----	u, v, θ_x, θ_s	w
III-III	θ_s	v, w, θ_x	u
I-III	v, θ_x	u, w, θ_s	----

Table 4.1 Boundary conditions for fixed-ends cylinder model

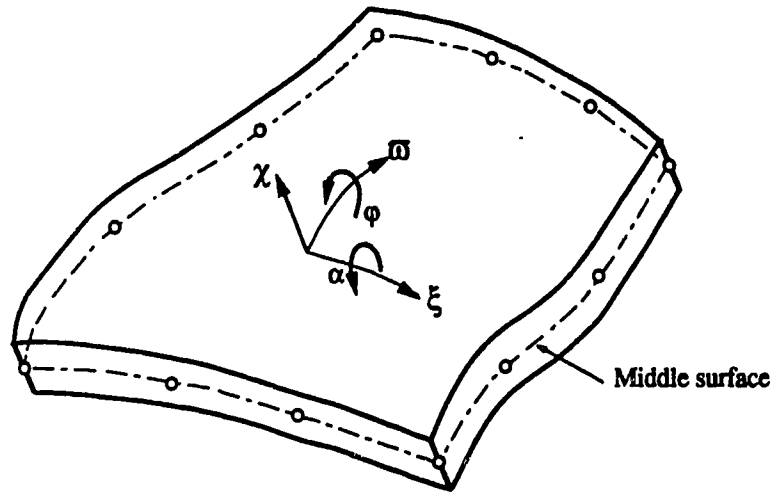


Section	Fixed DOF	Free DOF	Coupled DOF
I-I	$u, v, w, \theta_x, \theta_s$	----	----
III-III	----	$u, v, w, \theta_x, \theta_s$	----
I-III	v, θ_x	u, w, θ_s	----
II-II (CNT1)	v, θ_x	u, w	θ_s
II-II (CNT2)	v, θ_x	u, w, θ_s	----
II-II (CNT3)	----	u, v, w, θ_x	θ_s
II-II (CNT4)	----	$u, v, w, \theta_x, \theta_s$	----

Table 4.2 Boundary conditions for cantilever cylinder models (CNT series)

F.E. Model	R/t	R/L	Slope at ultimate load			Slope at max. displ.		
			Top band	Mid. band	Bot. band	Top band	Mid. band	Bot. band
MF1	150	1.00	45	43	40	47	46	44
MF2	150	0.75	45	42	36	46	43	38
MF3	150	0.50	41	39	33	39	37	36
MF4	188	1.0	43	43	43	45	44	44
MF5	188	0.75	--	38	37	47	42	42
MF6	188	0.50	--	38	37	39	38	32
MF7	250	1.00	48	45	39	45	43	43
MF8	250	0.75	48	44	37	47	39	39
MF9	250	0.50	40	38	38	39	37	36
M1-S1	185	0.53	40	40	40	37	34	34
M1-S2	185	0.76	48	42	37	42	42	40

**Table 4.3 Slope of the tension field bands (in degrees)
at and beyond the ultimate load**



Note: χ is normal to the surface

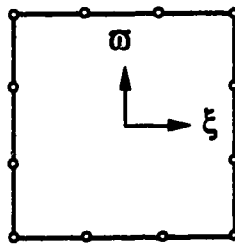


Fig. 4.1(a) Configuration of the isoparametric degenerated bi-cubic shell element

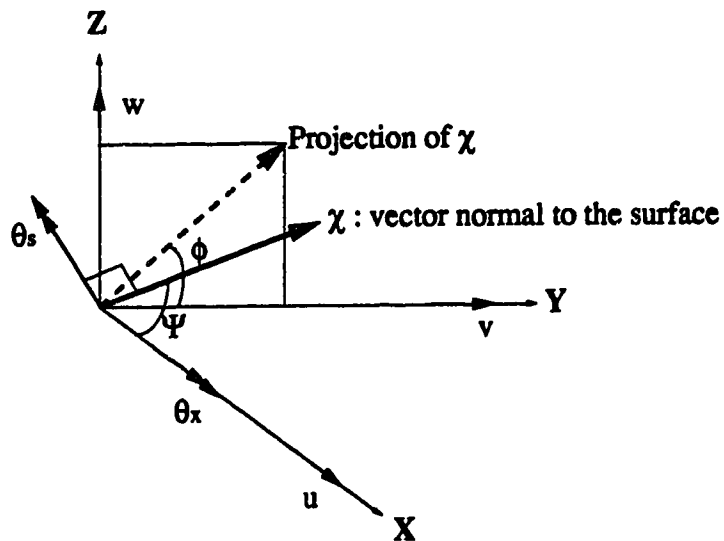
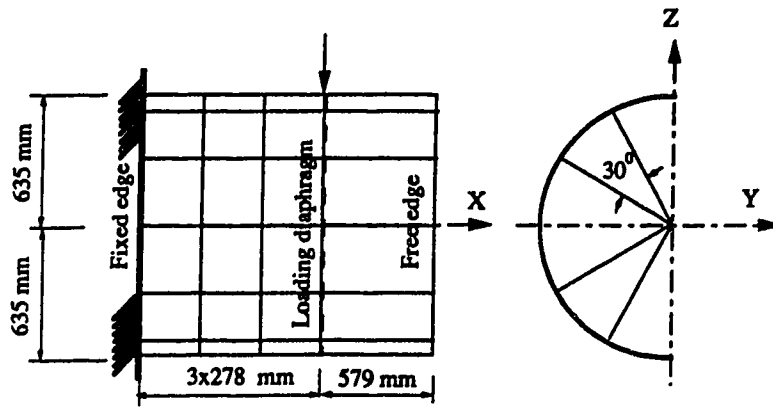
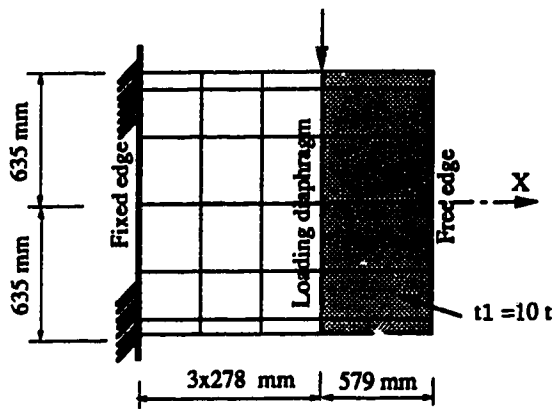


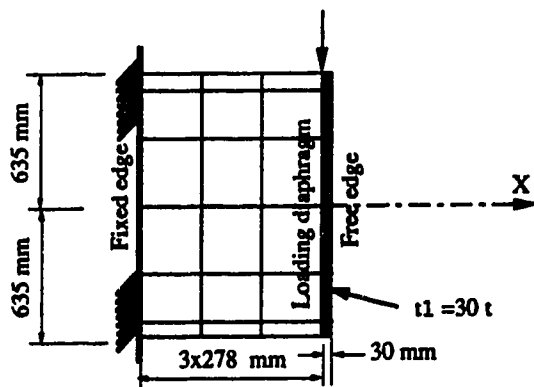
Fig. 4.1(b) Nodal degrees of freedom of the plate shell element in NISA80



Models CNT1 and CNT2



Model CNT3



Model CNT4

Fig. 4.2 Mesh arrangement of CNT models

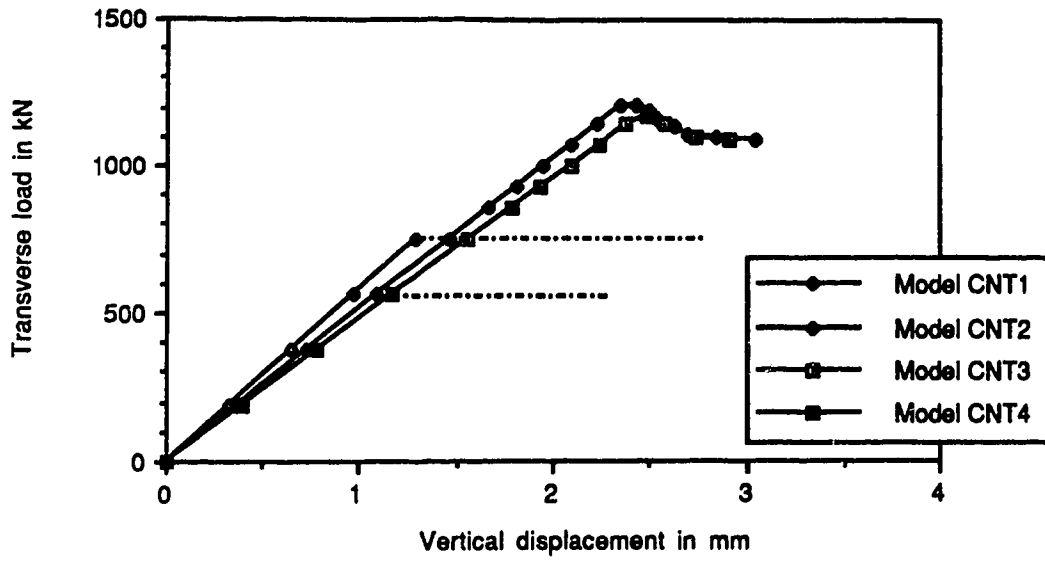


Fig. 4.3 Load-displacement curves for CNT series

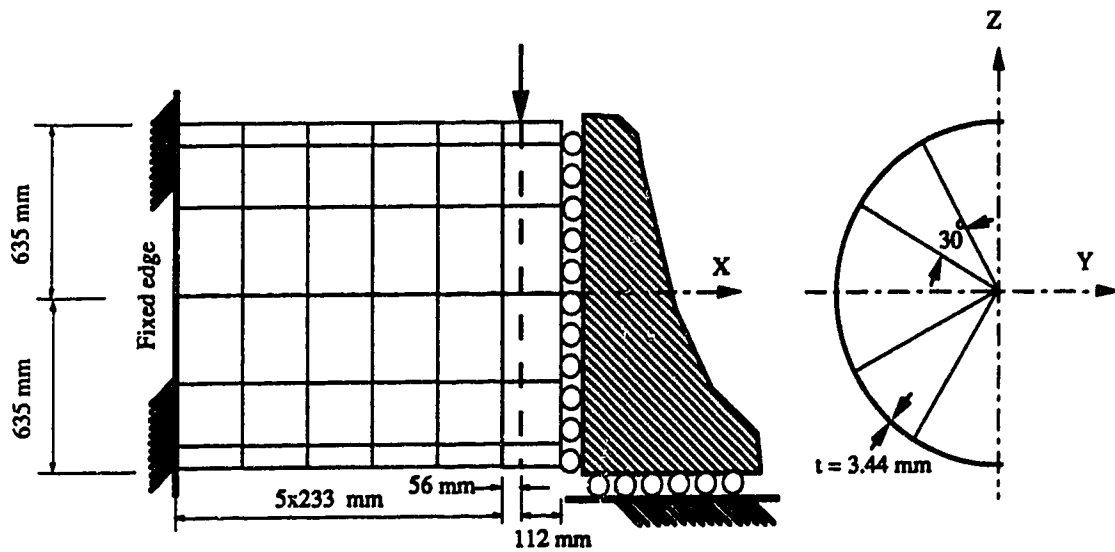
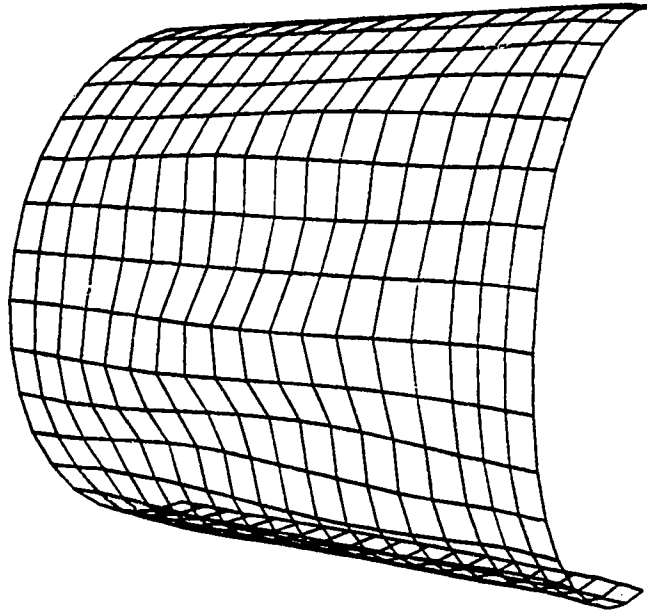
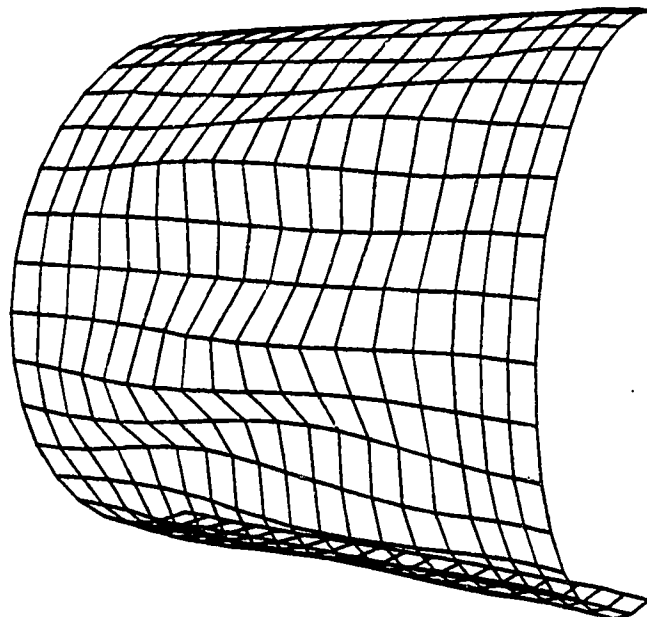


Fig. 4.4 Mesh arrangement of models M1-S1 and M2-S1



**Fig. 4.5(a) Mesh deformation for model M1-S1
at vertical displacement= 1.89 mm (magnified 30 times)**



**Fig. 4.5(b) Mesh deformation for model M1-S1
at vertical displacement= 2.38 mm (magnified 20 times)**

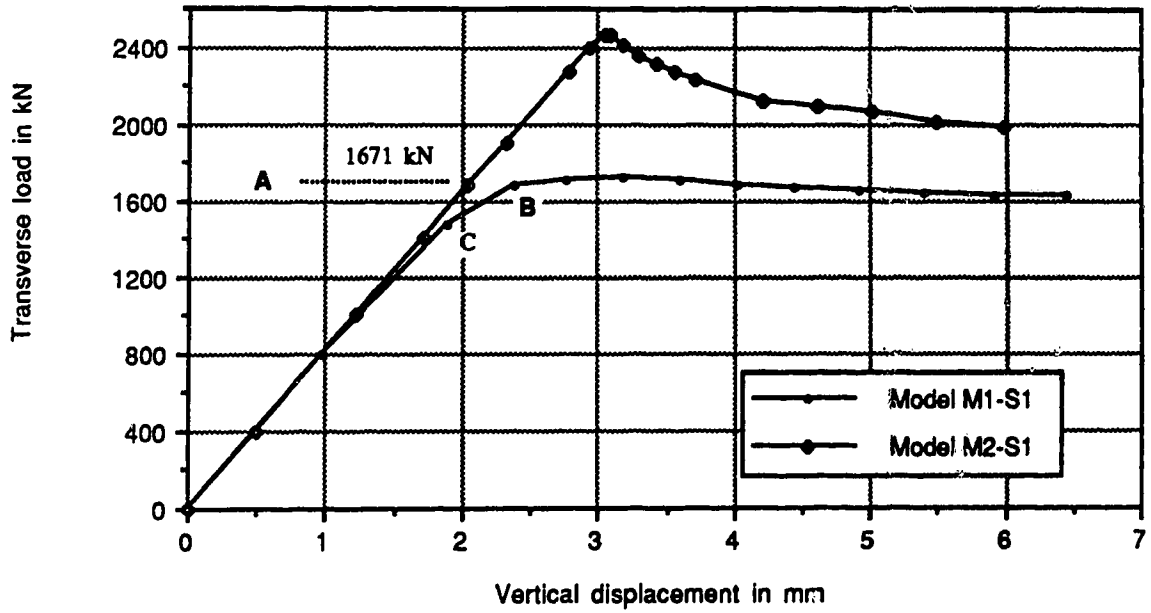


Fig. 4.6 Load-displacement curves for models of specimen S1

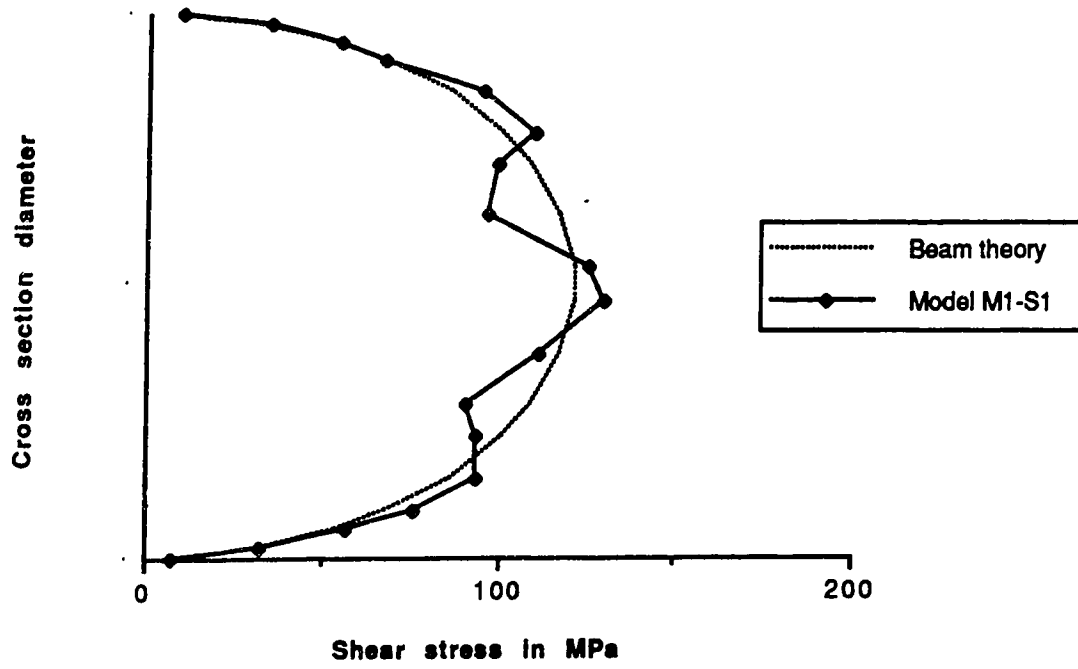


Fig. 4.7(b) Average shear distribution for M1-S1 at load = 1671 kN

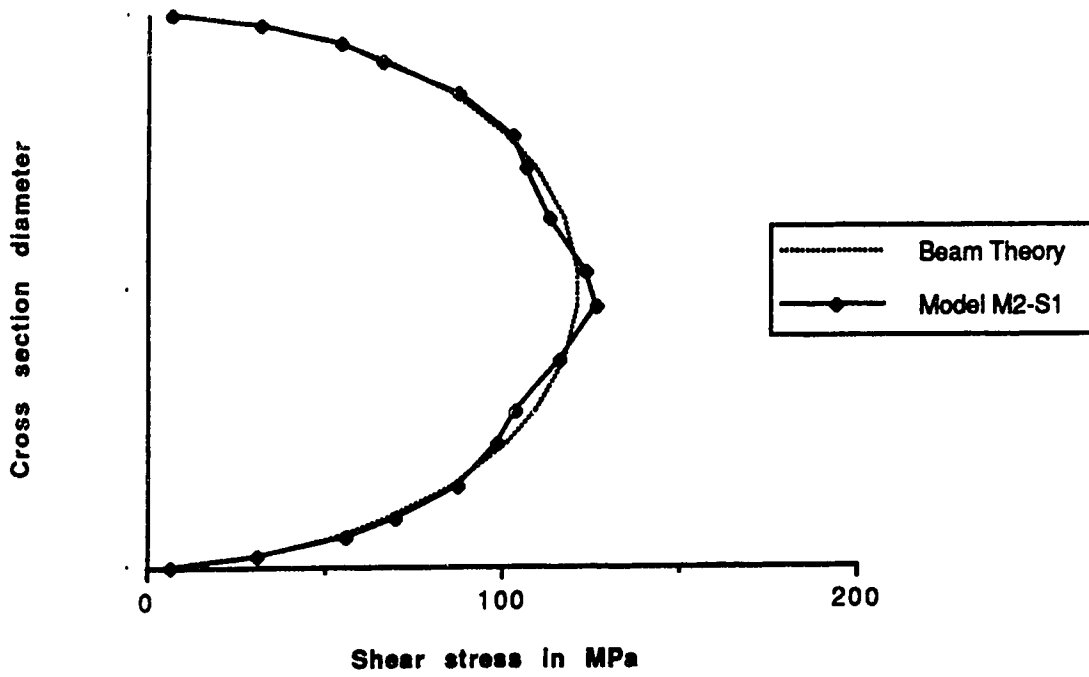


Fig. 4.7(a) Average shear distribution for M2-S1 at load = 1671 kN

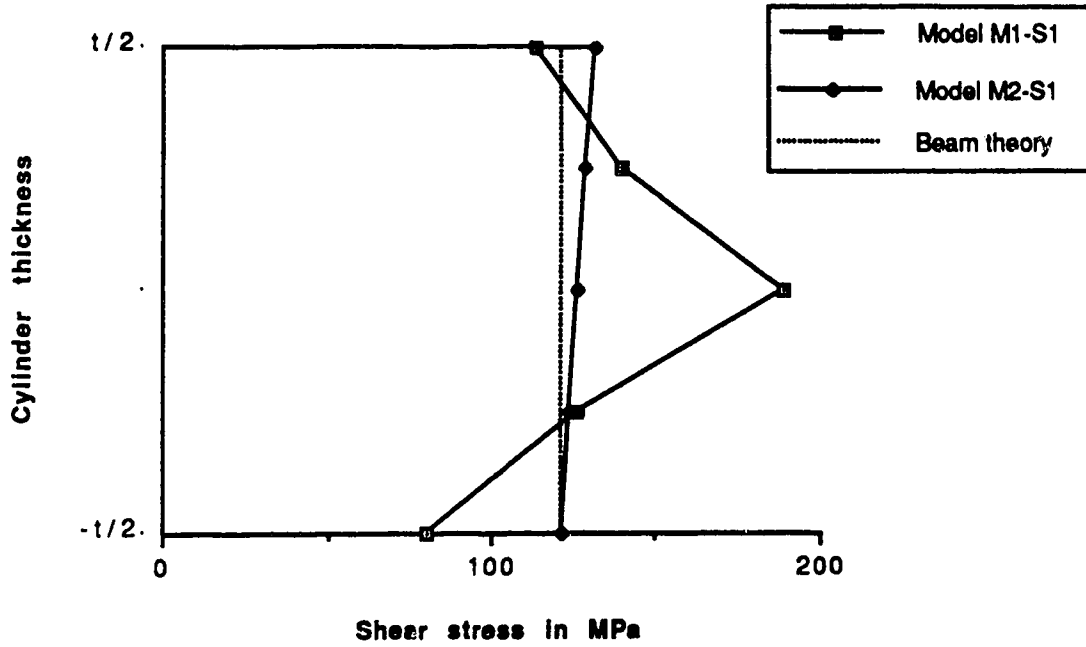


Fig. 4.8 Shear distribution across the thickness at load = 1671 kN

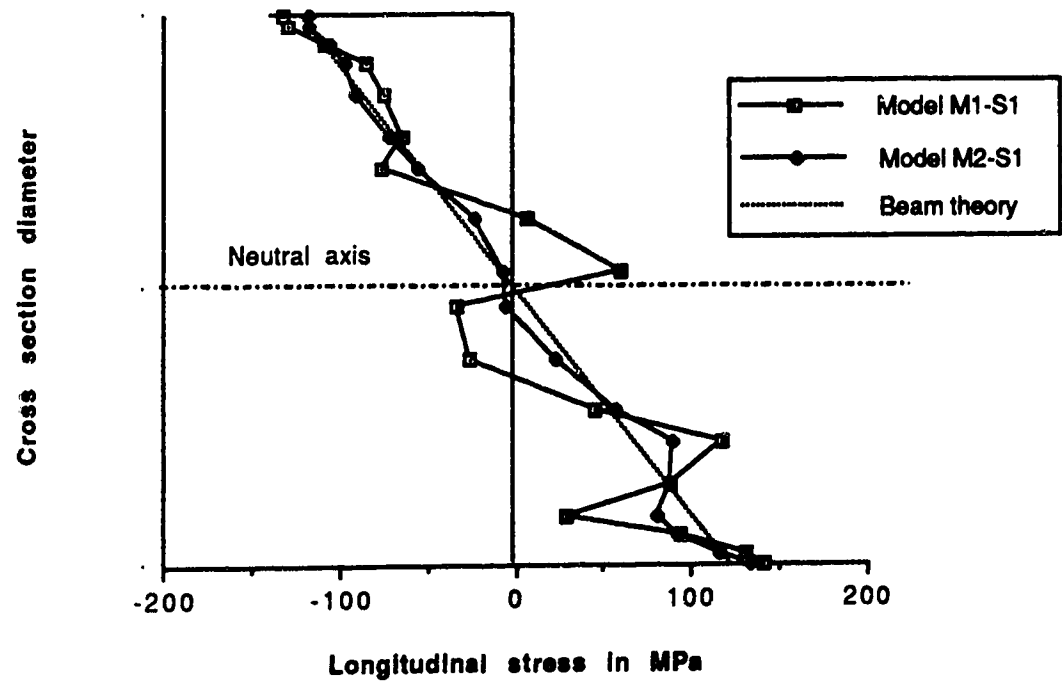


Fig. 4.9 Average longitudinal stress distribution at load = 1671 kN

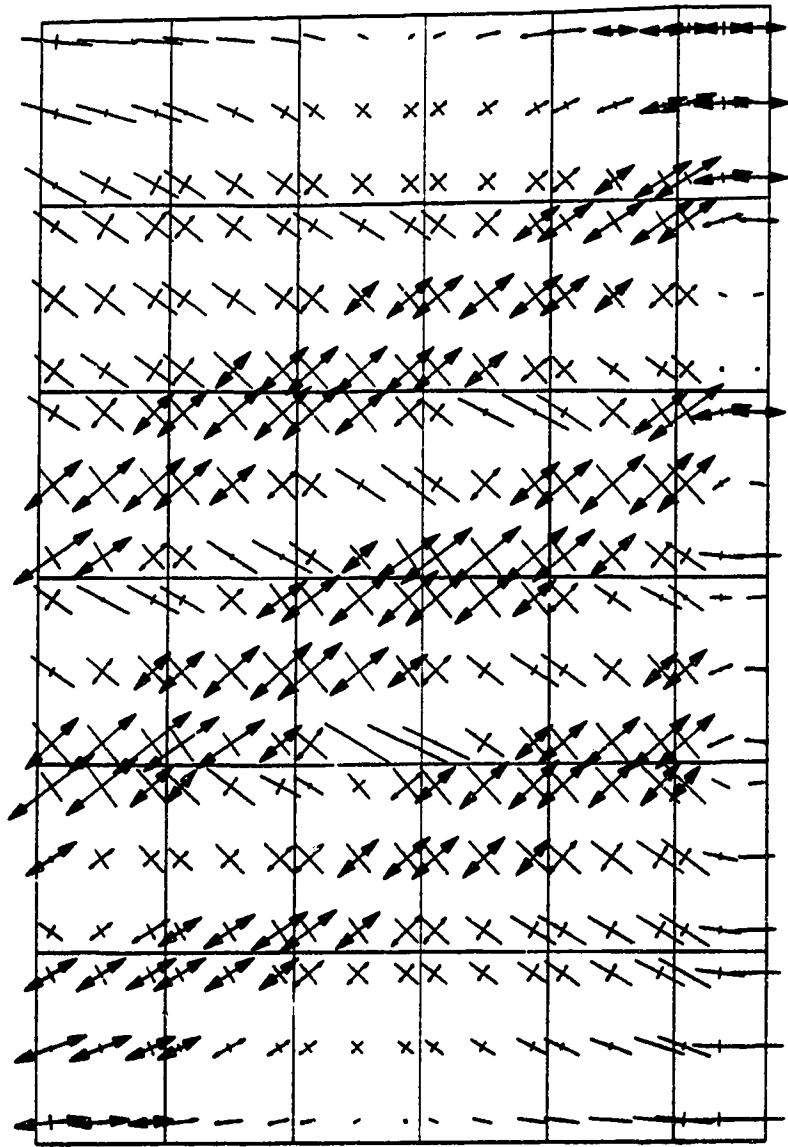
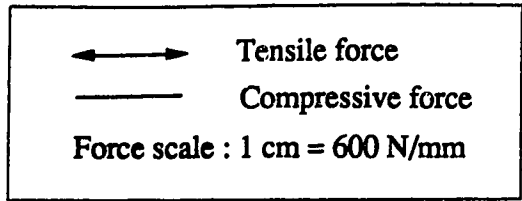


Fig. 4.10 Principal forces on the developed surface of model M1-S1 at vertical displacement = 3.18 mm

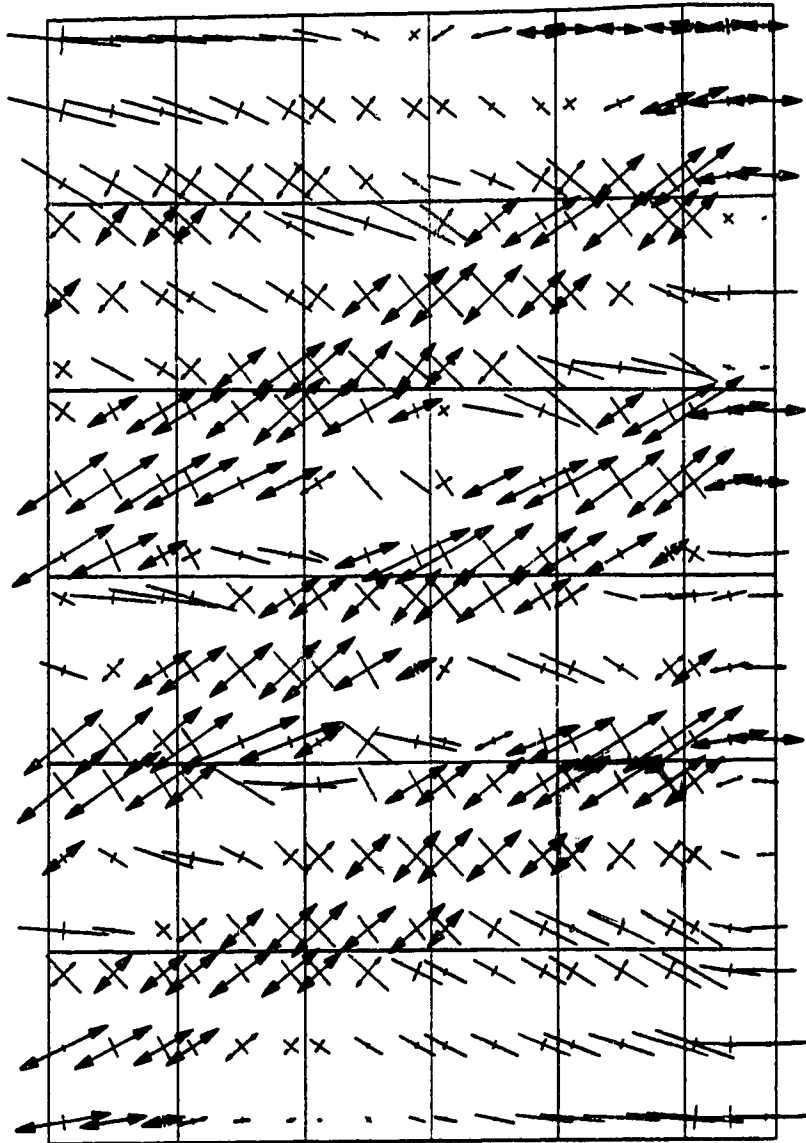
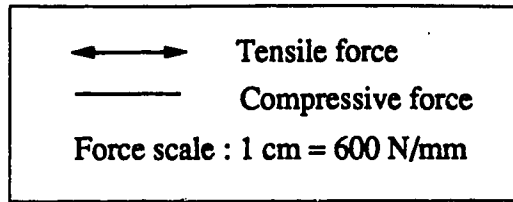


Fig. 4.11 Principal forces on the developed surface of model M1.S1 at vertical displacement = 6.42 mm

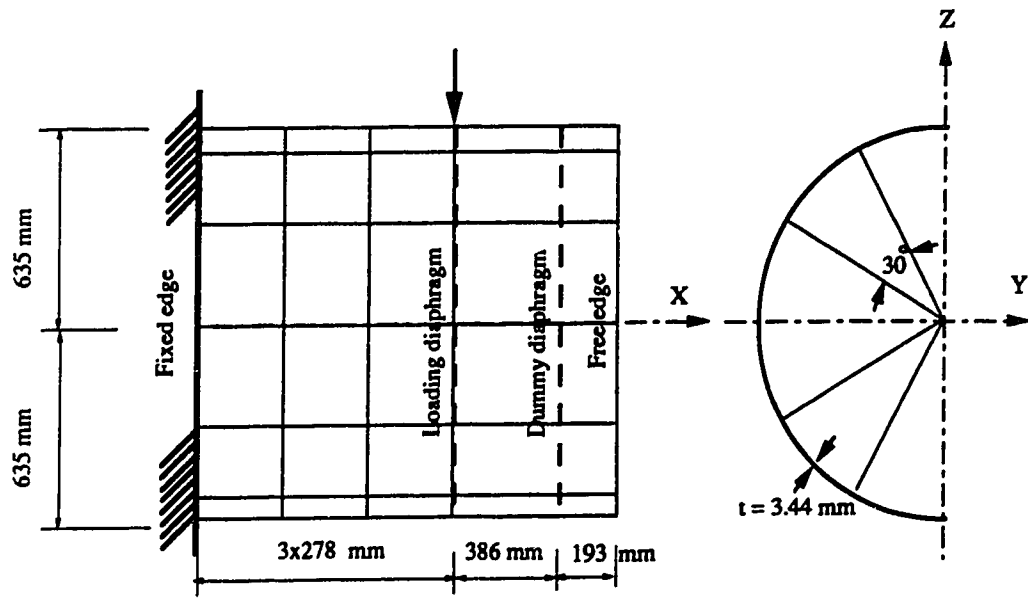


Fig. 4.12 Mesh arrangement of model M1-S2

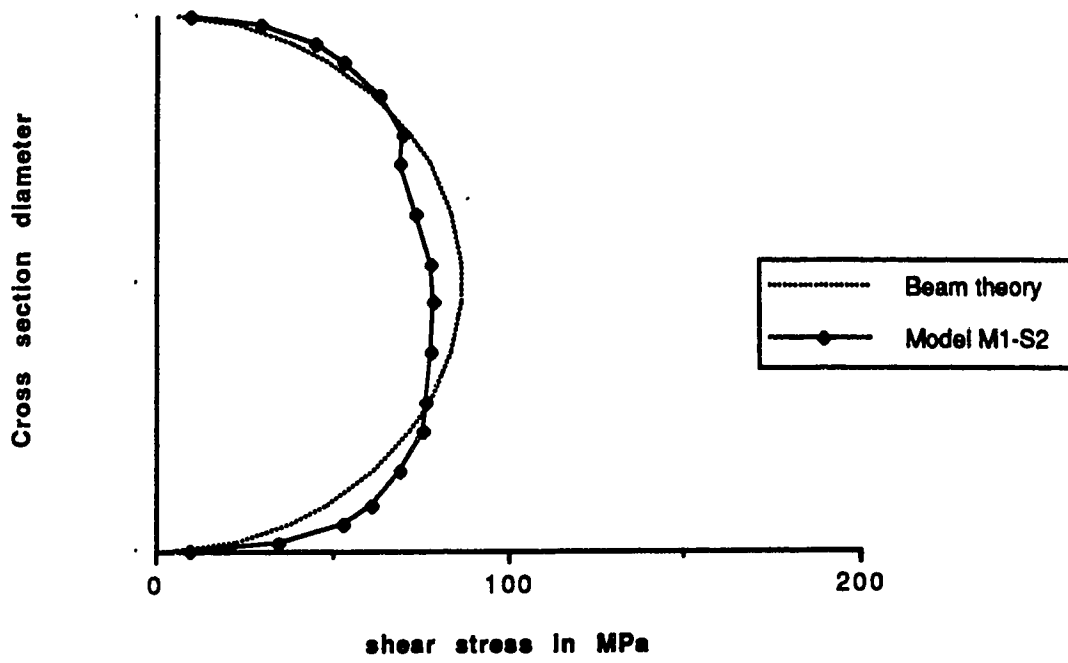


Fig. 4.13 Average shear distribution for M1-S2 at disp. = 0.99 mm

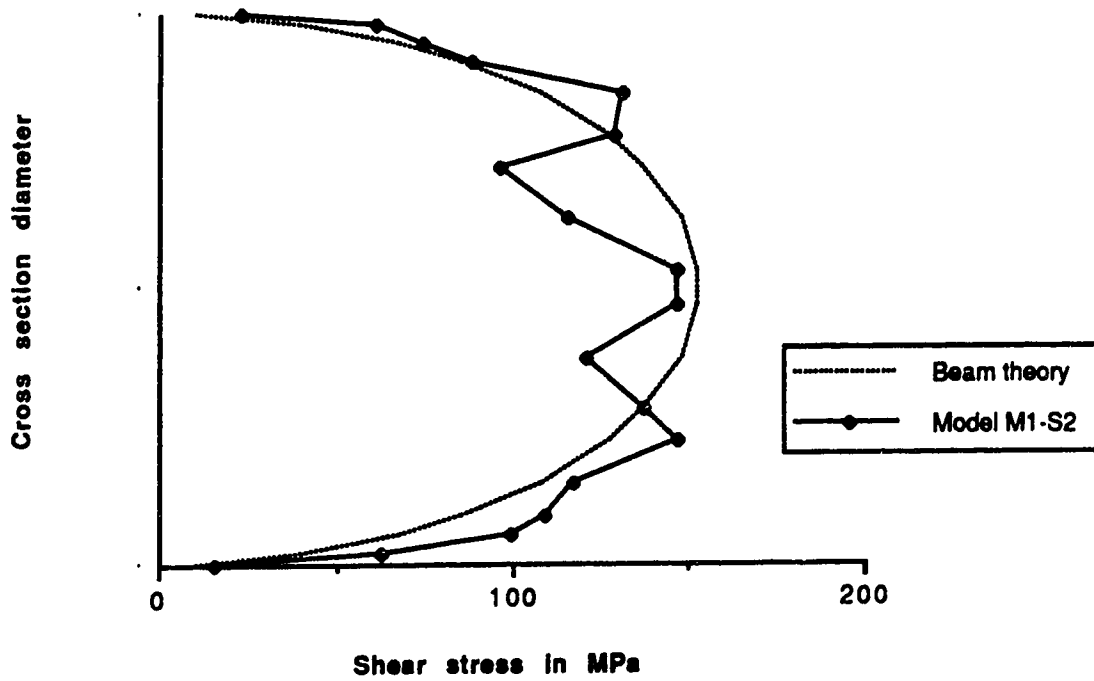


Fig. 4.14 Average shear distribution for M1-S2 at disp. = 2.22 mm

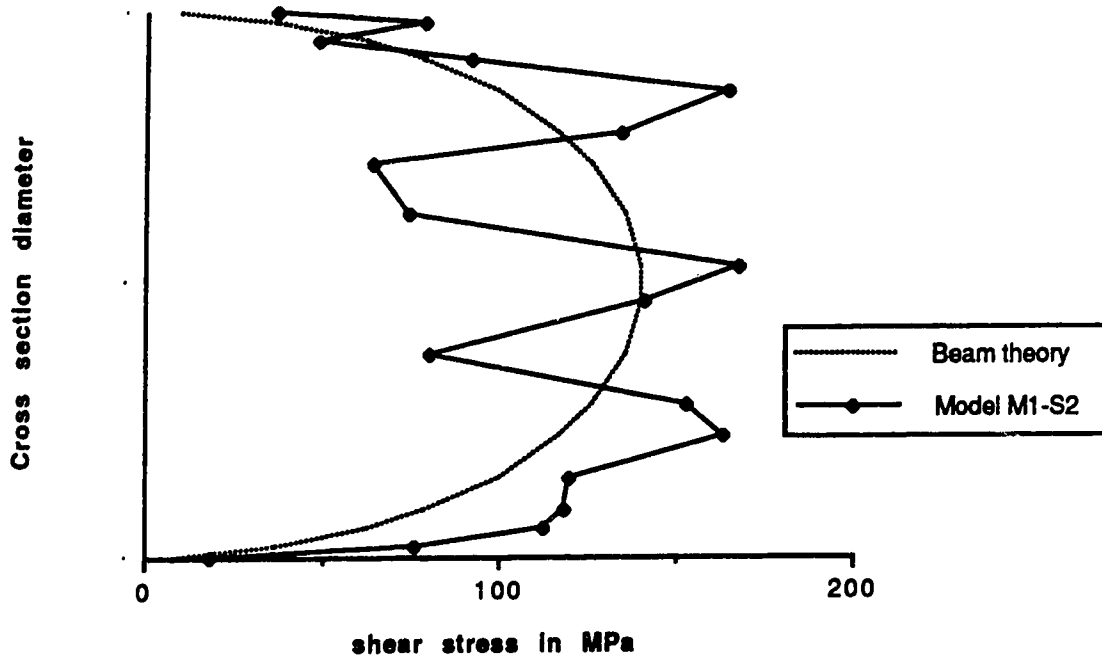


Fig. 4.15 Average shear distribution for M1-S2 at disp. = 3.41 mm

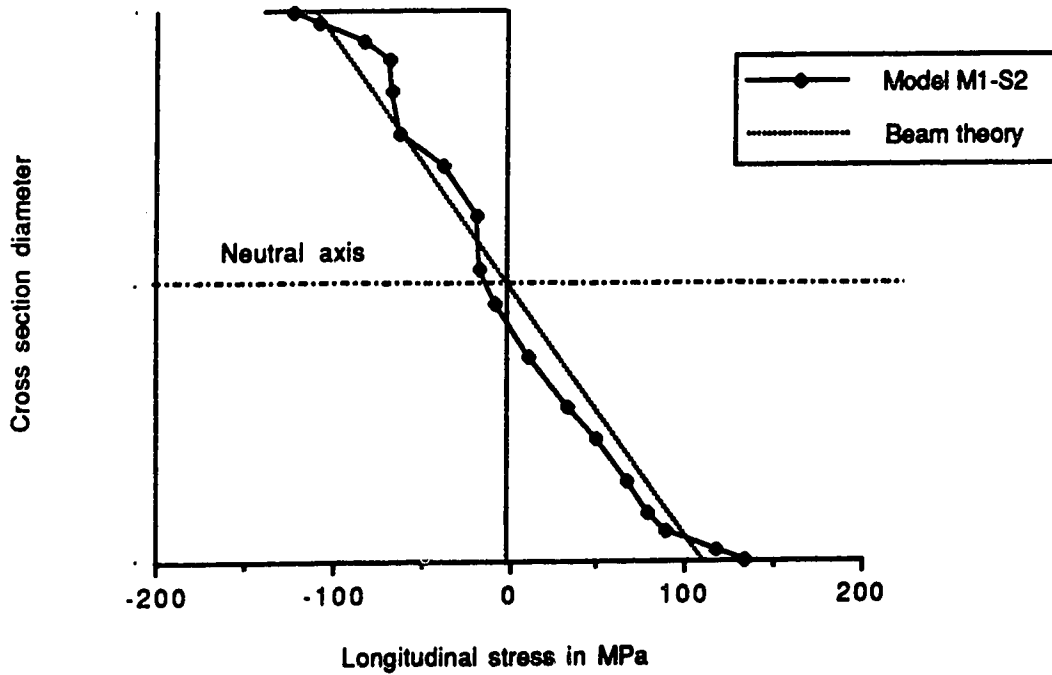


Fig. 4.16 Average longitudinal stress distribution at disp. = 0.99 mm

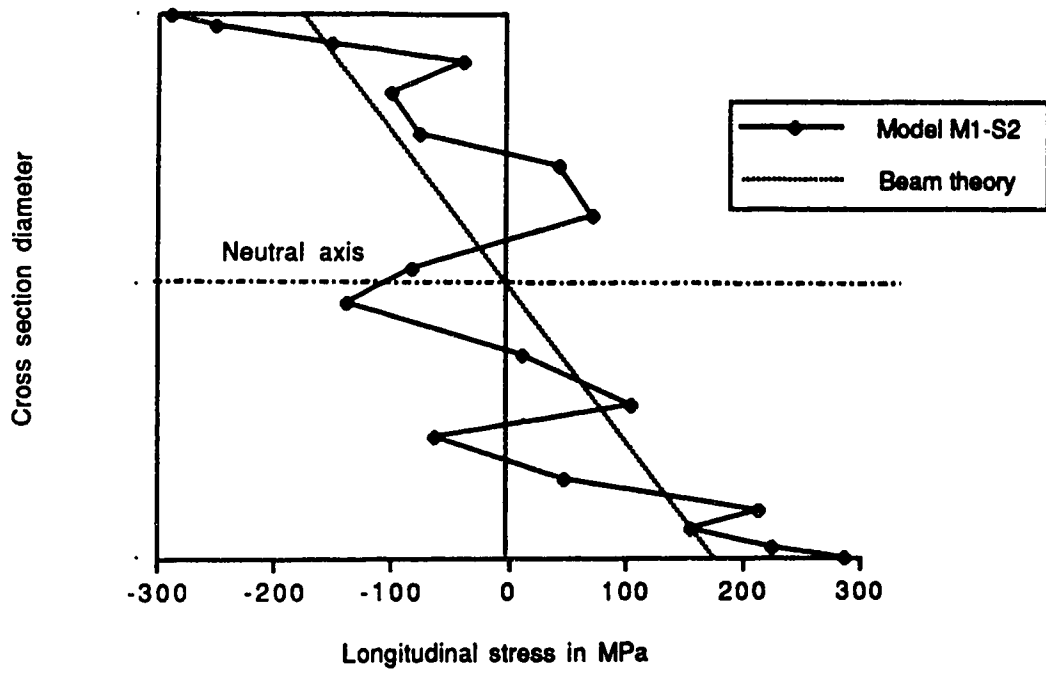


Fig. 4.18 Average longitudinal stress distribution at disp. =3.41 mm

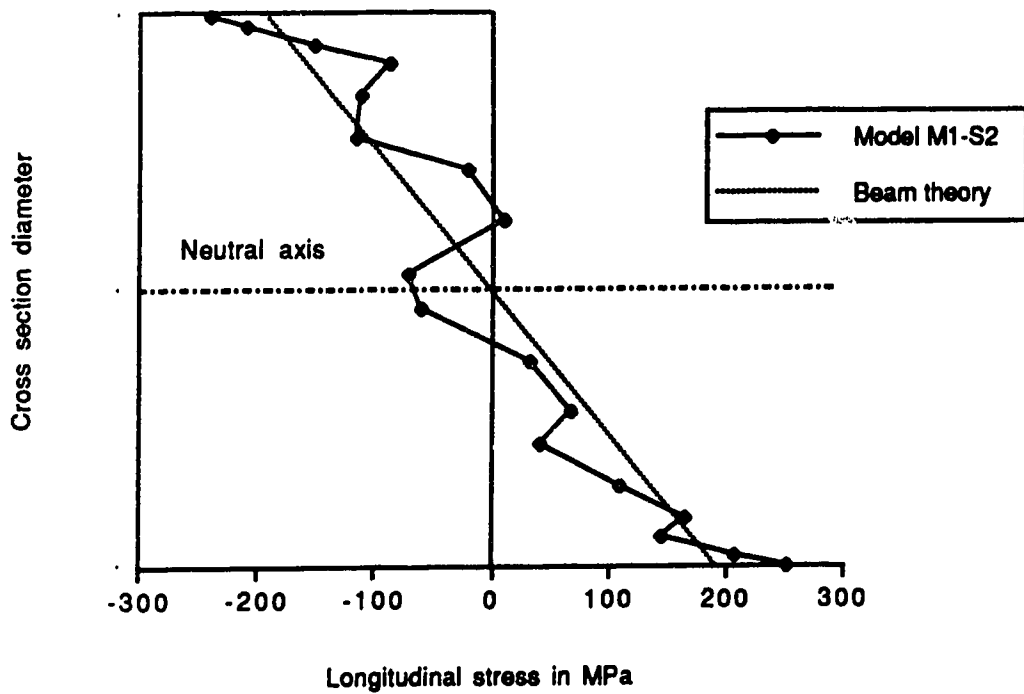


Fig. 4.17 Average longitudinal stress distribution at disp. =2.22 mm

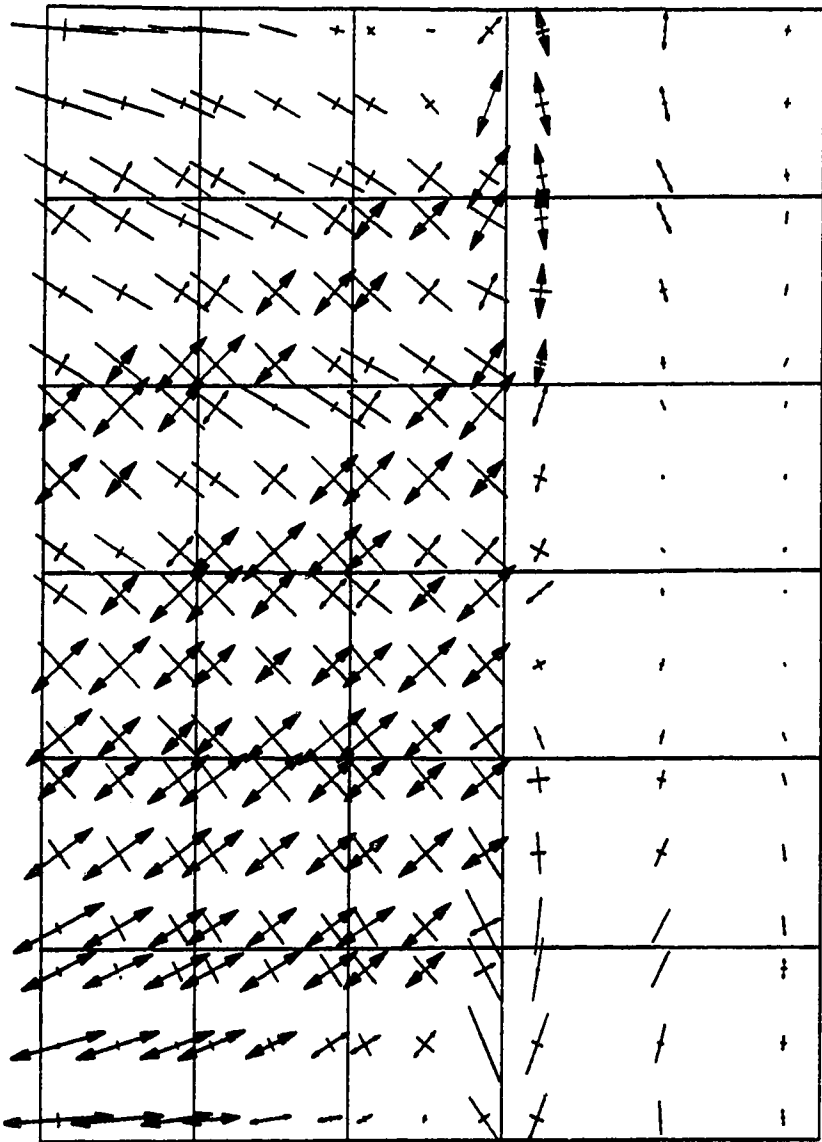
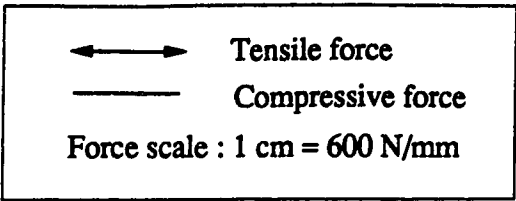


Fig. 4.19 Principal forces on the developed surface of model M1-S2 at vertical displacement = 2.44 mm

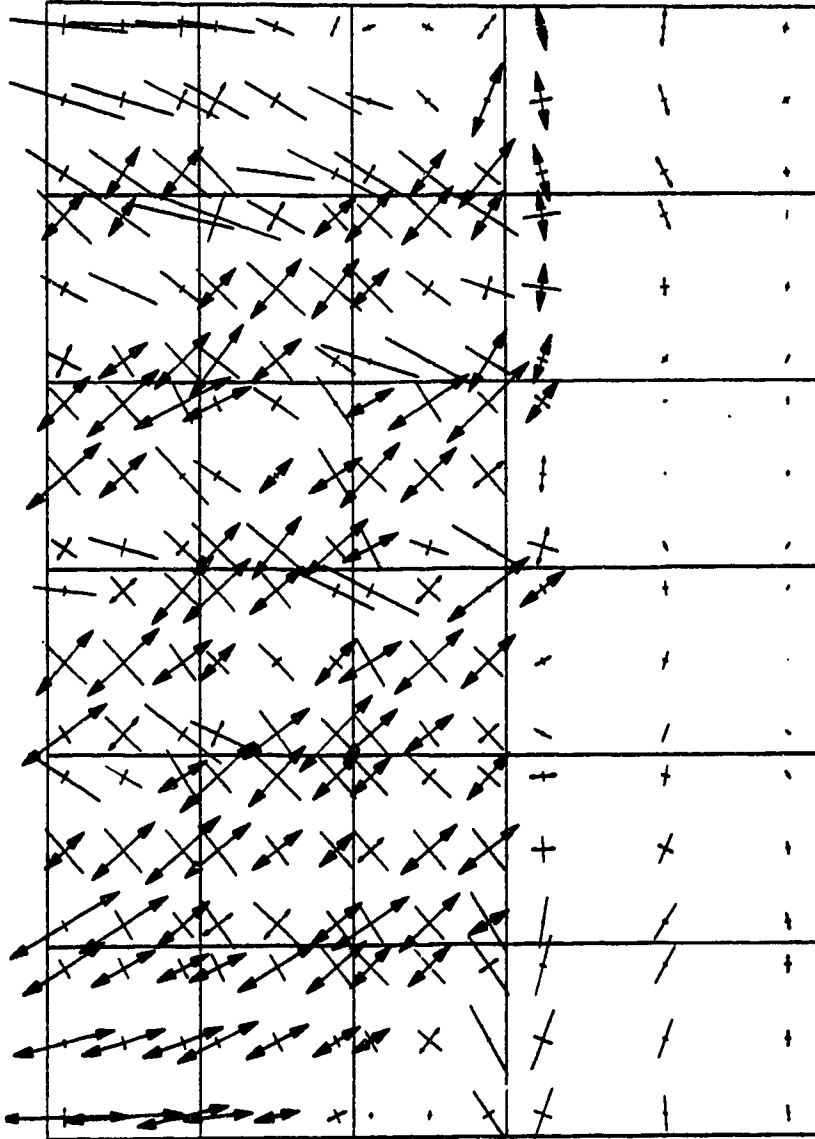
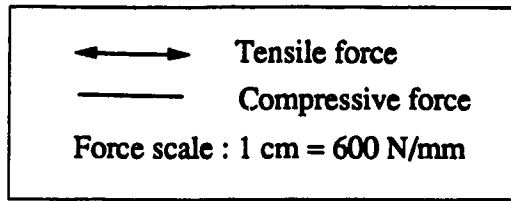
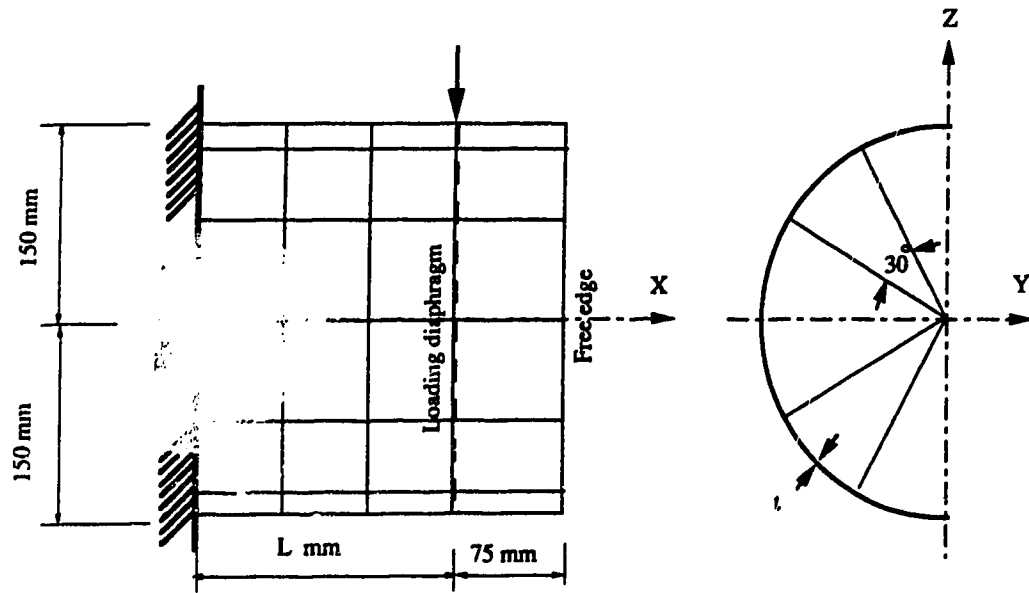


Fig. 4.20 Principal forces on the developed surface of model M1-S2 at vertical displacement = 4.63 mm



Model	R mm	L mm	t mm	R/t	R/L
MF1	150	150	1.0	150	1.00
MF2	150	200	1.0	150	0.75
MF3	150	300	1.0	150	0.50
MF4	150	150	0.8	188	1.00
MF5	150	200	0.8	188	0.75
MF6	150	300	0.8	188	0.50
MF7	150	150	0.6	250	1.00
MF8	150	200	0.6	250	0.75
MF9	150	300	0.6	250	0.50

Fig. 4.21 Mesh arrangement of MF series

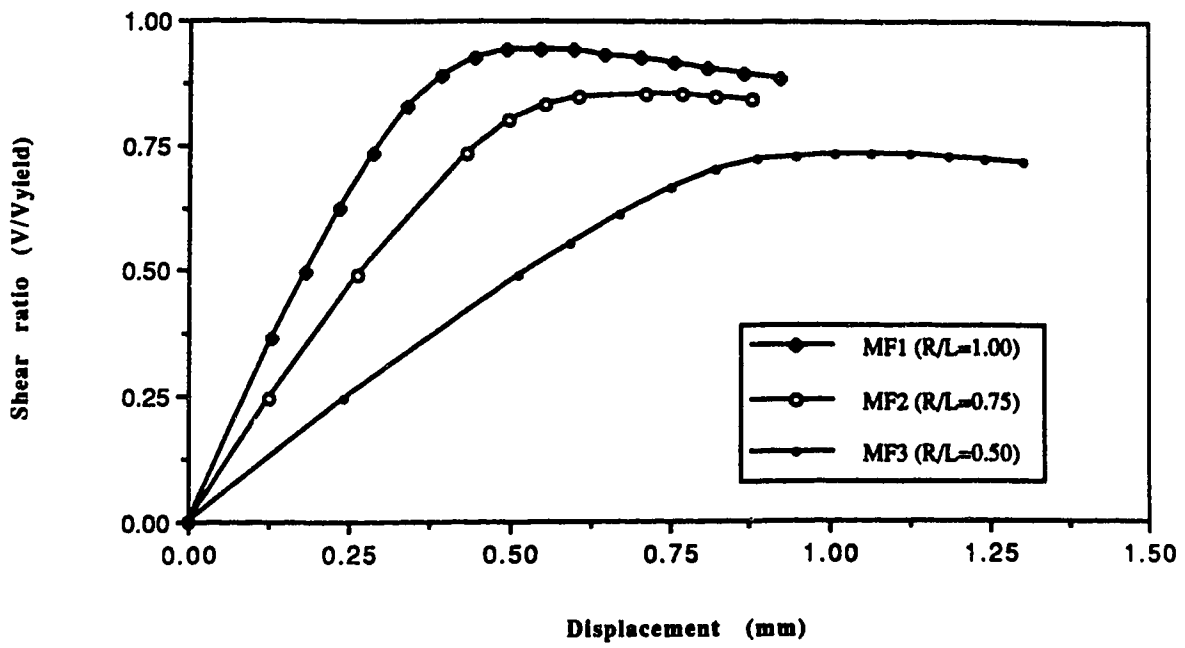


Fig. 4.22 Load-displacement curves for models with R/t ratio=150

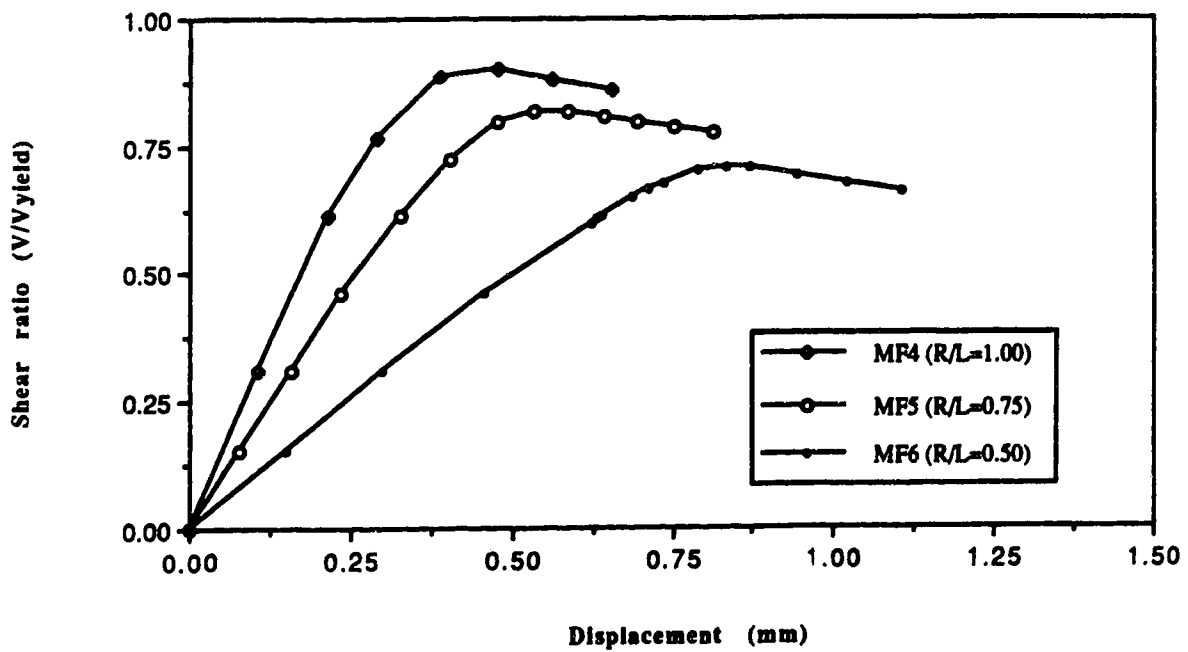


Fig. 4.23 Load-displacement curves for models with R/t ratio=188

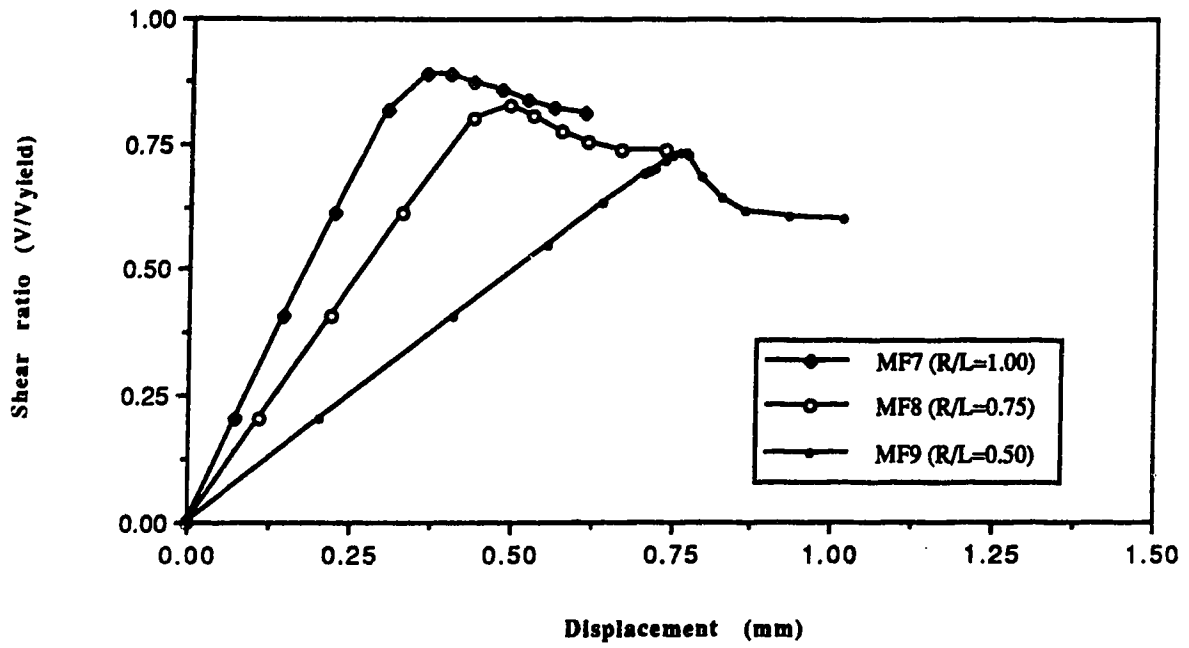


Fig. 4.24 Load-displacement curves for models with R/t ratio=250

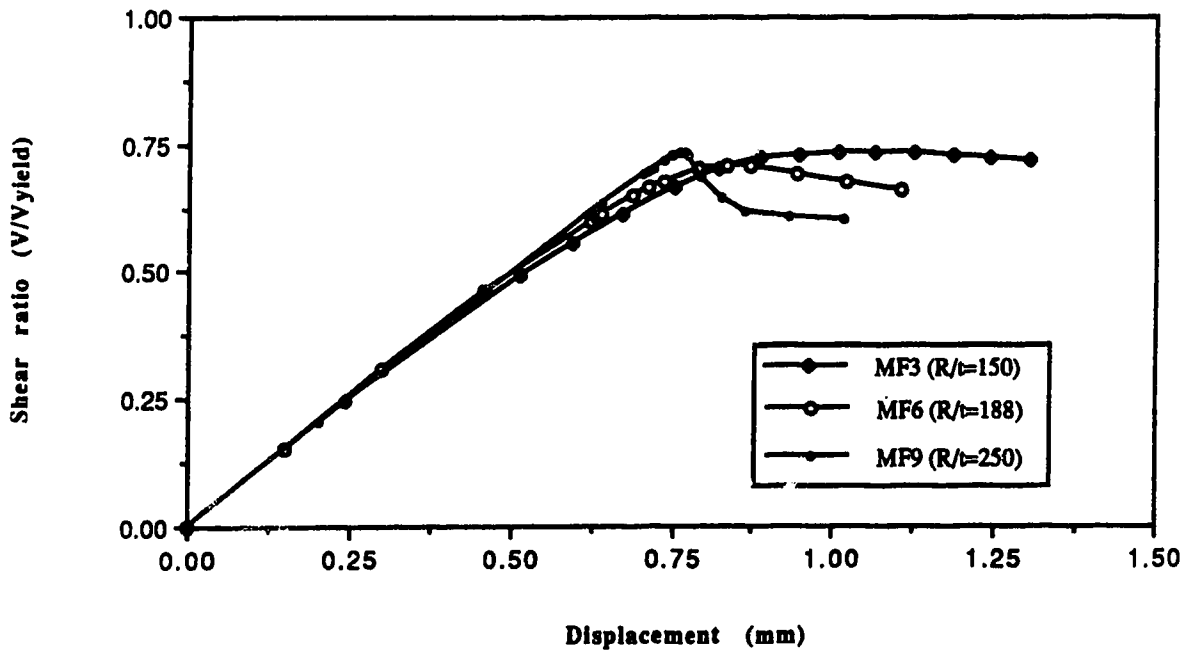


Fig. 4.25 Load-displacement curves for models with R/L ratio=0.5

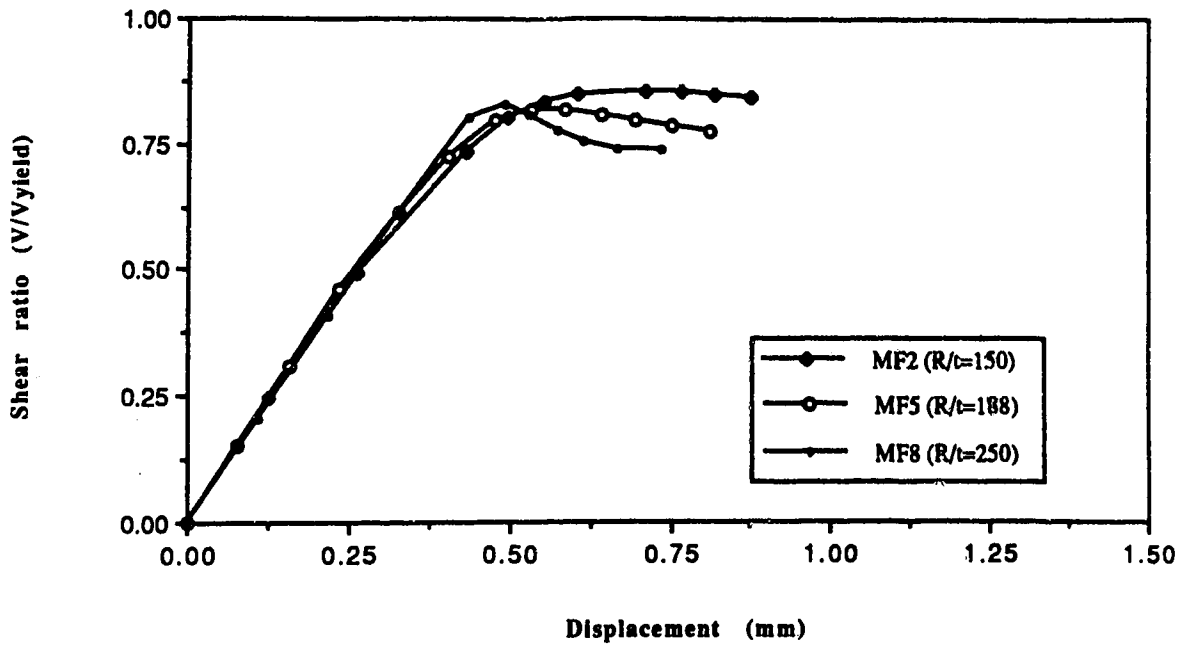


Fig. 4.26 Load-displacement curves for models with R/L ratio=0.75

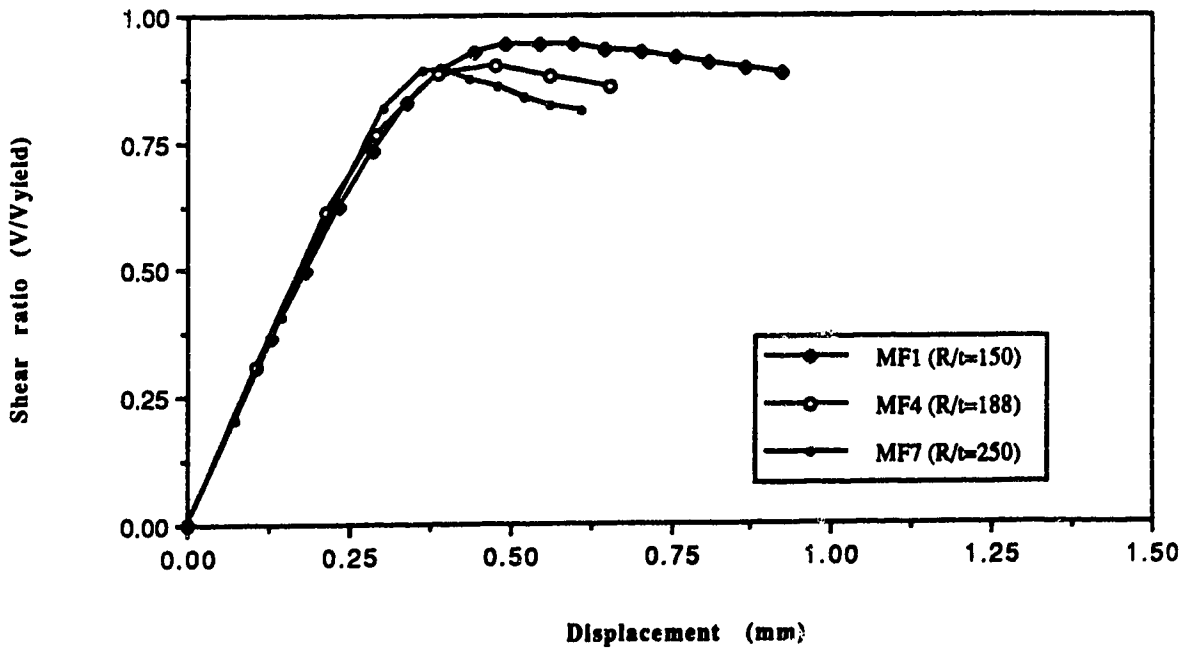


Fig. 4.27 Load-displacement curves for models with R/L ratio=1.0

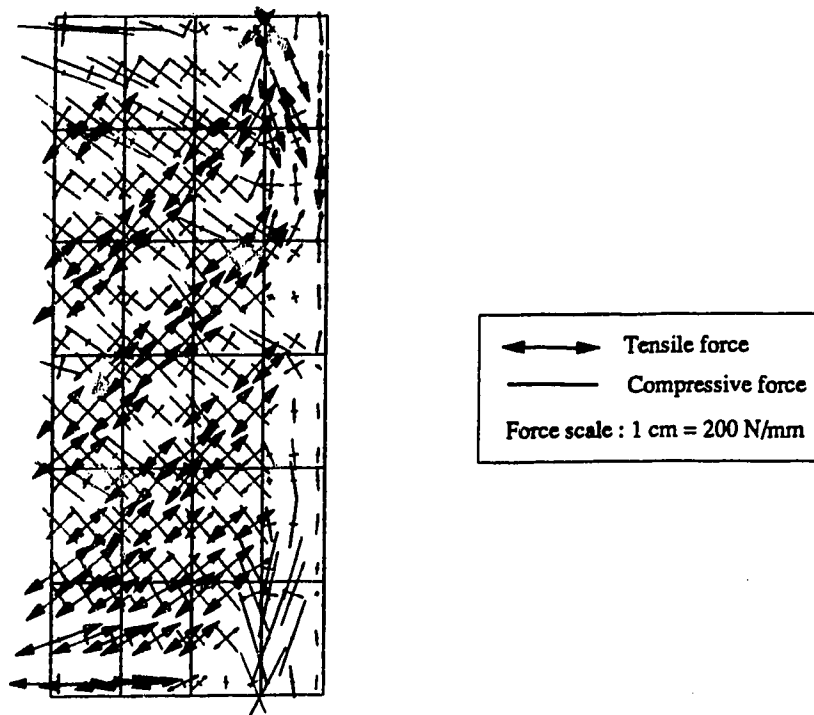


Fig. 4.28 Principal forces on the developed surface of model MF1 at vertical displacement = 0.93 mm

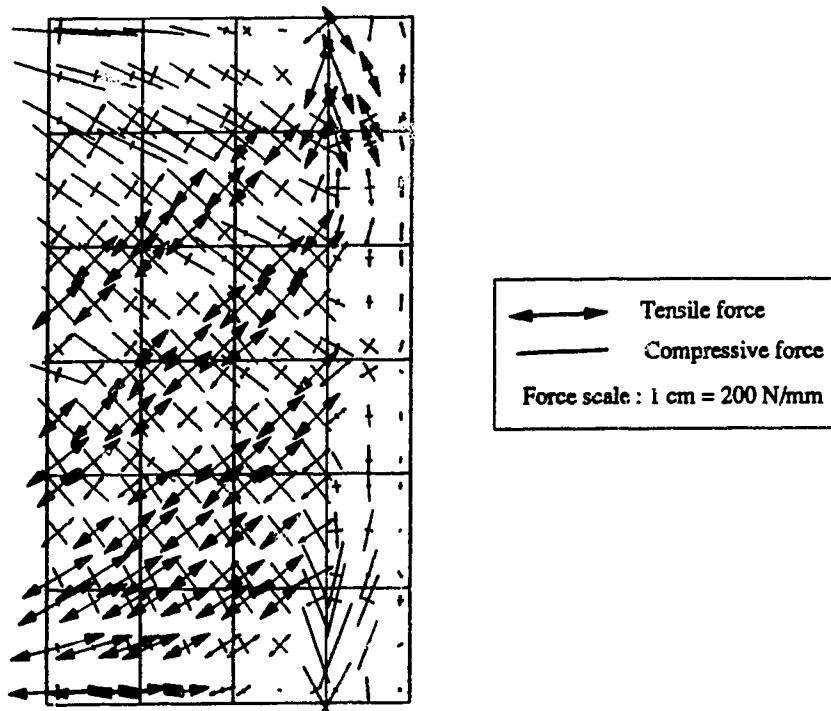


Fig. 4.29 Principal forces on the developed surface of model MF2 at vertical displacement = 0.88 mm

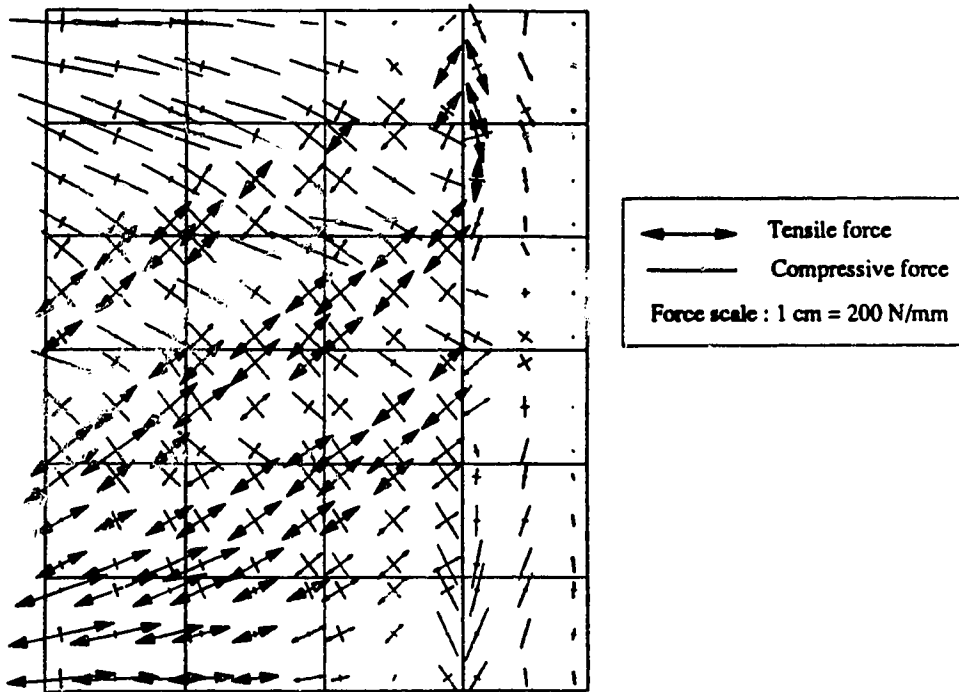


Fig. 4.30 Principal forces on the developed surface of model MF3 at vertical displacement = 1.30 mm

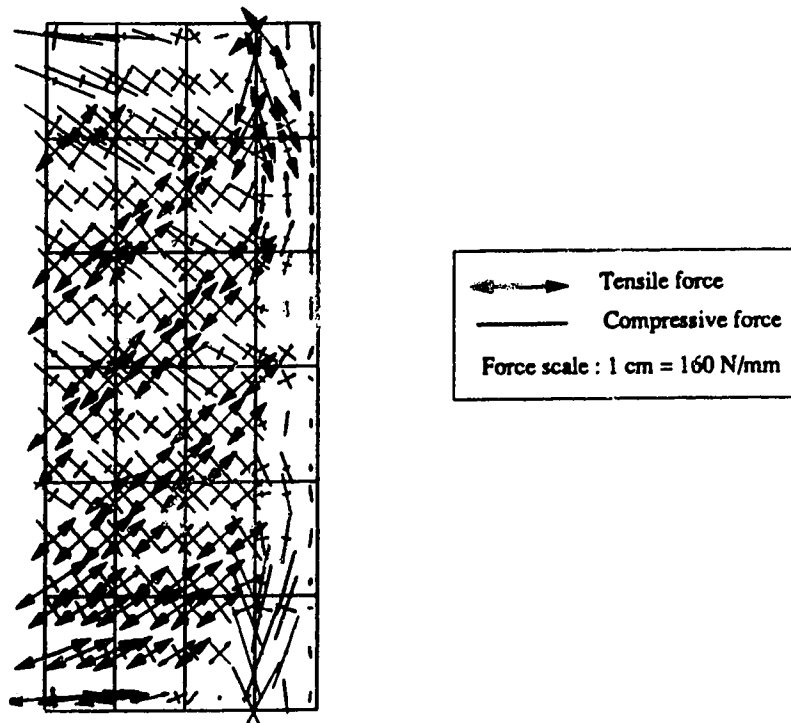


Fig. 4.31 Principal forces on the developed surface of model MF4 at vertical displacement = 0.65 mm

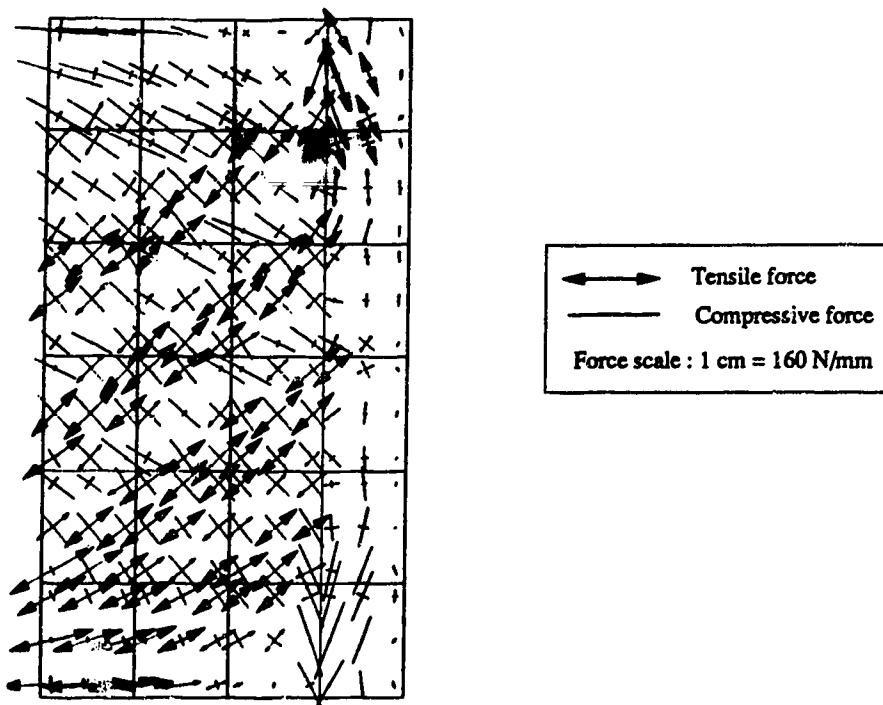


Fig. 4.32 Principal forces on the developed surface of model MF5 at vertical displacement = 0.81 mm

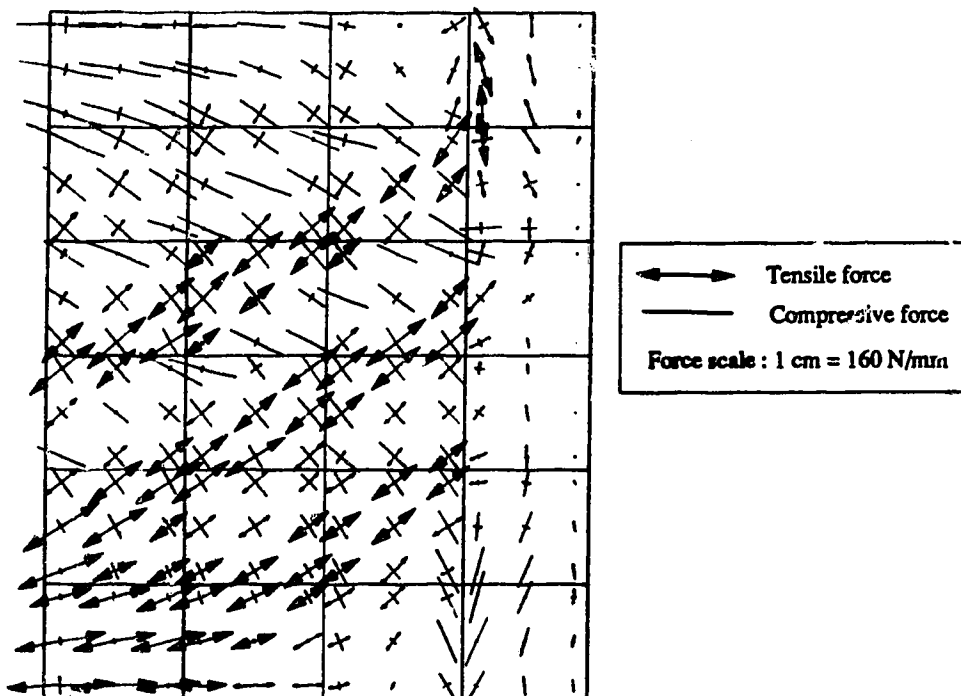


Fig. 4.33 Principal forces on the developed surface of model MF6 at vertical displacement = 1.10 mm

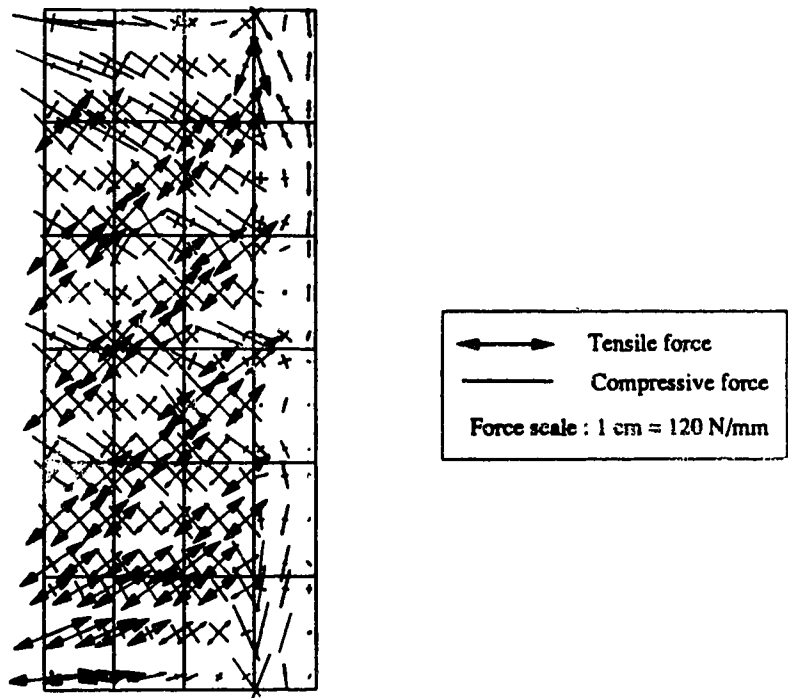


Fig. 4.34 Principal forces on the developed surface of model MF7 at vertical displacement = 0.61 mm

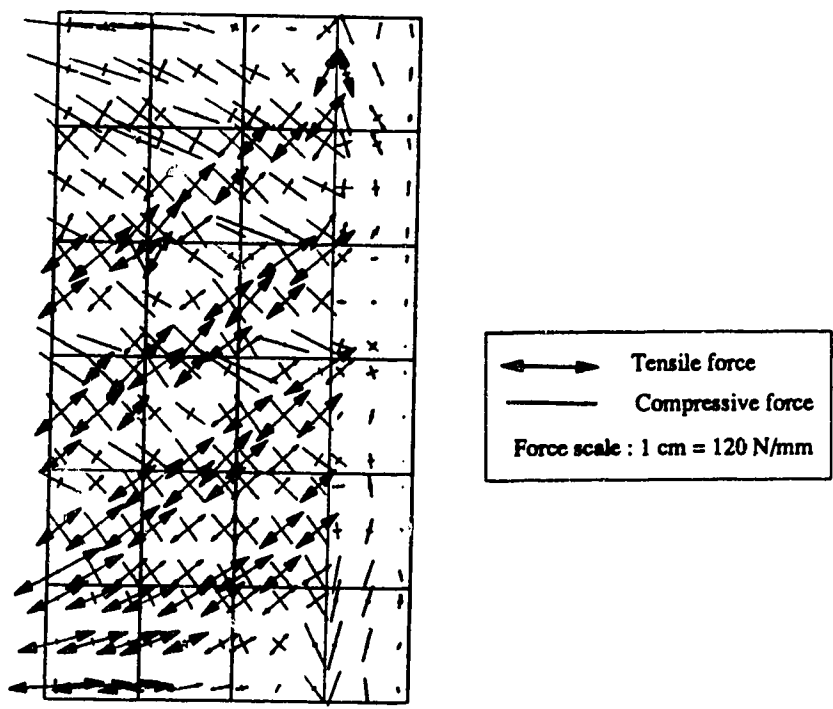


Fig. 4.35 Principal forces on the developed surface of model MF8 at vertical displacement = 0.69 mm

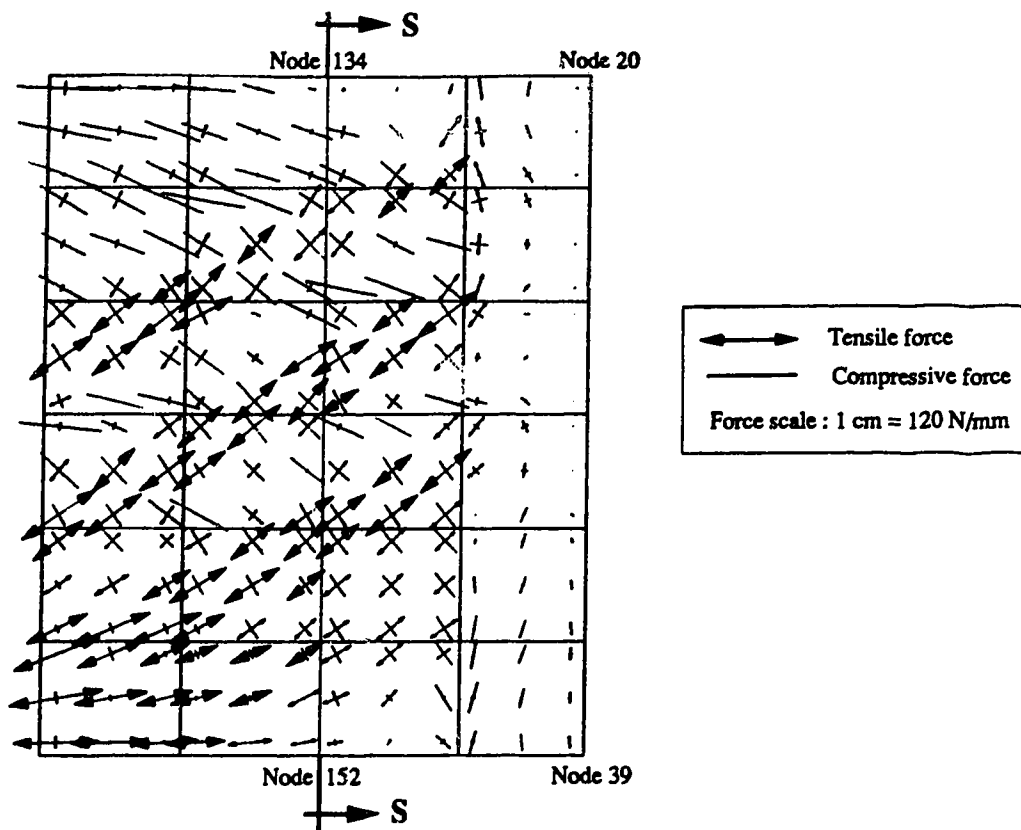


Fig. 4.36 Principal forces on the developed surface of model MF9 at vertical displacement = 1.01 mm

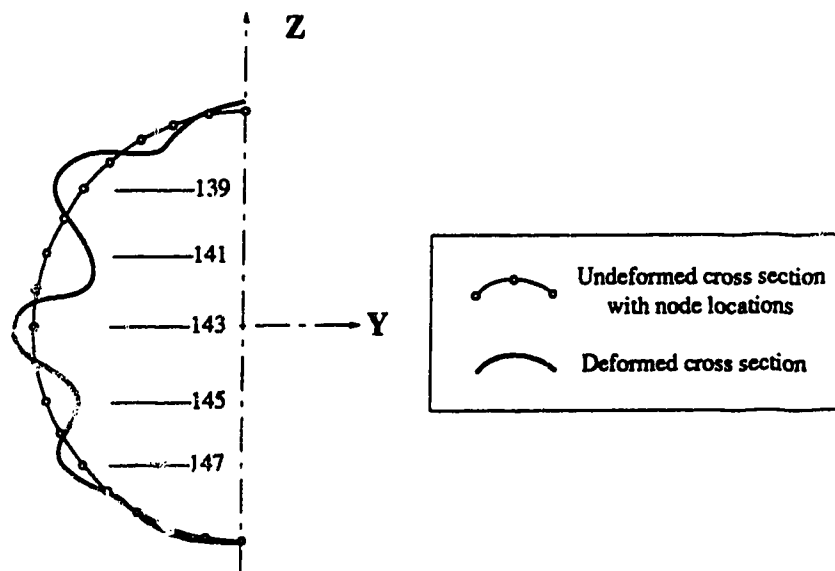


Fig. 4.37 Deformations of cross section, S-S, in model MF9 (magnified 75 times)

5. Regression Analysis

5.1 Introduction

The inelastic shear buckling capacity of fabricated steel thin-walled cylinders is affected by many factors. This is one reason why it is not possible at the present time to develop an analytically derived solution for the inelastic shear capacity of such members. Two alternatives are available in such cases. Either a sophisticated numerical analysis can be employed, which is usually expensive and not convenient for everyday design purposes, or empirical formulae based on experimental results can be developed.

In this chapter, regression models are developed which provide an estimate of the inelastic shear capacity of thin-walled cylinders. A number of linear and nonlinear models are fitted to the available experimental and numerical data. The effectiveness of these models is tested by several correlation criteria and a particular model is then recommended as an empirical design equation and compared with a currently used design equation (Eq. 2.17, Galletly and Blachut, 1985).

5.2 Regression Variables and Data Set

With the increasing emphasis on empirical research, along with the availability of prepared computer programs, regression analysis is now widely used in many fields. Regression analysis is the method of building a statistical model to describe in some sense the behavior of a random variable. A regression model uses information about a

set of independent variables in order to estimate the expected value of some dependent variable. The regression model is useful for estimating the response provided it is based on an understanding of the relations among the variables.

The elements of any regression analysis are the model, the variables, and the data set. In this Section, the variables contained within the inelastic shear buckling problem for thin-walled cylinders are defined and the regression data are presented.

For the problem of cylinder shear buckling, the shear capacity of the cylinder is the dependent variable. In order to generalize the analysis, the response (Y) is defined as the ratio of the maximum resisted shear force (V_{\max}) to the yield shear force (V_y):

$$Y = \frac{V_{\max}}{V_y} \quad (5.1)$$

In deriving expressions for V_{\max} and V_y , it is assumed that the relationship between the shear force and the shear stress is based on membrane theory, that is:

$$V = \pi R t \tau \quad (5.2)$$

The shear capacity of the cylinder is influenced by many parameters: cylinder radius (R), shear span (L), shell thickness (t), material yield strength (σ_y), elastic modulus (E), the degree and shape of imperfections which exist in the cylinder wall prior to loading, the residual stresses due to the manufacturing process, and the boundary conditions. A successful multiple regression model

includes the least possible number of independent variables that permit an adequate interpretation of the response. Multiple regression models that have fewer independent variables are inherently easier to analyze and interpret. Therefore, an attempt to reduce the eight independent variables mentioned above will be advantageous.

As discussed in Chapter 2, the influence of cylinder imperfections on the maximum shear capacity is considered to be relatively small, and, based on tests and numerical analysis, is reported to be less than 10% (Galletly and Blachut, 1985 and Roman and Elwi, 1986). Therefore, it is proposed to ignore imperfections as an independent variable in this analysis. However, the effect is included as a source of random error inherent in the test specimens used as the basis of the regression model.

For most of the cases in the data set, the boundary conditions are identical. This does not allow the effect of the boundary conditions to be examined in a worthwhile way, and therefore it has been omitted as a variable.

Residual stresses are mainly induced by the rolling and welding processes and by the type of material used. All the physical specimens were manufactured using the same fabrication procedure. Also, the finite element models included an estimate of the residual stresses equivalent to those induced by bending a flat plate to form a cylinder. The lack of variation in the residual stress patterns throughout the data set led to a decision to exclude them as a

variable in this analysis. However, the residual stresses caused by welding and the type of material are not the same in all the observations in the data set. Because of the insufficient information reported from the physical tests concerning these residual stresses, this difference is expected to induce some inevitable error in the analysis.

The remaining parameters (R , t , L , E , and σ_y) are used to define three dimensionless independent variables X_1 , X_2 , and X_3 as follows:

$$X_1 = R/t \quad (5.3)$$

$$X_2 = R/L \quad (5.4)$$

$$X_3 = E/\sigma_y \quad (5.5)$$

Since E is almost constant for different types of steel and since R does not independently affect the shear capacity as an individual variable, the defined variables X_1 , X_2 , and X_3 are in fact independent of one another. The thickness ratio (X_1) emphasizes the thin-wall aspect of the cylinder while the aspect ratio (X_2) emphasizes the effect of the shear span. The material ratio (X_3) introduces the effect of the grade of steel on the maximum shear stress. Defining the regression variables in this manner serves three purposes. It reduces the number of variables in the regression model, it generalizes the model by relating the shear capacity to nondimensional ratios, and brings it closer in form to the theoretical elastic shear buckling prediction (Schroder, 1972 and Yamaki et al., 1979), where the elastic shear stress (τ_e) is a function of the elastic modulus (E), the aspect ratio

(R/L), and the thickness ratio (R/t). (The elastic shear buckling equation is given by Eq. 3.2).

The data set chosen to develop the regression models covers a wide practical range of the three independent variables X_1 , X_2 , and X_3 , as shown in Table 5.1. The thickness ratio (X_1) varies from 125 to 250, the aspect ratio (X_2) varies from 0.50 to 1.37, and the stress ratio (X_3) varies from 457 to 841. It should be noted that the regression models can predict the response (Y) most accurately within the range of the independent variables from which they were derived. The model accuracy outside this range is indefinite.

The data set consists of 29 different data records and each record consists of the three variables X_1 , X_2 , and X_3 and the corresponding response Y . Seventeen of these records are obtained from physical tests, including G1 through G14 (Galletly and Blachut, 1985), B1 (Bailey and Kulak, 1984), and the tests S1 and S2 performed as part of this work and described in Chapter 3. The other data records are the results of the numerical analysis described in Chapter 4. The finite element models tend to slightly overestimate the maximum shear capacity of the cylinder. Therefore, it might be considered that a more rational regression model would be one based on the experimental data only. However, both approaches, including and excluding the finite element data, are investigated and criticized in the following sections.

5.3 Regression of the Data Set

5.3.1 Linear Model

The ultimate goal of any regression analysis is to develop the true relationship between the response and the independent variables. If the shape of this relationship or equation is known, then the remaining unknown constants can be evaluated from the data set using the least squares method or any other error minimization technique. However, in most cases the shape of the equation is also unknown and has to be determined. The simplest form of the regression models is the linear form. Using linear models in cases where the true behavior is certainly nonlinear is justified by Taylor's theorem (Burington, 1948), wherein any nonlinear function can be approximated to any desired degree of accuracy by a linear function with enough higher order terms. Simple linear models help to understand the strength of association between Y and each of the X-variables, while multiple linear models approximate the true function.

In selecting the best regression model of the simple linear models, one approach is to evaluate all possible models, especially if the number of X-variables is small (Berenson et al., 1983). For three independent variables, the possible simple linear regression models are :

$$\hat{Y} = a + b X1 \quad (5.6)$$

$$\hat{Y} = a + b X2 \quad (5.7)$$

$$\hat{Y} = a + b X_3 \quad (5.8)$$

$$\hat{Y} = a + b X_1 + c X_2 \quad (5.9)$$

$$\hat{Y} = a + b X_1 + c X_3 \quad (5.10)$$

$$\hat{Y} = a + b X_2 + c X_3 \quad (5.11)$$

$$\hat{Y} = a + b X_1 + c X_2 + d X_3 \quad (5.12)$$

where \hat{Y} is the predicted response and $a, b, c,$ and d are the regression constants. It is also possible to multiply two or more variables as follows (Berenson et al., 1983):

$$\hat{Y} = a + b X_1 X_2 \quad (5.13)$$

$$\hat{Y} = a + b X_1 X_3 \quad (5.14)$$

$$\hat{Y} = a + b X_2 X_3 \quad (5.15)$$

$$\hat{Y} = a + b X_1 X_2 X_3 \quad (5.16)$$

To test these models, a correlation criterion is needed, that is, a method is needed which measures the strength of association among the variables. One popular correlation criterion compares the coefficient of determination (r^2) of the different models (Wesolowsky, 1976). The coefficient of determination is defined as:

$$r^2 = 1 - \frac{SSE}{SST} = 1 - \frac{\sum_{i=1}^m (Y_i - \hat{Y}_i)^2}{\sum_{i=1}^m (Y_i - \bar{Y})^2} \quad (5.17)$$

in which m = the number of data records in the regression;
 SSE = the sum of the squares of the error for a model
and is a measure of the scatter of the observed
 Y data about the regression line \hat{Y} ; and
 SST = the sum of the squares of the total error and is
a measure of the variation of the observed Y
values around their mean \bar{Y} .

If the fit of the linear relationship \hat{Y} is perfect, that is, if all points fall on \hat{Y} , then $r^2 = 1$. If, on the other hand, the variation from the linear relationship is nearly as large as the variation about the mean \bar{Y} , then r^2 approaches zero. The value of r^2 is therefore a measure of the strength of the regression: the model fits the data best when the value of r^2 approaches unity.

Using the least squares method, the unknown constants a , b , c , and d of the linear models can be easily calculated. The constants and the corresponding correlation factors r^2 are presented in Table 5.2. Some important observations can be made from the data in this table. First, the coefficient of determination (r^2) for Eqs. 5.6 to 5.12 show that the accuracy increases when the model includes more parameters. They also show that the thickness ratio (R/t) and the aspect ratio (R/L) have a clear effect on the shear capacity ratio (Y), while the stress ratio (E/σ_y) does not seem to be linearly related to Y and its effect is, in fact, minimal. This is to be expected since the stress ratio includes two components, E , which is almost constant, and σ_y , which is present on both sides of the equation because it is proportional to τ_y .

Second, from Eqs. 5.13 to 5.16 it is noted that when X2 and X3 are combined, the degree of association with Y increases. This is most beneficial if the multiple linear models are used. The general multiple models contain higher powers of X as follows:

$$\begin{aligned} \hat{Y} = & a + b X1 + c X1^2 + d X1^3 + \dots + e X1^n \\ & + f X2 + g X2^2 + h X2^3 + \dots + k X2^n \\ & + l X3 + m X3^2 + n X3^3 + \dots + q X3^n \end{aligned} \quad (5.18)$$

Equation 5.18 is not convenient for design purposes. Even with only second powers, it would include seven terms. A simpler model which includes second order terms and makes use of the strength of the combined X2 and X3 is written as:

$$\hat{Y} = a + b (X1) + c (X1)^2 + d (X2 X3) + e (X2 X3)^2 \quad (5.19)$$

Eq. 5.19, which includes the additional second order terms, resulted in the largest value of r^2 . This is shown in Table 5.2. Although the accuracy may increase if more terms are added, it will be seen that the same accuracy can be achieved more easily by nonlinear models.

5.3.2 Nonlinear Models

5.3.2.1 Regression Subroutine

Nonlinear regression models are not usually as easy to solve as the linear models. Instead of using simple formulae to calculate the unknown constants, as is the case with linear models, computer subroutines designed for nonlinear regression must be used. The

subroutine RNLIN (IMSL, 1987) has been chosen to analyze the models proposed in the following sections.

Subroutine RNLIN fits a nonlinear regression model to a set of data using the least squares method. The nonlinear regression model is:

$$Y_i = F(X_i, C_i) + \varepsilon_i \quad (5.20)$$

where Y_i = the observed values of the dependent variable;
 X_i = the known independent variables;
 C_i = the unknown constants; and
 ε_i = independently distributed error with zero mean value and common variance S^2 such that

$$S^2 = \frac{1}{m-1} \sum_m^{i=1} (\varepsilon_i - \bar{\varepsilon})^2 \quad (5.21)$$

The program which provides the data and the function F to the solver subroutine RNLIN is listed in Appendix A. The output of this program includes the values of the regression constants (C_i -values), the sum of the squares of the error (SSE), and the coefficient of determination (r^2).

5.3.2.2 Model Groups

In this section, two groups of models are tested and compared with the data set. The general formula of each model is based on the general behavior of thin-walled cylinders under transverse loading. The first group is based on the interaction between the yield shear stress and the elastic shear buckling stress. The second group is

based on an examination of the shape of the response relative to each independent variable.

The *first group* is based on the interaction equation proposed by Galletly and Blachut (1985). This equation assumes that the inelastic shear buckling stress (τ_p) can be approximated by a quadratic interaction equation that uses the elastic shear buckling stress for simply supported cylinders under torsion (τ_e) and the yield shear stress (τ_y). The interaction equation takes the following form:

$$\frac{1}{\tau_p^2} = \frac{1}{\tau_e^2} + \frac{1}{\tau_y^2} \quad (5.22)$$

where τ_e is calculated according to Eq. 3.2. Although Galletly and Blachut compared the results of fourteen down-scaled model tests (300 mm in diameter) with the predictions of Eq. 5.22 and reported good agreement, this equation is not the best fit for the fourteen tests. In fact, if the difference between Eq. 5.22 and the test results is minimized using the least squares technique, the power "2" in the equation will be replaced by the power "2.33".

To expand on this idea, the interaction equation is assumed to have an unknown power n , this power is to be determined from the regression analysis of all the available data, namely Galletly's tests, Bailey's test (380 mm in diameter), the two full scale tests S1 and S2 (1270 mm diameter), and the finite element models. The power n of the interaction equation is no longer restricted to integer numbers and is calculated so that the equation is the best fit of the available

data set. The regression model is written in the general form as follows:

$$\frac{1}{\tau_p} = \frac{1}{\tau_e} + \frac{1}{\tau_y} \quad (5.23a)$$

Equation 5.23a has favorable convergence characteristics. When τ_e approaches infinity, the case of a very thick or a very short cylinder, the maximum shear stress approaches the yield shear stress. When τ_e approaches zero, the case of a very thin or a very long cylinder, the maximum shear stress converges to the elastic buckling stress. As a result, the inelastic buckling capacity acts as a smooth transition from the elastic buckling capacity to the yield capacity in a manner similar to that used to describe the inelastic buckling of steel columns. Eq. 5.23a can be rearranged in terms of \hat{Y} and X as follows:

$$\hat{Y} = \{ 1 + [(0.74 X_1^{-1.25} X_2^{0.5} X_3) 3^{0.5}]^n \}^{-1/n} \quad (5.23b)$$

As previously explained in Chapter 2, the constant, 0.74, that appears in Eq. 3.2 and 5.23(b), is actually a function of the boundary conditions as well as the thickness ratio (X1) and the aspect ratio (X2). For cylinders with fixed boundary conditions and with the range of X-values as in the data set, this constant ranges from 0.805 to 0.842, with an average of 0.825 (Yamaki, 1984). The constant 0.74 in Eq. 5.23b can therefore be replaced by 0.825. This is now re-introduced as another model, one that accounts for the effect of the boundary conditions:

$$\hat{Y} = \{ 1 + [(0.825 X_1^{-1.25} X_2^{0.5} X_3) 3^{0.5}]^n \}^{-1/n} \quad (5.24)$$

The two models, Eqs. 5.23(b) and 5.24, have the same accuracy with different values of the power n . The success of these models should be dependent on the accuracy of Eq. 3.2, which was originally derived for cylinders under pure torsion. After comparison with test results, Yamaki (1976) recommended the use of the same elastic buckling shear stress for cylinders under torsion and transverse loading. On the other hand, Schröder (1972) derived a capacity for cylinders under transverse loading which, although close to Yamaki's solution, is slightly different. Even though Schröder's solution is more accurate, it is available only in a chart format, and this discourages utilization in the interaction equation in place of Yamaki's solution. Also, the regression analysis performed on Eq. 5.23(b) and 5.24 minimizes the effect of the elastic solution and yields almost the same accuracy for both equations.

In order to limit the number of possible models in the analysis, an intuitive approach is adopted to select the *second group* of the nonlinear regression models. First, the general shape of the relationship between the response and each independent variable is described. Second, appropriate functions which are able to represent these relationships are suggested. Finally, different combinations of these functions are chosen to formulate the regression models.

To describe the relationships between Y and X , it is helpful to use the output of the linear regression analysis developed in Section 5.3.1. Equations 5.6 and 5.7 show that Y increases as $X_1 (=R/t)$

decreases or as $X_2 (=R/L)$ increases, while the small value of r^2 of Equation 5.8 shows only a small association between Y and $X_3 (=E/\sigma_y)$. Equation 5.12 indicates the importance of including all the X -variables in the model and Eq. 5.15 suggests a possible interrelation between X_2 and X_3 . Many functions can describe these relations: thus, more conditional characteristics have to be included. One way is to examine the theoretical shear capacity when the independent variables approach limit values. When the thickness ratio (R/t) approaches zero or when the aspect ratio (R/L) approaches infinity, the shear capacity converges to the yield shear capacity, or at least to a value close to the yield, depending on the initial residual stresses in the cylinder. In order to bring the regression model closer to the true behavior of cylinders, the selected functions should be able to satisfy these theoretical limits. Figures 5.1 and 5.2 show the desired general shape of the relationship between the shear force and the two variables R/t and R/L . They are best described by exponential functions. The following functions, $f1$ and $f2$, are suggested to simulate the curves in Fig. 5.1 and 5.2, respectively:

$$f1_1 = a X_1^{-b} \quad (5.25)$$

$$f1_2 = a e^{(-b X_1)} \quad (5.26)$$

$$f2_1 = a X_2^{+b} \quad (5.27)$$

$$f2_2 = a e^{(+b X_2)} \quad (5.28)$$

in which the subscripts describe different versions of the function f . Considering X_3 (the stress ratio), it is either treated similarly to X_2 or combined with it in f_2 as follows:

$$f_{2_3} = a (X_2 X_3)^b \quad (5.29)$$

From these functions, the following combinations are proposed as the second group of nonlinear regression models:

$$\hat{Y} = a X_1^b X_2^c X_3^d \quad (5.30)$$

$$\hat{Y} = a X_1^b (X_2 X_3)^c \quad (5.31)$$

$$\hat{Y} = a X_1^b X_2^c + d X_3 \quad (5.32)$$

$$\hat{Y} = a e^{(b X_1)} X_2^c X_3^d \quad (5.33)$$

$$\hat{Y} = a e^{(b X_1)} (X_2 X_3)^c \quad (5.34)$$

$$\hat{Y} = a X_1^b e^{(c X_2 + d X_3)} \quad (5.35)$$

$$\hat{Y} = a e^{(b X_1 + c X_2 + d X_3)} \quad (5.36)$$

It is also possible to approximate the interaction equation 5.23 by expanding it to a third degree polynomial (Appendix B):

$$\hat{Y} = a + b \Phi + c \Phi^2 + d \Phi^3 \quad (5.37)$$

in which Φ is Yamaki's elastic parameter ($X_1^{-1.25} X_2^{0.5} X_3$).

Equations 5.23, 5.24 (Group 1) and 5.30 to 5.37 (Group 2) are the proposed nonlinear models for inelastic shear buckling. The values of the constants a , b , c , and d are determined from a

regression analysis on the total data set shown in Table 5.1, which includes both the test results and the finite element parametric study results, and are listed in Table 5.3. By examining the correlation factor r^2 in Table 5.3, it can be seen that the proposed nonlinear models are more successful than most of the linear models. In particular, Eqs. 5.30, 5.31, and 5.33 are the most accurate models of the nonlinear groups. However, the values of r^2 have not increased to an acceptable degree of accuracy. This is due to the inclusion of the finite element data in the total set.

5.4. Regression of the Experimental Data

Regression analysis assumes that the least squares assumptions of normality, independence, and common variance are valid within the data set. When these assumptions are satisfied, the least squares estimates are the best (i.e. have the minimum variance) among all possible estimates. In reality, these assumptions hold only approximately (Rawling, 1988). Violating these assumptions may seriously affect the estimates of the regression, unless proper corrections are made.

Normality, the assumption that the residual errors are normally distributed, is valid in most practical cases. In the shear buckling problem, the major causes of residual errors are the random imperfections, the residual stresses, and the testing procedures. These factors are likely to have symmetrically bell-shape distributed errors. Even if the normality condition is not satisfied, the least squares estimates are still the best unbiased estimates if the other

assumptions are met. However, the tests of significance are affected by non-normality and would generally be incorrect.

The independence assumption means that, for a certain set of X-variables, there is no relationship between the residual errors. This assumption is satisfied in the data set of Table 5.1 since the variables X1, X2, and X3 are independent.

The common variance assumption requires that all the residual errors have the same variance S^2 , which also implies that every observation contains the same amount of information (Rawling, 1988). This assumption is violated in the regression of the data set of Table 5.1, mainly because of the existence of two types of data, numerical, and experimental. Finite element analysis is a deterministic method of analysis: in other words, it calculates a unique value of the shear capacity for a certain set of variables X1, X2, and X3. On the other hand, physical testing is subject to other factors (such as the random measuring errors) that contribute to the response beside these three variables. These errors cannot be modeled and this causes the numerical and the experimental sets to have different variance. Heterogeneous variance causes the least squares method to lose precision in the estimates and consequently to show poor accuracy. The remedy for this problem is to use one type of data.

Since the experimental data are believed to contain more information about the actual problem, the above discussion suggests that the finite element records be eliminated from the data set used

in order to satisfy the least squares assumptions. The number of records left (17 data records) may not be large enough to represent the whole population, but it is more consistent than the mixed data used in Section 5.3. Using the same linear and nonlinear models described in Section 5.3, the regression constants and the correlation factor of the regression of the experimental data are calculated and listed in Tables 5.4 and 5.5.

The first observation from Tables 5.4 and 5.5 is that a high level of correlation is achieved for both the multiple linear model (Eq. 5.19) and the nonlinear models, as demonstrated by the high values of r^2 (0.795 to 0.954). This is mainly due to the consistency of the data used. Comparison with the constants of Table 5.2 and 5.3 shows that some models, namely 5.15, 5.19, 5.32, and 5.35, changed drastically when a subset of the data is used. This sensitive dependency on the subset of the data decreases the confidence of the model. The other models were less sensitive and have more conservative predictions of the shear capacity when the experimental data were used alone. This is favorable from the design point of view. Models 5.12, 5.19, 5.30, 5.31, 5.33, and 5.34 have high values of r^2 for the regression of both the whole data and the experimental data, while model 5.37, based only on experimental data, has the best value of r^2 .

Among the equations in Tables 5.4 and 5.5, the best five are selected and re-examined in detail in order to select the one to represent the inelastic shear buckling capacity. Equations 5.19, 5.33, and 5.37 are chosen for their good accuracy. Equations 5.23 and 5.30 are also chosen; the former represents the interaction group and the

latter has the simplest form of all the models. Although Eqs. 5.12, 5.24, and 5.34 have good accuracy, they are similar to Eqs. 5.19, 5.23, and 5.33 and are less accurate. Thus, the equations selected are (renumbered):

$$\hat{Y} = 0.455 + 2.13 (10)^{-3} X_1 - 1.27 (10)^{-5} X_1^2 + 5.8(10)^{-4} X_2 X_3 + 4 (10)^{-8} X_2^2 X_3^2 \quad (5.38)$$

$$\hat{Y} = \{ 1 + (3^{0.5}(0.74 X_1^{-1.25} X_2^{0.5} X_3))^{-2.2} \}^{-1/2.2} \quad (5.39)$$

$$\hat{Y} = -0.98 + 4.24 \Phi - 3.383 \Phi^2 + 0.933 \Phi^3 \quad (5.40)$$

$$\hat{Y} = 0.345 X_1^{0.488} X_2^{0.42} X_3^{0.522} \quad (5.41)$$

$$\hat{Y} = 0.050 e^{(-3.383 X_1)} X_2^{0.387} X_3^{0.520} \quad (5.42)$$

Choosing one equation from these five equations cannot be based solely on the value of r^2 . Two other factors need to be examined; the behavior of the model outside the range of the independent variables used in the regression, and the scatter of the data about the regression model.

As already noted, the regression model best estimates the response in the range of the data upon which it was based. If the model is close to the physical behavior of the true problem, it should not predict unexpected physical response outside the range as well. The five equations are therefore plotted against the three independent variables R/t , R/L , and E/σ_y in Figs. 5.3, 5.4, and 5.5, respectively. Equation 5.38 unreasonably underestimates the response for thickness ratios outside the data range (125 to 250) and

over-estimates the response for aspect ratios above 1.5. Equation 5.39 has the closest shape to the physical problem outside the data range, as expected from any interaction equation. Equation 5.40 is unrealistic for $R/t < 100$ and $R/t > 350$. Equations 5.41 and 5.42 are reasonable except for low R/t ratios, where they over-estimate the response. This is especially true for Eq. 5.41.

One way of showing the scatter of the data around the regression line is to plot the predicted capacity ratio (\hat{Y}) versus the measured capacity ratio (Y). These plots are shown in Figs. 5.6 through 5.11 for the five equations 5.38 through 5.42, as well as for Galletly's equation 5.22. The plots are not different enough to be able to discriminate among them visually. The following gauges are suggested to rank the data scatter:

$$E_i = 100 \left(\frac{\hat{Y}_i - Y_i}{Y_{\text{yield}}} \right) \quad (5.43)$$

$$E_{\text{avg}} = \frac{1}{m} \sum_{i=1}^m |E_i| \quad (5.44)$$

$$E_{\text{max}} = \text{maximum} \{E_i\} \quad (5.45)$$

$$E_{\text{min}} = \text{minimum} \{E_i\} \quad (5.46)$$

$$S_{y/x} = \sqrt{\frac{\sum_{i=1}^m (\hat{Y}_i - Y_i)^2}{m - n}} \quad (5.47)$$

where Y_i = the shear capacity ratio for the "i" record of the experimental data set;

- E_i = the residual error as a percentage of the shear yield capacity of the cylinder;
- E_{avg} = the average of the absolute value of E_i -values;
- E_{max} = the maximum value of E_i -values;
- E_{min} = the minimum value of E_i -values;
- n = number of regression constants;
- m = number of observations; and
- $S_{y/x}$ = the standard error of estimate of the regression equation \hat{Y} measured in the same units of the dependent variable Y .

The first four gauges are direct error measurements, while the last one is a statistical measurement. If the errors are assumed to have a normal distribution probability function with zero mean and variance, then the probability of having data points less or more than that predicted by \hat{Y} can be calculated (Berenson et al., 1983). For example, the probability of having cylinders with shear capacity less than $\hat{Y} - 2S_{y/x}$ is 95.44% at the mean of the data. If $2S_{y/x}$ is small, the data will be close to the regression, and vice versa. Therefore, $2S_{y/x}$ can be taken as a measure of the data scatter about the regression equation. The values of these gauges, Eqs. 5.43 to 5.47, are listed in Table 5.6 for the five regression models. The most accurate model is Eq. 5.40 and the poorest is Eq. 5.39. However, the difference between them is not very large.

Equations 5.38 and 5.40, although they have the best accuracy, do not simulate the true shear capacity outside the range of X -variables, as shown in Fig. 5.3. They anticipate negative capacity for

larger values of R/t and a puzzling decrease or increase for the smaller values of R/t . These equations are also sensitive to any change in the data set, as can be seen from the values of the constants in Tables 5.2 and 5.4. In contrast, Eq. 5.39 behaves ideally outside the range of the X -values, as expected, but it has the poorest accuracy of the five models: $r^2 = 0.83$, $E_{avg.} = 5\%$ and $2S_{y/x} = 13.3\%$. Equations 5.41 and 5.42 are very close to each other, with the latter slightly more conservative and slightly more accurate. Both provide reasonable estimates of the shear capacity outside the range of X -variables except for R/t ratios less than 100, where they tend to over-estimate it.

In conclusion, Eq. 5.42 is considered the best regression model because it has good accuracy as well as reasonable predictions within the overall range of the independent variables. Galletly's predictor equation (Eq. 5.22) is also presented in Table 5.6 for comparison with the regression models. Equation 5.42 has an error range (E_{min} to E_{max}) of -7.5% to 11.8% , whereas Galletly's equation has a wider range, -11.6% to 14.7% . Equation 5.42 has an accuracy factor (r^2) of 0.91 and a scatter factor ($2S_{y/x}$) of 0.11, whereas the corresponding factors for Galletly's equation are 0.80 and 0.14.

5.5 Shear Capacity Equation

The currently used formula for identifying the inelastic shear capacity of transversely loaded cylinders is the quadratic interaction equation suggested by Galletly and Blachut (Eq. 5.22). This equation, although empirically based, is not the best fit for the group of tests

upon which it was based. In this chapter, a best fit regression model for all the available shear buckling physical tests has been determined as:

$$\frac{V_{\max}}{V_y} = 0.05 e^{(-0.0033 \frac{R}{t})} \left(\frac{R}{L}\right)^{0.387} \left(\frac{E}{\sigma_y}\right)^{0.52} \quad (5.48)$$

In addition, the maximum shear force resisted by the cylinder according to Eq. 5.48 should not exceed the yield shear force or the elastic buckling shear force:

$$\frac{V_{\max}}{V_y} < 1.0 \quad (5.49)$$

$$\frac{V_{\max}}{V_y} < \frac{\tau_e \pi R t}{V_y} \quad (5.50)$$

Where τ_e is the elastic buckling shear stress for cylinders under transverse loads as calculated from Eq. 2.15.

The predictions of Eq. 5.48 are most accurate within the following ranges:

$$125 < \frac{R}{t} < 250 \quad (5.51(a))$$

$$0.5 < \frac{R}{L} < 1.4 \quad (5.51(b))$$

$$450 < \frac{E}{\sigma_y} < 850 \quad (5.51(c))$$

Figure 5.12 shows the finite element results relative to equation 5.48. Clearly, the proposed design equation is a lower bound

on the best available theoretical prediction in addition to its excellent performance relative to the available test data.

Equation 5.48, which has better accuracy than Galletly's equation, is the empirical equation recommended for the determination of the inelastic shear buckling capacity of thin-walled fabricated steel cylinders under transverse loading.

Data		X1	X2	X3	Y	
Experimental data	Specimen S	Specimen S1	185	0.53	645	0.64
		Specimen S2	185	0.76	643	0.71
	Galletly's tests	Specimen B1	250	0.50	679	0.38
		Specimen G1	188	1.00	673	0.87
		Specimen G2	188	1.00	673	0.83
		Specimen G3	150	1.00	841	1.00
		Specimen G4	150	1.00	841	0.99
		Specimen G5	125	1.00	704	1.02
		Specimen G6	125	1.00	704	0.98
		Specimen G7	150	1.00	457	0.71
		Specimen G8	150	1.00	457	0.76
		Specimen G9	125	1.00	547	0.79
		Specimen G10	125	1.00	547	0.87
		Specimen G11	126	1.37	533	0.94
		Specimen G12	151	1.37	457	0.80
Specimen G13		129	0.83	533	0.83	
Specimen G14	155	0.83	457	0.72		
Finite Element data	Model M1-S	Model M1-S1	188	0.53	645	0.64
		Model M1-S2	188	0.76	643	0.80
	Model M1-B1	250	0.50	679	0.50	
	Model MF1	150	1.00	667	0.94	
	Model MF2	150	0.75	667	0.85	
	Model MF3	150	0.50	667	0.73	
	Model MF4	188	1.00	667	0.90	
	Model MF5	188	0.75	667	0.81	
	Model MF6	188	0.50	667	0.71	
	Model MF7	250	1.00	667	0.89	
Model MF8	250	0.75	667	0.83		
Model MF9	250	0.50	667	0.73		

Table 5.1 Variables of the regression data set

Eq. number	<i>a</i>	<i>b</i>	<i>c</i>	<i>d</i>	<i>e</i>	<i>r</i> ²
Eq. 5.6	1.129	-0.002	---	---	---	0.300
Eq. 5.7	0.457	0.400	---	---	---	0.459
Eq. 5.8	0.575	3.50E-4	---	---	---	0.058
Eq. 5.9	0.673	-8.70E-4	0.319	---	---	0.503
Eq. 5.10	0.807	-2.30E-3	6.20E-4	---	---	0.466
Eq. 5.11	-0.046	0.48	6.90E-4	---	---	0.661
Eq. 5.12	0.205	-1.20E-3	0.376	7.60E-4	---	0.739
Eq. 5.13	0.608	1.30E-3	---	---	---	0.121
Eq. 5.14	0.957	-1.40E-6	---	---	---	0.115
Eq. 5.15	0.391	7.60E-4	---	---	---	0.698
Eq. 5.16	0.593	2.30E-6	---	---	---	0.189
Eq. 5.19	0.476	-1.46E-3	1.55E-6	1.33E-3	-5.87E-7	0.766

Table 5.2 Regression constants of the linear models based on all data records

Eq. number	<i>a</i>	<i>b</i>	<i>c</i>	<i>d</i>	<i>r</i> ²
Eq. 5.23	2.5040	---	---	---	0.644
Eq. 5.24	2.1512	---	---	---	0.644
Eq. 5.30	0.0945	-0.2334	0.4094	0.5288	0.765
Eq. 5.31	0.1290	-0.1909	0.4478	---	0.756
Eq. 5.32	4.3932	-0.4386	0.7250	0.0006	0.712
Eq. 5.33	0.0366	-0.0013	0.4104	0.5256	0.764
Eq. 5.34	0.0584	-0.0011	0.4477	---	0.755
Eq. 5.35	1.1878	-0.2574	0.4442	0.0008	0.716
Eq. 5.36	0.4083	-0.0014	0.4459	0.0008	0.715
Eq. 5.37	-0.1717	2.3313	-1.8804	0.5440	0.677

Table 5.3 Regression constants of the nonlinear models based on all data records

Eq. number	<i>a</i>	<i>b</i>	<i>c</i>	<i>d</i>	<i>e</i>	<i>r</i> ²
Eq. 5.6	1.369	-3.55E-3	---	---	---	0.564
Eq. 5.7	0.371	0.464	---	---	---	0.427
Eq. 5.8	0.550	4.32E-4	---	---	---	0.114
Eq. 5.9	1.025	-2.65E-3	0.214	---	---	0.619
Eq. 5.10	1.041	-4.10E-3	6.80E-4	---	---	0.835
Eq. 5.11	-0.111	0.548	6.60E-4	---	---	0.679
Eq. 5.12	0.581	-3.02E-3	0.273	7.29E-4	---	0.923
Eq. 5.13	0.648	1.10E-3	---	---	---	0.044
Eq. 5.14	0.974	-1.66E-6	---	---	---	0.110
Eq. 5.15	0.329	-8.42E-4	---	---	---	0.722
Eq. 5.16	0.578	2.70E-6	---	---	---	0.170
Eq. 5.19	0.455	2.13E-3	-1.27E-5	5.84E-4	4.00E-8	0.940

Table 5.4 Regression constants of the linear models based on experimental data

Eq. number	<i>a</i>	<i>b</i>	<i>c</i>	<i>d</i>	<i>r</i> ²
Eq. 5.23	2.2040	---	---	---	0.830
Eq. 5.24	1.9370	---	---	---	0.795
Eq. 5.30	0.3446	-0.4883	0.4218	0.5215	0.894
Eq. 5.31	0.3545	-0.4399	0.4796	---	0.888
Eq. 5.32	43.200	-0.8950	0.6250	0.0005	0.821
Eq. 5.33	0.0493	-0.0033	0.3873	0.5202	0.912
Eq. 5.34	0.0652	-0.0028	0.4672	---	0.902
Eq. 5.35	5.9040	-0.5714	0.3802	0.0008	0.863
Eq. 5.36	0.6174	-0.0037	0.3473	0.0008	0.887
Eq. 5.37	-0.9799	4.2390	-3.3830	0.9332	0.954

Table 5.5 Regression constants of the nonlinear models based on experimental data

Test	E_i /Eq.5.38	E_j /Eq.5.39	E_k /Eq.5.40	E_l /Eq.5.41	E_m /Eq.5.42	E_n /Eq.5.22
Specimen S1	-2.61	3.76	-1.08	-4.07	-3.20	1.66
Specimen S2	-0.65	3.32	1.88	-1.49	-1.35	0.98
Specimen B1	1.79	16.14	0.41	14.10	11.76	14.70
Specimen G1	-4.79	-6.43	-6.65	-6.87	-7.46	-8.78
Specimen G2	-0.81	-2.35	-2.66	-2.88	-3.47	-4.80
Specimen G3	0.91	-8.04	-3.38	0.06	0.62	-10.03
Specimen G4	2.30	-6.66	-1.99	1.45	2.00	-8.65
Specimen G5	-6.96	-9.72	-0.19	-2.73	-2.93	-11.63
Specimen G6	-2.80	-5.56	3.97	1.43	1.22	-7.47
Specimen G7	5.60	6.03	5.38	1.92	2.38	3.63
Specimen G8	0.57	1.01	0.36	-3.11	-2.65	-1.39
Specimen G9	6.30	9.02	7.38	8.19	8.04	6.74
Specimen G10	-1.49	1.22	-0.42	0.40	0.25	-1.05
Specimen G11	2.76	-3.68	-3.41	3.81	2.65	-5.79
Specimen G12	6.85	1.58	1.19	2.80	2.42	-0.87
Specimen G13	-4.47	1.43	0.50	-4.52	-3.96	-0.99
Specimen G14	-0.94	0.41	-1.88	-5.52	-4.69	-1.87
Galletly's scaled tests						
E_{min} %	6.85	16.14	7.38	14.10	11.76	14.70
E_{max} %	-6.96	-9.72	-6.65	-6.87	-7.46	-11.63
E_{avr} %	3.09	5.07	2.51	3.84	3.59	5.35
$2 S_{y/1}$	0.091	0.133	0.076	0.116	0.105	0.140
r^2	0.94	0.83	0.95	0.89	0.91	0.80

Table 5.6 The error measurements of Eqs. 5.38 to 5.42 and of Galletly's equation 5.22

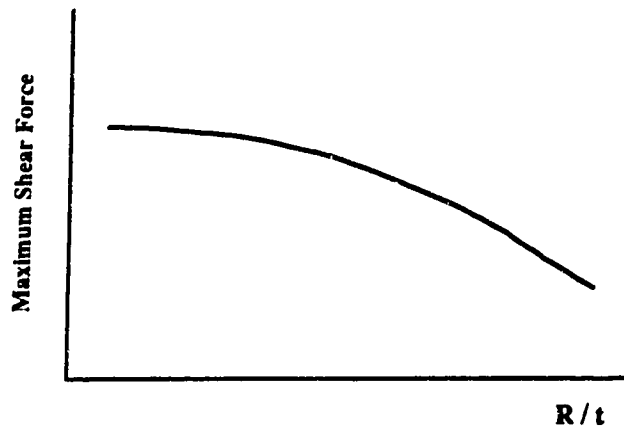


Fig. 5.1 The general shape of the shear capacity vs R/t

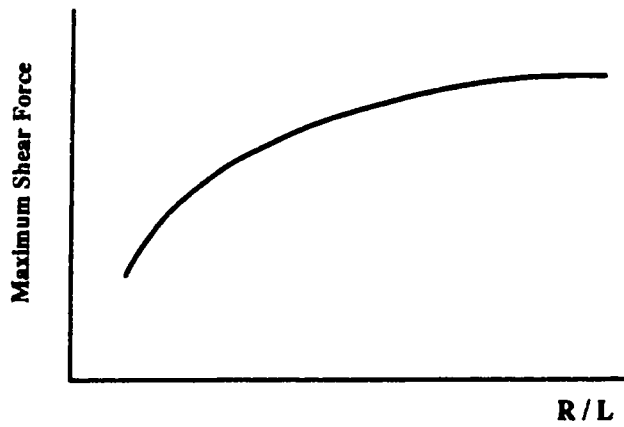


Fig. 5.2 The general shape of the shear capacity vs R/L

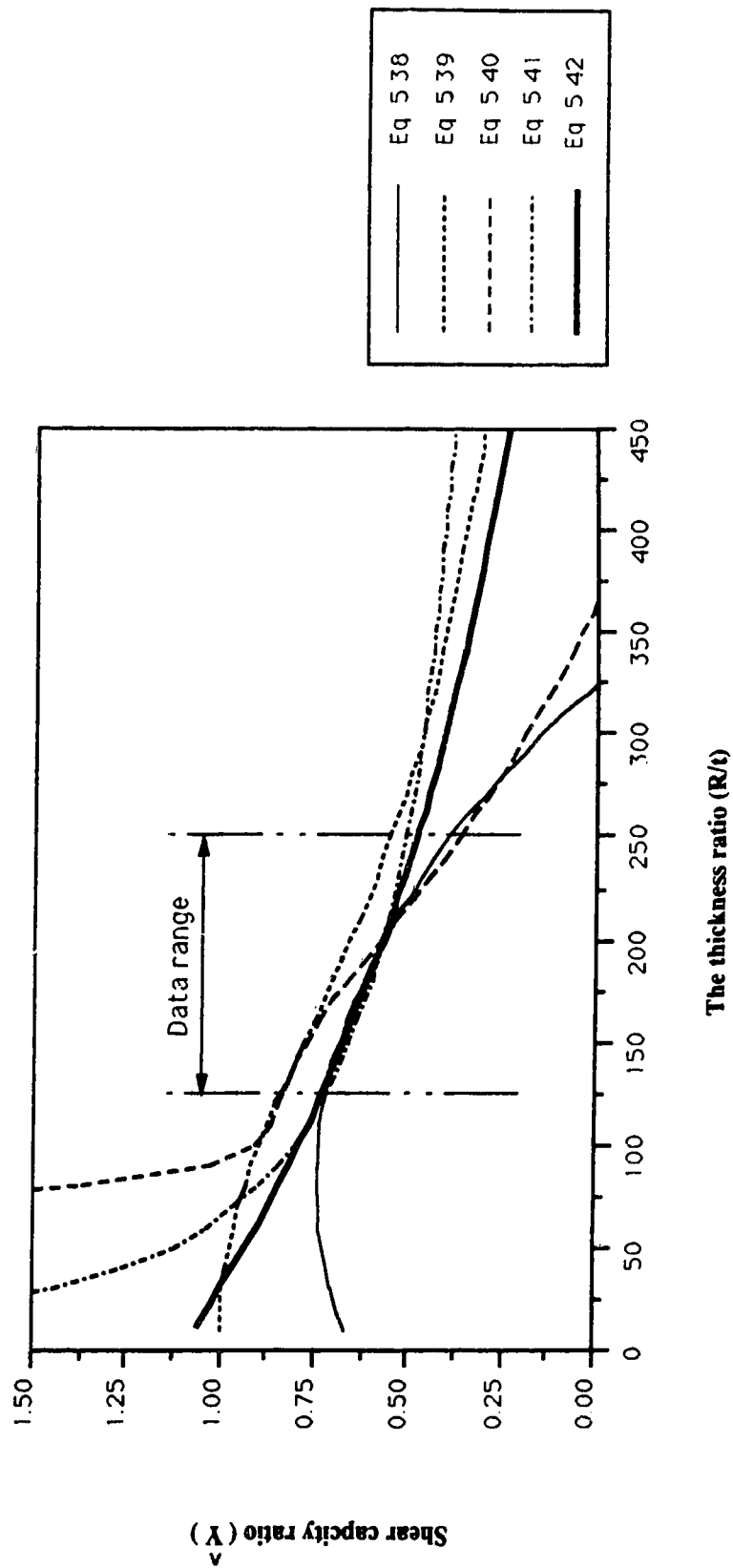


Fig. 5.3 Predictions of the regression models for different R/t

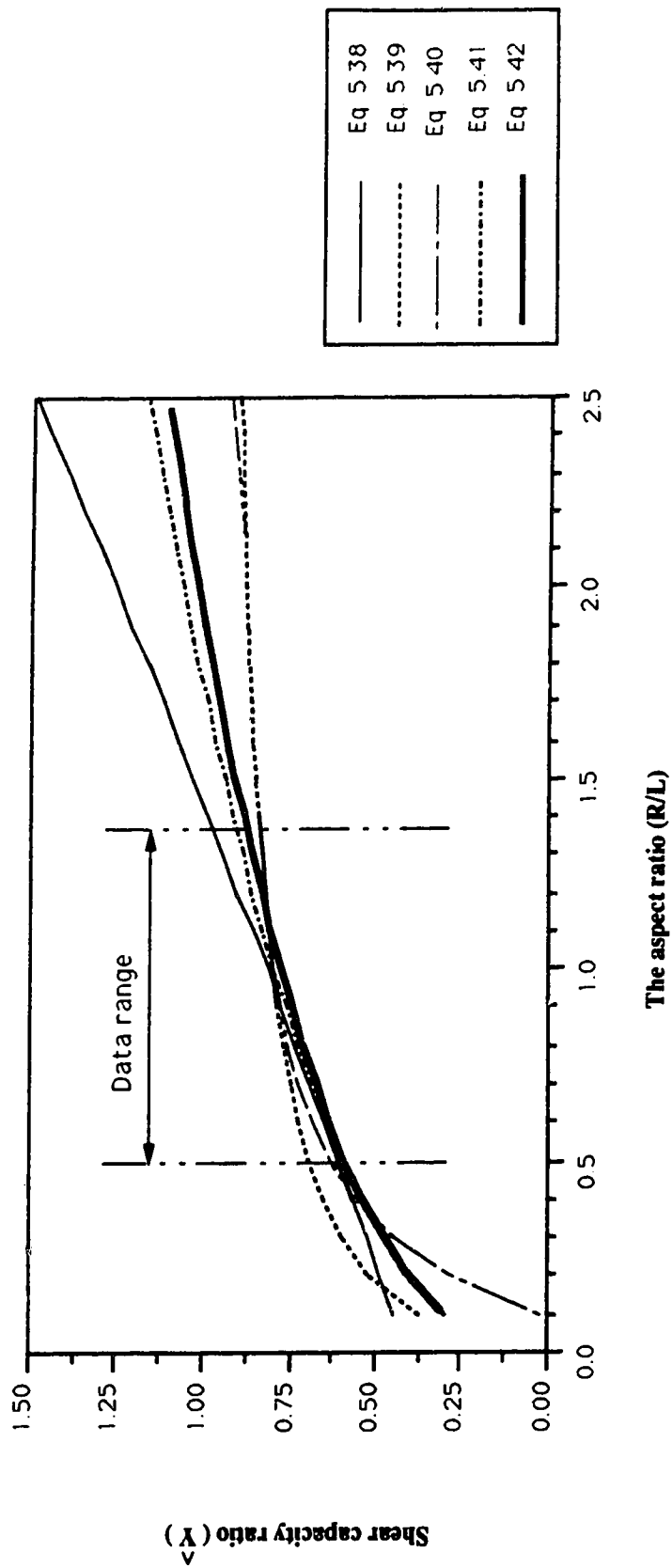


Fig. 5.4 Predictions of the regression models for different R/L

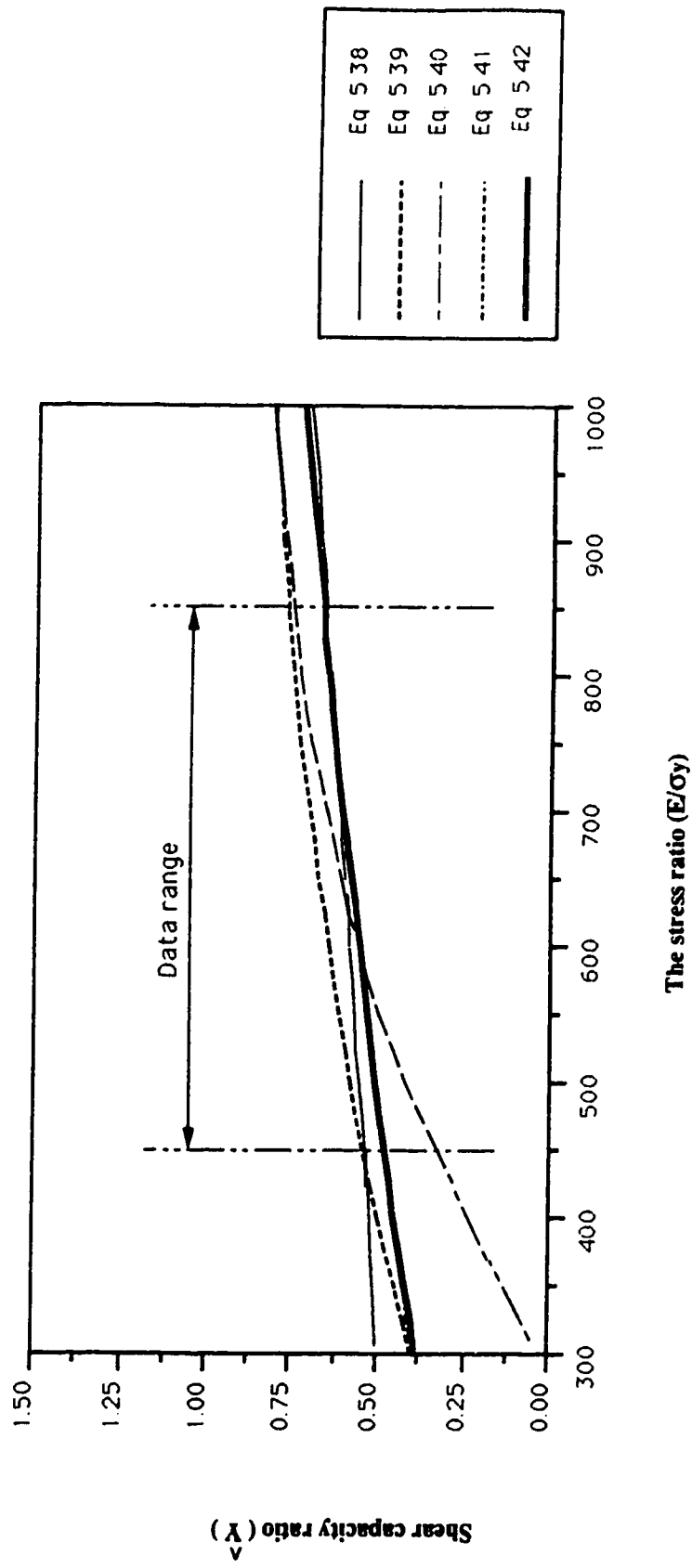


Fig. 5.5 Predictions of the regression models for different E/Oy

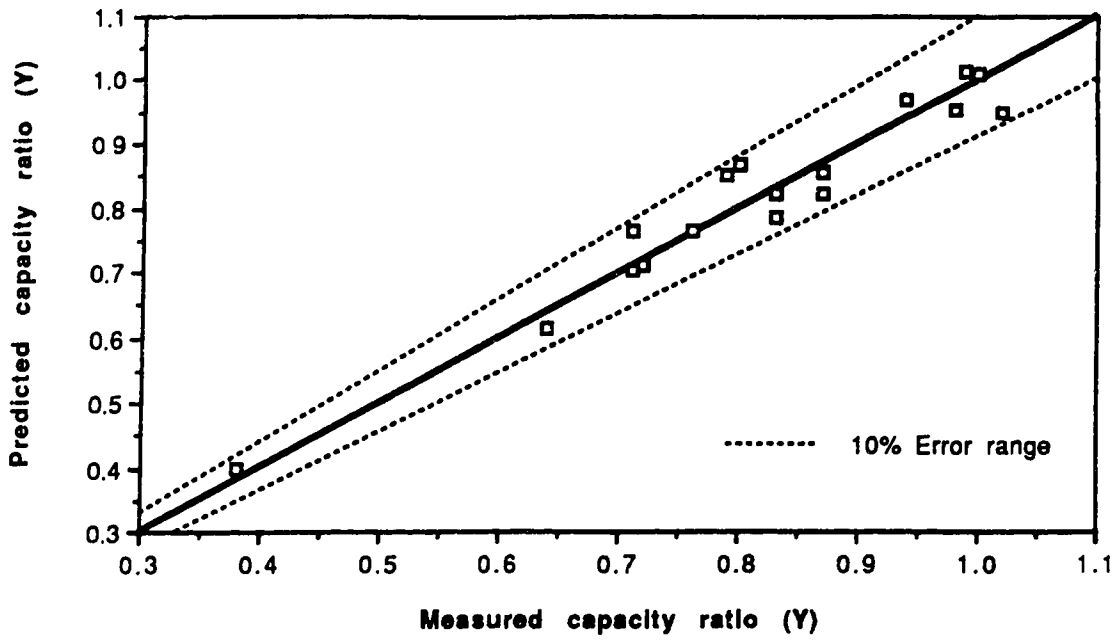


Fig. 5.6 Scatter of the test data about the regression Eq. 5.38

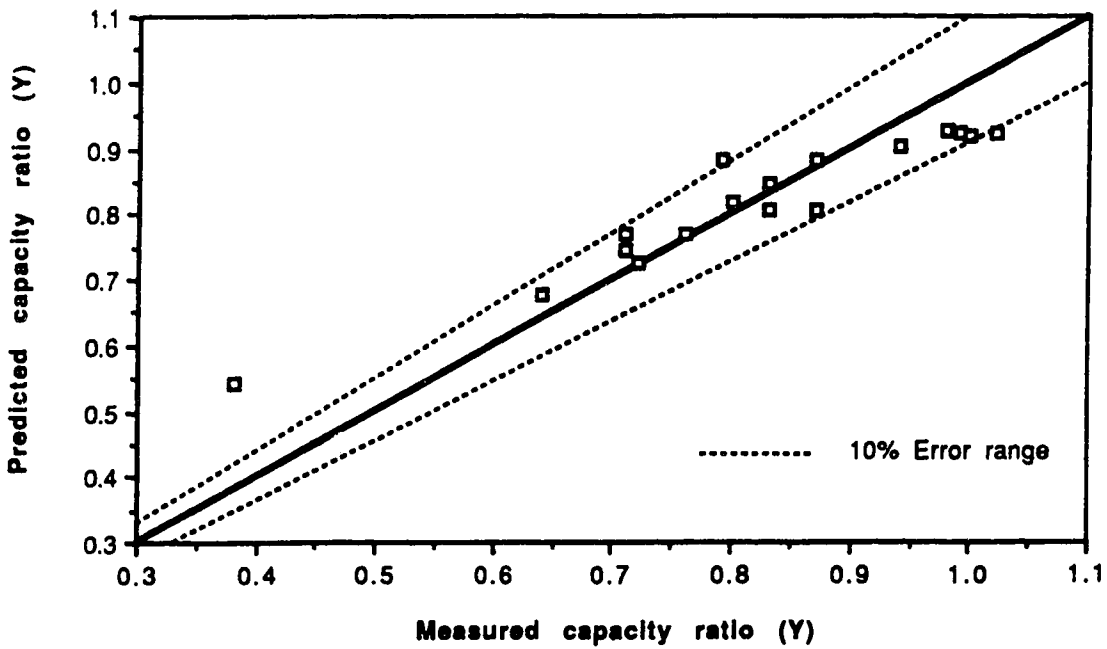


Fig. 5.7 Scatter of the test data about the regression Eq. 5.39

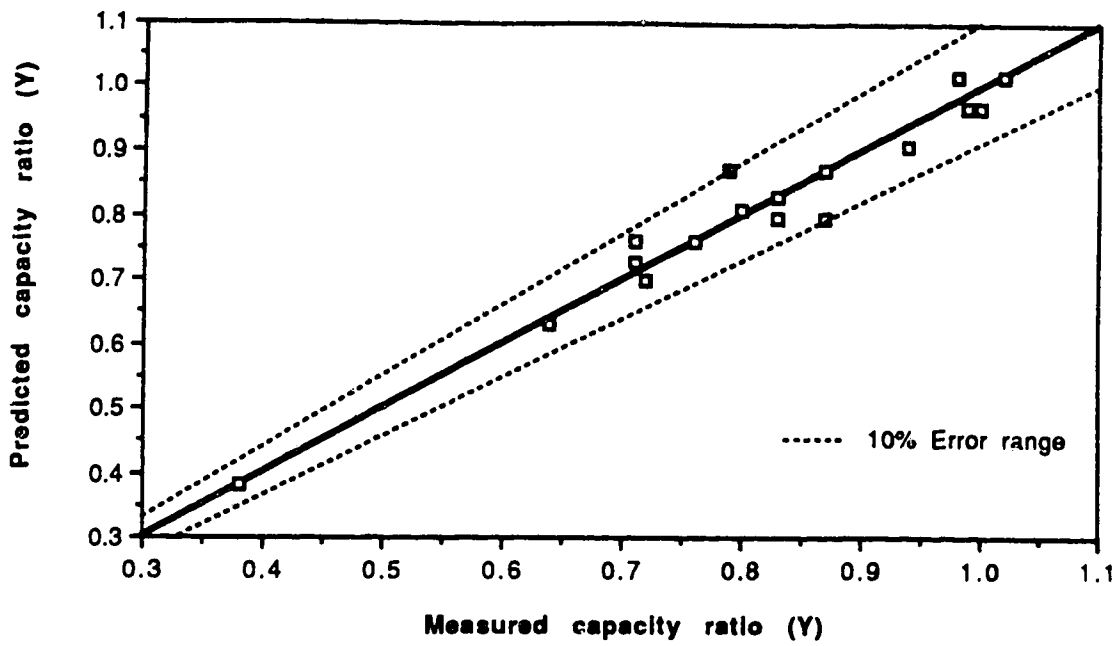


Fig. 5.8 Scatter of the test data about the regression Eq. 5.40

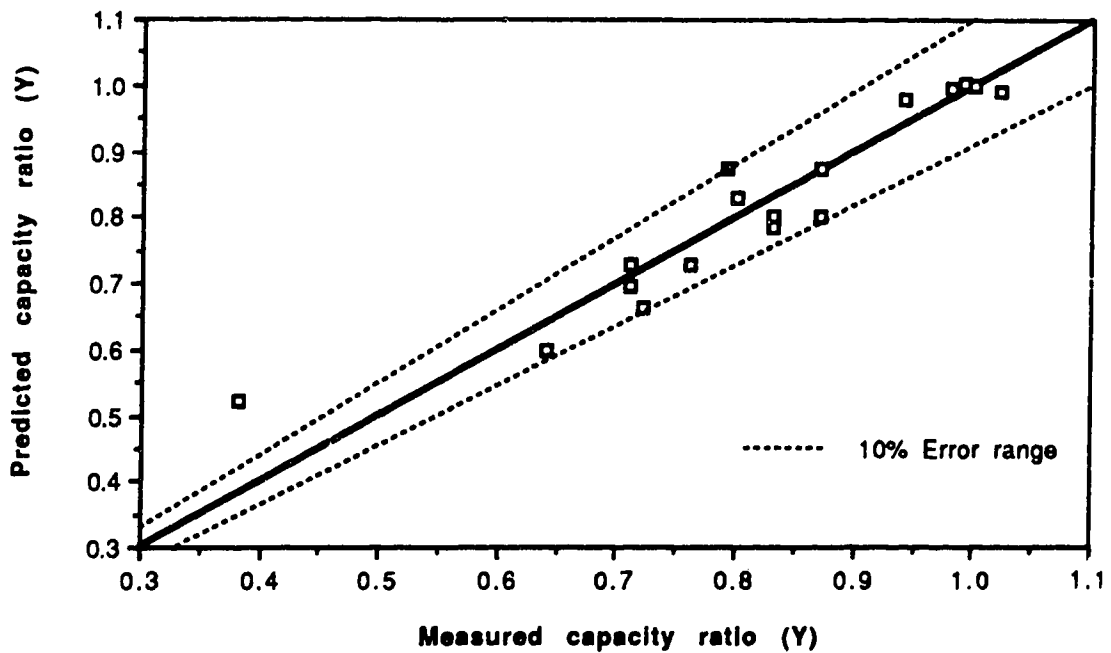


Fig. 5.9 Scatter of the test data about the regression Eq. 5.41

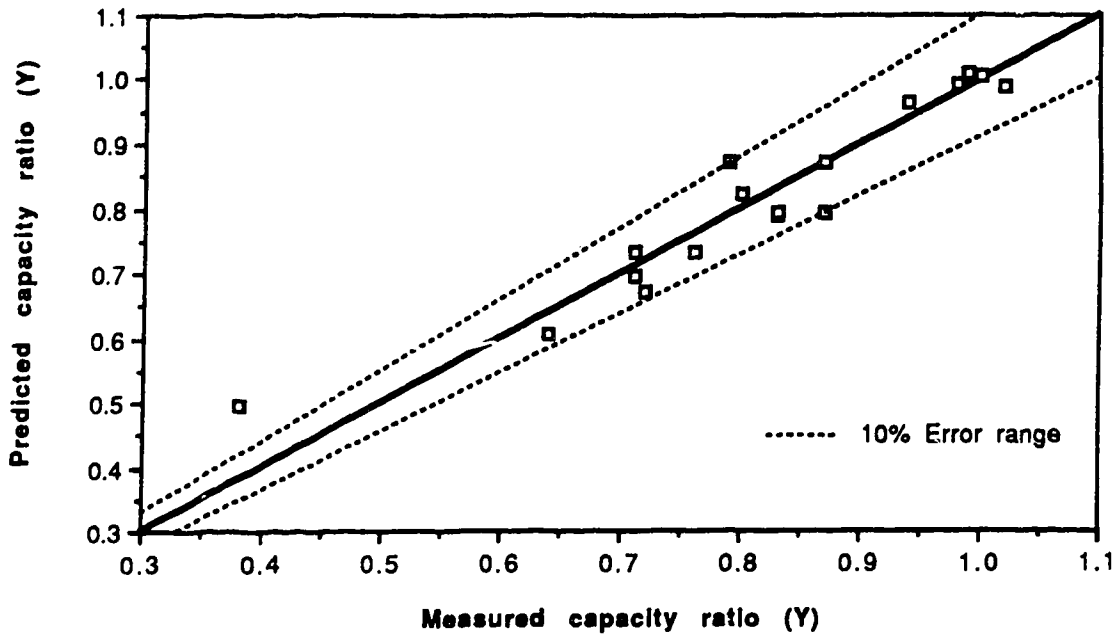


Fig. 5.10 Scatter of the test data about the regression Eq. 5.42

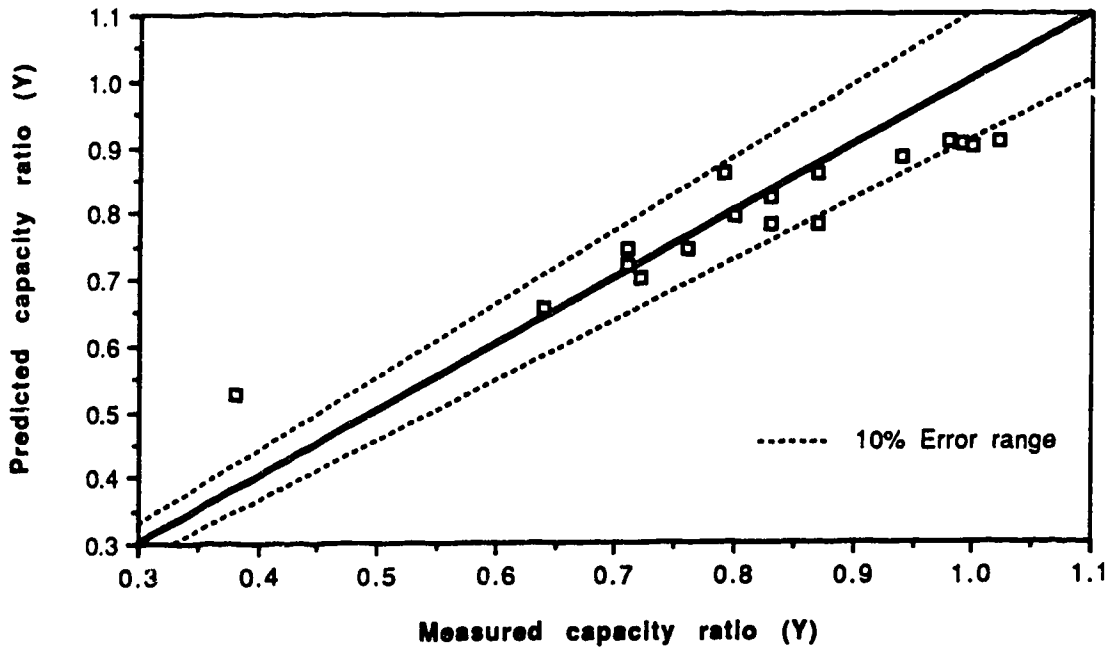


Fig. 5.11 Scatter of the test data about Galletly's equation 5.22

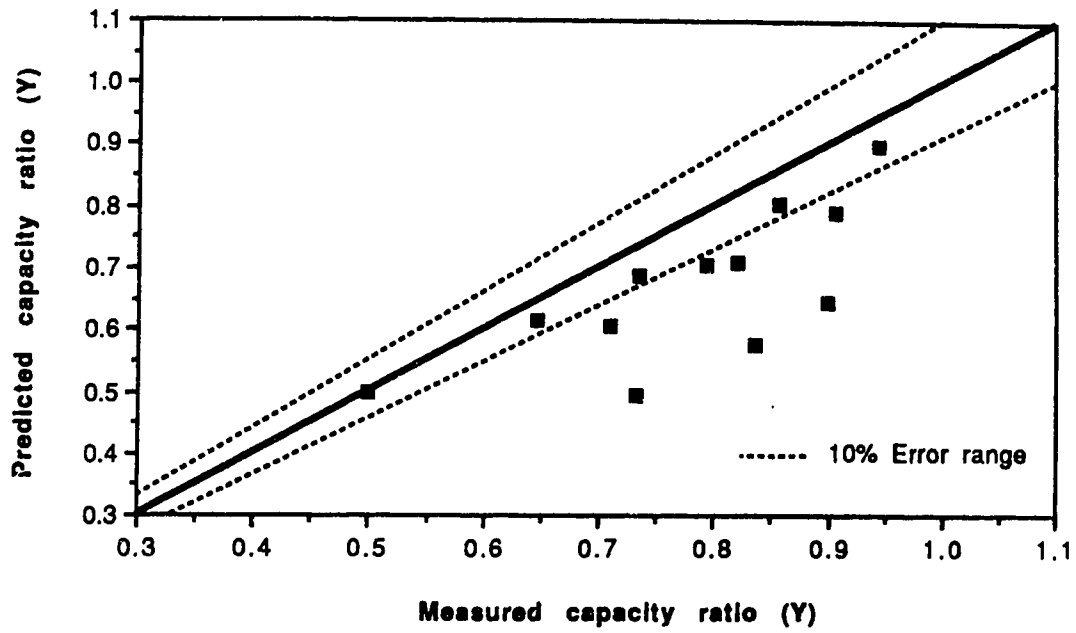


Fig. 5.12 Scatter of the finite element data about the regression Eq. 5.48

6. A Truss Model for the Post-Buckling Shear Capacity

6.1 Introduction

Prediction of the maximum shear capacity of cylinders under transverse loading, based on experimental, numerical and empirical studies, has been reported in the previous Chapters. Both the experimental and the numerical studies showed that there is significant secondary strength after buckling. This strength, which of course is lower than the buckling strength, can be utilized as a conservative estimate of the shear capacity of cylinders.

The shear tests of transversely loaded cylinders that were carried out in the post-buckling region, B1 and B2 (Bailey and Kulak, 1984) and S1 and S2 (Chapter 3), demonstrated a common post-buckling pattern. An example of the load-displacement relationship obtained during these tests is shown in Fig. 6.1. As the load reaches the buckling strength, diagonal buckles appear in the center of the shear span and the load level drops. After buckling, the load remains constant as the deformation of the cylinder increases in the plastic range.

There are similarities between the post-buckling behavior of thin-walled cylinders and that of plate girders. The buckled shape of plate girders and cylinders under transverse load is displayed in Figs. 6.2a and 6.2b, respectively. When a plate girder buckles in shear, truss action evolves to carry some of the shearing force. In this truss action, the tensile forces in the direction of the buckles are

carried by membrane action of the web and the compressive vertical and horizontal forces are carried by the stiffeners and the flanges. Similarly, when a cylinder buckles in shear, tensile membrane forces develop in the direction of the buckles. The vertical component of these diagonal forces is taken by the circumferential stiffeners or by the end diaphragm, while the horizontal component is resisted by compressive membrane forces in the direction opposite to the buckles.

Although the tension field mechanism in plate girders has been studied by many researchers (a summary of which is reported in Structural Stability Research Council Guide, 1988), few such studies have been identified in the case of thin-walled cylinders. Tension field action in cylinders was first observed by Bailey and Kulak (1984). Later, Mok and Elwi (1986) and Roman and Elwi (1987) attempted to predict the post-buckling capacity of one of the Bailey and Kulak tests by using the tension field action. In the following sections, a brief review and discussion of these studies is presented, and a general truss model for the shear buckling capacity of thin-walled cylinders is proposed and verified.

6.2 Tension Field Models for Thin-Walled Cylinders

When Bailey and Kulak (1984) tested two thin-walled cylinders (B1 and B2) under transverse loading, they noticed that the specimens had a buckle pattern similar to that of plate girders. As a result, they tried to adopt the tension field theory of plate girders to fit thin-walled cylinders. Bailey and Kulak assumed that a diagonal

tension field developed in the cylinder after buckling and that it was anchored in the vertical sides of the shear span, as illustrated in Fig. 6.3. They also assumed that this tension field had a constant tensile stress equal to the flexural buckling stress σ_{cr} . The slope of the tension field (ζ) was calculated by replacing the panel height and length in the corresponding plate girder equation for tension field slope (Salmon and Johnson, 1990) by the cylinder diameter ($2R$) and shear span (L). According to Bailey and Kulak, the shear strength (T_v), the arc width (ψ), and the slope (ζ) of the tension field are expressed in terms of the cylinder dimensions and the flexural buckling stress as follows:

$$T_v = 2 R t \sigma_{cr} (1 - \cos \psi) \sin \zeta \quad (6.1)$$

where $\psi = \pi - \cos^{-1} \left(1 - \frac{L}{R} \tan \zeta \right)$

$$\zeta = \frac{1}{2} \tan^{-1} \left(\frac{2L}{R} \right)$$

and σ_{cr} is the critical buckling stress in flexure (Stephens et al., 1981) and all other terms are shown in Fig. 6.3. Comparison of predictions made using Eq. 6.1 with the two tests available (B1 and B2), led Bailey and Kulak to conclude that an improved shear strength predictor equation would depend on R/t ratio. They subsequently proposed the following format:

$$V_u = k_{11} T_v \quad (\text{high } R/t \text{ ratio}) \quad (6.2)$$

$$V_u = k_{12} T_v + k_{y1} T_y \quad (\text{intermediate } R/t \text{ ratio}) \quad (6.3)$$

$$V_u = k_{y2} T_y \quad (\text{low } R/t \text{ ratio}) \quad (6.4)$$

where V_u is the ultimate shear strength of the cylinder, T_v the tension field shear strength, T_y the yield strength of the cylinder and k_{t1} , k_{t2} , k_{y1} , and k_{y2} are functions of R/t ratio and the material properties. The first term in Eq. 6.3 is referred to as the "tension field shear" part, whereas the second term is called the "beam shear" part.

Mok and Elwi (1986) adopted Eq. 6.3 as a shear buckling formula for the B1 test and attempted to evaluate the tension field and the beam shear parts. Their assumptions regarding the shape, the slope, and the stress distribution of the tension field were the same as those of Bailey and Kulak. However, they calculated the tension field stress σ_t differently. Whereas Bailey and Kulak assigned the flexural buckling stress σ_{cr} to the tensile stress, Mok and Elwi determined it from a yield condition. They assumed that the cylinder buckles at a critical shear stress which is proportional to the elastic buckling shear stress (τ_{cr}) proposed by Batdorf et al. (1947). After buckling occurs, additional shear stress is carried by the tension field action. Assuming that the state of stress in the tension field reaches the Von Mises yield criterion, the tension field stress can then be determined. The components of Eq. 6.3 according to Mok and Elwi are:

$$K_{t2} = \left\{ 1 - \frac{\delta^2 \tau_{cr}^2}{\sigma_y^2} \left(3 - \frac{9}{4} \sin^2 2\zeta \right) \right\}^{\frac{1}{2}} - \frac{3 \delta \tau_{cr}}{2 \sigma_y} \sin 2\zeta \quad (6.5)$$

$$T_v = R t \sigma_y \left(2 - \frac{L}{R} \tan \zeta \right) \sin \zeta \quad (6.6)$$

$$K_{y1} = \sqrt{3} \frac{\delta \tau_{cr}}{\sigma_y} \quad (6.7)$$

$$T_y = \sqrt{3} \pi R t \sigma_y \quad (6.8)$$

where σ_y is the yield stress and δ is a reduction factor which is applied to the elastic buckling stress (τ_{cr}) to account for the effect of the initial imperfections. Mok and Elwi did not determine a specific value for δ , and therefore no comparison between Eq. 6.3 and the tests was made.

Several criticisms can be directed toward each of these models. The Bailey-Kulak model dealt with the cylinder as a flat plate when calculating the angle of inclination of the tension field, ζ , neglected the compressive membrane forces, and used an ambiguous definition of the tension field stress, σ_t . Bailey and Kulak (1984) were not able to provide supportive evidence for their assumption about the tension field stress, while Mok and Elwi (1986) left the tension field stress as a function of the unknown factor δ .

Roman and Elwi (1987) used extensive finite element analysis of the first shear test of Bailey and Kulak in order to develop a truss model which addressed these criticisms. The Roman-Elwi model, shown in Fig. 6.4, has a helix-shaped tension field and an equilibrating compression strut. The total shear capacity (V_{tm}) of the model is evaluated not only from the integration of the vertical component of the tension field (T_v), but also from the vertical component of the compression strut (C_v). In this model, it is assumed that the shear capacity after buckling is dependent on the tension

field action alone. In other words, the beam shear contribution is neglected.

To define the tensile stress σ_t , Roman and Elwi proposed two limiting bounds for the tensile stress in the tension field. The lower limit corresponds to a sinusoidal distribution of stress in the direction of the buckles accompanied by a cross-bending moment equal to the yield moment due to the deformations of the buckle waves. The upper limit corresponds to constant yield stress accompanied by cross-bending moment equal to the plastic moment. These limits are represented by a reduction factor (α) which is applied to the yield stress. The factor α is equal to 0.438 for the lower limit and 0.750 for the upper limit. The post-buckling shear strength of cylinders according to Roman and Elwi is described by the following equations:

$$V_{tm} = T_v + C_v \quad (6.9)$$

where $T_v = \alpha R t \sigma_y (1 - \cos \psi) \sin 2\zeta$

$$C_v = 2 \alpha R t \sigma_y \psi \frac{R}{L} (1 + \cos \psi) \cos^2 \zeta$$

$$\psi = \pi - \frac{L}{R} \tan \zeta$$

$$\zeta = \tan^{-1} \left(1 + \cos \left(\frac{L}{R} \tan \zeta \right) \right) \operatorname{cosec} \left(\frac{L}{R} \tan \zeta \right) \cos^2 \zeta$$

It can be demonstrated that the shear capacity of the truss model according to Eq. 6.9 is independent of the thickness ratio, R/t . This is not consistent with the test observations. The ratio of the

shear capacity calculated using the lower limit of Eq. 6.9 to that measured from the tests which have the same R/L ratio is 1.62 for B1 ($R/t = 250$), 1.04 for S1 ($R/t = 185$), and 0.78 for B2 ($R/t = 75$). The discrepancy is mainly due to the fact that the model is independent of the R/t ratio. Equation 6.9 does give satisfactory results within a narrow range of the R/t ratio, but it does not give good predictions over a broader range.

There are also some inconsistencies in the Roman-Elwi model regarding the definition of the compression strut. First, the strut (C), which is the resultant of the compressive membrane forces, and the resultant of the tension field (T) do not intersect at the same point on the circumferential stiffeners. Thus, the model violates equilibrium conditions. As shown in Fig. 6.4, the compression strut intersects the stiffener at angle equal to $(\pi - \psi)$, while the resultant of the tension field intersects the stiffeners at $(\psi / 2)$. Second, the stress concentration at one end of the strut is theoretically equal to infinity since the strut starts from the extreme point of the cross section. Finally, the slope of the tension field, ζ , was chosen to maximize the shear component of the tension field, T_v . This is a reasonable assumption in plate girders, where the compressive forces in the flanges do not contribute to the shear capacity. On the other hand, the shear capacity V_{tm} in Eq. 6.9 consists of two segments, T_v and C_v , and maximizing only one of them is not easily justifiable.

In summary, the concept of tension field action can be reasonably employed to determine the shear capacity of thin-walled cylinders in the post-buckling range. The tension field models which

are available do not satisfactorily predict the test results, however. An attempt to develop a tension field model which can address the deficiencies of the previous models and predict the shear capacity of thin-walled cylinders will be presented.

6.3 Proposed Truss Model

The models summarized in Section 6.2 were constructed to fit cylinders with fixed-end boundary conditions, such as the B1 and B2 tests of Bailey and Kulak. As discussed in Chapter 3, the bending moment distribution of the fixed-end test S1 along the shear span is sensitive to the support movements. It was also observed that even small deformations in the supporting elements change the bending moment significantly and that such deformations cannot be avoided. As a result, the degree of indeterminacy in the tests and the post-buckling models increases. To decrease the number of unknowns, and consequently the number of assumptions in the proposed model, the boundary conditions will be limited to simple and cantilever supports. For these cases, the middle of the shear span is susceptible to shear buckling while one end of the shear span is susceptible to local flexural buckling.

6.3.1 Assumptions

The truss model adopted in this study is illustrated in Fig. 6.5. The model consists of three main elements; the tension field that develops after buckling, the compression strut that must be present to balance the horizontal component of the tension field, and the circumferential stiffeners that support the vertical thrust of the

inclined force fields. In order to view the model in a two-dimensional plane, the cylinder is cut with a vertical plane and then unfolded as shown in Fig. 6.6. This two-dimensional plot will be referred to as the developed surface of the cylinder.

In the following, the basic aspects of behavior in the post-buckling range are discussed and the assumptions necessary to construct a truss model of the behavior are set out.

1. When a cylinder buckles in shear due to transverse loading, the ultimate shear capacity immediately drops to a lower load level and then stabilizes, as seen in Fig. 6.1. Such typical post-buckling behavior has been observed in all shear buckling tests (B1, B2, S1 and S2) which were continued into the post-buckling range. During buckling, the load-carrying mechanism changes from beam-type to truss-type in a way similar to that of plate girders except that the post-buckling capacity of cylinders is, herein, assumed to be dependent on the truss mechanism alone. An explanation of this observed behavior was offered by Roman and Elwi (1987). They suggested that outward shear buckles help develop the inclined tensile membrane forces while the inward buckles reduce these forces significantly due to the reduction in length of the buckles. With the increase of deformations in the post-buckling range this results in unloaded strips of forces, which in turn causes the beam-type shear to diminish.

2. After buckling, tensile forces are developed in approximately the same direction and location as the buckles. This field of forces has a helical shape, which means it appears as a straight strip on the developed surface of the cylinder (Love, 1944). This assumption is supported by the results of the finite element analyses (Chapter 4), which showed that the principal tensile forces in the post-buckling range always appear as straight, parallel rays. An example of these analyses is displayed in Fig. 6.7, where the principal forces in the post-buckling range are plotted on the developed surface of specimen S2.
3. Examination of Fig. 6.7 shows that the compression field is not as clearly defined as the tension field. The compressive principal forces at different points on the cylinder do not have the same slope, neither do they have a definable shape. However, the compression field can be replaced by an equivalent compressive strut in deriving the truss model capacity. This strut must be in equilibrium with the resultant of the tension field.
4. The compression and tension fields can receive anchorage only in the circumferential stiffeners. In other words, the unstiffened parts of the cylinder cannot provide anchorage to the inclined force fields. This behavior, which helps in defining the width of the force fields, was observed in the tests (Figs. 3.10, and 3.22) and it is also consistent with the numerical analysis (Fig. 6.7).

5. The stresses in the force fields are redistributed as the deformations increase until they reach maximum values—yield stress in tension and buckling stress in compression. As suggested by the finite element analyses (Chapter 4), the stresses in the tension field tend to be high at the crests of the buckles (yield value) and low at the valleys (almost zero value), creating banded strips of forces as shown in Fig. 6.7. Therefore, it is reasonable to assume that the stress distribution in the tension field has a sine wave variation as shown in Fig. 6.6. The number of buckles observed in tests S1 and S2 (Chapter 3) was three and thus, the stress distribution in Fig. 6.6 has also three waves. (Subsequent examination of the effect of the assumed number of waves on the truss model capacity showed that it is minimal). On the other hand, the stresses in the compression field at the support tend to intensify near the top of the cross section and diminish towards the neutral axis. The stresses in the compression field, therefore, are assumed to have a triangular distribution, with a maximum value at the crest of the cross section equal to the critical compressive stress in buckling due to bending.
6. During redistribution of the stresses in the post-buckling range, the direction of the tension field changes accordingly until the capacity stabilizes. It is reasonable to postulate that when the shear capacity of the cylinder stabilizes, the tension field slope reaches an optimum value such that the

shear capacity of the truss model is maximized. This assumption is analogous to the one made by Basler (1961) regarding the post-buckling shear capacity of plate girders.

6.3.2 Derivation of Shear Capacity

The shear capacity of the truss model can now be derived. From the definition of the helix shape of the tension field, the angle ψ (Fig. 6.6) which defines the width of the tension field is calculated as follows:

$$\psi = \pi - \frac{L}{R} \tan \zeta \quad (6.10)$$

in which L is the length of the shear span, R is the cylinder radius and ζ is the slope of the tension field.

Consider an element of width dw oriented in the direction of the tension field (Fig. 6.6). If the stress acting on the end area of this element is σ_t and the cylinder wall thickness is designated as t , then the infinitesimal force acting on the element in the direction of the tension field can be written as:

$$dT = \sigma_t t dw \quad (6.11)$$

(Note that, because of the presence of cross-bending moment as a buckle forms, σ_t is not, in fact, a uniform stress acting on the end area of the element, although it will be convenient to think of it that way. The influence of the cross-bending moment on σ_t will be developed subsequently.)

The component of the infinitesimal force, dT , in the direction of the applied shear is written as:

$$dT_v = \sigma_t t dw \sin \zeta \sin \theta \quad (6.12)$$

where θ is the angle between the infinitesimal strip and the vertical axis.

The width (dw), which is defined as the dimension of the strip normal to the tension field, can be expressed in terms of the infinitesimal angle ($d\theta$), the radius (R), and the slope of the tension field as follows:

$$dw = R d\theta \cos \zeta \quad (6.13)$$

Substituting Eq. 6.13 into Eq. 6.12 and using a trigonometric identity, one obtains:

$$dT_v = \frac{1}{2} \sigma_t t R (\sin 2\zeta) \sin \theta d\theta \quad (6.14)$$

Before integrating Eq. 6.14, the tensile stress, σ_t , first has to be defined. Using the assumed sinusoidal distribution of σ_t shown in Fig. 6.6, the tensile stress (σ_t) at a strip dw can be expressed as a function of the peak value of the distribution (σ_y) and the strip location angle (θ). It can be shown that this function is:

$$\sigma_t = \frac{\sigma_y}{2} \left(1 + \sin \left(\frac{6\pi\theta}{\psi} - \frac{\pi}{2} \right) \right) \quad (6.15)$$

Equation 6.15 is still incomplete because it does not take into account the variation of the tensile stress through the cylinder

thickness (t). As already noted, the shape of deformation in the buckled zone implies that in addition to the tensile stress that exists in the direction of the tension field, there is also stress normal to it due to the cross-bending moment. For example, when the surface buckles outward at a particular cross-section, the outside half of the thickness will be subjected to tensile stress normal to the tension field stress while the inside half of the thickness will be subjected to compressive stress. This biaxial state of stress may prohibit the tensile stresses in the direction of the tension field from reaching the yield value (σ_y). To determine the tensile stress distribution, the biaxial state of stress first needs to be identified.

As the deformations in the post-buckling range increase, the cross-curvature of the buckles increases, thereby creating high local cross-bending moments. These moments can be as high as the plastic moment after a sufficient degree of deformation is reached in the stable post-buckling path (Roman and Elwi, 1986). The stresses (σ_{cm}) associated with the cross-bending moment will limit the maximum stress (σ_{ta}) that can be reached in the direction of the tension field. Adopting the Von Mises yield criterion, shown graphically in Fig. 6.8, the relationship between the biaxial stresses takes the form:

$$\sigma_{ta}^2 + \sigma_{cm}^2 - \sigma_{ta} \sigma_{cm} - \sigma_y^2 = 0 \quad (6.16)$$

The distribution of the cross-bending stress, σ_{cm} , through the thickness is determined from the cross-bending moment due to the buckle deformation. The distribution of the maximum stress in the direction of the tension field, σ_{ta} , around the cylinder can then be calculated from Eq. 6.16. The tension field stress, which was assumed

to be uniform through the thickness, is now adjusted so that it does not exceed the maximum stress, σ_{ta} . Finally, an equivalent uniform stress, σ_{te} , is calculated as the average value of the adjusted tension field distribution through the thickness. This equivalent uniform stress, σ_{te} , is now the one that considers the effect of the cross-bending moment at the chosen location.

An example of this procedure is illustrated in Fig. 6.8. The section considered in this figure is the crest of a buckle where the thickness is fully plastified. It is logical to assume that the stress in the direction of the tension field must be between 0 and $+\sigma_y$. Equation 6.16 will show, therefore, that this stress (σ_{ta}) will be $+\sigma_y$ and that it will be present only in the outside half of the thickness. The adjusted tension field distribution in this case is similar to the σ_{ta} distribution and the equivalent stress (σ_{te}) is equal to $0.5\sigma_y$. Defining μ as the ratio between the equivalent stress and the tension field stress, μ at the crest location is 0.5. This ratio, first introduced by Roman and Elwi (1987), is a reduction factor which should be used in Eq. 6.15 to take the effect of the cross-bending moment into account at the crest location. After some further discussion of the value of μ , its introduction will be made in Eq. 6.17.

The steps for calculating σ_{ta} , σ_{te} , and μ are repeated for different locations on the buckle wave. Figure 6.9 shows the distributions of the cross-bending moment M_c , the tensile stress σ_t , and the reduction factor μ along one half of a buckle wave.

Instead of including the distribution of μ in Eq. 6.15 as a function of θ , an average value of μ for the whole tension field width can be calculated by integrating the distributions of μ and σ_t . This average value is calculated as 0.820, which is slightly less than the value of 0.875 suggested by Roman and Elwi (1986) using a similar approximation. Equation 6.15 is now modified to include the effect of the cross-bending moment.

$$\sigma_t = \frac{0.82\sigma_y}{2} \left(1 + \sin\left(\frac{6\pi\theta}{\psi} - \frac{\pi}{2}\right) \right) \quad (6.17)$$

Substituting Eq. 6.17 into Eq. 6.14, one obtains:

$$dT_v = \frac{0.82 R t \sigma_y}{4} \sin 2\zeta \left(1 + \sin\left(\frac{6\pi\theta}{\psi} - \frac{\pi}{2}\right) \right) \sin \theta d\theta \quad (6.18)$$

Integrating Eq. 6.18 over the range of $d\theta$ (from 0 to ψ), the contribution of the tension field to the shear capacity can be evaluated as:

$$T_v = 0.205 R t \sigma_y \sin 2\zeta (1 - \cos \psi) \left[\frac{36 \pi^2}{\psi^2 + 36 \pi^2} \right] \quad (6.19)$$

The horizontal component of the tension field can also be determined in the same manner:

$$dT_x = \sigma_t t dw \cos \zeta \quad (6.20)$$

$$T_x = 0.41 R t \sigma_y \psi \cos^2 \zeta \left[\frac{36 \pi^2}{\psi^2 + 36 \pi^2} \right] \quad (6.21)$$

To satisfy equilibrium, the horizontal component of the compression field (C_x) is set equal to the horizontal component of the tension field (T_x). The compression force (C) can then be calculated from T_x as:

$$C = \frac{T_x}{\cos \eta} \quad (6.22)$$

in which η is the slope of the compression strut. The compression force (C) is also given by the resultant of the triangular compression stress distribution shown in Fig. 6.6. The width (B) of this distribution at the supporting diaphragm is given by:

$$B = \frac{2 C}{t \sigma_{cr}} \quad (6.23)$$

in which σ_{cr} is the buckling compressive stress (Stephens et al., 1981). The vertical distance b , shown in Fig. 6.6 as the distance between the compressive strut (C) and the top of the cylinder, is dependent on B :

$$b = \frac{B}{3 \cos \eta} \quad (6.24)$$

Substituting Eqs. 6.21, 6.22 and 6.23 into Eq. 6.24, b is written as:

$$b = 0.273 R \psi \left[\frac{\sigma_y \cos^2 \zeta}{\sigma_{cr} \cos^2 \eta} \right] \left[\frac{36 \pi^2}{\psi^2 + 36 \pi^2} \right] \quad (6.25)$$

There are three unknowns (b , η , and ζ) in Eq. 6.25; therefore, two extra conditions are needed. Since the compression strut has a helical shape, its slope (η) is governed by the location of the tension

field resultant and the centroid of the stress triangle. This condition is expressed as:

$$\tan \eta = \frac{1}{L} \left(\frac{R\psi}{2} - b \right) \quad (6.26)$$

Substituting Eq. 6.25 into Eq. 6.26, the value of η can be determined as a function of ζ . Roman and Elwi (1986) assumed incorrectly that η is equal to ζ , while Bailey and Kulak (1984) neglected the compression strut altogether. After calculating η , the contribution of the compression field to the shear capacity can be obtained.

$$C_v = T_x \tan \eta \sin \frac{\psi}{2} \quad (6.27)$$

The total shear capacity of one half of the cylinder is simply the summation of the tension component (Eq. 6.19) and the compression component (Eq. 6.27). For the whole cylinder, the post-buckling shear capacity according to the truss model is written as:

$$V_{tm} = 2 (T_v + C_v) \quad (6.28)$$

Equation 6.28 is a function of the slope of the tension field, ζ , which is still unknown. To determine the value of ζ , the assumption that the slope will be that which produces maximum shear will be applied:

$$\frac{d V_{tm}}{d \zeta} = 0 \quad (6.29)$$

The nonlinearity of Eqs. 6.28 and 6.29 prevents the derivation of a closed form solution for the post-buckling shear force V_{tm} .

However, numerical techniques are suitable in such cases to determine the maximum value of the post-buckling shear force V_{tm} . One possible algorithm is to assume different values of ζ in the practical range (0 to $\pi/2$) and to calculate Eq. 6.28 for each value of ζ . Subsequently, the maximum value is selected and the first derivative (Eq. 6.29) is checked to ensure that it is almost zero. Appendix C lists a FORTRAN subroutine that was written to perform these calculations. The input data of this subroutine are the cylinder variables, namely the aspect ratio (R/L), the thickness ratio (R/t), and the material ratio (E/σ_y). The output data are the slope of the tension field (ζ), the slope of the compression strut (η), and the ratio of post-buckling shear stress to the yield stress (τ_{tm}/σ_y). This shear stress is related to the shear force V_{tm} of Eq. 6.28 by the simple beam shear relationship:

$$V_{tm} = \pi R t \tau_{tm} \quad (6.30)$$

The process of selecting the maximum shear stress (τ_{tm}) for different values of R/t , E/σ_y , and R/L is demonstrated graphically in Figs. 6.10, 6.11 and 6.12, respectively. Each curve in these figures shows the post-buckling shear stress ratio (τ/σ_y) versus the slope of the tension field (ζ) and each figure shows the effect of changing certain cylinder variables on the τ - ζ relationship. The global maximum of each curve is selected as the shear value for the truss model capacity (τ_{tm}). Examining these maximum values, it is observed that the post-buckling shear stress τ_{tm} increases with increasing values of R/L and E/σ_y , but decreases as the R/t ratio

increases. These relationships agree with the observations of the full-scale tests B1, B2, S1, and S2.

In addition to the global maximum values, there are some local maximum values at a tension field slope greater than that of the global maximum. These values correspond to horizontal compression struts, that is, the slope η is equal to zero. In other words, these local maximum values represent cases when the shear capacity is due to the tension field alone.

Figures 6.10 and 6.11 indicate that when the shear strength is generated from the tension field alone (T_v), it is not a function of the ratios R/t and E/σ_y . On the other hand, Fig. 6.12 shows that T_v is a function of the aspect ratio R/L . Indeed, when R/L decreases to a certain limit, the tension field contribution becomes the only active shear component. This limit is a function of the thickness ratio and the material ratio. The curve with $R/L = 0.5$ in Fig. 6.12 shows that the global maximum value is only slightly greater than the local maximum value. Further examination showed that for $R/L < 0.35$, the local maximum becomes the global maximum.

6.3.3 Model Mechanism

To understand the role of R/L and R/t ratios in developing the post-buckling shear force V_{tm} , the shear resistance is separated into two components; the tension field component, T_v , and the compression field component, C_v . The two components, as well as the slopes of the tension and compression strut, are displayed on the developed surface of the cylinder in Figs. 6.13 and 6.14. Figure 6.13

points out the change in the slopes due to variation of the R/L ratio. It is noticed that the shorter the shear span L , the steeper the slopes of the tension and compression struts, and, consequently, the higher the shear components. Figure 6.14 illustrates the effect of the R/t ratio. When the cylinder thickness is reduced, the critical compression stress is also reduced. Thus, the compression strut, which should balance the horizontal component of the tension field, is forced to have a smaller slope η and it therefore provides a smaller vertical component. Even though the slope of the tension field increases to compensate for the loss of the compression strut shear contribution, the shear capacity of the whole model diminishes as the thickness ratio, R/t , increases.

Although Figs. 6.13 and 6.14 utilized specific values of the aspect ratio and the thickness ratio, the same conclusions can be drawn for any value of R/t and R/L . This can be seen in Figs. 6.15, 6.16 and 6.17. As the shear span decreases, the shear capacity and the slopes ζ and η increase. As the cylinder thickness decreases, the shear capacity and the slope of the compression strut decrease, while the slope of the tension field increases.

6.3.4 Design Charts

The subroutine described in Appendix C can be used to produce design charts for the post-buckling shear capacity by repeating the process for different cylinder variables. Some examples of these charts are presented in Figs. 6.18(a), 6.18(b), and 6.18(c). The shear force ratio (V_{tm}/V_y) is plotted against the aspect ratio (R/L) for

selected increments of the thickness ratio (R/t). Since the shear capacity is not sensitive to the variation of the material ratio (E/σ_y), it is better to choose a constant value for the E/σ_y ratio rather than to complicate the chart. The values of E/σ_y chosen for Figs. 6.18(a), 6.18(b), and 6.18(c) are 400, 600, and 800, respectively. In these figures, the shear ratio is increasing as the aspect ratio increases, except for small values of the R/t ratio (about 0.5 or less). At these small values, the compression strut is horizontal and not contributing to the shear capacity of the cylinder.

Three limitations were imposed on the design charts in the above figures. The first limit is the yield limit, wherein the yield shear stress, τ_y , is considered as an upper bound to the truss model shear stress, τ_{tm} . When the shear stress predicted by the truss model is larger than the yield shear stress ($\tau_{tm} > \tau_y$), the yield shear stress is plotted instead. This condition occurs at low values of the thickness ratio, R/t , and can be observed as the horizontal lines seen in Figs. 6.18(a), 6.18(b), and 6.18(c).

The second limit is the elastic buckling limit, wherein the elastic shear stress (τ_e , calculated from Eq. 2.10 with K_s conservatively taken equal to 0.74) is also an upper bound to the truss model shear stress, τ_{tm} . When the shear stress predicted by the truss model (Eq. 6.28) is larger than the elastic buckling shear stress (Eq. 2.10), the elastic buckling shear stress is plotted instead. This condition occurs at high values of the thickness ratio, R/t , and low values of the material ratio, E/σ_y . It can be observed in Fig. 6.18(a), wherein the curves for R/t ratios greater than about 250 show

slightly shallower slopes because they represent Eq. 2.10 rather than Eq. 6.28.

The third limit deals with the failure mode. When the R/L ratio is small, the shear capacity of the truss model, V_{tm} , is larger than the load required to cause buckling due to bending. In these cases, the curves were terminated so that they do not identify shear resistances which in fact cannot be delivered. This condition occurs at values of R/L that are slightly smaller than those which have a horizontal compression strut. The shear resistance corresponding to a bending buckling limit is calculated as M/L , where M is the bending moment (case of a cantilever or a simply supported cylinder) and the buckling stress due to bending is evaluated as suggested by Stephens et al. (1981).

In general, the shear capacity ratio in the design charts decreases as the R/L ratio decreases, except for R/L ratios less than about 0.50, where the carrying mechanism becomes a function of the tension field alone. It also happens that at these values of R/L, the buckling mode changes to bending-type rather than shear-type.

6.4 Assessment of the Proposed Model

6.4.1 Comparison with Tests

The known cylinder shear tests are B1 and B2 (Bailey and Kulak, 1984), S1 and S2 (Chapter 3), and G1 through G14 (Galletly and Blachut, 1985). The first four tests (B1, B2, S1, and S2) were the only ones for which the pre-buckling and post-buckling behavior

was reported and, therefore, the only ones that can be directly compared to any post-buckling model. The last three tests of this set (B2, S1, and S2) also happen to be large-scale tests carried out on specimens that use hot-rolled steel.

The truss model contained in Eq. 6.28 was derived primarily for simply supported and cantilever cylinders, which leaves only one test (S2) that can be compared directly with the truss model. Although the B1, B2, and S1 tests were intended to have fixed-end supports, the support rotations could not be prevented completely. This caused the bending moments to be redistributed towards that of simply supported members. The degree of success the truss model will have in predicting these tests is dependent on the degree of this moment redistribution. Notwithstanding the boundary condition effect, the truss model will be evaluated using the four tests B1, B2, S1 and S2.

The comparison is illustrated in Fig. 6.19, where the predicted and measured capacity ratios (the ratio of the post-buckling shear capacity to the yield shear capacity, V_p/V_y) are plotted against one another. The diagonal line in Fig. 6.19 represents the ideal condition. Values above the line are conservative model predictions, and values below the line are unconservative predictions. It is clear that the truss model is close to the test results, especially for S2. Following the same definition of the error measurements E_r , suggested in Chapter 5 (Eq. 5.43), the error between the truss model predictions and the test results is 5.0%, -13.5%, -11.0%, and -1.5% for B1, B2, S1, and S2, respectively.

The slopes of the inclined buckles measured from the tests are compared to the slope of the tension field calculated according to the truss model in Table 6.1. Only three tests (B1, S1, and S2) are compared to the truss model in Table 6.1 because the B2 test and all of Galletly's tests did not report the buckle slopes. Although the slopes predicted by the truss model are reasonably close to the measured ones, no general conclusion can be made until more test data are available.

Although tests G1 through G14 did not report the post-buckling capacity, were carried out on very small specimens (150 mm in diameter), and in some cases were not made of hot-rolled steel, they could be used indirectly in the comparison with the tests. The ratios of the stable post-buckling load to the buckling load for the tests, B1, B2, S1, and S2, were 0.800, 0.700, 0.823, and 0.797, respectively. Except for B2, these ratios are unusually close to one another. This closeness suggests that the ratio of the stable post-buckling load to the buckling load for the tests that did not report the post-buckling capacity and have the same range of variables may also be in the neighborhood of 0.805, the average of B1, S1, and S2. Galletly's tests also had a range of variables closer to B1, S1 and S2 than to B2. The range of R/t ratios is 125 to 188 for Galletly's tests, 185 to 250 for B1, S1 and S2 tests, and 75 for B2 test.

In order to utilize the results of G1 through G14, it will be assumed that the ratio of the post-buckling capacity to the buckling capacity of these tests is 0.805, which is the average ratio of the three tests B1, S1, and S2. The comparison between the truss model

and G1 through G14 tests is shown in Fig. 6.20. The test results cluster around the model predictions in a reasonable way. The error (E_r) between the truss model predictions and the results of G tests range from -8.1% (case of G3) to 16.5% (case of G12).

Considering all experimental results, the proposed model has an error range of -13.5% to 16.5% with an overall average of 7.1%. Taking into consideration the approximations made to compensate for the limited information obtained from some of the tests, it appears that the proposed model has good potential for estimating the post-buckling capacity of thin-walled cylinders.

Although the numerical parametric study described in Chapter 4 is not a "physical test", it is worthwhile to examine the correlation of the finite element results with the truss model. The post-buckling capacity measured from the results of the finite element analysis is compared to the post-buckling capacity predicted by the proposed truss model in Fig. 6.21. It is clear that the truss model prediction is a lower bound on the finite element model. This observation is similar to that illustrated in Fig. 5.12 for the relationship between the finite element and the regression model.

6.4.2 Comparison with Buckling Equation

In Chapter 5, the buckling capacity was estimated by the inelastic buckling equation 5.48. If the assumption made in the previous section regarding the ratio between the buckling and the post-buckling capacities is valid in the prescribed range of variables, then the results from an ideal truss model should be approximately

80% of the results obtained using the buckling equation. On the other hand, if the assumption is not valid and both the buckling and post-buckling models are accurate, then the ratio between them would give an idea about the ideal relationship between the buckling and post-buckling capacity.

The shear force ratio calculated from Eq. 5.48 is plotted against the cylinder variables R/L , R/t , and E/σ_y in Figs. 6.22, 6.23, and 6.24, respectively. In order to compare the buckling load with the post-buckling capacity, two truss model curves are also plotted in these figures; the proposed truss model (Eq. 6.28) and the Roman-Elwi model (Eq. 6.9). As for Eq. 6.28, it can be noticed that it is generally a lower bound solution for the buckling strength. However, the truss model results are not exactly proportional to those of Eq. 5.48. In fact, the ratio between the truss model predictions and Eq. 5.48 changes from 0.69 to 1.00 in the prescribed range of variables for the inelastic buckling Eq. 5.48 ($125 < R/t < 250$, $0.50 < R/L < 1.40$, and $450 < E/\sigma_y < 850$).

Unfortunately, no solid conclusions regarding the ratio between the post-buckling and buckling strength can be drawn because the test results available are limited. However, the proposed truss model demonstrated the favorable attribute of being a lower limit to the buckling shear capacity: therefore, at least it can be used as a conservative predictor of the shear capacity for most practical cases.

6.4.3 Comparison with Other Post-Buckling Models

The model proposed by Roman and Elwi (1987) to simulate the post-buckling behavior of large diameter cylinders is the model chosen herein for comparison. In Figs. 6.22, 6.23, and 6.24, the predictions of the Roman-Elwi model, Eq. 6.9, for different values of the cylinder variables are shown simultaneously with the proposed truss model, Eq. 6.28.

Figs. 6.22 through 6.24 show that Eq. 6.9 is below the expected shear capacity for large values of the aspect ratio, small values of the thickness ratio or large values of the material ratio. In fact, Eq. 6.9 lacks the effect of the cylinder thickness ratio (R/t) and the material ratio (E/σ_y) completely. Therefore, it is expected that Eq. 6.9 may be very conservative in cases of relatively short thick cylinders with low yield stress. For example, the ratio of the shear capacity calculated using Eq. 6.9 to that measured from the G11 test (which has $R/L = 1.37$) is 0.80. The same ratio for G4 test (which has $E/\sigma_y = 840$) and G5 test (which has $R/t = 125$) is as low as 0.75 and 0.74, respectively.

On the other hand, Eq. 6.28 appears to include the desirable effect of all the variables (R/L , R/t , E/σ_y) that influence the shear capacity. For example, the ratio of the shear capacity calculated using Eq. 6.28 to that measured from the tests chosen above, G11, G4, and G5, is 1.14, 0.91, 0.90, respectively. Thus, it is concluded that the proposed model provides better agreement with the buckling behavior of thin-walled cylinders than does the Roman-Elwi model.

Test	R/t	R/L	Angle between buckle and longitudinal axis of the cylinder (in degrees)				
			Measured *			Calculated	
S1	185	0.53	23.0 ,	25.0 ,	24.0 ,	27.0	24.0
S2	185	0.73	21.0 ,	27.0	---	---	29.0
B1	250	0.50	24.0	---	---	---	26.0

* Individual numbers in the same test correspond to different buckles

Table 6.1 Comparison between measured and predicted buckle slopes

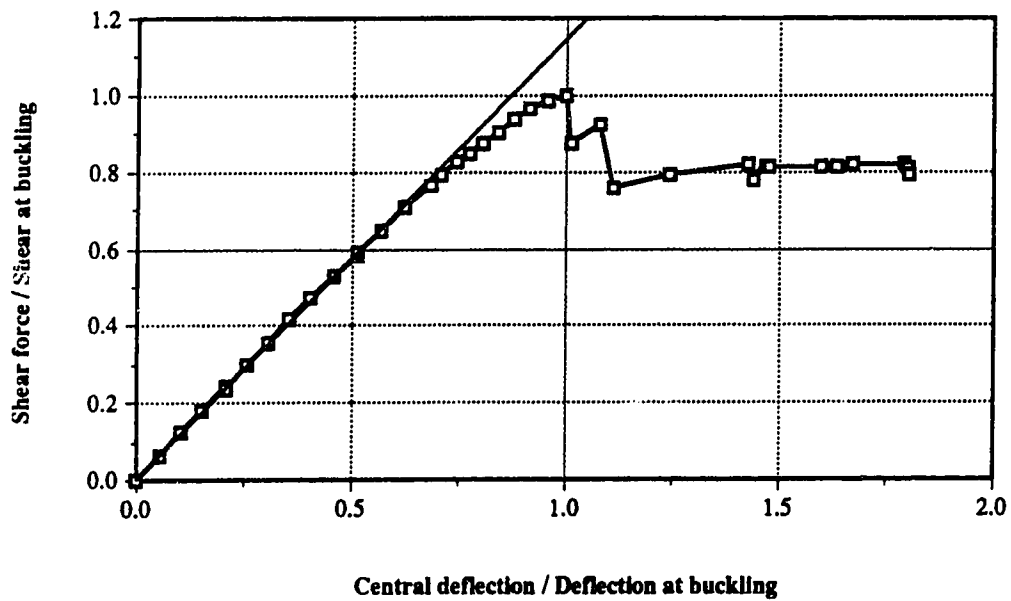


Fig. 6.1 Behavior of large diameter tubes in post-buckling range (typical)

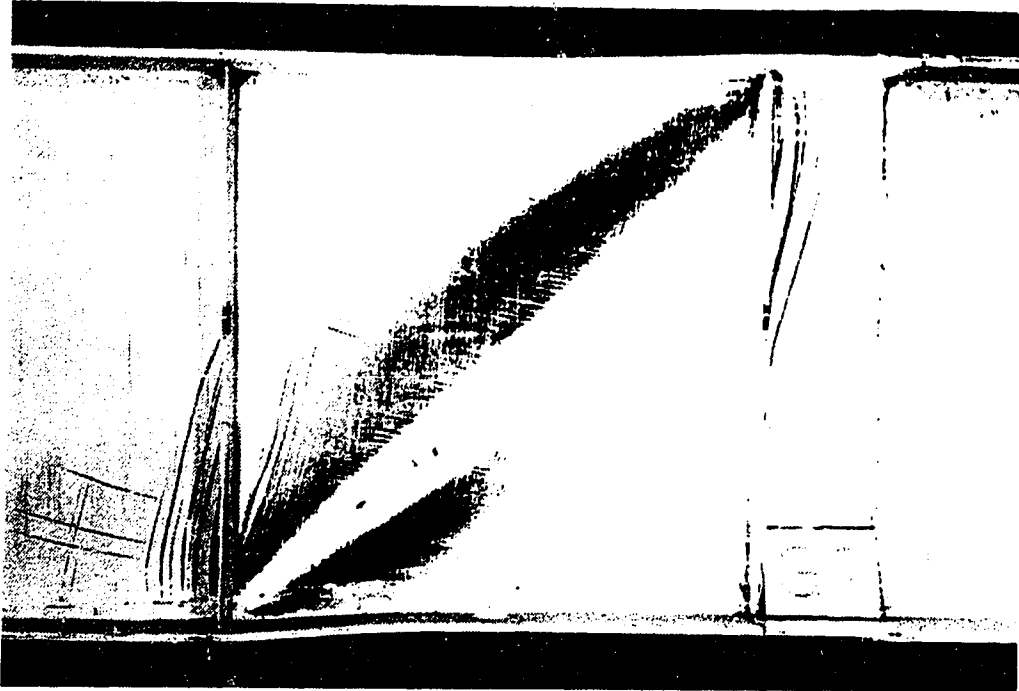


Fig. 6.2a Tension field action in plate girders

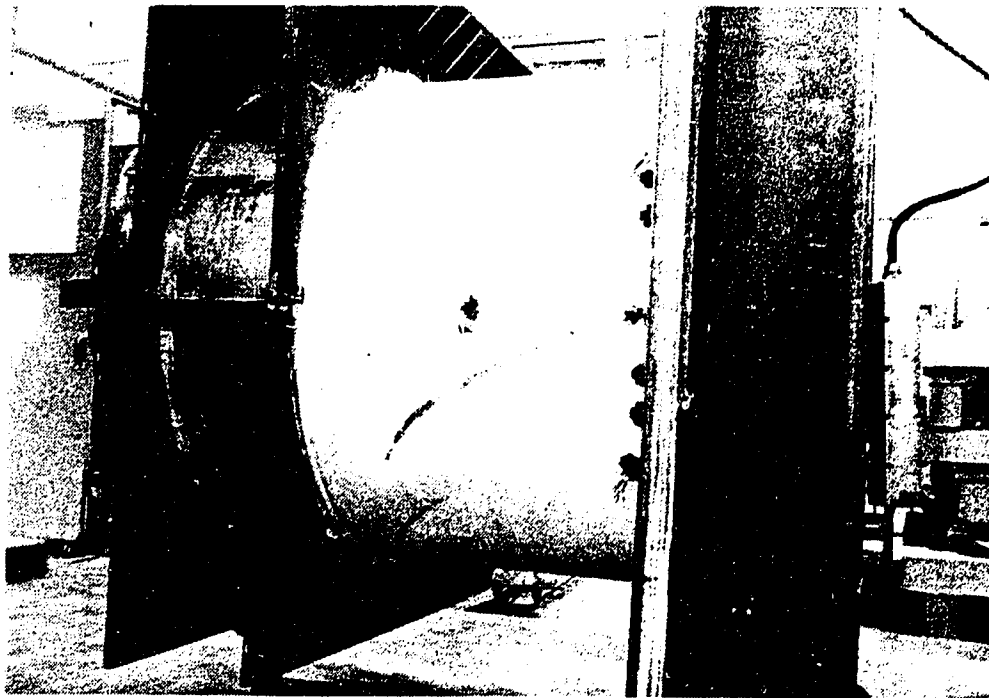


Fig. 6.2b Tension field action in thin-walled cylinders

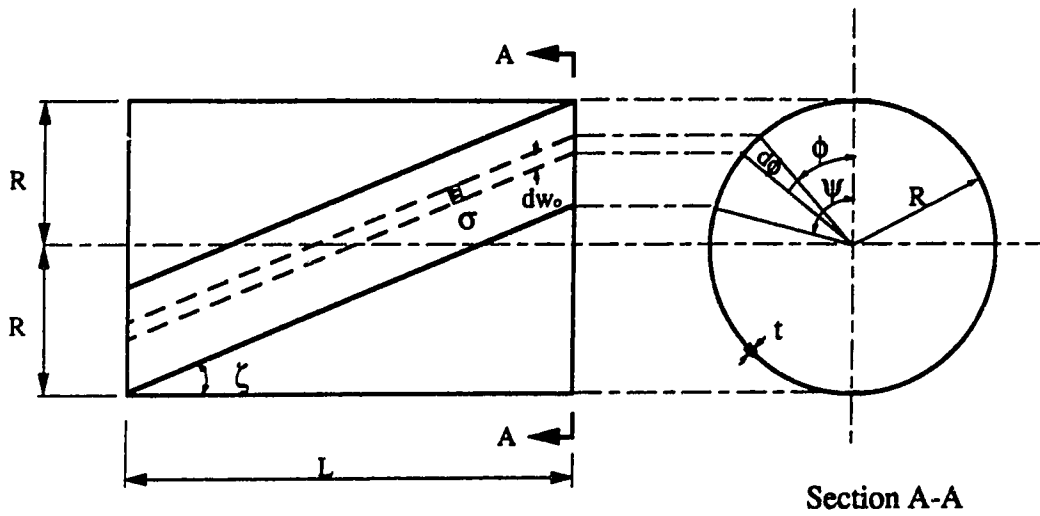


Fig. 6.3 Tension field action in the Bailey - Kulak model (after Bailey and Kulak, 1984)

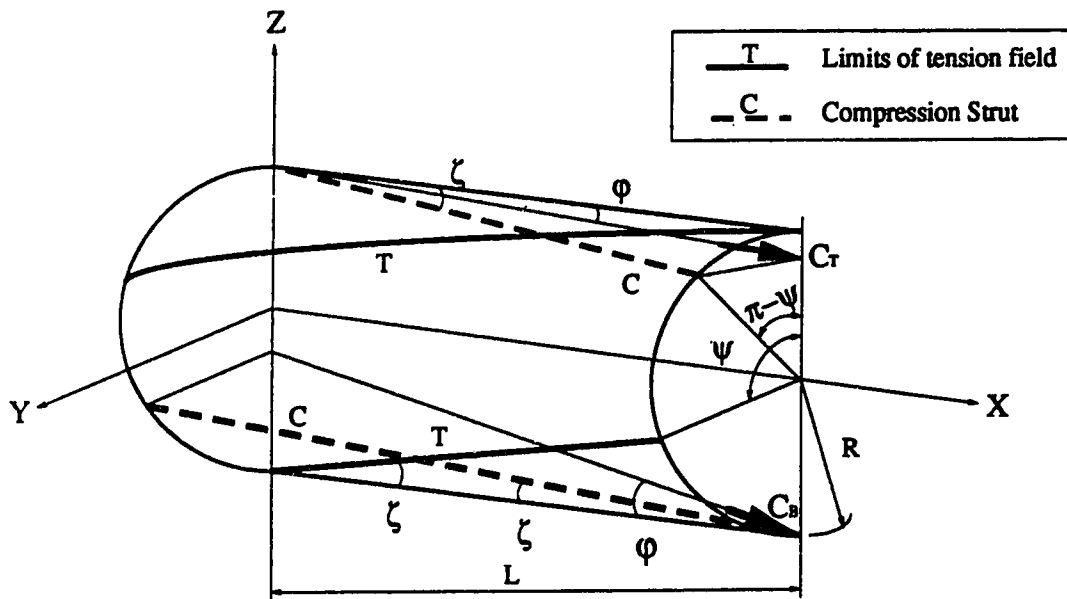
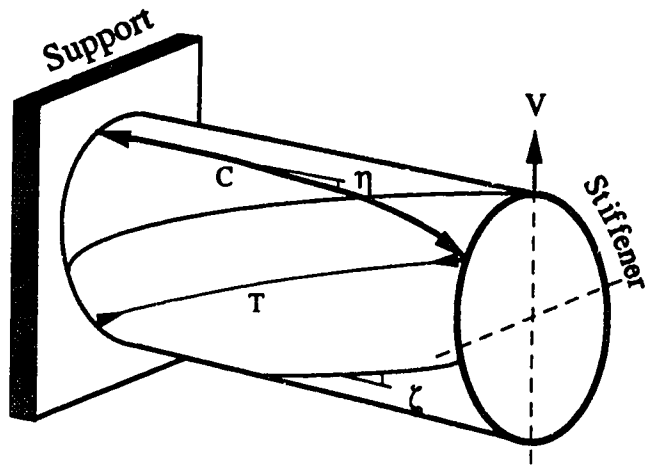
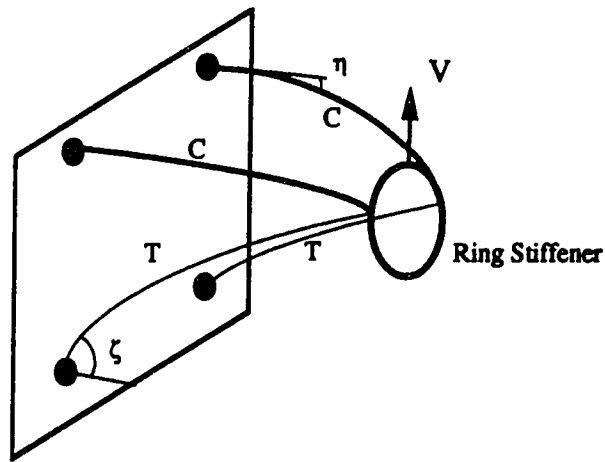
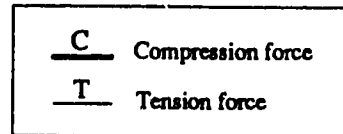


Fig. 6.4 Tension field action in the Roman - Elwi model (after Roman and Elwi, 1987)



Force fields in the cylinder



Truss model

Fig. 6.5 Proposed truss model

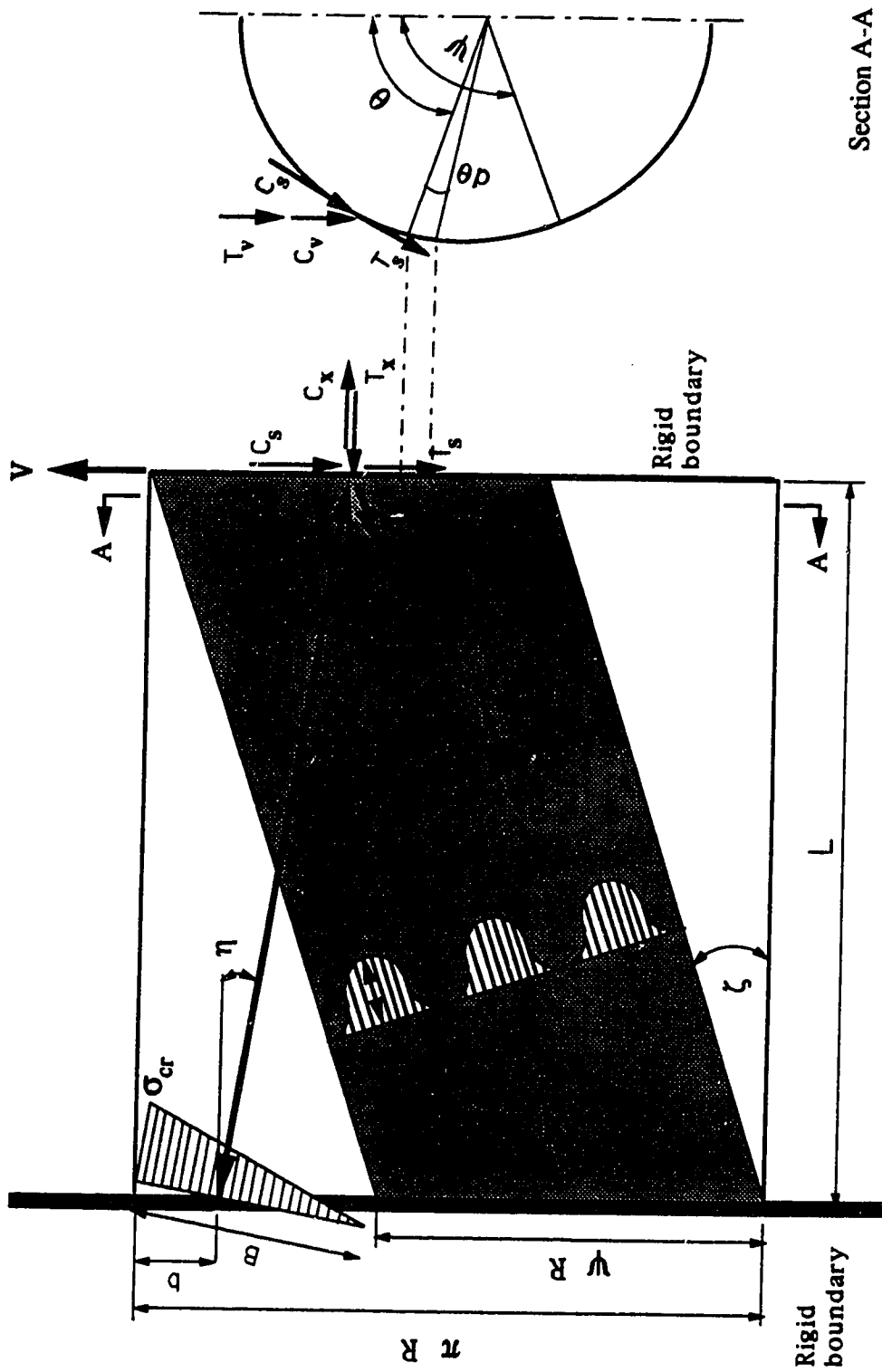


Fig. 6.6 The truss model on the developed surface of the cylinder

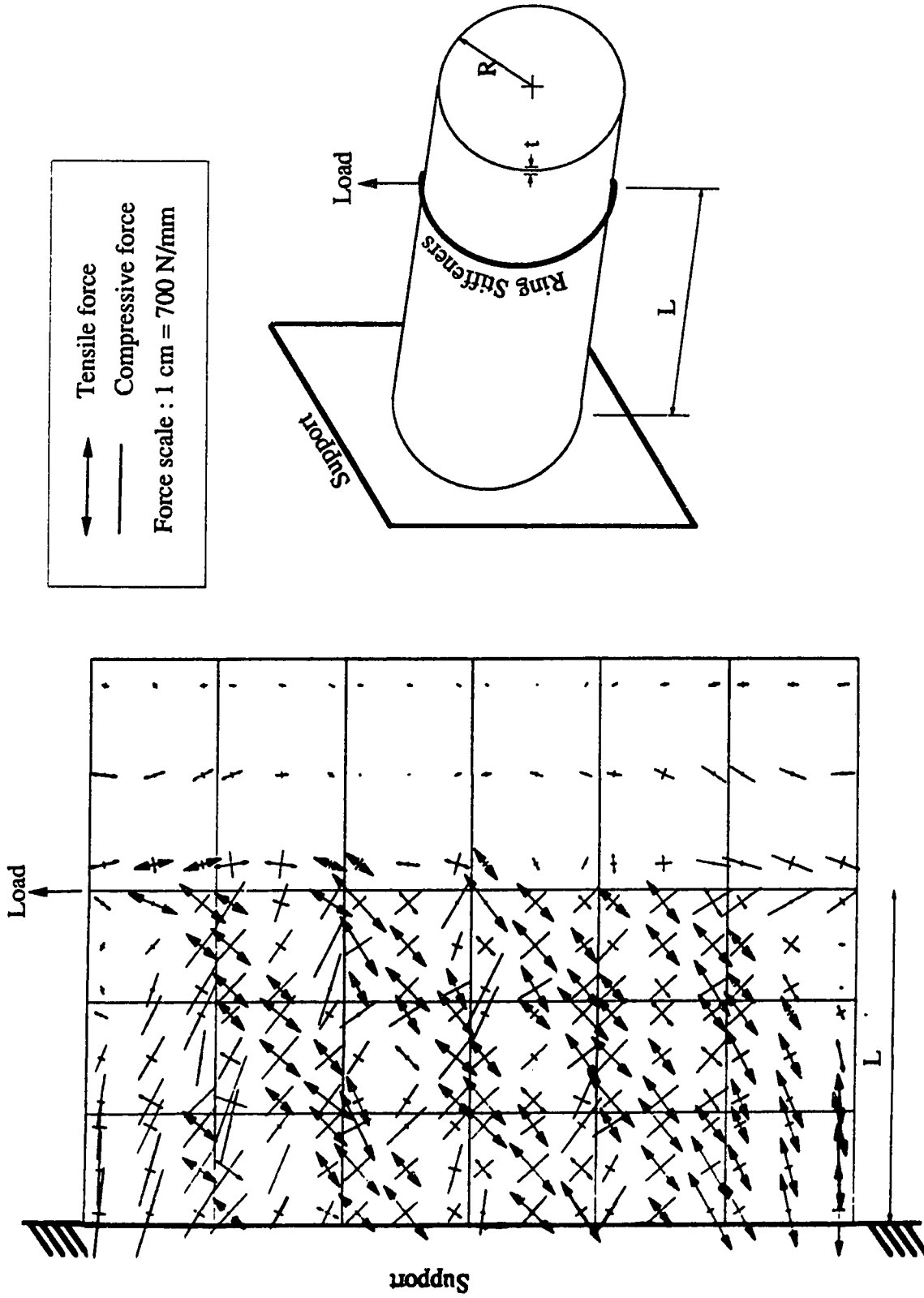


Fig. 6.7 Post-buckling principal forces on the developed surface of specimen S2

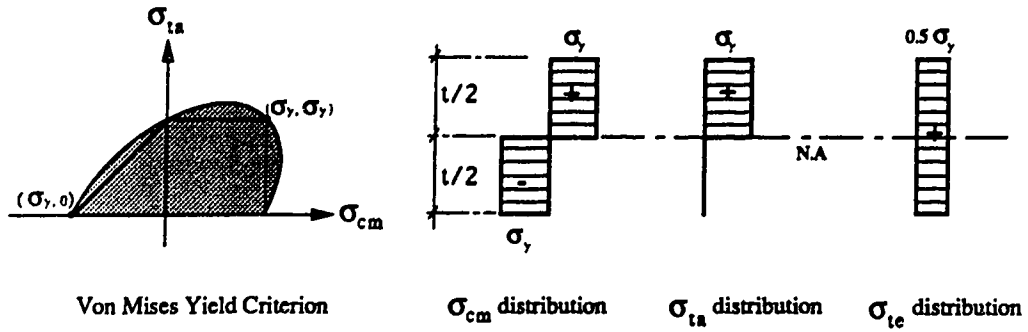


Fig. 6.8 Effect of biaxial stress state at the crest of a buckle

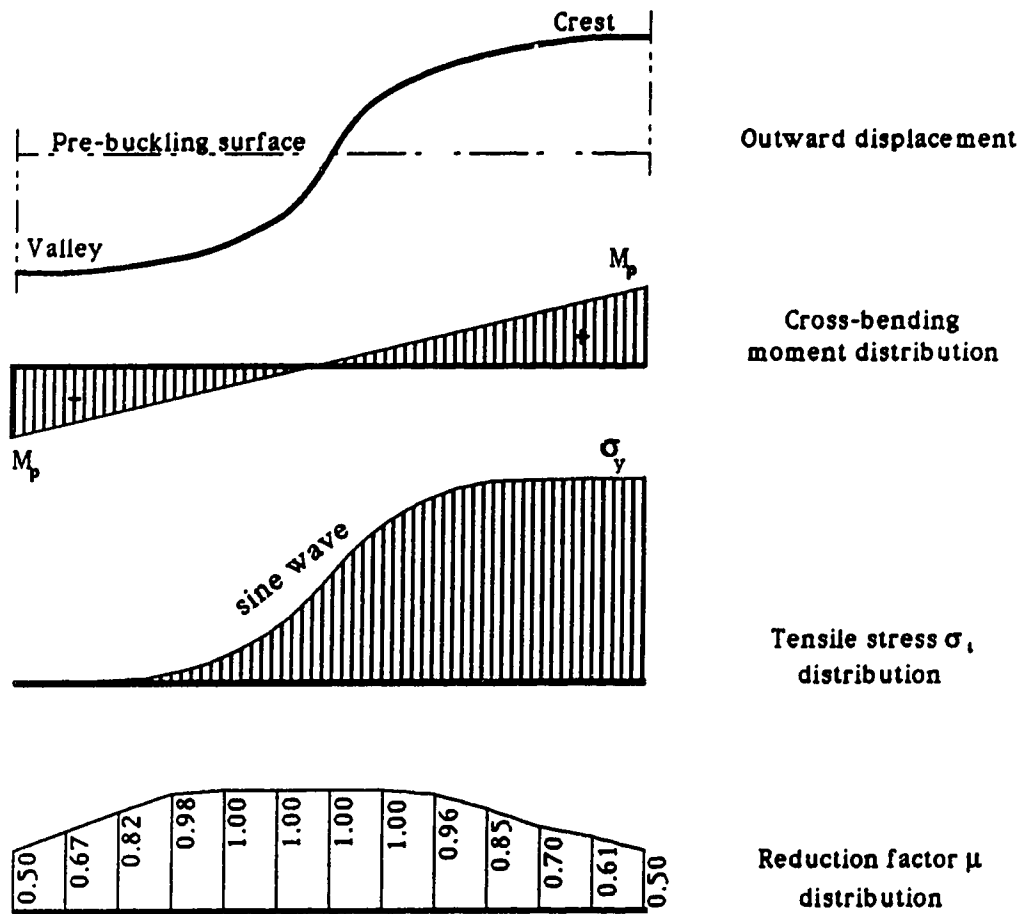


Fig. 6.9 Distributions of M_p , σ_t , and μ for half buckle wave in the tension field

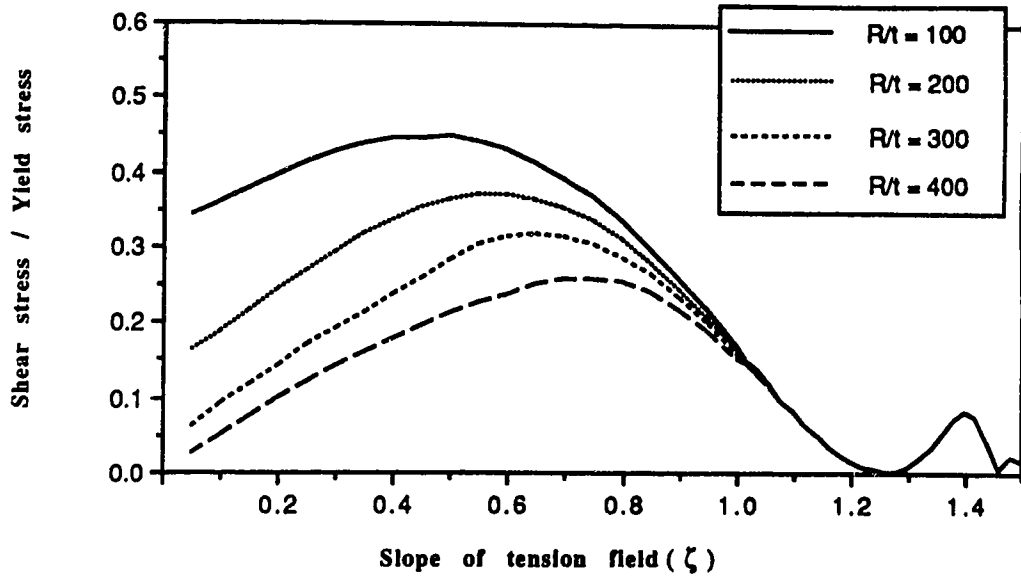


Fig. 6.10 Effect of thickness ratio on post-buckling shear stress ($R/L=1.0, E/\sigma_y=600$)

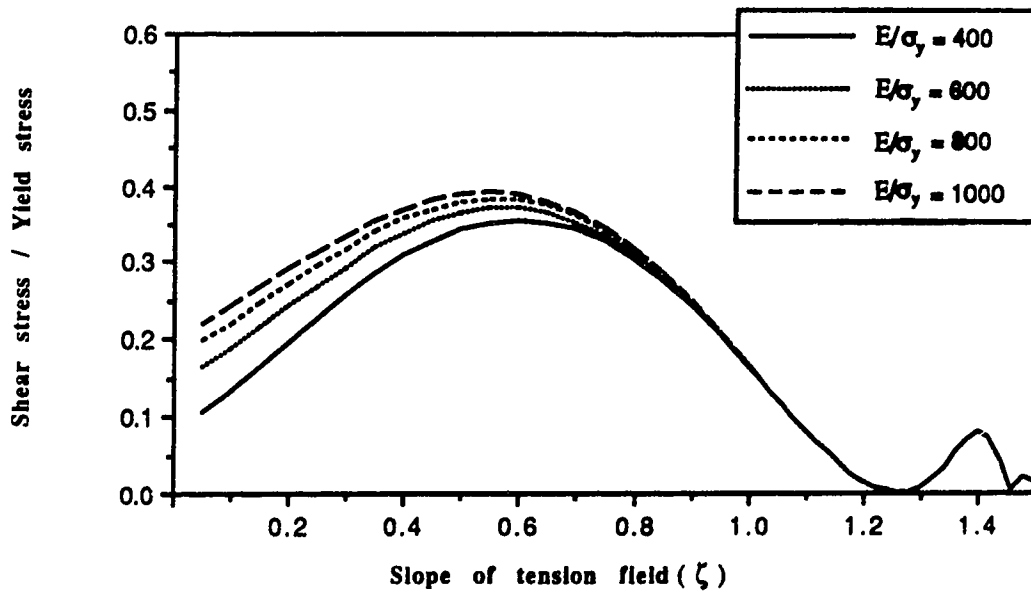


Fig. 6.11 Effect of material ratio on post-buckling shear stress ($R/L=1.0, R/t=200$)

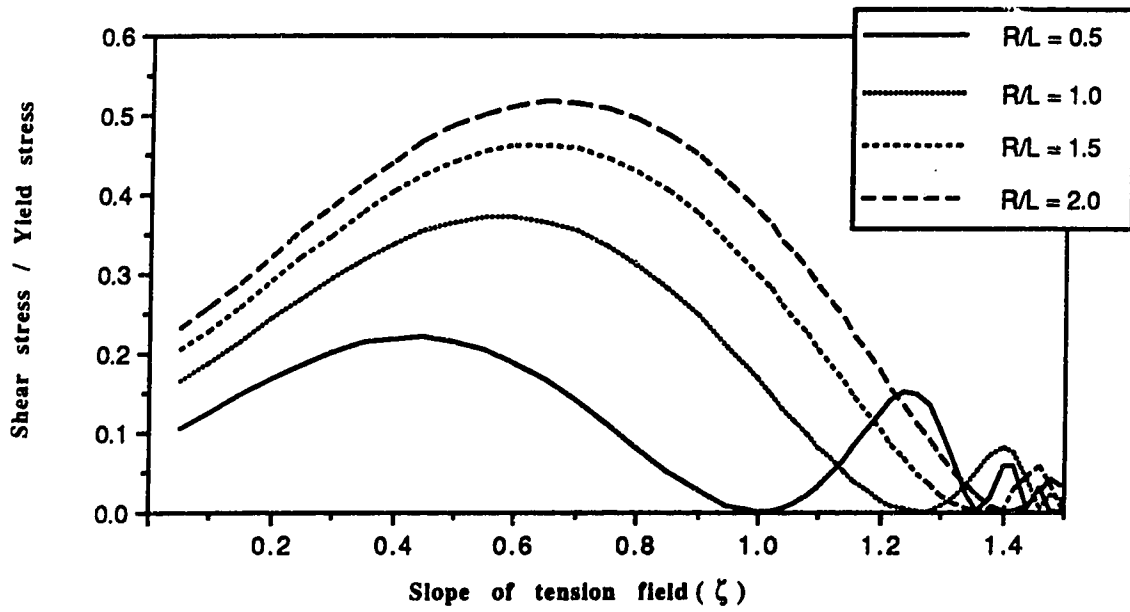


Fig. 6.12 Effect of aspect ratio on post-buckling shear stress
 ($R/t=200, E/\sigma_y=600$)

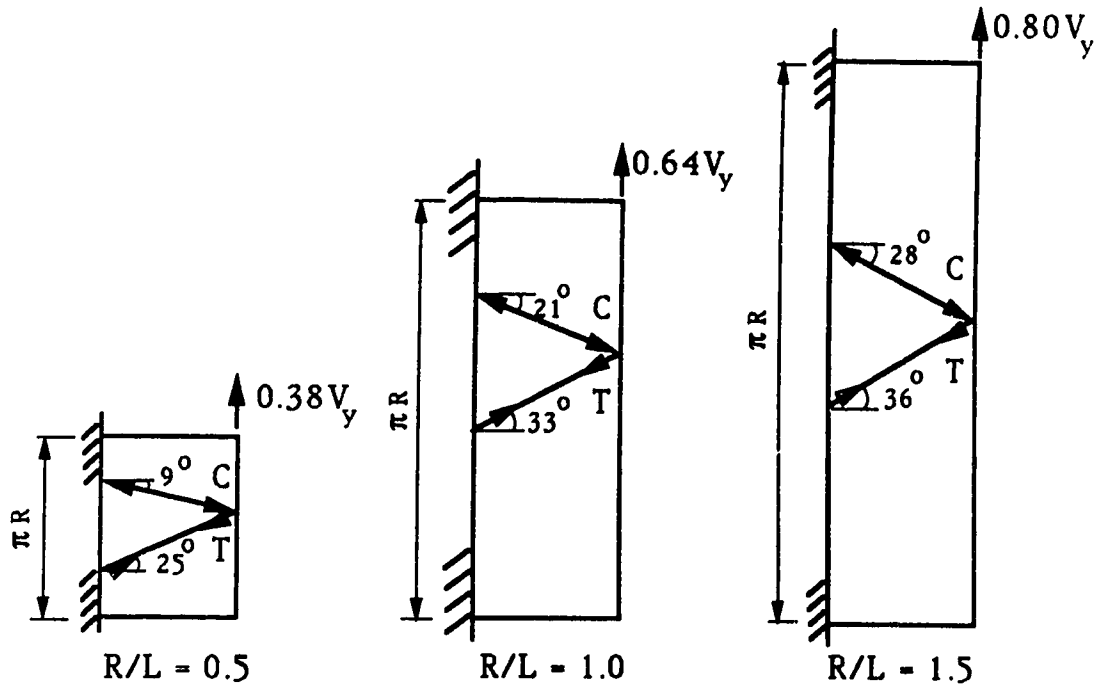


Fig. 6.13 The truss elements on the developed surface for different R/L ratios
 ($R/t = 200$ and $E/\sigma_y = 600$)

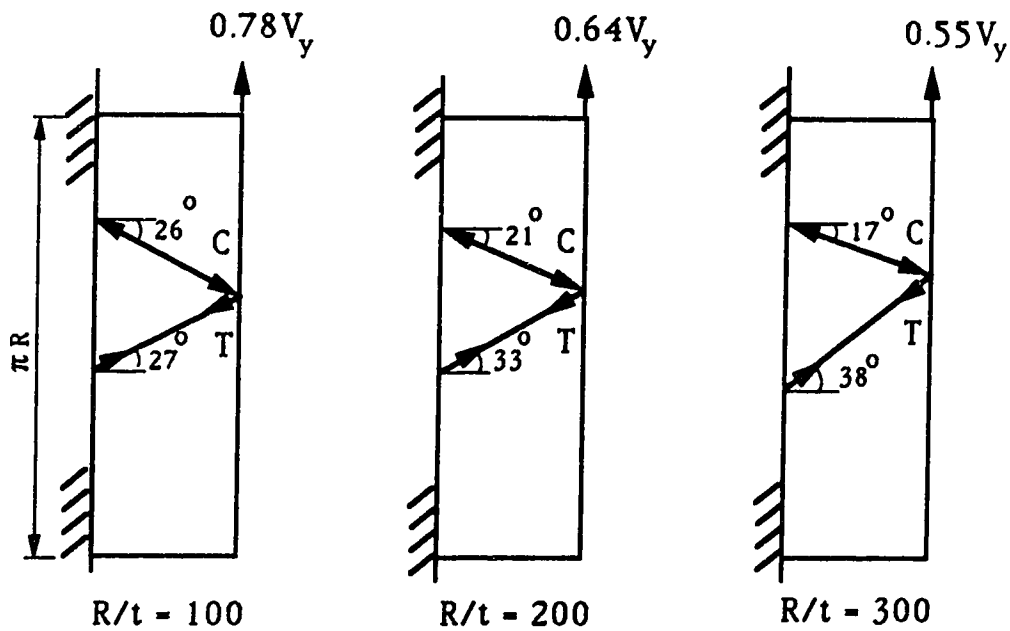


Fig. 6.14 The truss elements on the developed surface for different R/t ratios
 ($R/L=1.0$ and $E/\sigma_y = 600$)

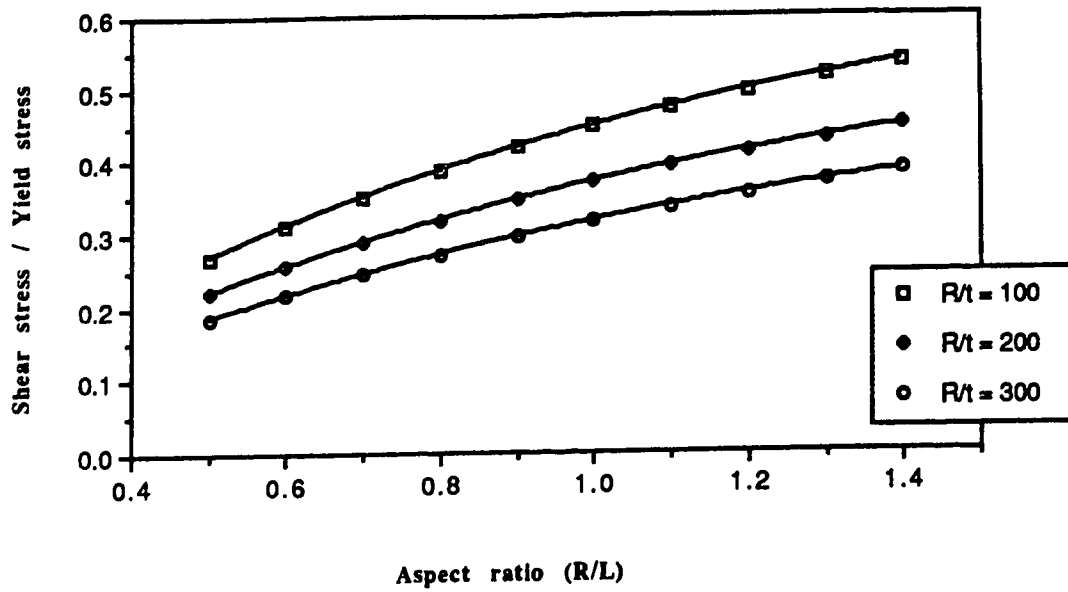


Fig. 6.15 Shear capacity of the truss model

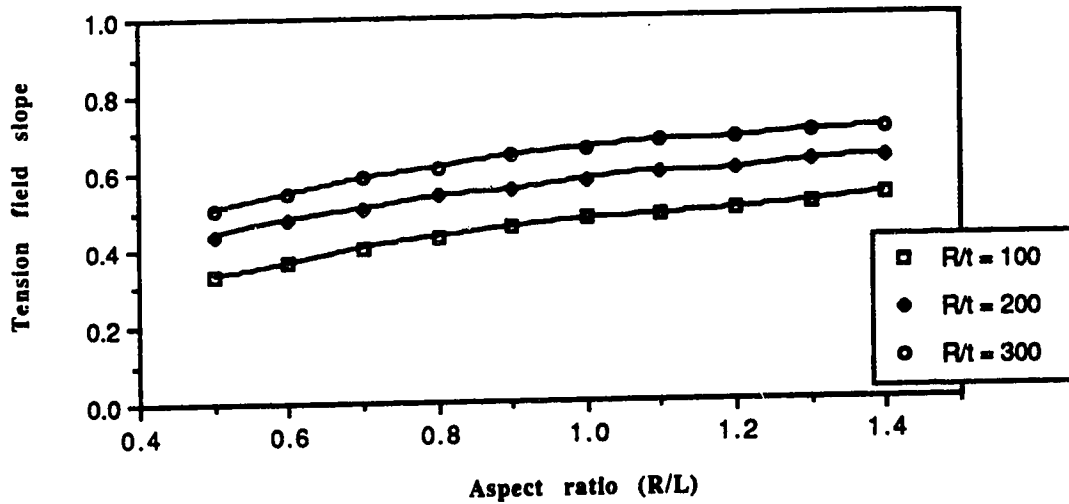


Fig. 6.16 Tension field slope of the truss model

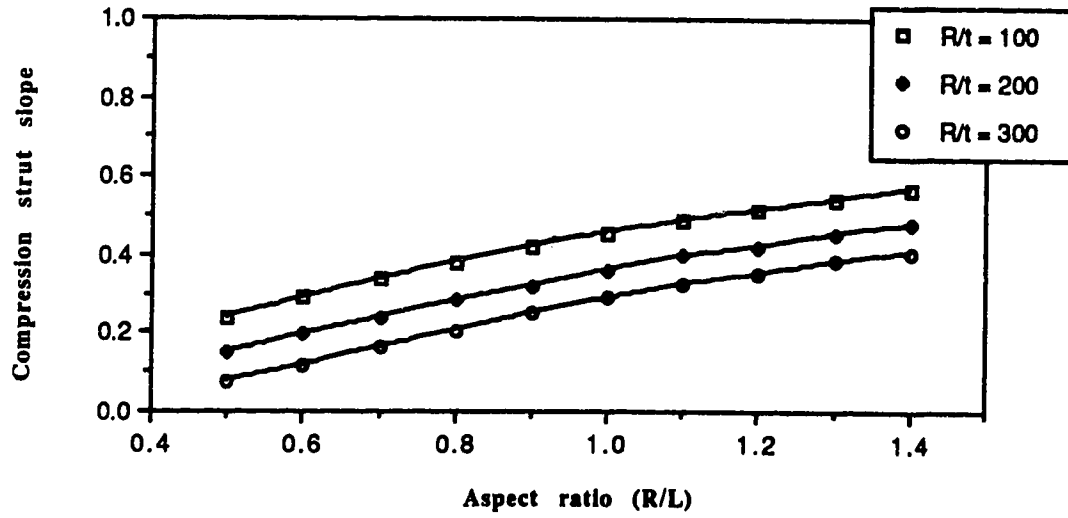


Fig. 6.17 Compression strut slope of the truss model

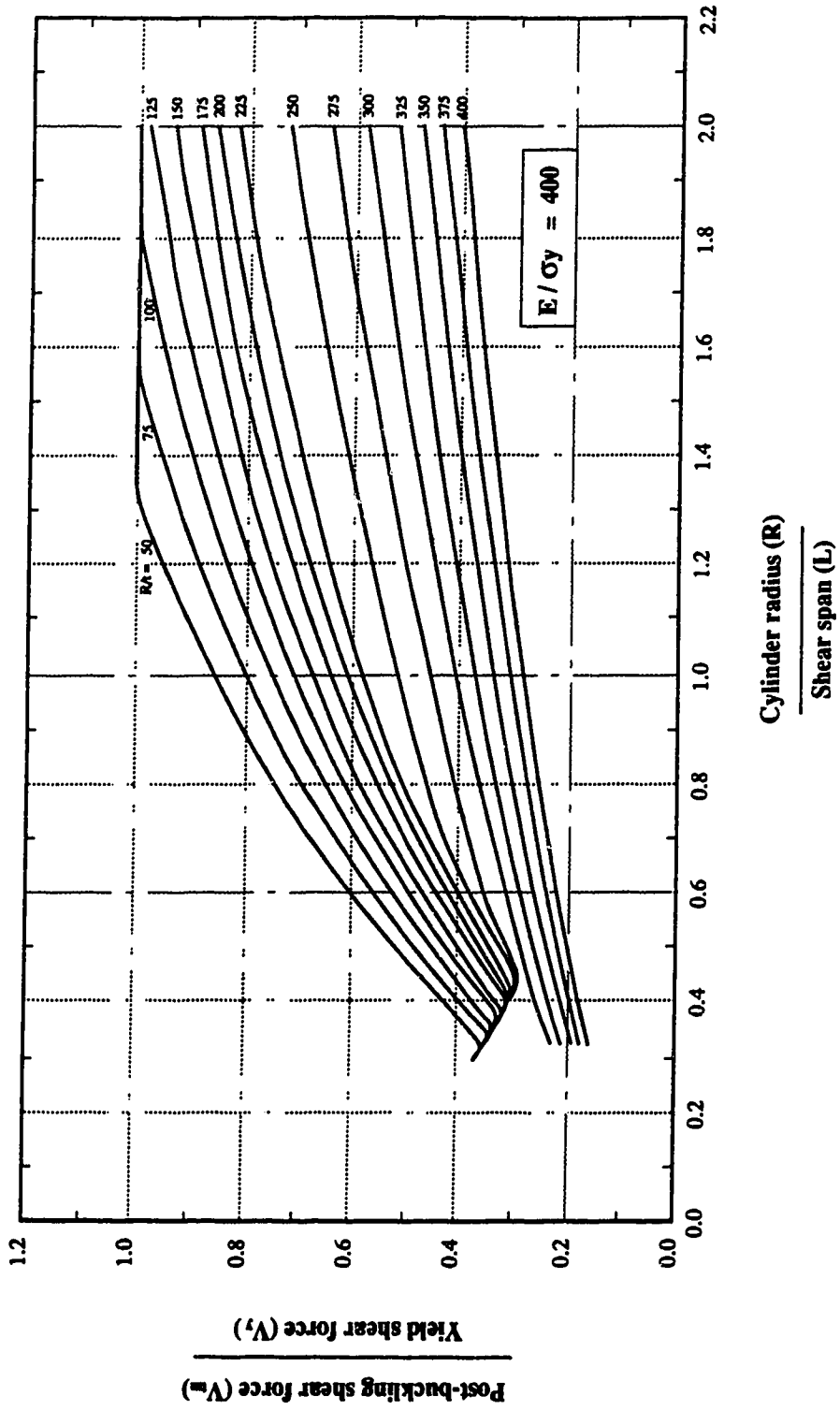


Fig. 6.18(a) Post-buckling shear capacity for thin-walled cylinders

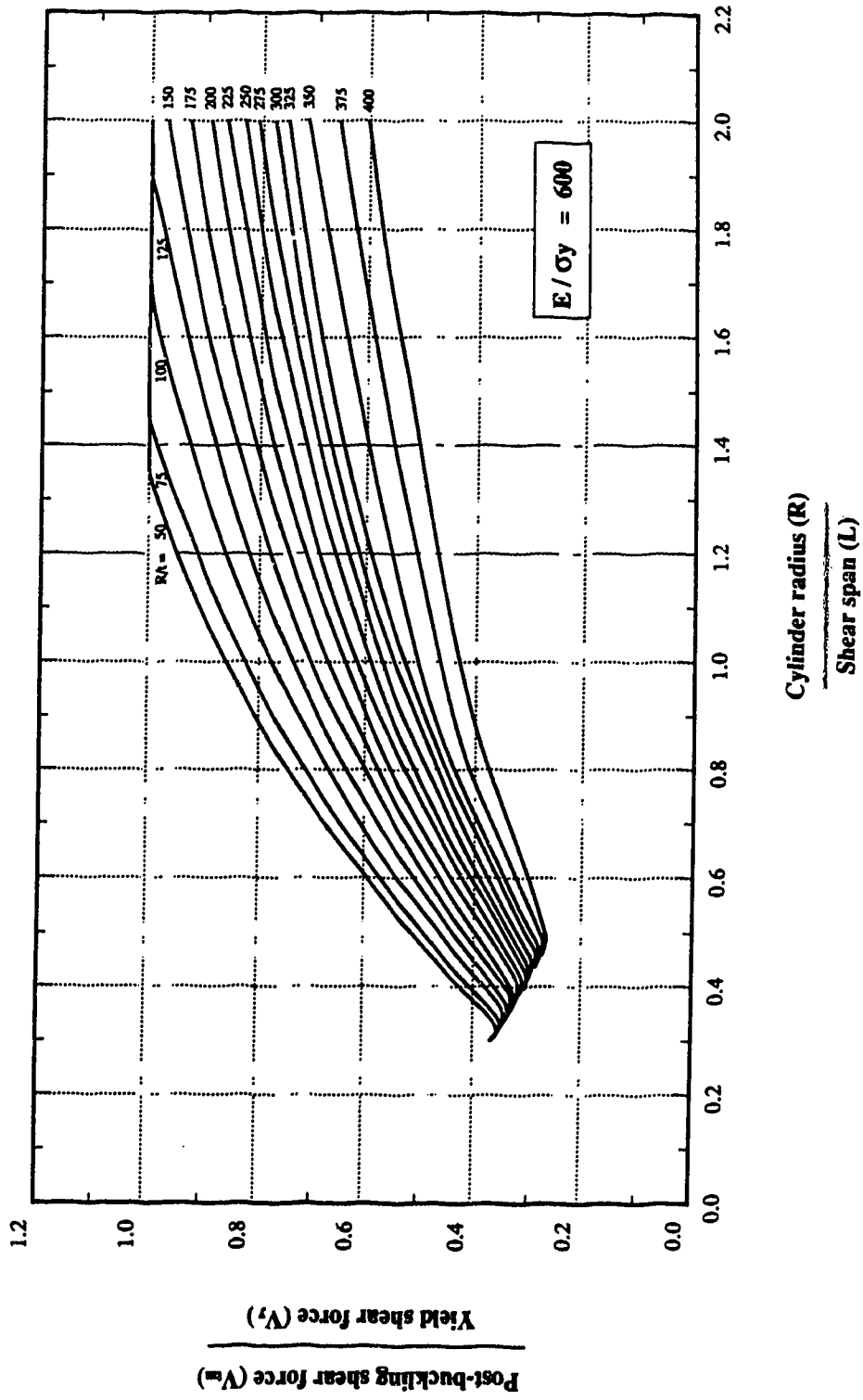


Fig. 6.18(b) Post-buckling shear capacity for thin-walled cylinders

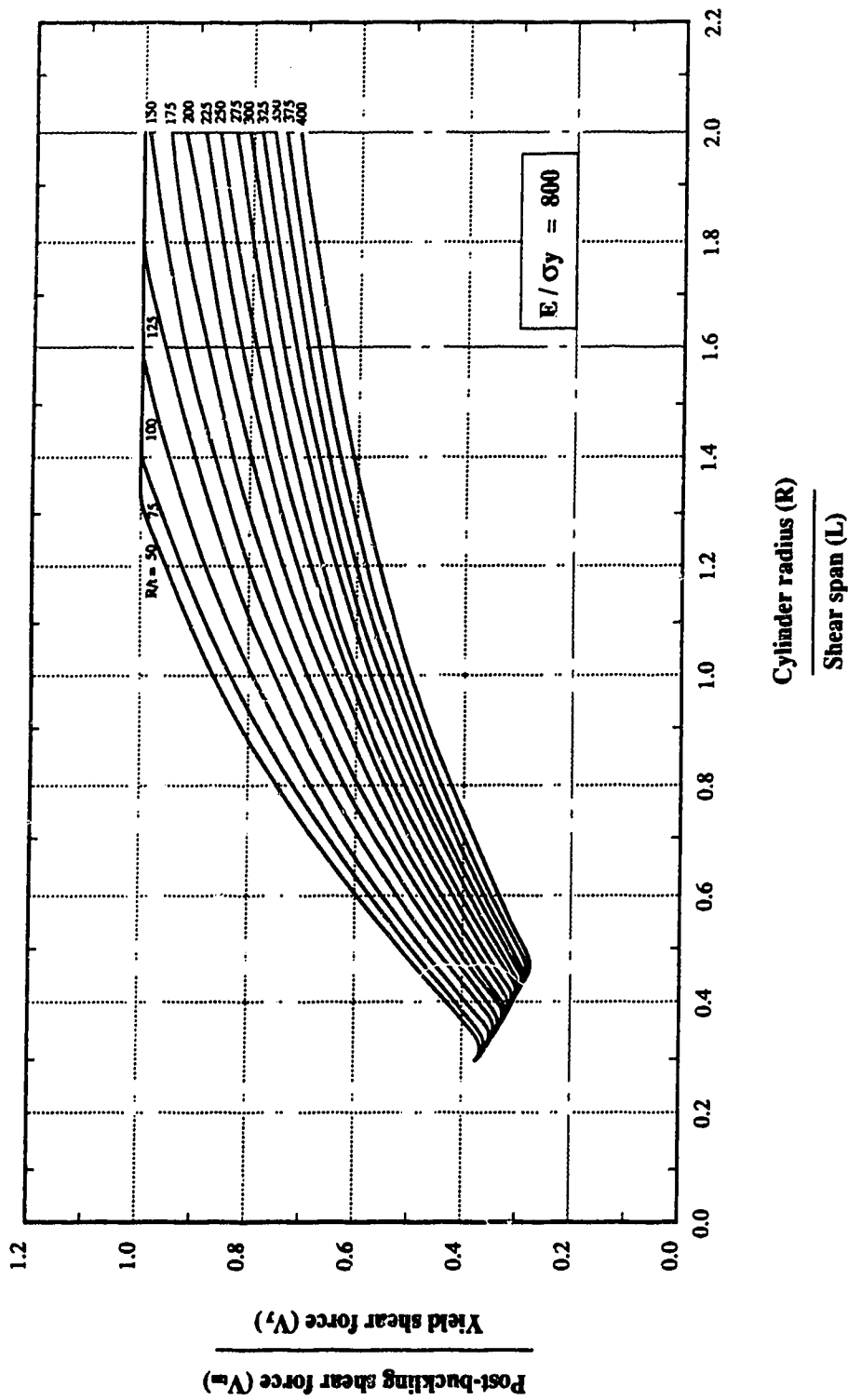


Fig. 6.18(c) Post-buckling shear capacity for thin-walled cylinders

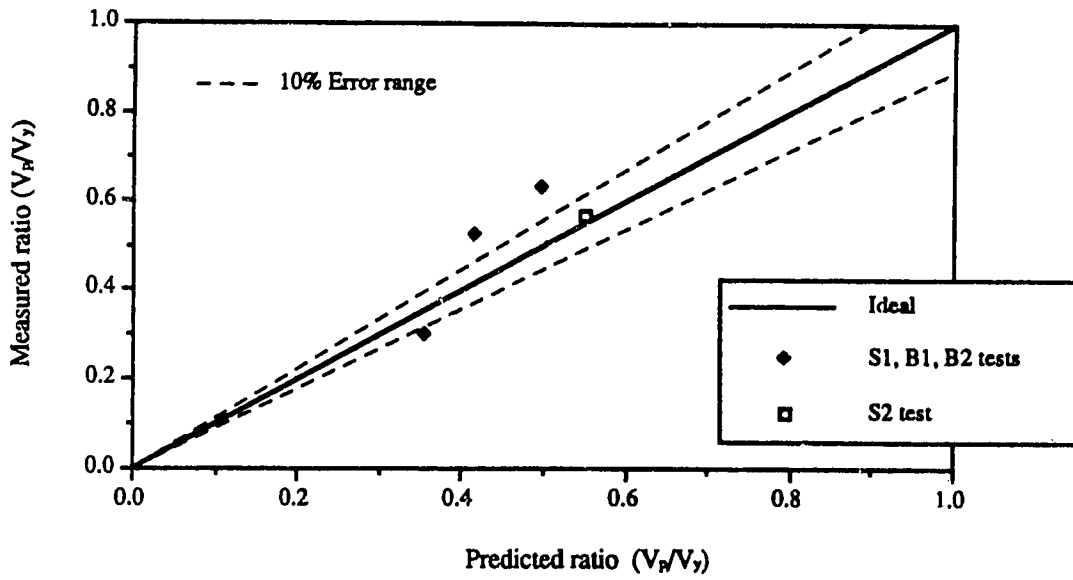


Fig. 6.19 Comparison between the truss model and full-scale tests

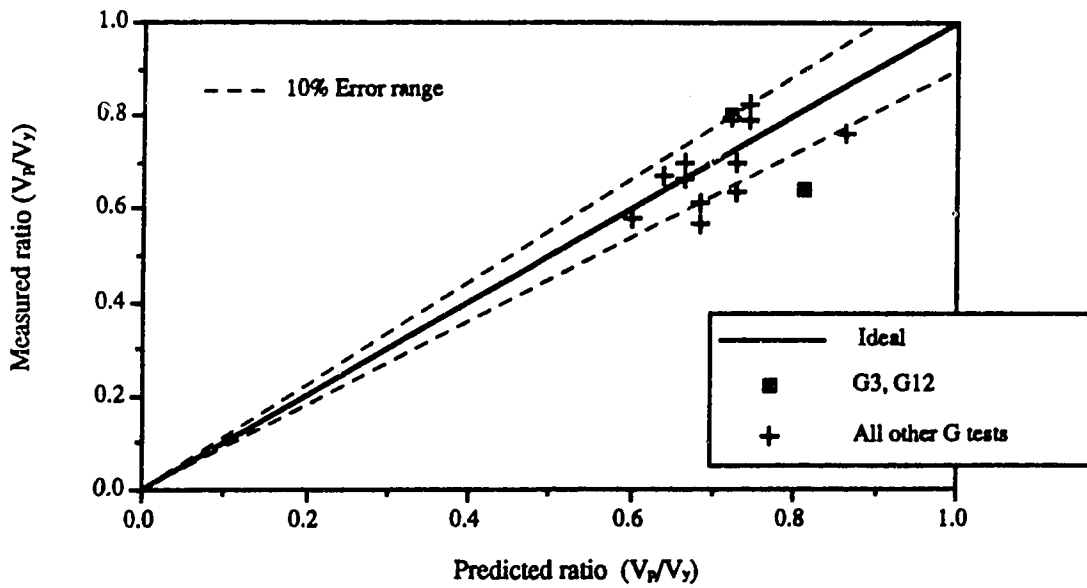


Fig. 6.20 Comparison between the truss model and Galletly's tests

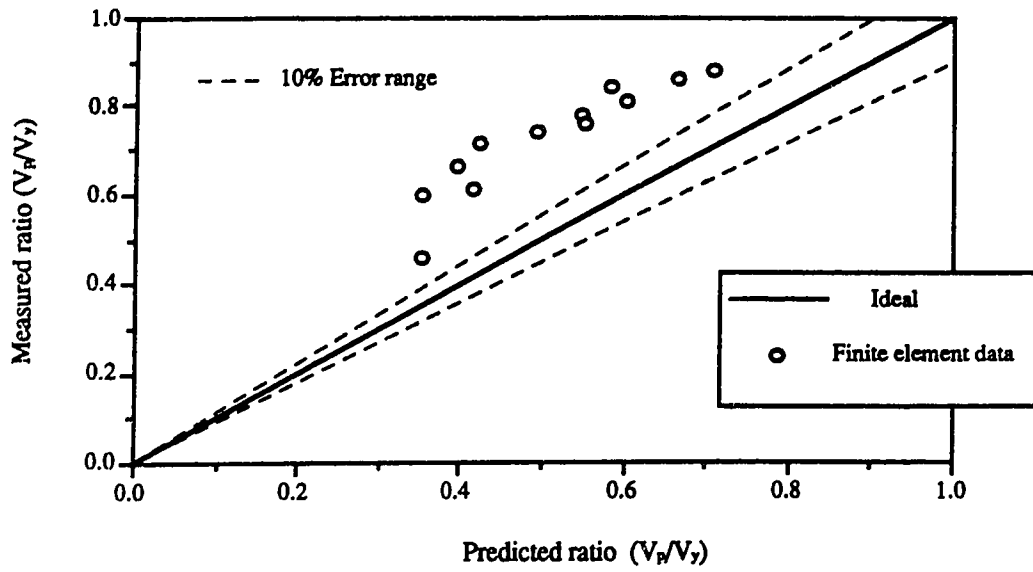


Fig. 6.21 Comparison between the truss model and finite element results

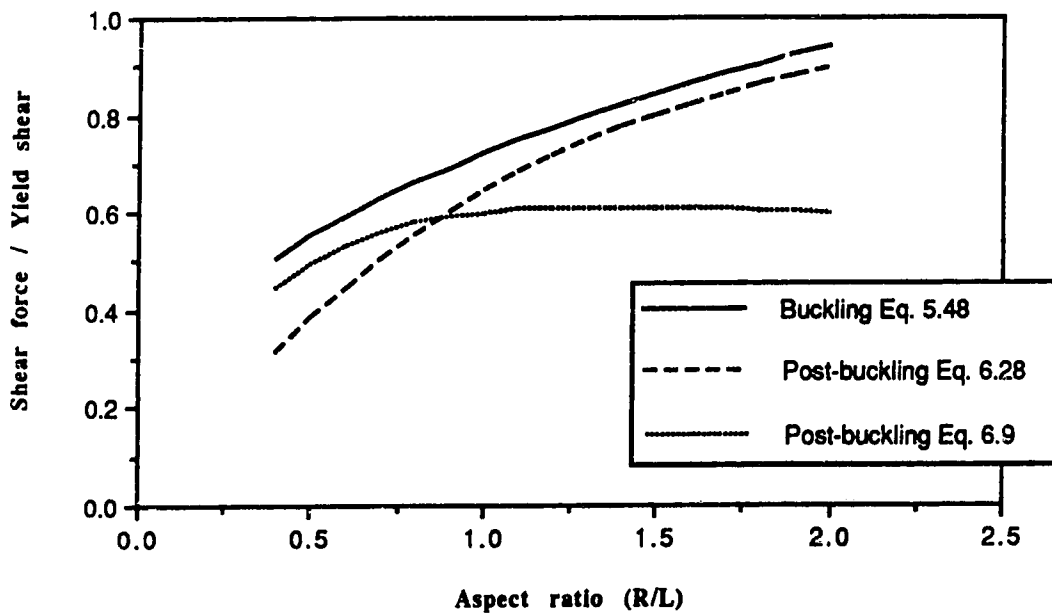


Fig. 6.22 Comparison between buckling and post-buckling strength for different aspect ratios ($R/t=200$, $E/\sigma_y=600$)

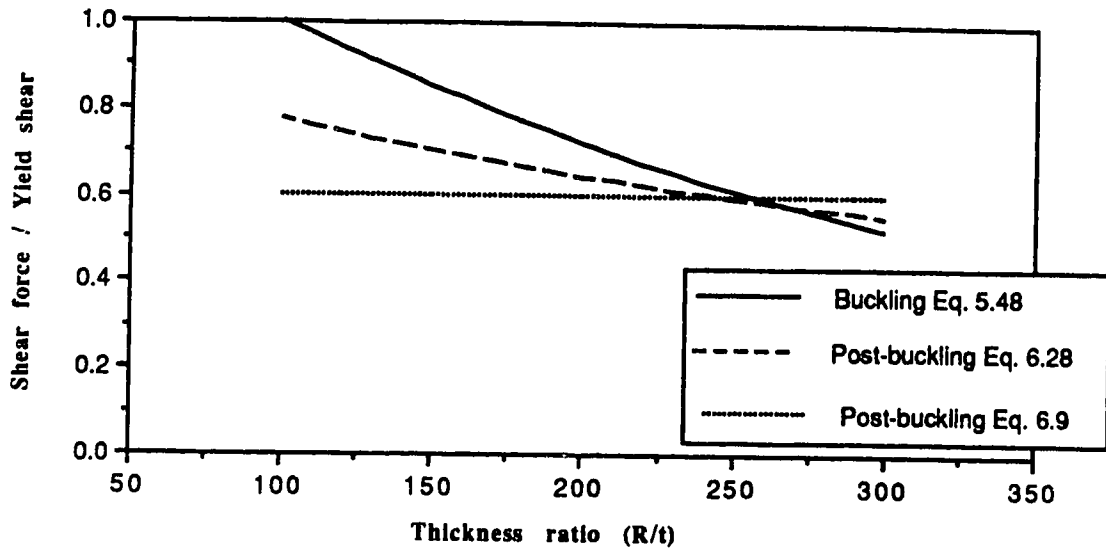


Fig. 6.23 Comparison between buckling and post-buckling strength for different thickness ratios ($R/L=1.0$, $E/\sigma_y=600$)

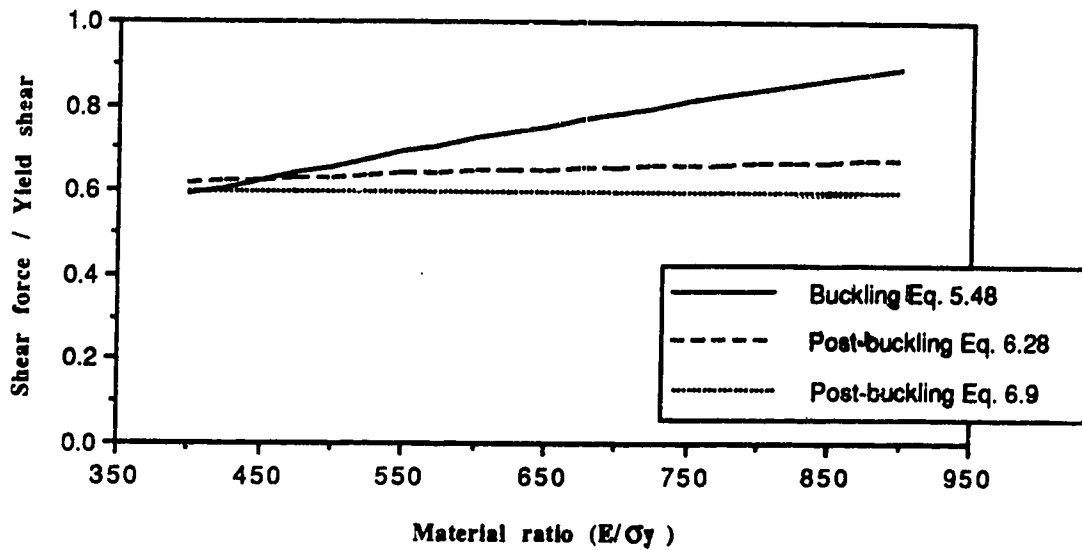


Fig. 6.24 Comparison between buckling and post-buckling strength for different material ratios ($R/t=200$, $R/L=1.0$)

7. Summary and Conclusions

7.1 Summary and Conclusions

The inelastic shear behavior of large-diameter cylindrical shells subjected to transverse loads was investigated both experimentally and numerically. Two specimens of 1270 mm diameter were tested under different boundary conditions. After the buckling load was reached, testing was continued in order to determine the post-buckling characteristics of the transversely loaded cylinders. Numerical analysis was performed *a priori* to help plan the tests and to offer insight into the findings. Subsequently, two design approaches were proposed. One approach was based on a regression analysis of the available test data as well as a parametric numerical analysis. The other approach was based on a mechanistic truss model.

The experiments confirmed that thin-walled tubes loaded in transverse shear behave in a linear elastic manner up to a proportional load level. Following this, the response becomes gradually non-linear until inelastic buckling occurs. In the linear elastic range, the stresses could be estimated according to the classical beam theory. Beyond the proportional load level the presence of the initial stresses and initial imperfections distort the predictions of the beam theory. After reaching the ultimate load, the cylinder shear capacity drops to a stable lower level. This secondary post-buckling capacity is conditional on the existence of stiff elements in the boundaries of the shear span, such as ring stiffeners

or end diaphragms. Some of the aforementioned observations were also reported by other investigators (Bailey and Kulak, 1984).

The behavior of the tested specimens was successfully simulated using nonlinear finite element analysis. A 16-node degenerated plate-shell element was used to predict the cylinder response. The analysis incorporated the geometric imperfections measured in the test and the locked-in stresses initiated due to cold bending. The analysis showed that shear buckling of thin-walled tubes is not sensitive to geometric imperfections. Meanwhile, locked-in stresses proved to be an important factor in determining the inelastic buckling strength. Insensitivity to imperfection was also observed by others (Galletly and Blachut, 1985, and Roman and Elwi, 1987).

In order to properly model the test specimen, the boundary conditions that actually existed in the test (frame and fixture stiffness) have to be introduced in the numerical model. Allowing for these effects, the numerical simulations carried out in this work matched closely the response of the full-scale test results with respect to both strength and stiffness.

The numerical analysis was used to generate data beyond that relating to the test specimens. Once the numerical study had been used to establish trends, only the test data were used to determine the empirical design equation that predicts the ultimate capacity of thin-walled cylinders under transverse loads. The proposed equation, Eq. 5.48, is a best-fit regression model of all the available test results,

and is therefore more accurate in predicting the shear test results than the empirical interaction equation proposed by Galletly and Blachut (1985). Equation 5.48 has two upper limits; the yield shear capacity (Eq. 5.49) and the elastic shear capacity (Eq. 5.50). The recommended equation was derived for cylinders within specific ranges of geometric and material variables (Eq. 5.51). The accuracy of the equation outside these ranges is uncertain.

An alternate method, also suited for design purposes, was developed to predict the post-buckling shear capacity of thin-walled tubes. Based on the test results in the post-buckling range and the results of the numerical analyses, a truss model which simulates the load carrying mechanism beyond the limit point was proposed and compared with other models. The proposed model idealizes the cylinder behavior by two force fields, tension and compression, acting together to support the transverse load. The tension field takes the general direction of the diagonal buckles, while the compression field takes a crossing direction to balance the horizontal component of the tension field. Both force fields anchor in the stiff vertical boundaries (ring stiffeners or end diaphragms).

The truss model predictions compare well with the post-buckling test information available. The proposed truss model demonstrates the favorable attribute of being a lower limit to the ultimate shear capacity presented by equation 5.48. Thus, the truss model can be used as a conservative predictor of the shear capacity. The model also shows better agreement with the buckling behavior of thin-walled cylinders than does the Roman-Elwi model. The shear

capacity of the proposed truss model is presented in the form of design curves (Figs. 6.18(a), 6.18(b), and 6.18(c)). Limits on the shear capacity derived using the truss model are the yield shear capacity and the elastic buckling shear capacity of the cylinder. It is to be noted that the strength curves given in Fig. 6.18 were terminated when the shear span was long enough to induce a flexural buckling mode rather than a shear buckling mode.

7.2 Recommendations for Future Research

When the experimental program was planned, it was decided to test a few full-scale specimens rather than a large number of small scale specimens. Obviously, large-diameter specimens provide a clear and accurate view of the shear buckling problem especially in the post-buckling range. However, the number of full-scale tests carried out so far is still small and more tests are desirable in order to improve the confidence in the design models.

The minimum rigidity of the circumferential stiffeners required to anchor the tension and compression fields needs to be investigated. Spacing of ring stiffeners defines the length of the shear span and controls the ultimate shear strength. They also provide the support for the inclined force fields in the post-buckling range. The rigidity of the ring stiffeners therefore has a direct effect on the shear capacity.

References

- Adams, C. M., "*Cooling Rates and Peak Temperatures in Fusion Welding*," *Welding Journal* 37(5), pp. 2105, May, 1958.
- Ahmad, S., Irons, B. M., and Zienkiewicz, O. C, "*Analysis of Thick and Thin Shell Structures by Curved Finite Elements*," *International Journal for Numerical Methods in Engineering*, Vol. 2, pp. 419-451, 1970.
- American Society for Testing and Materials, *Standard Methods of Tension Testing of Metallic Materials*, ASTM Standard, 01.01 E 8M-88a, 1989.
- American Water Works Association, *AWWA Standard for Steel Water Tanks, Standpipes, Reservoirs, and Elevated Tanks for Water Storage*, AWWA D101-53, 1986.
- Arbocz, J. and Babcock, C. D., "*Prediction of Buckling Loads Based on Experimentally Measured Initial Imperfections*," *Proceedings IUTAM, Symposium on Buckling of Structures*, edited by B. Budiansky, Springer-Verlag, Heidelberg, pp. 291-311, 1976.
- Arbocz, J. and Babcock, C. D., "*The Buckling Analysis of Imperfect Sensitive Shell Structures*," Contractor report-3310, NASA, 1980.
- Arbocz, J., "*The Effect of Initial Imperfections on Shell Stability*," *Thin-Shell Structures. Theory, Experiment and Design*.

edited by Y. C. Fung and E. E. Sechler, Prentice-Hall, Englewood Cliffs, N. J., 1974.

Babcock, C. D., "*Experiments on Shell Buckling*," Thin-Shell Structures, Theory, Experiment and Design, edited by Y. C. Fung and E. E. Sechler, Prentice-Hall, Englewood Cliffs, N. J., 1974.

Bailey, R. W. and Kulak G. L., "*Flexural and Shear Behavior of Large Diameter Steel Tubes*," Structural Engineering Report No. 119, Dept. of Civil Engineering, University of Alberta, November 1984.

Baker W. E. and Bennett J. G., "*Experimental Investigation of the Buckling of Nuclear Containment-like Cylindrical Geometries under Combined Shear and Bending*," Nuclear Engineering and Design, Vol. 79, n2, pp. 211-216, May, 1984.

Basler, K., "*Strength of Plate Girders in Shear*," Journal of the Structural Division, Proc. of the ASCE, Vol. 87, No. ST7, October, 1961.

Batdorf, S. B., Stein, M., and Schildcrout, M., "*Critical Stress of Curved Rectangular Panels*," Technical Note No. 1348, NACA, Washington, D.C., May, 1947.

Batdorf, S. B., Stein, M., and Schildcrout, M., "*Critical Stress of Thin-Walled Cylinders in Torsion*," Technical Note No. 1344, NACA, Washington, D.C., June, 1947.

- Bathe, K. J. and Ho, L. W., "*A Simple and Effective Element for Analysis of General Shell Structures*," *Computers and Structures*, Vol. 13, pp. 673-681, 1981.
- Berenson, M. L., Levine, D. M. and Goldstein, M., "*Intermediate Statistical Analysis and Applications, a Computer Package Approach*," McGraw-Hill, Inc., 1983.
- Bridget, F. J., Jerome, C. L., and Vosseller, A. B., "*Some Experiments on Buckling of Thin-Walled Constructions*," *Trans. of the ASME, APM 56-6*, Vol. 56, No. 8, pp. 569-578, August, 1934.
- Burington, R. S., "*Handbook of Mathematical Tables and Formulas*," Handbook Publishers, Inc., 1948.
- Canadian Standards Association, *Structural Quality Steels, CSA-G40.21-M87*, 1987.
- Chalhoub, M. S., and Kelly, J. M., "*Earthquake Simulator Testing of Cylindrical water tanks in Base Isolated Structures*," 1988 ASME Pressure Vessels and Piping Conference, Publ. by ASME, PVP Vol. 147, New York, N. Y., pp. 51-64, 1988.
- Chen, W. F., Bubenik, T. A., and Sohal, I. S., "Effect of Pressure on Tubular Beam-Column Capacity," *Journal of Constructional Steel Research*, Vol. 13, No. 1, pp. 23-42, 1989.
- Corona, E., and Kyriakides, S., "*On the Collapse of Inelastic Tubes Under Combined Bending and Pressure*," *International*

Journal of Solids and Structures, Vol. 24, No. 5, pp. 505-535, 1988.

Crisfield, M. A., "A quadratic Mindline Element Using Shear Constraints," Computers and Structures, Vol. 18, pp. 833-852, 1984.

Donnell, L. H. and Wan, C. C., "Effect of Imperfections on Buckling of Thin Cylinders and Columns under Axial Compression," Journal of Applied Mechanics, Trans. of the ASME, Vol. 17, pp. 73-83, March, 1950.

Donnell, L. H., "A New Theory for the Buckling of Thin Cylinders Under Axial Compression and Bending," Trans. of the ASME, Aer-56-12, Vol. 56, pp. 795-806, 1934.

Donnell, L. H., "Stability of Thin-Walled Tubes Under Torsion," Technical Note No. 479, NACA, Washington, D.C., June, 1933.

Ellinas, C. P., Supple, W. J., and Walker, A. C., "Buckling of Offshore Structures, A State-of-the-Art-Review of the Buckling of Offshore Structures," prepared by J. P. Kenny and Partners Ltd., Granada Publishing Ltd., London, 1984.

European Convention for Constructional Steelwork, "Buckling of Steel Shells, European Recommendations," Technical Committee 8 - Structural Stability, Technical Working Group 8.4 - Stability of Shells, 1988.

- Galletly, D. G. and Blachut, J., "*Plastic Buckling of Short Cylindrical Shells Subjected to Horizontal Edge Shear Loads*," Journal of Pressure Vessel Technology, Trans. of the ASME, Vol. 107, pp. 101-107, May 1985.
- Galletly, G. D., James, S., Kruzelecki, J., and Pemsing, K., "*Interactive Buckling Tests on Cylinders Subjected to External Pressure and Axial Compression*," Journal of Pressure Vessel Technology, Vol. 109, pp.10-18, Feb., 1987.
- Gerard, G. and Becker, H., "*Handbook of Structural Stability, Part III, Buckling of Curved Plates and Shells*," Technical Note No. 3783, NACA, Washington, D.C., August, 1957.
- Gerard, G., "*Compressive and Torsional buckling of thin wall Cylinders in Yield Region*," Technical Note No. 3726, NACA, Washington, D.C., August, 1956.
- Gerard, G., "*Introduction to Structural Stability Theory*," McGraw-Hill Book Co., Inc., New York, N. Y., 1962.
- Häfner, L., Ramm, E., Sättele, J. M., and Stegmüller, H., "*NISA 80-Programmdokumentation-Programmsystem*," Bericht Des Institut Für Baustatik, Universität Stuttgart, Stuttgart, West Germany, 1981.
- Huang, H. C. and Hinton, E, "*A New Nine Node Degenerated shell Element with Enhanced Membrane and Shear Interpolation*," International Journal for Numerical Methods in Engineering, Vol. 22, pp. 73-92, 1986.

- IMSL, Inc., "*STAT/LIBRARY, FORTRAN Subroutines for Statistical Analysis*", 1987.
- Love, A. H., "A Treatise on the Mathematical Theory of Elasticity," Dover Publications, N. Y., 1944.
- Lu, S. Y., "*Plastic Stability Theory of Thin Shells*," AIAA Journal, Vol. 3, Part 2, pp. 2350-2351, December, 1965.
- Lundquist, E. E., "*Strength Tests of Thin-Walled Duralumin Cylinders in Combined Transverse Shear and Bending*," Technical Note No. 523, NACA, Washington, D.C, April 1935.
- Lundquist, E. E., "*Strength Tests on Thin-Walled Duralumin Cylinders in Torsion*," Technical Note No. 427, NACA, Washington, D.C, Aug. 1932.
- Mok, J. and Elwi, A. E., "*Shear Behavior of Large Diameter Fabricated Steel Cylinders*," Structural Engineering Report No. 136, Dept. of Civil Engineering, University of Alberta, June, 1986.
- Kui, L. X., Liu, G. Q., and Zienkiewicz, O. C., "*A Generalized Displacement Method for the Finite Element Analysis of Thin Shells*," International Journal of Numerical Mathematical Engineering, Vol. 21, pp. 2145-2155, 1985.
- Pascoe, K. L., "*Strength of Cold-Formed Cylindrical Steel Plates*," Journal of Strain Analysis, Vol. 6, Part 3, 1971.

- Pawsey, S. F. and Clough, R. W., "*Improved Numerical Integration of Thick Shell Finite Element*," International Journal for Numerical Methods in Engineering, Vol. 3, pp. 575-586, 1971.
- Petrick, J. D., "*Nonlinear Finite Element Analysis of Thin-Walled Cylindrical Shells Subject to Pure Bending*," Department of Civil Engineering, University of Manitoba, Winnipeg, Manitoba, 1985.
- Pinkney, R. B., Stephens, M. J., Murray, D. W., and Kulak, G. L., "*Use of Measured Imperfections to Predict the Buckling of Axially Loaded Cylindrical Shells*," Canadian Journal of Civil Engineering, Vol. 10, No. 4, pp. 662-669, 1983.
- Plantema, F. J. "*Collapsing Stresses of Circular Cylinders and Round Tubes*," Nat. Luchtvaartlaboratorium, Amsterdam, Holland, Report S.280, 1946.
- Ramm, E., "*A Plate/Shell Element for Large Deformations and Rotations*," Formulations and Computational Algorithms in Finite Element Analysis, Edited by Bathe, K. J., Oden, J. T., Wunderlich, W., MIT Press, Boston, 1977.
- Ramm, E., "*A Plate/Shell Element for Large Deformations and Rotations*," Nonlinear Finite Element Analysis in Structural Mechanics, Edited by, Wunderlich, W., Stein, E. and Bathe, K. J., Proceedings of the Europe-U.S Workshop,

Ruhr Universitat, Bochum, West Germany, pp. 63-89, 1980.

Ramm, E. and Matzenmiller, A. "*Large Deformation Shell Analyses Based on the Degeneration Concept*," State-of-the-art Texts on Finite Element Methods for Plate and Shell Structures, Edited by Hughes, T. J. R. and Hinton, E., Pineridge Press, Swansea, UK, 1986.

Rawling, J., "*Applied Regression Analysis: a Research Tool*" , The Wadsworth & Brooks/Cole Statistics/Probability Series, 1988.

Roman, V. G. and Elwi, A. E., "*Post-buckling Behavior of Thin Steel Cylinders under Transverse Shear*," Structural Engineering Report No. 146, Dept. of Civil Engineering, University of Alberta, May, 1987.

Ross, D. A. and Chen, W. F., "*tests of Fabricated Tubular Columns*," ASCE Nat. Water Resources and Ocean Engineering Convention, San Diego, Calif., Reprint 2660, April, 1976.

Rotter, J. M., "*Recent Advances in the Structural Design of Steel Bins and Silos*," Proc. of the Pacific Structural Steel Conference, Publ. by New Zealand Heavy Engineering Research Assoc., Manukau City, N. Z., Vol. 4, pp. 177-194, 1986.

Salmon, C. G. and Johnson, J. E., "*Steel Structures, Design and Behavior*," Third Edition, Harper and Row, 1990.

- Schilling C. G., "*Buckling Strength of Circular Tubes*," Journal of the Structural Division, Proc. of the ASCE Vol. 91, pp. 325-349, October, 1965.
- Schroder, V. P., "*Über die Stabilität der Querkraftbelasteten Dünwandigen Kreiszyllinderschale*," (an English translation) Zeitschrift für Angewandte Mathematik und Mechanik, T145-T148, 1972.
- Seide, P. and Weingarten, V. I., "On the Buckling of Circular Cylindrical Shells Under Pure Bending," Journal of Applied Mechanics, Trans. of the ASME, Vol. 28, pp. 112-116, March, 1961.
- Sherman, D. R., "*Changes in Tubular Design Codes*," Proc. Structures Congress 89, Publ. by ASCE, New York, N.Y., pp. 175-184, 1989.
- Stander, N., Matzenmiller, A., and Ramm, E. "*An Assessment of Assumed Strain Methods in Finite Rotation Shell Analysis*," Engineering Computation, Vol. 6, March, pp. 58-66, 1989.
- Stegmüller, H., "*NISA- Input Description*," Institut für Baustatik, Universität Stuttgart, Stuttgart, West Germany, April 20, 1984.
- Stegmüller, H., Häfner, L., Ramm, E., and Sättele, J. M., "*Theoretische Grundlagen Zum FE-Programm System NISA80*," 1983.

- Stephens, M. J., Kulak, G. L. and Montgomery, C. J., "*Local Buckling of Thin-Walled Tubular Steel Members*," Structural Engineering Report No. 113, Dept. of Civil Engineering, University of Alberta, February, 1982.
- Structure Stability Research Council, "*Guide to Stability Design Criteria for Metal Structures*," T. V. Galambos, Editor, Fourth Edition, John Wiley and Sons, New York, N. Y., 1988.
- Tennyson, R. C., "*An Experimental Investigation of the Buckling of Circular Cylindrical Shells in Axial Compression Using the Photoelastic Technique*," Institute of Aerospace Sciences, University of Toronto, Report - 102, Nov., 1964.
- Timoshenko, S., and Gere, J., "*Theory of Elastic Stability*," McGraw Hill, New York, N. Y., pp. 465, 1961.
- Wesolowsky, G. O., "*Multiple Regression and Analysis of Variance, an Introduction for Computer Users in Management and Economics*", Wiley-Interscience Publication, 1976.
- White, J. D. and Dwig, J. B., "*Weld Shrinkage in Large Stiffened Tubulars*," International Conference in Residual Stresses in Welded Construction and Their effects, Welding Institute, Cambridge , pp. 337-348, 1976.
- Wilson, W. M. and Newmark, N. M., "*The Strength of Thin Cylindrical Shells as Columns*," University of Illinois, Engineering Experiment Station, Bull. 255, 1933.

- Yamaki, N., "*Elastic Stability of Circular Shells*," North-Holland Series in Applied Mathematics and Mechanics, Elsevier Science Publisher B.V., 1984.
- Yamaki, N., "*Experiments on the Post-buckling Behavior of Circular Cylindrical Shell under Torsion*," Proceedings IUTAM, Symposium on Buckling of Structures, edited by B. Budiansky, Springer-Verlag, Heidelberg, pp. 312-330, 1976.
- Yamaki, N., Naito, K. and Sato, "*Buckling of Circular Cylindrical Shells under Combined Action of a Transverse Edge Load and Hydrostatic Pressure*," Proceedings of the International Conference on Thin-Walled Structures, University of Strathclyde, Glasgow, April 1979.
- Zienkiewicz, O. C, Taylor, R. L., and Too, J. M., "*Reduced Integration Technique in General Analysis of Plates and Shells*," International Journal for Numerical Methods in Engineering, Vol. 3, pp. 275-290, 1971.

Appendix A

Regression Analysis Program

```
C=====
C
C THIS FORTRAN PROGRAM PROVIDES REGRESSION DATA AND REGRESSION
C MODEL TO THE REGRESSION ANALYSIS SUBROUTINE RNLIN AND PRINT
C THE REGRESSION CONSTANTS AND CORRELATION FACTOR R2.
C
C=====
```

```
INTEGER LDR, NOBS, NPARM
PARAMETER *(NOBS=29, NPARM=4, LDR=NPARM)
INTEGER IDERIV, IRANK
REAL DEF, FUNC, R(LDR, NPARM), SSE, PAR(NPARM),
& X1DATA(NOBS), X2DATA(NOBS), X3DATA(NOBS),
& YDATA(NOBS)
EXTERNAL FUNC, RNLIN
```

```
C===== THE INITIAL REGRESSION CONSTANTS =====
10 READ(5,*) PAR
IF(PAR(1).EQ.999) GO TO 20
WRITE(6,*) 'PAR INITIAL = ', PAR
IDERIV = 0
```

```
C===== THE SOLVER SUBROUTINE =====
CALL RNLIN (FUNC, NPARM, IDERIV, PAR, R, LDR, IRANK, DEF,
& SSE)
WRITE(6,*) 'PAR = ', PAR
```

```
C===== THE CORRELATION FACTOR =====
RSQU= 1.0-SSE/0.5936764
WRITE(6,*) 'IRANK = ', IRANK, ' DEF = ', DEF, ' SSE = ',
& SSE, ' R2 = ', RSQU
GOTO 10
20 END
```

```
C===== THE FUNCTION SUBROUTINE =====
SUBROUTINE FUNC (NPARM, PAR, IOPT, IOBS, FRQ, WT,
& E, DE, IEND)
INTEGER NPARM, IOPT, IOBS, IEND
REAL PAR(NPARM), FRQ, WT, E, DE(1)
INTEGER NOBS
```

```

PARAMETER (NOBS=29)
REAL EXP, X1DATA(NOBS), X2DATA(NOBS), X3DATA(NOBS),
&      YDATA(NOBS)
COMMON /XYDATA/ X1DATA, X2DATA, X3DATA, YDATA
INTRINSIC EXP
IF (IOBS .LE. NOBS) THEN
WT   = 1.0E0
FRQ  = 1.0E0
IEND = 0

```

C===== THE REGRESSION MODEL =====

```

E = YDATA(IOBS)*1.73205-PAR(1)*EXP(X1DATA(IOBS)*PAR(2))
&   *X2DATA(IOBS)**PAR(3)*X3DATA(IOBS)**PAR(4)
ELSE
IEND = 1
END IF
RETURN
END

```

C===== THE REGRESSION DATA =====

```

INTEGER NOBS
PARAMETER (NOBS=29)
REAL X1DATA(NOBS), X2DATA(NOBS) X3DATA(NOBS)
&   ,YDATA(NOBS)
COMMON /XYDATA/ X1DATA, X2DATA, X3DATA, YDATA

DATA YDATA/.368,.371,.409,.46,.219,.286...5,.477,
&      .577,.569,.591,.567,.409,.438,.457,.502,.544,.462,
&      .479,.414,.423,.493,.543,.41,.47,.52,.423,.48,
&      .513/
DATA X1DATA/188.,188.,188.,188.,250.,250., 188.,188.,
&      150.,150.,125.,125.,150.,150.,125.,125.,126.,151.,
&      129.,155.,150.,150.,150.,188.,188.,188.,250.,250.,
&      250./
DATA X2DATA/.53,.53,.76,.76,.5,.5, 1.,1.,
&      1.,1.,1.,1.,1.,1.,1.,1.,1.37,1.37,
&      0.83,0.83,.5,.75,1...5,.75,1...5,.75,
&      1./
DATA X3DATA/645.,645.,643.,643.,679.,679., 671.,671.,
&      840.,840.,704.,704.,457.,457.,547.,547.,533.,457.,
&      533.,457.,667.,667.,667.,667.,667.,667.,667.,667.,
&      667./
END

```

Appendix B

Taylor's expansion of Eq. 5.23

Equation 5.23 can be written in terms of one variable Z as follows :

$$Y = (1 + Z^{-n})^{-1/n} \quad (\text{B.1})$$

in which $Z = 0.74 (3.0^{0.5}) X_1^{-1.25} X_2^{0.5} X_3$. Using Taylor's theorem, Eq. B.1 can be expanded into a polynomial of n^{th} degree.

$$Y = Y(h) + Y'(h) (Z-h) + \frac{Y''(h)}{2!} (Z-h)^2 + \frac{Y'''(h)}{3!} (Z-h)^3 + \dots + \frac{Y^{(n)}(h)}{n!} (Z-h)^n + R_n \quad (\text{B.2})$$

In which the superscript on $Y(h)$ defines the derivative with respect to Z , h is an arbitrary value and R_n is the remainder after n number of terms and it is equal to $Y(Z_1)^{(n)}(Z-h)^n/n!$ where Z_1 is a value between Z and h . Since the value of Z for the data in Table 5.1 varies from 0.6 to 2.2, then if h is chosen as 1.4, $(Z-h)^n$ will be numerically small and R_n can be neglected. Consequently, Eq. B.1 can be accurately approximated by a third degree polynomial of Z or any parameter that is proportional to Z as Φ . Therefore, Y can be written as follows:

$$Y = a + b \Phi + c \Phi^2 + d \Phi^3 \quad (\text{B.3})$$

For a specific h , the constants a , b , c and d can be calculated from Eq. B.2 or, alternatively, they can be tailored by determining them from the regression analysis of the data set.

Appendix C

Truss Model Subroutine

```
C===== C
C THIS PROGRAM CALCULATES THE TRUSS MODEL EQUATIONS 6.10 TO 6.28 C
C FOR INCREMENTS OF THE TENSION FIELD SLOPE  $\zeta$  AND CHOOSES THE C
C MAXIMUM VALUE  $\tau_{tm}$ . THE PROGRAM ALSO CHECK THE DERIVATIVE C
C ACCORDING TO EQUATION 6.29. C
C===== C
```

```
REAL RT,RL,ES,A,ETA,ETAC1,ETAC,SC,EM,ETAC1
REAL ETAC2,GAMAS,VER,VG,VK,AA,PA,PA0,VT,VC,ERR
REAL ETA0,FF,VK1,VK2,VK3,VMAX,ETAM,ETACM
```

```
C
C ACU IS AN ITERATIONS INCREMENT FACTOR :
C ACU = 1.0 GIVES LOW ACCURACY
C (ANGLES' INCREMENT IS 0.57 DEGREES AND TOLERANCE IS 1.0%)
C ACU = 10.0 GIVES HIGH ACCURACY
C (ANGLES' INCREMENT IS .057 DEGREES AND TOLERANCE IS 0.5%)
C
C
```

```
WRITE(6,*) ' PLEASE, ENTER E / $\sigma_y$ , R/t, R/L, ACU (1 to 10) '
99 READ (5,*) ES, RT, RL, ACU
TOLEC = .01 / ACU
STEEC = .01 / ACU
STEET = .01 / ACU
ETA0 = .01
VMAX = 0.0
ETAM = 0.0
ETACM = 0.0
KOKO = 1.57/STEET
```

```
C===== ITERATION ON THE TENSION FIELD SLOPE ===== C
```

```
DO 30 K=1,KOKO
ETA0 = ETA0 + 3.*STEET
DO 33 KK = 1,3
ETA = ETA0 + STEET*(KK-2)
AA = 3.1415927-TAN(ETA)/RL
EM = 0.82*0.5*355.3/(355.3+AA**2)
ETAC1 = RL/2.*AA
GAMAS = RT**(-1.5)*ES**0.5
IF (GAMAS.LE.0.0036) THEN
SC = 119.3*GAMAS
ELSE
IF (GAMAS.GE.0.0527) THEN
SC = 1.0
ELSE
SC = 1.625+0.489*ALOG10(GAMAS)
ENDIF
ENDIF
```



```

ENDIF
ETAC2 =RL/1.5*COS(ETA)**2.*AA*EM/SC
ETAC1 =0.0
LOLO = 1.57 / STEEC

```

===== ITERATION ON THE COMPRESSION FIELD SLOPE =====

```

DO 40 M=1,LOLO
  ETAC1 =ETAC1+STEEC
  PA0 =ETAC1-ETAC2/COS(ETAC1)/COS(ETAC1)
  IF (PA0 .LT. 0.0 ) THEN
    ETAC = 0.0
    GO TO 50
  ELSE
    PA =ABS(TAN(ETAC1)-PA0)/TAN(ETAC1)
    IF (PA.GT.TOLEC) GO TO 40
    ETAC = ETAC1
    GO TO 50
  ENDIF
CONTINUE
40  WRITE (6,70)
50  VT =SIN(2*ETA)*(1-COS(AA))/2.
    VC =COS(ETA)**2*AA*SIN(AA/2.)*TAN(ETAC)

```

===== CALCULATION OF THE POST-BUCKLING SHEAR RATIO =====

```

VK =EM*(VT+VC)*2/3.1415927
IF (VMAX .LT. VK) THEN
  VMAX = VK
  ETAM =ETA
  ETACM =ETAC
ELSE
  ENDIF
IF (KK .EQ. 1) VK1=VK
IF (KK .EQ. 2) VK2=VK
IF (KK .EQ. 3) VK3=VK
33  CONTINUE
    DERV =(VK3-VK1)/2./STEET
30  CONTINUE

```

===== CHECKING THE DERIVATIVE =====

```

IF ( DERV.GT.TOLER) THEN 80
WRITE (6,60) ES,RT,RL,ETA,ETACM ,VMAX
60  FORMAT( ' ',6(F7.3,1X))
70  FORMAT (3X,'ERROR *** COULD NOT FIND  $\eta$  , ZERO SLOPE IS
    ASSUMED')
80  WRITE(6,88) DERV
88  FORMAT (3X,'ERROR *** DERIVATIVE OF MAXIMUM SHEAR IS
    'F7.3, ' GREATER THAN TOLERANCE.')
    GO TO 99
END

```